THE EVOLUTION OF URANINITE, COFFINITE AND BRANNERITE FROM THE OLYMPIC DAM IRON OXIDE-COPPER-GOLD-SILVER-URANIUM DEPOSIT: LINKING TEXTURAL OBSERVATIONS TO COMPOSITIONAL VARIABILITY

EDELTRAUD MACMILLAN

B.Eng. (Chem) with 1st Class Honours (2005) & B.Sc. (2005), The University of Adelaide

Grad.Dip. Metallurgy (2009), Curtin University of Technology

This thesis is submitted for the degree of Doctor of Philosophy

in the

School of Physical Sciences

at

The University of Adelaide

THE UNIVERSITY of ADELAIDE

August 2016

Adelaide, Australia

TABLE OF CONTENTS

ABSTRACT

Interpretations of mineral textures have long been used to better understand the processes involved in the formation of mineral deposits. At the Olympic Dam iron-oxide-copper-gold (IOCG)-Ag-U deposit, South Australia, the genesis and evolution of the U-mineralization is difficult to reconstruct unequivocally. Uraninite, coffinite and brannerite are the dominant U-minerals, however previous studies have focussed on the parts of the deposit which have elevated U-grade and are dominated by massive- or vein-type uraninite. Few prior studies documented the textural and chemical variability of these minerals from a broad range of samples throughout the deposit. Based on detailed mineralogical and microanalytical analysis, this study has addressed some of these shortcomings. The data and interpretation thereof allow for models and hypotheses to be made about the formation and alteration mechanisms involved in forming the mineral textures as observed today.

Two generations of uraninite have been identified, and these can be split into four main textural classes. The early generation consists of the primary, zoned and cob-web textural classes. These represent single uraninite crystals with high-Pb and ΣREE+Y (ΣREY), which have been progressively altered both chemically and texturally. The simplest cubic, euhedral morphology is displayed by the primary uraninites, which also often exhibit oscillatory and sectorial zonation of lattice-bound Pb and ΣREY, and commonly have elevated Th contents. Zoned uraninites are typically coarser, sub-euhedral to prismatic grains and contain unique zonation patterns defined by distinct zones of high- and low-Pb and ΣREY which differ to the zoning contained within the primary uraninites. The greatest heterogeneity is observed within the cob-web class, with variable hexagonal to octagonal morphologies, varying degrees of rounding, and rhythmic intergrowths of uraninite with Cu-(Fe)-sulfides ± fluorite from core to margin. There is also a late generation of uraninite which occurs in the highest-grade parts of

the deposit and exists as μm-sized grains to aphanitic varieties which form larger (up to mm-sized) aggregates and vein-fillings. Late uraninites typically have lower-Pb, but higher Ca±Si contents compared to the early generation. The early crystalline uraninites are only sparsely preserved, with the more massive-aphantitic uraninite representing the majority of the uraninite contained within the deposit.

Nanoscale characterization of selected uraninite crystals from the early generation has revealed these have a defect-free fluorite structure, and contain lattice-bound Pb+ΣREY within chemically distinct zones or domains. Micro- and nanoscale inclusions of galena, Cu-(Fe)-sulfides and REY-minerals are also present within the cob-web uraninites. The presence of both lattice-bound Pb within distinct zones and domains, as well as inclusions of galena within these uraninites, are attributed to healing of radiogenic damage via solid-state trace-element mobility, and subsequent fS_2-driven percolation of a Cu-bearing fluid allowing for inclusion nucleation and recrystallization. Crystal-structural formulae for uraninite have been calculated, and the key underlying assumption for these formulae is that lattice-bound radiogenic Pb is present, at least in part, in the tetravalent state. To distinguish the two uraninite generations, in addition to the textural and chemical differences, the oxidation state $[U^{6+}/(U^{4+}+U^{6+})]$ was calculated and it was revealed that these potentially experienced different formation conditions. The early uraninites are thought to have formed from higher temperature, granite-derived hydrothermal fluids, with later hydrothermal alteration of the zoned and cob-web types; whereas the late uraninites have formed hydrothermally at lower temperatures (<250 °C).

Additional characterization of the zoned and cob-web uraninite using electron backscatter diffraction (EBSD) has further developed our understanding of the processes involved in their evolution. Zoned uraninite has been interpreted to have formed as a result of multiple

superimposed effects, including alteration of initial oscillatory zoning (as displayed by the primary uraninite) from interaction with hydrothermal fluids and/or from self-annealing of radiation damage. Zones of weakness were created within uraninite as a result of the accumulation of defects and dislocations into tilt boundaries that correlate to one of the active slip systems in uraninite. High diffusivity pathways were generated along these zones of weakness, and aided in element mobility and exchange between uraninite and the hydrothermal fluid/s. The rhythmic intergrowths of uraninite and Cu-(Fe)-sulfides, of which the cob-web uraninites comprise, are attributed to replacement of uraninite by bornite. Replacement is thought to be controlled by the inherent chemical zoning (of Th) within the uraninite crystal, and part of the replacement occurs via coupled dissolution-reprecipitation (CDR) reaction. Initially, the bornite inherits the crystallographic orientation of the parent uraninite, but different orientations of bornite are possible due to epitaxial nucleation. Based on the presence of Cu-(Fe)-sulfide ± fluorite inclusions and the chemistry of the proposed replacement, it is suggested that replacement was driven by a F-rich hydrothermal fluid that was also enriched in Cu, S, Fe and Ca. This is the first known study which integrates the use of EBSD and other micro- and nanoscale characterization techniques to study uraninites and associated minerals. The application of CDR-driven replacement to systems which have no common chemical constituents is also at present unique. The combined use of various micro- and nanoscale characterization techniques has therefore provided some fresh insights into the reactions and enhanced our knowledge about the evolution and progressive *in-situ* alteration of uraninite at Olympic Dam.

Much of the past work conducted on the U-minerals at Olympic Dam has indicated that there were numerous cycles of U dissolution and reprecipitation, but few studies have further explored this hypothesis. Both brannerite and coffinite have also been characterized in the present study. Brannerite has a diverse morphology which ranges from complex irregular-

shaped aggregates, irregularly-shaped blebs, replacement bands, and discrete elongate seams. The internal structure of brannerite consists of randomly orientated hair-like needles and blades to a mix of uniform-massive or bleb-like irregular masses. Compositions range between that of uraniferous rutile and stoichiometric brannerite. The more uniform-massive brannerite blebs, typically have higher ΣREY, Pb, Nb ± As contents compared to the more needle-like, irregular-shaped, aggregated brannerite which contains elevated Fe, Mg ± Mn ± Na ± K. Based on chemical and textural observations, brannerite has been grouped into four distinct groups. Coffinite is typically globular to collomorph in appearance, and is often found on the margin of quartz grains and nucleates from a range of minerals including Cu-(Fe)-sulfides, galena, brannerite, uraninite, and chlorite. Variations in Ca, ΣREY, P ± As ± Nb appear to be responsible for much of the chemical heterogeneity. Three different coffinite groups have been identified based on chemical variability and textural observations, however there are some textural differences and variable mineral associations within these groups. It is likely that the textural heterogeneity is due to local variation in fluid-rock interactions.

It is concluded that brannerite and coffinite are a result of a late-stage U-event(s), and this may have involved the dissolution and/or reprecipitation of earlier precipitated uraninite, or may have involved a fresh influx of U. Factors which support late-stage formation of both brannerite and coffinite include their low-Pb contents and the occurrence of coffinite on the edges of uraninite or brannerite, indicating that the coffinite may have formed after either of these minerals. Additional features like banding, scalloped edges, alteration rinds, variable compositions etc. are also indicative that these minerals may have formed as a result of alteration and by processes which occur after initial deposition of the mineral on which they occur.

The precipitation of uraninite, brannerite and coffinite all require different conditions and chemical components, thus it is unlikely a single fluid could precipitate all of these minerals at one time. It is clear that some of the uraninites precipitated early in the formation of the deposit, but deciphering the subsequent generations of U-minerals is somewhat subjective. The results of this study will clearly document the range of textures and compositions of uraninite, brannerite and coffinite found within the Olympic Dam deposit and will provide evidence for a number of mechanisms which have contributed to their textural appearance. But, the genetic implications of these findings and what they mean for the genesis of the deposit remains unconstrained and will undoubtedly form the basis for future research.

DECLARATION

I certify that this work contains no material which has been accepted for the award of any other degree or diploma in my name, in any university or other tertiary institution and, to the best of my knowledge and belief, contains no material previously published or written by another person, except where due reference has been made in the text. In addition, I certify that no part of this work will, in the future, be used in a submission in my name, for any other degree or diploma in any university or other tertiary institution without the prior approval of The University of Adelaide and where applicable, any partner institution responsible for the joint-award of this degree.

I give consent to this copy of my thesis when deposited in the University Library, being made available for loan and photocopying, subject to the provisions of the Copyright Act 1968.

The author acknowledges that copyright of published works contained within this thesis resides with the copyright holder(s) of those works.

I also give permission for the digital version of my thesis to be made available on the web, via the University's digital research repository, the Library Search and also through web search engines, unless permission has been granted by the University to restrict access for a period of time.

Signed _____ Date _____

ACKNOWLEDGEMENTS

The completion of my Ph.D. studies and production of this thesis would not have been possible without the help and support from numerous people. First and foremost, I would like to thank all of my supervisors, Prof. Allan Pring, Prof. Nigel Cook, Dr. Kathy Ehrig and Prof. John Foden for supporting and guiding me through completing this project. The completion of this project, which at times seemed insurmountable, may not have been possible without their continual advice, support, encouragement, inspiration and enthusiasm throughout the duration of my Ph.D. candidature.

I would sincerely like to thank Dr. Cristiana Ciobanu in teaching me how to use the FIB-SEM, and for numerous insightful discussions which often challenged some of my interpretations and conclusions, and definitely helped guide me in producing some stronger arguments in many of my manuscripts. I am grateful for all of the training and assistance provided by staff at Adelaide Microscopy in the use of FESEM, EPMA, FIB-SEM, and FIB-EBSD, namely Mr. Angus Netting, Dr. Benjamin Wade, Mr. Ken Neubauer, Miss Aoife McFadden and Dr. Animesh Basak. Further thanks are given to Dr. Kan Li for conducting some of the preliminary hydrothermal experiments which were designed to test some of the key conclusions drawn from my research; and also to Miss Nicole Allen for her assistance with EPMA data collection and in collating the copious SEM images which I collected. I would also like to acknowledge Prof. Joël Brugger and Dr. Barbara Etschmann who introduced me to synchrotron technology. The help and assistance provided by Debra Burrows (ALS Mineralogy, Brisbane), Andrew Gasiorowski (Intertek Minerals, Adelaide), Mark Raven (CSIRO, Adelaide), and Maya Kamenetsky (University of Tasmania, Hobart) is also gratefully acknowledged. For anyone else who may have helped me, and whom I have not specially mentioned, I offer a sincere thank you.

I am indebted to BHP Billiton and colleagues with whom I work, in particular, Dr. Kathy Ehrig for providing the funds and allowing me time to complete this project. I have been working full-time for the entire duration of my Ph.D. candidature, and without the full support of my colleagues I would not have been able to complete this project.

Last, but by no means least, I would like to thank my husband, Robbie, and my family and friends for their help and support through this very hectic and challenging phase of my life. I hope that I have, and always will continue to make you proud!

PREFACE

This thesis comprises of a portfolio of publications which have either been published, or submitted for publication. The journals in which these papers have been published and/or submitted are American Mineralogist, The Canadian Mineralogist, and Mineralogical Magazine. All of the manuscripts are closely related, and summarize much of the micro-and nanoscale analytical data and observations that were made as part of this project. Many recommendations have been made at the end of this thesis as a direct result of the key findings of this research, and it is hoped that many of these are further explored at a later date.

The key aims of this project and significance of the work undertaken are addressed in the Abstract and Section 1.5. There are four papers which form the basis of this thesis:

1. Macmillan, E., Cook, N.J., Ehrig, K., Ciobanu, C.L. and Pring, A. (2016) Uraninite from the Olympic Dam IOCG-U-Ag deposit: linking textural and compositional variation to temporal evolution. American Mineralogist, 101, 1295-1320, <http://dx.doi.org/10.2138/am-2015-5411>.

2. Macmillan, E., Ciobanu, C.L., Ehrig, K., Cook, N.J., and Pring, A. (2016) Chemical zoning and lattice distortion in uraninite from Olympic Dam, South Australia. American Mineralogist <http://dx.doi.org/10.2138/am-2016-5753>.

3. Macmillan, E., Ciobanu, C.L., Ehrig, K., Cook, N.J., and Pring, A. (2016) Replacement of uraninite by bornite via coupled dissolution-reprecipitation: evidence from texture and microstructure. Submitted to The Canadian Mineralogist (in review at the time of thesis submission).

4. Macmillan, E., Cook, N.J., Ehrig, K., and Pring, A. (2016) Chemical and textural interpretation of late stage coffinite and brannerite from the Olympic Dam IOCG-Ag-

U deposit. Submitted to Mineralogical Magazine (in review at the time of thesis submission).

The final chapter of this thesis consists of a complete reference list of all publications cited within any of the manuscripts and chapters contained in this thesis. To avoid duplication, individual chapters do not contain their own reference lists, unless this list is part of a publication. All supplementary data submitted with each of the four main papers can be found in the appendices, as can additional conference abstracts, and other co-authored publications that have been produced. The appendices consist of the following:

A. Supplementary data for Paper 1.

B. Supplementary data for Paper 2.

C. Supplementary data for Paper 3.

D. Supplementary data for Paper 4.

E. Macmillan, E. and Pring, A. (2014) An integrated analytical approach in deciphering complex uranium mineral textures. Proceedings of the Joint International Conference on Nanoscience and Nanotechnology (ICONN) and Australian Conference on Microscopy and Microanalysis (ACMM), 2014, Adelaide, Australia.

F. Macmillan, E., Cook, N.J., Pring, A., Ehrig, K., and Foden, J. (2014) Evolution of uraninites at Olympic Dam: Deciphering complex textures, chemistry and temporal history. Poster presented at the 11th South Australian Exploration and Mining Conference, Adelaide, Australia.

G. Macmillan, E., Cook, N.J., Ciobanu, C.L., Ehrig, K., Kamenetsky, V.S., Thompson, J., and Pring, A. (2015) Evolution of uranium minerals at Olympic Dam, South Australia.

Proceedings from SEG2015 – Conference of the Society of Economic Geologists: World-Class Ore Deposits: Discovery to Recovery, 2015, Hobart, Australia.

H. Macmillan, E., Cook, N.J., Ehrig, K., Ciobanu, C.L. and Pring, A. (2016) The evolution of uraninite, coffinite and brannerite at the Olympic Dam IOCG-U-Ag deposit – linking textural observations to compositional variability. Abstract for Australian Earth Sciences Convention 2016, Adelaide, Australia.

I. Cook, N.J., Ciobanu, C.L., Ehrig, K., Macmillan, E. and Netting, A. (2015) Mineralogical and microanalytical characterization of uranium mineralization. Australian Institute of Mining and Metallurgy (AusIMM) Uranium Conference, Adelaide, June 2015.

J. Ehrig, K., Liebezeit, V., Macmillan, E., Lower, C., Kamenetsky, V.S., Cook, N.J. and Ciobanu, C.L. (2015) Uranium mineralogy versus the recovery of uranium at Olympic Dam. Australian Institute of Mining and Metallurgy (AusIMM) Uranium Conference, Adelaide, June 2015.

K. Li, K., Pring, A., Etschmann, B., Macmillan, E., Ngothai, Y., O'Neill, B., Hooker, A., Mosselmans, F. and Brugger, J. (2015) Uranium scavenging during mineral replacement reactions. American Mineralogist, 100, 1736-1743.

L. Li, K., Brugger, J., Pring, A., Ngothai, Y., Etschmann, B., Zhao, J., and Macmillan, E. (2013) Uranium transport and deposition in iron-oxide-copper-gold deposits (IOCG's): An experimental approach. Goldschmidt 2013 Conference Abstracts, Florence, Italy.

CHAPTER 1

INTRODUCTION

CHAPTER 1: INTRODUCTION

The complex history of any ore deposit may be revealed by studying the textural and chemical variability of the minerals contained within the deposit. A mineral texture can be defined as the general character or appearance of a rock or mineral aggregate as indicated by relationships between components within it (Lapidus, 1990). Features which can be ascribed to a mineral texture include grain size and shape, degree of crystallinity, and arrangement. In many rocks which have experienced some form of disequilibrium, there are chemical, mineral, or textural patterns (i.e., sedimentary banding, metamorphic layering, oscillatory zoning, exsolution patterns etc.), which formed as a result of geochemical self-organization from an unpatterned to a patterned state (Nicolis and Prigogine, 1977; Ortoleva et al., 1987). For many years, the study of ore minerals and their intergrowths has led numerous researchers to describe their observations, and in some cases link these observations to possible mechanisms of ore deposit formation (e.g., Ramdohr, 1969; Augustithis, 1995).

To be able to decipher the detailed micro- and nanoscale observations, the broader context of the mineral of interest within a given deposit must be at least partially understood. Thus, understanding the diversity of deposit types in which a particular mineral may be found, possible conditions at which it forms, alteration mechanisms to which it could be exposed, or having an appreciation of the intrinsic properties of the mineral itself, or other chemically or structurally analogous minerals, are all important factors in unravelling the often complex and tortuous observations and interpretations of various mineral textures. For these reasons, this section contains a brief introduction into the diversity of uranium mineral deposits, a discussion of the geological setting and uranium mineralization of Olympic Dam, a summary of the chemistry of the key minerals of interest, as well as an outline of possible alteration processes which may have impacted on the observed mineral textures. This chapter does not

provide a complete comprehensive literature review of the intricacies of each of the uranium minerals and associated mineral textures; these can be found in subsequent chapters. Rather it highlights some of the key background information required to set a context and purpose for the research that has been conducted.

1.1 Uranium mineral deposit diversity

Uranium minerals can be found in a diverse range of environments and geological settings, and numerous classification schemes have been proposed based on: (1) host lithology and orebody morphology, as defined by Dahlkamp (1978) and IAEA (2009); (2) genesis, as defined by Kyser and Cuney (2009); and (3) geological setting (i.e., igneous, metamorphic or sedimentary) as defined by Plant et al. (1999). Uranium mineral deposits can form in all types of geological settings including metamorphic, plutonic, volcanic, metasomatic, hydrothermal, sedimentary and superficial environments (Dahlkamp, 1978; Plant et al., 1999). There are, however, three dominant deposit types which host more than 75% of the known worldwide uranium resources: unconformity-related deposits, iron-oxide-copper-gold (IOCG) deposits, and sandstone-hosted deposits (Cuney, 2009). Of interest here are the IOCG deposits which contain uranium, of which Olympic Dam is the archetype. These uranium bearing polymetallic iron-oxide breccia complex deposits occur in hematite-magnetite-rich breccia (i.e., Olympic Dam and Ernest Henry, Australia) and metasedimentary-metavolcanic breccia units (i.e., Salobo, Carajas District, Brazil) (Fayek, 2013).

The initial definition of IOCG deposits was given by Hitzman et al. (1992) after the discovery of the Olympic Dam deposit, and this definition has subsequently been used to classify a diverse range of deposits (e.g., Groves et al., 2010; Barton, 2014, and references therein). In general, the bulk geochemistry of the mineralization defines deposits which belong to the IOCG-type; they typically contain >10% low-Ti Fe-oxides and contain elevated

concentrations of Cu, Au, REE+Y (hereafter ΣREY), P, U, Ag and Co (Barton, 2014). Geologically, IOCG-type deposits are diverse, and are usually structurally or stratigraphically controlled and often temporally and spatially associated with Na-Ca-K metasomatism. As a group, these deposits are poorly defined in terms of the geologic processes which may have formed these deposits, and the respective geological settings. They lack tectonic and igneous correlations which are characteristic of, for example, many magmatic-hydrothermal systems (Barton, 2014). There have been numerous attempts to divide members of the IOCG-type into sub-types based on economic metals, deposit mineralogy, and possible origins (e.g., Williams et al., 2005; Groves et al., 2010; Williams, 2010).

Provinces which include IOCG deposits are found throughout the World, and range in age from Archean to Cenozoic. A summary of the occurrences of these deposits can be found in Barton (2014), but in brief the most important regions include (in order of age): the central Andes (Mesozoic; Cu + Fe); the lower Yangtze (Mesozoic; Fe ± Cu); the southern Urals (Paleozoic; Fe); South Australia (Mesoproterozoic; Cu + U + Au); northern-central Australia (Paleo- to Mesoproterozoic; Cu + Au); northern Baltic (Paleoproterozoic, Fe ± Cu); and the Carajas District (Late Archean, Cu + Au). Moreover, IOCG deposits are irregularly distributed throughout time, and their formation appears to be related to amalgamation and breakup of supercontinents, as discussed by Groves et al. (2010). The large Cu-rich deposits are typically Precambrian and only occur in a few regions (i.e., Carajas, South Australia, central Andes). The largest of these deposits are located in intracratonic settings that are within (~100 km) margins of Archean or Paleoproterozoic cratons or other lithospheric boundaries, and formed approximately 100 to 200 million years after supercontinent assembly. However, the Precambrian IOCG deposits which are P-rich or related to magnetite-apatite (i.e., northern Baltic, Kiruna-type) are thought to have formed in convergent margin settings prior to, or following supercontinent assembly. Deposits formed during the

Phanerozoic are typically penecontemporaneous with convergent margin settings, though deposits like Candelaria (Chile) occur in anomalous extensional to transtensional zones. Thus, due to these differing formation settings (Barton, 2014), there are many key characteristics which can be linked to the geological age of the deposit. These include, the nature of the host rocks, nature of magmatism, nature of fluids, mineralization depths, and superposition of later geological events (e.g., metamorphism). Nevertheless, the processes involved in the formation of IOCG deposits, and whether they are enriched in metals (like Cu, Au, U) remains contentious.

All uranium-enriched IOCG deposits are characterized by their high hematite or magnetite content and all display extensive iron metasomatism (Plant et al., 1999). For the majority of these deposits, sodic alteration occurs at depth, grading to potassic and sericitic alteration and silicification toward the surface. Numerous hypotheses have been put forward regarding the genesis of these deposits. Models have included liquid immiscibility of an iron-oxide melt, exhalation of iron-rich fluids, and hydrothermal replacement of alumina-silicates by iron-rich fluids (see Oreskes and Hitzman, 1993). The most favoured model to date is based on the Olympic Dam deposit, where it has been suggested that the deposit formed, at least in part, as a result of circulation of hydrothermal fluids in shallow crust. The breccia zones which host the mineralization formed via hydraulic fracturing, faulting, chemical corrosion, and gravity collapse associated with a near-surface eruptive environment (Reeve et al., 1990). It is thought that the fluids involved in the formation of these deposits included (oxidizing) groundwater that mixed with (reducing) magmatic brines, thus allowing for precipitation of the U-minerals (Reeve et al., 1990; Haynes et al., 1995). The elevated concentrations of many metals and elements, like U, is attributed to leaching of these from large volumes of crustal material (Hitzman and Valenta, 2005). More detail about the regional and local geology of the Olympic Dam deposit will now be discussed.

1.2 Regional and local geology of the Olympic Dam deposit

The Olympic Dam (OD) iron-oxide copper-gold (IOCG)-silver-uranium deposit is located 520 km NNW of Adelaide in South Australia, on the eastern edge of the Gawler Craton (Figure 1.1) and is part of the larger Olympic Cu-Au-(U) province (e.g., Skirrow et al., 2007). Units which are found within the Gawler Craton include Meso- to Neoarchean complexes surrounded by Paleoproterozoic to Mesoproterozoic successions (Swain et al., 2005; Fanning et al., 2007; Fraser et al., 2010). The dominant Mesoproterozoic successions of the central and eastern Gawler Craton include the Hiltaba Intrusive Suite (HIS, 1595-1575 Ma; Hand et al., 2007) and the Gawler Range Volcanics (GRV, ~1591 Ma; Fanning et al., 1988), which together have been termed the Gawler Silicic Large Igneous Province (SLIP; Allen et al., 2008). The orebody is hosted by the Olympic Dam Breccia Complex (ODBC), which is contained within the Roxby Downs Granite (RDG), a member of the HIS. From U-Pb dating of hydrothermal zircon, the Hiltaba Suite granitoids cluster around 1588 to 1596 Ma (Mortimer et al., 1988; Creaser and Cooper, 1993; Johnson, 1993; Johnson and Cross, 1995), and more recent work has estimated the age of the RDG as 1594 ± 5 Ma (Jagodzinski, 2014). Rocks of the HIS are enriched in K, Rb, Ba, Th, U, ΣREY, Nb, and Zr, which are typical of A-type high-K calc-alkaline granites (Giles, 1988). The RDG and ODBC are covered by a thick Mesoproterozoic to Cambrian sedimentary sequence, which is part of the Stuart Shelf (Preiss, 1993).

The Paleoproterozoic sedimentary and igneous units were deformed during the Cornian and Kimban Orogenies (~1850 Ma and 1730-1690 Ma, respectively; Hand et al., 2007); whereas the GRV and younger units are generally flat lying or gently dipping and have not been metamorphosed. Any younger regional deformation events (i.e., post ~1590 Ma) involve

reactivation of faults and shear zones (Hand et al., 2007), and are further discussed below. Gairdner Dyke swarms (~825 Ma; Zhao and McCulloch, 1993 and Wingate et al., 1998), each comprising numerous mafic dykes, have also been identified within the eastern and northern Gawler Craton.

Genetic models for the OD deposit have evolved since the deposit was first discovered using an exploration model based on sediment-hosted stratabound Cu deposits. Initially, it was believed that mineralization was sediment hosted (Roberts and Hudson, 1983), but later magmatic-hydrothermal mineralization was postulated (Oreskes and Einaudi, 1990; Reeve et al., 1990; Oreskes and Einaudi, 1992; Haynes et al., 1995; Johnson and Cross, 1995). The magmatic-hydrothermal formation of the deposit was long thought to be associated with multiple mafic maar-diatreme volcanoes venting via magmatic, phreatic and hydrothermal explosions (Reeve et al., 1990; Haynes et al., 1995; Johnson and Cross, 1995). Individual diatremes were interpreted as the roots of maar volcanoes, and thus acted as sites where hydrothermal and phreatomagmatic eruptions could occur. More recently, opinion has shifted towards formation beneath and partly within a sedimentary basin (McPhie et al., 2011b; McPhie et al., 2016). Five main sedimentary facies associations (Figure 1.2) have been identified and these reflect different sources (McPhie et al., 2016): 1) interbedded sandstone and red mudstone (granitoid-dominated); (2) well sorted quartz-rich sandstone (Paleoproterozoic and older basement provenance); (3) green sandstone and mudstone (mafic volcanic source); (4) polymictic volcanic-clast conglomerate (mixed felsic-mafic volcanic source); and (5) thinly bedded green and red mudstone (partly hydrothermal and volcanic source). All of these facies are unique, four are interbedded, and three of them can be mapped across the southern area of the deposit. This implies that the original depocentre was much larger than the areas where these facies are preserved, and therefore it is now thought (McPhie et al., 2016) that deposition of these sedimentary facies did not occur within separate maar

craters, but beneath a larger sedimentary basin. The bedded clastic facies were present when the ODBC formed, and when the mineralizing hydrothermal system was active. It is therefore likely that these sediments played a pivotal role in the formation of the OD orebody.

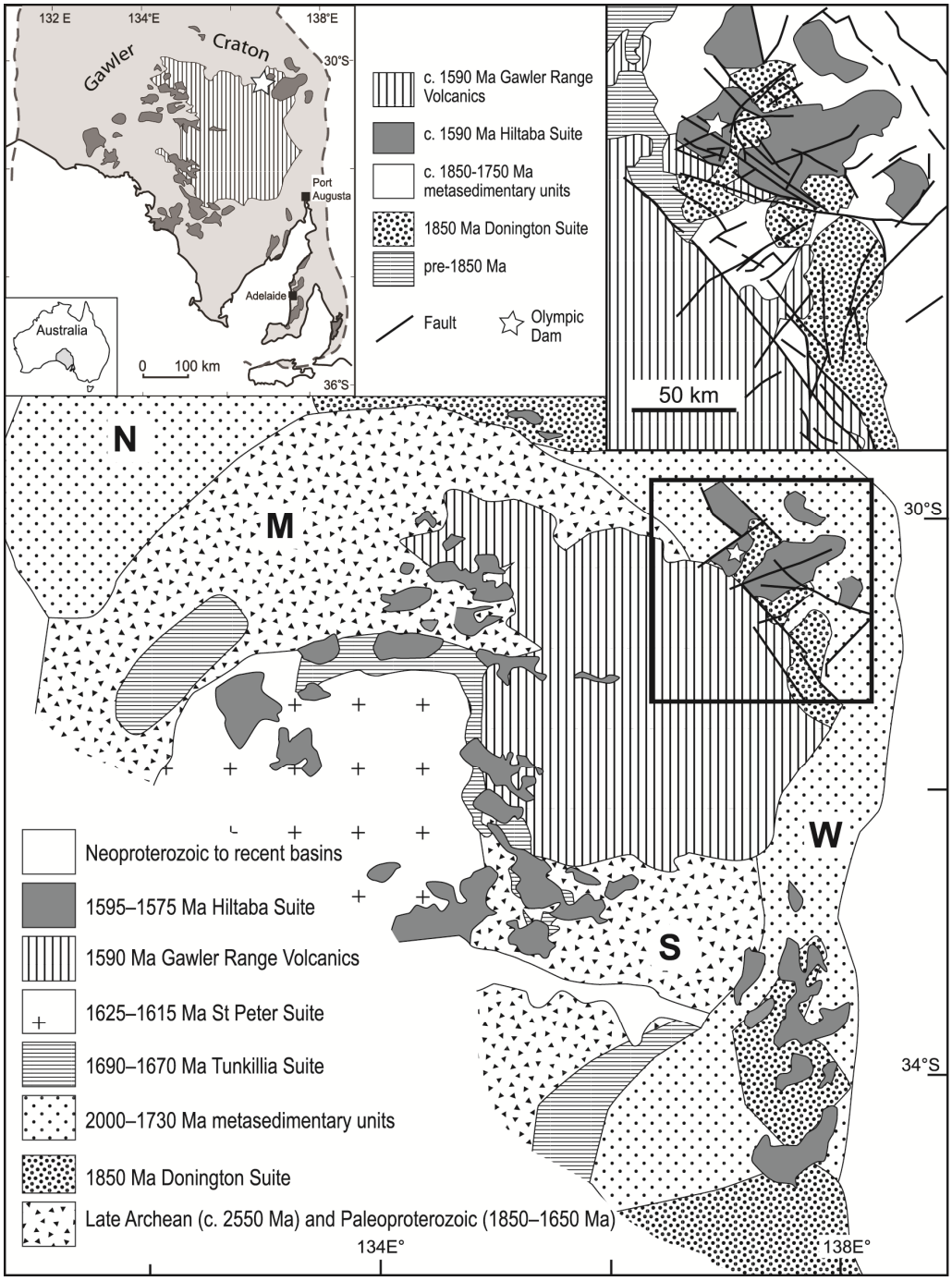

Figure 1.1: Regional geological map displaying the distribution of major rock units according to age. Top left inset: location of the Gawler Craton, South Australia. Top right inset: close-up of geological setting in vicinity of OD. N=Nawa Domain, W=Wallaroo Group, M=Mulgathing Complex, S=Sleaford Complex. Sourced from McPhie et al. (2016).

1.2.1 The Olympic Dam Breccia Complex

The ODBC is approximately 6 × 8 km in size (Figure 1.2), with the principal component of the ODBC complex being derived from the RDG, and minor components comprising of GRV, some bedded clastic facies, as well as hydrothermal inputs (Reeve et al., 1990; Ehrig et al., 2012). The breccia complex is zoned, with a central barren quartz-hematite breccia associated with volcaniclastic rocks, surrounded by variably mineralized hematite-granite breccias. Several types of breccia have been documented, but as outlined by Reeve et al. (1990), the orebody can best be thought of as a continuum from granite breccia (<10% hematite) to various forms of hematite-rich breccia (from 10% to >90% hematite). There are also heterolithic breccias which contain clasts of surficial sedimentary and volcaniclastic rocks. The ODBC can be broadly defined as having concentric zonation of the major lithological/alteration units, with more hematite-rich lithologies toward the centre, grading to more granitic-rich lithologies at the periphery of the deposit. The margins of the ODBC are indistinct, and are thought to be gradational and change from altered granite breccia, to partially brecciated granite, to fractured granite (Reeve et al., 1990). The numerous breccia types indicate that processes like hydraulic fracturing, tectonic faulting, chemical corrosion, phreatomagmatism, and gravity collapse all played a pivotal role in forming the ODBC (Reeve et al., 1990). These brecciation events generated potential fluid pathways and allowed for circulation of hydrothermal fluids within and around the deposit.

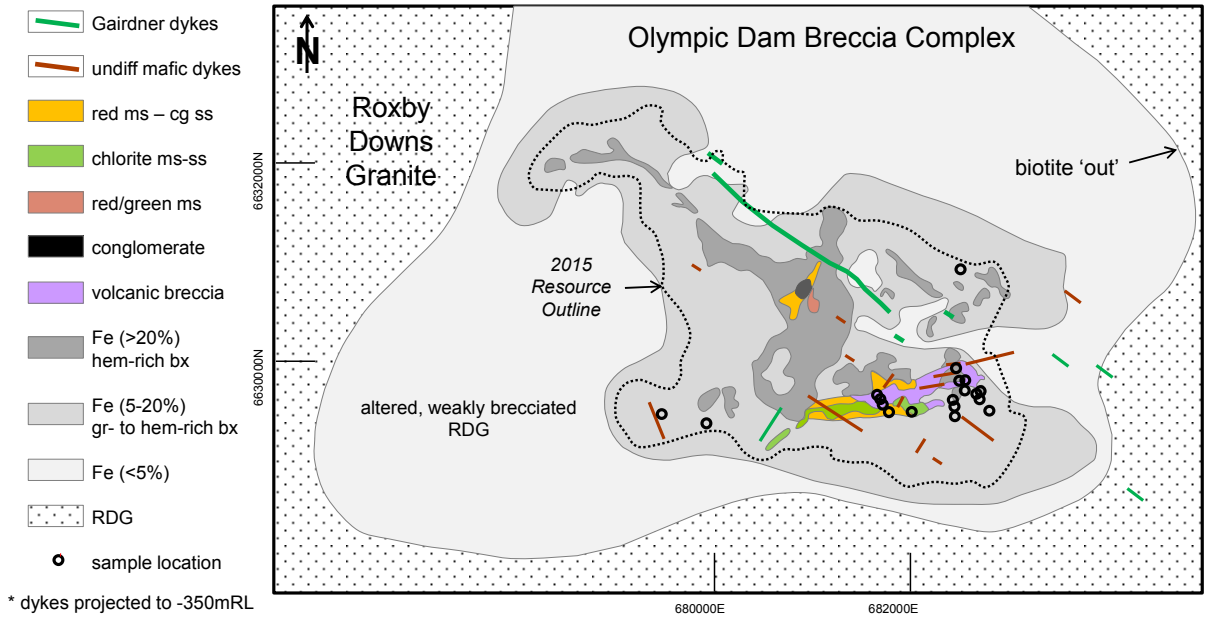

Figure 1.2: Simplified lithological/hematite alteration map of the OD deposit at -350 mRL with marked sample locations. Abbreviations: 'red ms – cg ss' = well-bedded, hematite-rich sandstone, mustone, and conglomerate breccias; 'chlorite ms-ss" = chlorite-bearing, laminated sandstone and mudstone; 'red/green ms' = thinly laminated, very hematite-rich mudstones; 'hem' = hematite, 'gr' = granite; 'bx' = breccia; 'RDG' = Roxby Downs Granite. Adapted from Ehrig et al. (2012).

1.2.2 Resetting events

Numerous events have impacted on the orebody and/or surrounding region, especially in relation to hydrothermal activity. These include: (1) intrusion of the Hiltaba Suite Granitoids and the extrusion of the GRV (~1588 to 1596 Ma; references mentioned above); (2) the Kararan Orogeny (~1565-1540 Ma; Flint et al., 1993); (3) sealing of the unconformity above the deposit in the Late Proterozoic (Trueman et al., 1986); (4) intrusion of dolerite dykes (~820-830 Ma; Huang et al., 2015 and Apukhtina et al., 2016); (5) intrusion of picrites (Ehrig et al., 2012); and (6) the Delamerian Orogeny (~490-514 Ma; Foden et al., 2006). Each of the aforementioned events may represent sources of heat and/or allowed for fault reactivation that

may have driven hydrothermal circulation, alteration and associated remobilization of ore components.

Systematic isotopic dating of different minerals (Huang et al., 2015; Apukhtina et al., 2016; Kirchenbaur et al., 2016) has allowed revision of the genetic model. It is now apparent that deposition of hydrothermal mineralization was associated with fault-bounded tectonism, magmatism, depression and sedimentation at the time initial fragmentation of the Columbia supercontinent at ~1600 Ma. Subsequently, the deposit underwent at least three phases of overprinting, corresponding to sedimentation and metamorphism during the final break-up of Columbia and Rodinia assembly between ~1400 to ~1200 Ma, Rodinia break-up at ~800 Ma, and amalgamation of Gondwana at ~500 Ma (Delamerian Orogeny). The latter two events are expressed by emplacement of Gairdner dolerite dykes (Huang et al., 2015), and crosscutting fluorite-barite-carbonate veins, respectively. Debate persists, however, about whether these events were associated with input of additional ore components, or were drivers of deposit-scale cycles of remobilization and recrystallization.

1.2.3 Alteration and mineralization

Alteration and mineralization which occurred within the ODBC appear to be multistage, but it appears that the initial event occurred shortly after deposition of the ~1594 Ma host RDG (Johnson and McCulloch, 1995; Ciobanu et al., 2013). The OD deposit is strongly enriched in a wide range of elements, including Ag, As, Au, Ba, Bi, C, Cd, Co, Cr, Cu, F, Fe, In, Mo, Nb, Ni, P, Pb, S, Sb, Se, Sn, Sr, Te, U, V, W, Zn, and ΣREY, especially La and Ce; and over 90 minerals have been identified within the deposit (Reeve et al., 1990; Ehrig et al., 2012). There are 3 hydrothermal alteration assemblages: 1) magnetite, apatite, siderite, chlorite, quartz (reduced Fe-oxide); 2) hematite, sericite, fluorite (oxidized Fe-oxide); and 3) hematite, quartz,

barite (Ehrig et al., 2012). Assemblages (1) and (2) occur toward the periphery of the deposit and grade to the central parts of the deposit where assemblage (3) is dominant.

The principal sulfide phases are pyrite, chalcopyrite, bornite, and chalcocite (also including other $Cu_{2-x}S$ phases such as djurleite and digenite), and Cu-U-Au mineralization is generally associated with hematite-rich breccias, but also occurs within granite-rich breccias (Roberts and Hudson, 1983; Reeve et al., 1990; Ehrig et al., 2012). These minerals show clear spatial zonation, with pyrite at the margins of the deposit, through chalcopyrite, bornite and chalcocite ± native copper toward the centre of the deposit. Generally, these sulfide species occur discretely or as binary pairs (Ehrig et al., 2012). Chalcocite is rarely observed together with chalcopyrite and/or pyrite, and bornite is rarely found with pyrite. Copper mineralization usually consists of disseminated sulfide grains which range in size from <20 μm to several millimetres, and some are present as veinlets, although this style of mineralization is much less abundant (Reeve et al., 1990; Ehrig et al., 2012).

Some veins exist within the deposit and these have been described by Reeve et al. (1990). Veins which are distributed throughout the entire deposit include mono-mineralic veins which contain hematite, sericite, or chlorite, and those containing a variety of minerals including hematite-siderite, and barite-fluorite (± hematite, siderite, quartz and chalcopyrite). The bulk of the mineralization is disseminated, but within the mineralized zones, veinlets (microns up to a few millimetres in size) containing Cu-(Fe)-sulfides ± uraninite with variable amounts of fluorite ± barite can be found. There are also late stage barite-quartz ± fluorite veins, and chalcopyrite veinlets which infill irregular hairline fractures and superimpose the overall sulfide zonation pattern. Although sulfide veins have been identified, these are subordinate in abundance compared to the disseminated sulfide mineralization.

Ore genesis is attributed to coupled redox reactions, where a hot, granitic magma sourced fluid (reducing, highly saline, and Fe-rich), subsequently mixed with a cooler, meteoric (oxidizing) fluid (Reeve et al., 1990; Oreskes and Einaudi, 1992; Haynes et al., 1995). The transportation and precipitation of Fe and U are thought to be related to the U content of hematite, since much of the hematite contains finely disseminated U-minerals (mostly uraninite; Oreskes, 1990). Moreover, Ciobanu et al. (2013) have shown that hematite features oscillatory and sectorial compositional zoning with respect to U, Pb, W and Mo. Pb-Pb ages of approximately ~1.6 Ga were obtained from the high-U zones in hematite, indicating that the magmatic-hydrothermal events which occurred at this time are also potentially important for U-precipitation within host minerals (like hematite). Another potential source of both fluids and metals for the OD hydrothermal system may be the newly identified sedimentary succession (McPhie et al., 2011b, 2016). The generation of the Fe-Cu-rich fluids is still poorly constrained, and the source of metals is often linked to the local granitic rocks. However, Johnson and McCulloch (1995) infer that the Cu and ΣREY are sourced from mafic components based on Sm-Nd data. Likewise, Oreskes (1990) suggests that the observed Eu anomaly found within many of the REY-minerals is due to mafic sources.

In addition, the abundance of fluorite veins, and elevated levels of fluorine contained within sericites, may indicate that some of the low and moderately high-temperature fluids contained relatively high-concentrations of fluoride (Reeve et al., 1990). The often observed amoeboid clast shapes within the breccia, led McPhie et al. (2011a) to suggest that the elevated fluoride contained in these fluids, was responsible for some of the corrosion of silicates. These authors therefore inferred that hydrofluoric acid, the most corrosive acid known, contributed to the formation of the hydrothermal breccia by causing dissolution. It is thought that F-rich fluids were crucial in formation of the hydrothermal alteration of OD, and these F-rich fluids allowed for complexing of U and ΣREY, thus allowing these elements to be transported in the

more reduced, higher-temperature Fe-rich fluids (Oreskes and Einaudi, 1990; McPhie et al., 2011a). Fluorine has therefore likely played an important role in the hydrothermal alteration of OD.

1.2.4 Uranium mineralogy

The OD deposit is the largest known uranium (U) resource, with uraninite/pitchblende (hereafter referred to as uraninite), coffinite and brannerite being the dominant U-bearing minerals. Minor to trace amounts of uranium can also be found in uranothorite, thorite, thorianite, crandallite, xenotime, zircon, fluoroapatite, other REY-group minerals (i.e., bastnäsite, florencite, monazite, synchysite), sulfides, and hematite (Roberts and Hudson, 1983; Reeve et al., 1990; Ehrig et al., 2012; Ciobanu et al., 2013). The proportion of uraninite relative to coffinite and brannerite increases with total Fe content throughout the deposit, with the average relative proportions of 13, 56, and 31 wt%, respectively (Ehrig et al., 2012). Moreover, local mineralogical variation throughout the deposit vastly impacts which U-mineral is most abundant. Uraninite appears to be more strongly associated with hematite and sulfides, whereas coffinite and brannerite tend to be more strongly associated with gangue (e.g., quartz, sericite, chlorite, hematite) minerals. Unlike sulfides, uranium minerals do not appear to display deposit-scale zonation, and tend to be disseminated and complexly intergrown with all minerals. Where uranium concentrations are particularly high, micro-veinlets of uraninite are common. The average grain sizes of the uranium minerals (greater than >0.5 μm) are 20 μm, but range from <0.5 μm to >1 mm.

Much of the earlier work conducted on the uranium minerals at OD focused on uraninites in higher-grade, central parts of the deposit where the more massive, stringer-like uraninite textures are present (e.g., Roberts and Hudson, 1983; Trueman et al., 1986; Oreskes and Einaudi, 1990; Reeve et al., 1990; Johnson, 1993). Also described in this early work were

uraninite spherules, blebs or pisoliths, as well as minor occurrences of granular coffinite, which was associated with uraninite (Reeve et al., 1990). Brannerite was also identified, but was classified as rare and associated with anatase, rutile or zircon within granite-rich mineralized zones. Uraninite euhedra were identified as inclusions within Cu-(Fe)-sulfides, and some of the granite identified to contain primary uranothorite. As discussed in more recently reported work (e.g., Ehrig et al., 2012), many of the early observations pertaining to the U-mineralization at OD still remain true, however these early studies focused on the higher-grade areas of the deposit. With the ever-increasing geological and mineralogical dataset that has been collected at OD since it was first discovered in 1975, it is now possible to also sample in lower-grade and peripheral areas of the deposit. This has led to a more comprehensive understanding of the distribution of U-minerals throughout the entire deposit.

Moreover, much of the early work was focused on obtaining dates of mineralization. One such study was conducted by Trueman et al. (1986) who used ion and electron microprobe analyzes of high-grade uranium ores to obtain U-Pb discordia, and thus identified three main populations of uraninite: initial crystallization at ~1400 Ma, and two lead-loss events at 490 Ma and 600 Ma. One interpretation of these latter events, is that they represent periods of major leaching and U redistribution, possibly coincident with the sealing of the unconformity and deposition of the mid-Proterozoic sediments. Little analysis was however conducted on low-grade ores. Later U-Pb geochronology was conducted by Johnson (1993), who described fine grained disseminations of uraninite in hematitic breccias and cavity-filling colloform, crustiform and vein occurrences of uraninite in hematitic and altered granitic rocks. The latter of which, were thought to represent secondary styles of mineralization due to their variable modes of occurrence. A primary mineralization age of ~1590 Ma was proposed by Johnson (1993) from dating of magmatic zircons. This was in conflict to the primary mineralization age of ~1400 Ma attained from dating of uraninite presented by Trueman et al. (1986).

When all of the samples analyzed by both Johnson (1993) and Trueman et al. (1986) were considered, four distinct ages of uraninite growth were determined: ~1350-1400 Ma, ~1220 Ma, ~830 Ma, and ~570 Ma. Four distinct Pb-loss ages were also suggested: 633 ± 246 Ma, 257 ± 50Ma, 101 ± 76 Ma, and recent. The range of ages of uraninite growth and Pb-loss were interpreted as being reflective of either: 1) the ease at which U may be dissolved and reprecipitated; or 2) uraninite that has been deposited at one time, but has experienced variable Pb-loss dependent on location within the deposit, and the degree of hydrothermal alteration experienced in that particular locality.

The broad scatter of apparent ages attained for uraninite growth and Pb-loss events highlights the ease at which uraninite is isotopically disturbed. It is well documented that U is easily mobilized in oxidized environments (refer Section 1.3). At OD, since ore formation likely occurred in a near-surface environment, and involved various fluxes of hydrothermal fluids (Oreskes and Einaudi, 1990; Reeve et al., 1990), it seems likely that this broad scatter of data is attributable to the varying degrees of U dissolution and reprecipitation. Moreover, the discrepancy between the primary mineralization age attained from the zircon and uraninite dating is likely due to the perturbed U and Pb systematics of the uraninites. The age of U-mineralization remains poorly constrained for OD, and as suggested by Cuney and Kyser (2009) and others, more work in understanding the different types of U-minerals, as well as their ages is required to better understand the genesis of the U mineralization at OD. Much of the earlier work has indicated that the U-minerals at OD have a complex history with repeated cycles of precipitation, dissolution and reprecipitation (Reeve et al., 1990; Johnson, 1993; Ehrig et al., 2012). Most recently, it has been suggested that the U-mineralization developed over >1000 Ma (Kirchenbaur et al., 2016) and was influenced by the numerous resetting events that have impacted the orebody. Kirchenbaur et al. (2016) suggest, that the uranium is sourced from upper crustal lithologies (likely igneous), and there was a gradual addition of U

in several stages. They found no evidence of fission fragment contributions (i.e., fissionogenic Sm) within the high-grade ores that were analyzed. This elucidates that the age of deposition or re-deposition is substantially younger than the initial ~1594 Ma age of the earliest U-mineralization, and thus supports recent suggestions that U ore deposition occurred over a longer time span (i.e., >1000 Ma). Also, isotopic fractionation trends of U can be used to interpret the processes involved in the formation of the U-mineralization. Important factors which may influence the $^{238}U/^{235}U$ ratio include: temperature of formation, initial U isotopic signature of the source rock, as well as mass balance considerations (Chernyshev et al., 2014; Uvarova et al., 2014). There is an inverse temperature dependence of isotopic fractionation, with heavier isotopes generally partitioning into the reduced species (Schauble, 2007). Thus, if U was remobilized from earlier deposited uraninite, it would be expected that the residual uraninite would have higher ^{238}U contents (Uvarova et al., 2014) and the re-deposited uraninite would contain more ^{235}U. Furthermore, $\delta^{238}U$ signatures can be used to determine whether a deposit formed under low- or high-temperature conditions. Elevated $\delta^{238}U$ signatures are characteristic of deposits formed in low-temperature, sedimentary-type deposits. Kirchenbaur et al. (2016) did not find evidence of elevated $\delta^{238}U$ signatures, and the $\delta^{238}U$ signatures recorded were similar to that of other hydrothermal U-deposits with U sourced from granitoid/volcanic/volcanogenic rocks. It is nonetheless possible that post-depositional/re-depositional processes may have destroyed any evidence of high $\delta^{238}U$; and thus the possibility that low-temperature fluids played a role in forming the U-mineralization at OD is therefore not ruled out. Despite the above, the sources of metals (including U), and exact mechanisms of ore formation remain poorly constrained for the OD deposit and further work in exploring the U-minerals is required to better constrain the formation of this deposit.

1.3 Chemistry of uranium minerals

Due to the range of possible formation conditions in which uranium minerals form, they are usually chemically and structurally complex, and there are more than 200 identified uranium mineral species (Fleischer and Mandarino, 1995). There are generally two main types of uranium minerals, these being either the reduced (U^{4+}) or the oxidized (U^{6+}) species, and there are a few minerals which contain a mixture of both species (Burns and Finch, 1999).

In terms of abundance and economic value, the most important U^{4+}-mineral is uraninite (Finch and Murakami, 1999). The next most important mineral based on economics is coffinite, but this mineral is usually only found in deposits that formed by low-temperature processes, often as an alteration product of uraninite (Janeczek and Ewing, 1992a; Plant et al., 1999). Brannerite is probably the third most abundant U^{4+}-mineral. Uraninite, coffinite and brannerite are all present at Olympic Dam (e.g., Reeve et al., 1990), so a brief outline of their structural and chemical variability, as reported by other researchers, is provided here.

1.3.1 Uraninite

Uraninite has an ideal formula of UO_2, but is known to contain between 77 and 98 wt% UO_2, for Oklo and Alm Bos, respectively (Janeczek et al., 1996). In nature it is often inhomogenous and contains various impurities including: Ca, Pb, ΣREY, Th, Fe, Si, P, Al, Mg, Mn, K, and many other elements (e.g., Janeczek and Ewing, 1992c; Finch and Murakami, 1999; Alexandre and Kyser, 2005). Furthermore, uraninite is often at least partially oxidized in nature. The presence of all of these impurities as well as the potential multiple valencies of U, has led numerous researchers to propose various forms of the generalized crystal structure for uraninite. One such interpretation of a structural formula for uraninite was given by Janeczek and Ewing (1992c) as:

$$\left(U^{4+}_{1-x-y-z}U^{6+}_{x}REY^{3+}_{y}M^{2+}_{z}\right)O_{2+x-0.5y-z}$$

This equation incorporates both U^{4+} and U^{6+}, and allows for the presence of REY^{3+}, as well as various divalent metals (i.e., Ca, Pb, Fe). Of all impurities, Pb is typically one of the main impurities found in uraninite, and is usually attributed to the decay of U isotopes (^{238}U and ^{235}U) which form radiogenic Pb (^{206}Pb and ^{207}Pb, respectively). Some of the oldest known uraninites contain up to 20 wt% PbO (Janeczek and Ewing, 1995), however PbO contents of 7-10 wt% are more common. The next most abundant impurity elements are Ca and ΣREY. Uraninites containing elevated Th and ΣREY are typically associated with higher-temperature magmatic or magmatic-hydrothermal fluids (Mercadier et al., 2011), whereas those formed under lower-temperature conditions typically contain more Ca (Janeczek and Ewing, 1992b; Fayek et al., 2000).

U-minerals (particularly uraninite) are known to retain much of their evolutionary history and as such can be used as indicators of the geochemical environments in which they formed (Mercadier et al., 2011; Depiné et al., 2013; Frimmel et al., 2014). Moreover, Hazen et al. (2009) have shown that uranium minerals can be used to discuss the Earth's geotectonic and geobiological histories. Thus understanding the chemical variability of uraninites can be important in understanding their evolution.

Texturally and morphologically, uraninite is also very diverse. Uraninite is defined as being cubic and has a fluorite-type structure with space group *Fm*3*m* (Frondel, 1958). When precipitated under lower-temperature conditions, it often forms botryoidal, reniform aggregates or microcrystalline masses with spheroidal microstructures that display concentric banding (e.g., Ramdohr, 1969). At higher-temperatures it grows as individual crystals which may display sector zoning (e.g., Alexandre et al., 2015). Rhythmic intergrowths of sulfides with crystalline uraninite have also been identified (e.g., Ramdohr, 1969; Polito et al., 2009).

1.3.2 Coffinite

Coffinite is tetragonal and can be represented by the formula $USiO_4.nH_2O$, with space group $I4_1/amd$ and Z=4 (Fuchs and Gebert, 1958). Ideal hydrated coffinite contains 73.75 wt% UO_2, 16.41 wt% SiO_2 and 9.84 wt% H_2O, whereas ideal anhydrous coffinite contains 81.80 wt% UO_2, 18.20 wt% SiO_2 (Janeczek and Ewing, 1992a, 1996). Elements which are thought to replace U within coffinite include: Zr, Th, Hf, Ca, Fe, ΣREY, whereas P, As, V, S, F, OH are thought to replace Si (Stieff et al., 1956; Hansley and Fitzpatrick, 1989; Janeczek and Ewing, 1992a; Förster, 2006). Coffinite is known to form numerous solid solutions with many isostructural minerals including: zircon ($ZrSiO_4$) – thorite ($ThSiO_4$) – xenotime (YPO_4) – ningyoite ($UCa[PO_4]_2.1\text{-}2H_2O$) (e.g., Speer, 1980; Pointer et al., 1988; Finch and Hanchar, 2003; Förster, 2006). Both P and ΣREY appear to be the most common substituents within coffinite, possibly due to coffinite solid solution with xenotime.

Coffinite is typically associated with low-temperatures of formation, including in granitic rocks where uranium has been remobilized via hydrothermal and meteoric waters (Dahlkamp, 1978; Leroy and Turpin, 1988), or in Si-rich reducing conditions by the alteration of uraninite (Janeczek and Ewing, 1992a). In terms of morphology, coffinite is typically very fine grained, and contains radiating fibers, and bushel-formed aggregates which may form large single crystals (Ramdohr, 1969). Coffinite often forms aggregates which appear as radiating botryoidal masses around quartz grains, or it is found replacing uraninite crystals.

1.3.3 Brannerite

Brannerite is monoclinic and can ideally be represented by the formula UTi_2O_6, with space group $C2/m$ (Ruh and Wadsley, 1966). Stoichiometric brannerite contains 62.8 wt% UO_2 and 37.2 wt% TiO_2 (Frondel, 1958). Like both uraninite and coffinite, brannerite too has been shown to have variable chemical composition, and has been reported to have U substituted by

Pb, Ca, Fe, Th, ΣREY , and Ti substituted by Si, Al, or Fe, as well as many other substituents (e.g., Ferris and Ruud, 1971; Szymanski and Scott, 1982; Saager and Stupp, 1983; Lumpkin et al., 2012). Substituents which are generally of the highest concentration are Ca, Pb, ΣREY, Fe and Si (Saager and Stupp, 1983; Lumpkin et al., 2012).

The first detailed description and photomicrographs of brannerite and associated mineral intergrowths were provided by Ramdohr (1957), who described the often delicate and complex internal network of blades and intergrowths of brannerite aggregates. Brannerite is commonly thought to form as a result of the "Pronto reaction" where brannerite replaces ilmenite under hydrothermal conditions and temperatures of ~225°C (Ramdohr, 1957; Schidlowski, 1966), or at even lower-temperatures by varying Eh and pH conditions (Adams et al., 1974). Thus, like coffinite, brannerite is also thought to form in low-temperature hydrothermal environments. Brannerite may be found as individual tabular crystals, as aggregated crystals, or in cases where it has formed as a result of replacement of uraninite and rutile, it grows from the outside of the aggregate inwards, and forms a network of bladed and irregular masses of intergrown brannerite and rutile (Ramdohr, 1969).

1.4 Alteration of uranium minerals

The alteration of any mineral involves changes in the chemical composition or mineralogical features of that mineral. Alteration of a mineral can occur via a number of methods, but of relevance here are the processes linked to radioactive decay and exposure to hydrothermal fluids, as discussed below.

1.4.1 Radiation damage in uranium minerals

All U- and Th-bearing minerals experience radioactive decay, with the decay chain of ^{238}U having eight α-decay events (Bourdon et al., 2003). As a result of the radioactive decay

process, a mineral will attain an aperiodic structure or metamict state (Hoffmann, 1987). The effects of radiation damage vary within different U-bearing minerals. Minerals like zircon often retain radiation damage, and it is therefore often used as a case example to describe the process of metamicitzation (e.g., Ewing et al., 2003). Each α-decay event dissipates most of its energy by an ionization process over a range of 10 to 20 μm, but elastic collisions occur along the path of the α-particle to produce several hundred isolated atomic displacements (Hazen et al., 2009), all of which cause damage to the structure of the mineral.

Uraninite is known to be quite resistant to α-decay damage due to its relatively rapid annealing kinetics (Eyal and Fleischer, 1985; Stout et al., 1988; Janeczek and Ewing, 1991), and it therefore has the ability to self-heal radiation damage and this prevents metamictization. Conversely, both brannerite and coffinite are reported to be completely or partially amorphous due to radiation damage (Smith, 1984; Janeczek and Ewing, 1992a; Deditius et al., 2009; Lumpkin et al., 2014). The metamict nature of these minerals may explain why they are able to incorporate large amounts of impurities into their structure; whereas for uraninite, some of the commonly observed chemical zonation patterns may in-part be due to its ability to self-heal.

Other consequences of radioactive decay include the formation of cracks and porosity within the U-mineral due to the release of daughter gases like He and Rn (e.g., Roudil et al., 2008), and even for minerals like uraninite which do not retain radiation damage, the radioactive decay process may still result in the redistribution of key elements, like Pb. If exposed to a hydrothermal fluid, these processes (i.e., enhanced percolation of fluid from cracking/porosity generation, or chemical differences between zones) may render the radiation effected mineral more susceptible to alteration.

As a result of the accumulation of Pb from radioactive decay, two destabilization mechanisms have been identified to occur within uraninite (Finch and Murakami, 1999): (1) "auto-oxidation" occurs when where U^{4+} decays to Pb^{2+}, but this can cause an imbalance between the amount of U^{4+} and U^{6+} (Frondel, 1958); and (2) accumulation of Pb^{2+} to levels which cannot be accommodated within the uraninite structure. Recent studies (e.g., Utsunomiya et al., 2004; Kramers et al., 2009) suggest that radiogenic Pb can be tetravalent rather than divalent, and thus substitute directly for U^{4+}, thus potentially eliminating the need for the "auto-oxidation" process. Alternatively, recent experimental and *ab initio* crystal modelling studies (e.g., Desgranges et al., 2009; Andersson et al., 2013) show that U^{6+} may be incorporated into several long-range ordered compounds with large unit cells like U_4O_{9-y} and U_3O_7, which may offer charge balancing mechanisms required for "auto-oxidation" to proceed. Regardless of whether "auto-oxidation" plays a pivotal role in alteration of uraninite, when Pb levels become too high to be retained within the uraninite structure, it may: (1) develop Pb-rich and –poor domains (Finch and Murakami, 1999); (2) form various Pb-uranyl minerals (e.g., Isobe et al., 1992); or (3) form galena if sufficiently high fS_2 are available (Janeczek and Ewing, 1995).

1.4.2 Mineral replacement and coupled dissolution reprecipitation reactions

Replacement of one mineral by another occurs when a mineral assemblage and fluid phase interact and they are not at equilibrium. Processes like metamorphism, metasomatism, albitization and diagenesis are all examples of where there is some redistribution of chemical constituents and there is a replacement of one mineral by another (Putnis, 2002). The re-equilibration of minerals in the presence of fluids can involve dissolution or precipitation, and in some cases these can occur together and be spatially coupled. Coupled dissolution-reprecipitation (CDR) reactions is the term given to spatially linked replacement reactions,

and these may be relevant in any deposit where hydrothermal fluids have played an active role. There are a number of microstructural features which can be used to identify if replacement has occurred via CDR reaction (Putnis, 2002, 2009): (1) preservation of the shape and volume of the mineral being replaced (i.e. product pseudomorphs the reactant grain); (2) a sharp reaction front between the original and replacing minerals since lattice diffusion is negligible as the process occurs quickly; (3) the replacing mineral generally, but not exclusively, contains numerous pores and/or cracks so that the reactant may reach the reaction front; (4) suitable chemical (e.g., composition, pH) and physical (e.g., temperature, pressure) conditions to encourage the reaction to proceed; and (5) the distance between the dissolution front and site of precipitation can vary. In some cases, the replacing mineral inherits the crystallographic information of the original mineral (i.e., controlled epitaxial growth), and the dissolution and precipitation processes are spatially coupled. These special cases are called interface-coupled dissolution-reprecipitation reactions (ICDR) since the dissolution step of the reaction is rate limiting, thereby controlling the reaction interface and the subsequent precipitation of the product phase (Xia et al., 2009a, 2009b).

For any replacement process to proceed, the fluid requires access into the mineral that is being replaced. Mechanisms that may provide these pathways include: twin boundaries/crystal faces/cleavage planes (Putnis and Putnis, 2007; Pearce et al., 2013), grain boundaries (Engvik et al., 2009), and fractures (Jamtveit et al., 2009). Such features are advantageous since nucleation may occur on these boundaries which already have a surface energy, and hence nucleation is easier than within the crystal lattice.

There are numerous examples of replacement processes which occur via CDR reaction, including: (1) replacement of calcite by fluorite (Putnis, 2009); (2) replacement of calcite by dolomite and siderite (Pearce et al., 2013); (3) replacement of pentlandite ($[Fe,Ni]_9S_8$) by

violarite ($[Ni,Fe]_3S_4$) (Xia et al., 2009a); (4) replacement processes involved in metasomatization of apatite (Harlov et al., 2002; Harlov and Förster, 2004; Harlov et al., 2005); and (5) re-equilibration of zircon in aqueous fluids (Geisler et al., 2007; Rubatto et al., 2008; Schwartz et al., 2010). In each of these replacements, there are compositional and crystallographic similarities between parent and daughter. All experimental studies to-date, have focused on mineral systems in which at least some of the chemical components are common to both the parent and the product mineral. However, Putnis (2009) also provide examples of unusual parent/product mineral pairs including limestone which is replaced by silica, and with no common chemical components, botryoidal sphalerite which is replaced by dolomite.

Mineral replacement reactions are driven by the presence of hydrothermal fluids, since these are responsible in moving reactants to and from the reactant sites, but in many cases it is difficult to ascertain the fluid properties as replacement proceeds. However, the presence of inclusions and/or porosity within a mineral may provide some information as to the chemistry of the fluid responsible for replacement. Closure of porosity by coarsening occurs to reduce the free energy of the system. Coarsening may trap the fluids that were at the reaction interface as mineral inclusions, and these may be the only remnants that such alteration occurred (e.g., Putnis and Putnis, 2007). Analysis of these inclusions can therefore elucidate some of the conditions at the time of closure.

1.4.3 Cycles of crystallization, dissolution and reprecipitation

Not all replacement reactions are spatially coupled, and constituents of the parent mineral may be transported and reprecipitated as a new mineral elsewhere. The distance from which the new minerals precipitate may range from micrometres to kilometres. Uraninite is known to be a chemically active mineral and is able to exchange elements or recrystallize if exposed

to subsequent fluid-circulation events (Grandstaff, 1976; Finch and Ewing, 1992; Kotzer and Kyser, 1993; Alexandre and Kyser, 2005). This may be of relevance at OD, particularly since much of the uraninite appears to display alteration textures and have perturbed U and Pb contents as previously discussed.

There appear to be numerous fluids responsible in the formation of OD (refer Section 1.2.3), and it seems highly probable that both reducing and oxidizing fluids have been involved at some point in the formation of this deposit. The types of fluids available for U-mineral formation, and the redistribution of U vastly impacts on the types of minerals that are precipitated. The transport of U can occur in both reducing and oxidizing environments. Under reducing conditions (i.e., U^{4+}), the U can typically be transported fractions of a centimetre, however if either F^- or Cl^- ligands are available, these can stabilize the U^{4+} in solution and transport may be much further (Keppler and Wyllie, 1990). Also, the presence of CO_2^{3-} and Cl^- have been shown to form complexes with U, but not with Th (Keppler and Wyllie, 1991). Both F- and CO_2-rich fluids have been used to explain the mobility of ΣREY-U-Th in many deposits (Oreskes and Einaudi, 1990; Agangi et al., 2010).

Under oxidizing conditions, the uranyl ion (UO_2^{2+}) and related complexes can allow for U migration many kilometres away from its source until the solution chemistry changes sufficiently to allow for precipitation of U minerals (Finch and Murakami, 1999). Regardless of whether the U has been transported near or far, when the oxidized uranyl ion experiences more reducing conditions (like the presence of organic matter or sulfides), the U is reduced and U^{4+}-dominated minerals may be precipitated from solution. An example of where this occurs is in the Franceville basin (i.e. Oklo, Bangombé), where a U-rich oxidizing fluid met reducing conditions from adjacent hydrocarbon accumulations, and subsequently uraninites have been deposited around nodules of organic matter which infill some of the secondary

porosity of the host sandstone (Gauthier-Lafaye et al., 1996). Other suggested reductants to precipitate oxidized U from solution include sulfides (e.g., Goldhaber et al., 1987; Hansley and Fitzpatrick, 1989), and even aluminosilicates (like chlorite) in host rocks which contain reduced Fe (Komninou and Sverjensky, 1996; Gregory et al., 2005).

Both brannerite and coffinite usually form in low-temperature hydrothermal environments, and their presence at OD in addition to uraninite is not well understood. Key questions addressed as part of this research project were: Are the coffinite and brannerite a result of dissolution and subsequent reprecipitation of U which was sourced from earlier precipitated uraninite? Or do they represent yet another U-mineralizing event which occurred at OD? Were reducing and/or oxidizing fluids responsible for the mobility of U around the deposit?

1.5 Research objectives

Although previous work has made considerable contributions to the understanding of the U-minerals at OD, these studies were limited to higher-grade samples within the deposit and to areas of the deposit that were being sampled and mined at the time. Also, when these previous studies were conducted, characterization of these minerals was effectively impossible due to the complex nature and <20 μm grain size of the uranium minerals. But now, with the substantial advances in microanalytical technology over the past decade, like smaller spot sizes, and improved imaging for many of the electron-based techniques, characterization of fine-grained mineral intergrowths, is possible. This is partly due to improved resolution, but also to the advancement of digital technology and computational power, which have enabled more information to be captured and subsequently analyzed. Considerable geological knowledge has also been gained about the OD deposit over the past 20 years from the extensive drill-hole and mineralogical database (see Ehrig et al., 2012). This permits more targeted sampling not only in high-grade uranium zones, but also in lower-grade and

peripheral areas of the deposit, which in the past could not be accessed. This therefore provides an opportunity to study the U-minerals in a much broader context than was previously possible and allows further development of the ideas generated from earlier work conducted at OD.

The principal objective of this project is to better understand the U-minerals in terms of their chemistry and mineral textures, and to explore some of the mechanisms involved in their formation and subsequent alteration. To achieve this, petrographic observations supported by a range of complementary microbeam analytical techniques, as described in Chapter 2, were used to probe the U-minerals on a micro- and nanoscale. The results from this analysis are presented within four separate studies. The first, presented as Chapter 3, is a textural, morphological and chemical characterization of uraninite from samples throughout the OD orebody. There were three main goals of this work: (1) to define the structural formula of uraninite and its variation; (2) to quantify the chemical and textural heterogeneity of uraninite, and determine if there are different generations of this mineral; and (3) to explore whether the variability of minor and/or trace elements within uraninite can be used to track the evolution of uraninite. Four key classes of uraninite (primary, zoned, cob-web and massive) were distinguished based on textural and chemical features, and all display some type of chemical zoning and/or inclusions. Nanoscale characterization will ascertain whether the changes in concentration of minor elements within the uraninite are due to various elements being either lattice-bound or inclusion-hosted. Conclusions will also be drawn about whether auto-oxidation plays a significant role in accommodating Pb within uraninite and altering the U^{4+} and U^{6+} content within these uraninites. The key findings outlined in Chapter 3 were seminal in designing the subsequent studies outlined in Chapters 4 and 5, which explore the formation mechanisms of some of the mineral textural features observed in the earlier study. The zoned uraninites, as defined in Chapter 3, contain unique chemical zoning patterns which differ to

the oscillatory zonation pattern as identified within the primary uraninites. Thus, the main goal of the subsequent study, as detailed in Chapter 4, is to determine whether microstructures can be identified to constrain the formation of the unique chemical zoning. This is the first known application of electron backscattered diffraction (EBSD) analysis to uraninite. The final chapter discussing the heterogeneity of uraninite is Chapter 5. The primary goal within this chapter is to document the cob-web uraninite texture, as defined in Chapter 3, and to understand the processes involved in formation of this texture, particularly with respect to the rhythmic intergrowth of uraninite and bornite, and the presence of fluorite. Crystallographic relationships between uraninite, bornite and fluorite will be explored. It will be shown that partial replacement of uraninite by bornite occurred via a CDR reaction driven by a F-rich and Cu-(Fe)-sulfide-bearing hydrothermal fluid. This is unique in that bornite and uraninite are chemically dissimilar, and most recorded CDR reactions have some chemical commonality.

The study of uraninite has formed the major part of the research conducted within this project. Nevertheless, both brannerite and coffinite have also been studied, though no nanoscale characterization of these minerals has been conducted to-date. Chapter 6 presents the first detailed study of the chemical and textural relations of brannerite and coffinite at OD. It has long been proposed (Ehrig et al., 2012, and references therein) that the uranium minerals have a complex history with repeated cycles of precipitation, dissolution and reprecipitation, so this study will further investigate this statement and provide detailed chemical and textural information about both the brannerite and coffinite found at OD.

The penultimate chapter in this thesis, Chapter 7, summarizes the key findings of all work conducted as part of this project, and contains suggestions for potential future research directions. This compilation of work further documents key observations about the chemical and textural heterogeneity of the U-minerals at OD, and it is envisaged will provide some

fundamental findings that will be used to drive future research projects. Chapter 8 is a collation of all references cited within this thesis.

CHAPTER 2

RESEARCH METHODOLOGY

CHAPTER 2: RESEARCH METHODOLOGY

This chapter provides a brief summary of the samples which have been analyzed, sample preparation techniques, as well as an outline of the analytical techniques and methods which were employed as part of this study. Analytical techniques used for data measurement are discussed below and included: scanning electron microscopy (SEM), Mineral Liberation Analysis (MLA), electron probe micro-analysis (EPMA), focussed ion beam – scanning electron microscopy (FIB-SEM), focussed ion beam – electron backscattered diffraction (FIB-EBSD), and transmission electron microscopy (TEM).

2.1 Sample selection

A total of 24 samples from existing BHP Billiton diamond drill-core were selected to target key mineralogical and chemical variability from various localities around the Olympic Dam deposit. The samples (Tables 2.1 and 2.2, Figures 1.2 and 2.1) were selected to target a range of: (1) U and Pb grades; (2) rock type (granitic with various degrees of hematite alteration); (3) sulfide mineralogy; (4) variability in gangue mineralogy (i.e. carbonates, barite, fluorite); (5) depth and location within the deposit. Of particular importance for the current study, is that the samples selected contained a range of U_3O_8 grades, as it was thought that this provided the best chance of obtaining variation in the relative abundances of the U-minerals. Most samples were from the periphery of the deposit (Figures 1.2 and 2.1). This was intentional, as towards the centre of the deposit, textural overprinting during exposure to more intense brecciation and alteration makes interpretation difficult or impossible. The mineralogical variability of the samples analyzed as part of this study, as displayed in Figures 2.2 and 2.3, is typical of the variability observed for OD ores.

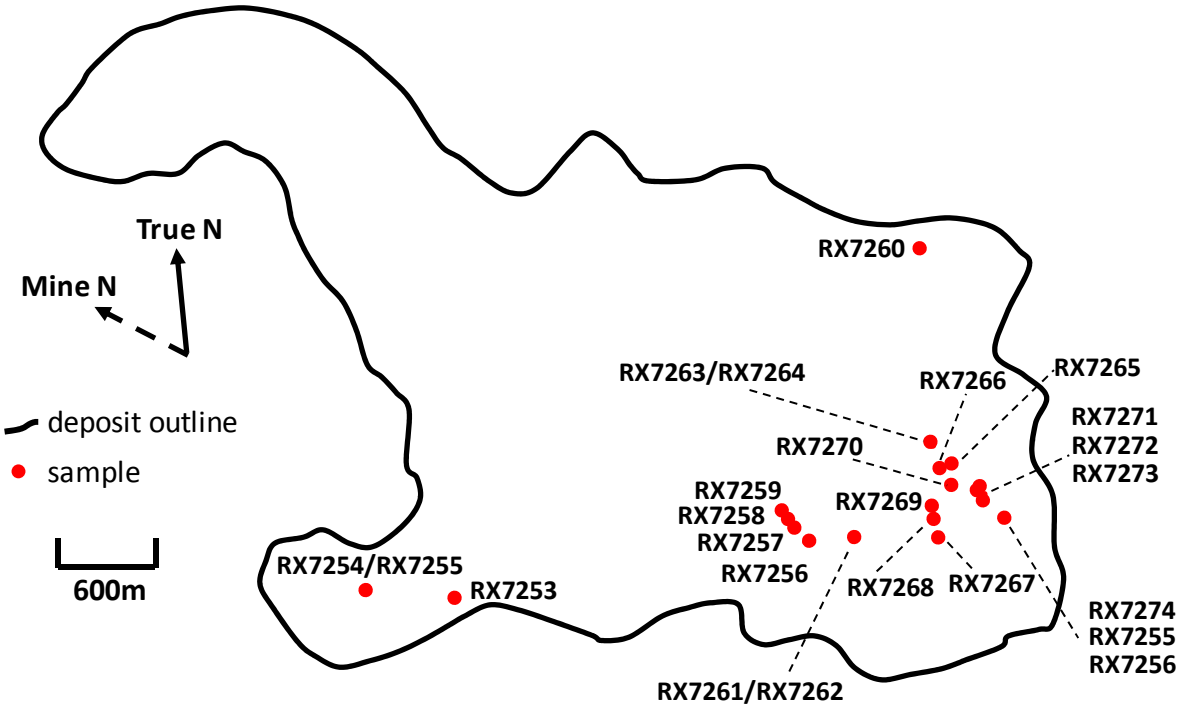

Figure 2.1: Schematic plan-view diagram of samples analyzed within this study relative to the OD deposit outline.

Table 2.1: Details relating sample ID to drillhole ID, depth, U_3O_8 grade, breccia type and dominant sulfides identified within each sample.

Sample ID	Hole ID	Depth (m)	U_3O_8 Grade (ppm)	Breccia Type[a]	Dominant Sulfides[b]
RX7253	RD1303	471.9	21326	GRNH	Bn-Ccp
RX7254	RD1304	890.1	781	HEMH	Py-Ccp
RX7255	RD1305	691.0	364	GRNL	Ccp-Py
RX7256	RD1988	880.8	6914	HEMH	Bn-Cct
RX7257	RD1988	1618.9	597	HEM	Bn
RX7258	RD1988	1768.8	408	HEM	Ccp
RX7259	RD1988	1808.9	369	HEM	Ccp
RX7260	RD2080	479.7	1686	GRNL	Bn
RX7261	RD3000W1	936.3	387	HEMH	Bn-Cct
RX7262	RD3000W1	948.2	382	HEMH	Ccp-Bn
RX7263	RD3002	470.9	145840	HEM	Ccp-Bn
RX7264	RD3002	472.4	119	HEM	Ccp-Py
RX7265	RD3022	921.6	2244	HEM	Ccp-Py
RX7266	RD3022	968.2	731	HEM	Ccp
RX7267	RD3035	675.5	1293	HEMH	Ccp
RX7268	RD3035	876.8	638	HEM	Ccp
RX7269	RD3035	970.5	1605	HEMF	Bn
RX7270	RD3307	1092.8	1153	HEM	Bn
RX7271	RD3554	455.9	424	GRNH	Ccp
RX7272	RD3554	494.4	425	GRNH	Bn
RX7273	RD3554	498.2	139	GRNH	Bn
RX7274	RD3560	716.3	11259	GRNL	Bn-Cct
RX7275	RD3560	719.6	494	GRNL	Bn-Cct
RX7276	RD3560	726.7	408	GRNL	Bn

a) Breccia types: GRNH = Roxby Downs Granite (RDG; 90-70%) with some hematite (10-30%) breccia, matrix contains hematized sericite, quartz; GRNL = RDG (70-40%) with hematite (30-60%) breccia, granitic clasts with hematite-rich matrix; HEMH = Hematite (60-90%) with RDG (40-10%) breccia, hematite-rich matrix supported breccia with hematitic clasts; HEM = Hematite (>90%) with RDG (<10%) breccia, hematite-rich matrix and clasts with strong hematite alteration; HEMF = Hematite with GRV clasts, often porphyritic with chloritized phenocrysts.

b) Sulfides listed in order of abundance as determined by MLA modal analysis. Single sulfide listed when dominant sulfide >90% of relative sulfide abundance. Abbreviations: Cct = Chalcocite, Bornite = Bn, Ccp = Chalcopyrite, Py = Pyrite.

Table 2.2: Relative proportions of coffinite/brannerite/uraninite as determined by Mineral Liberation Analysis (MLA) sparse phase liberation mapping (SPL_Lite) data.

Sample No.	U-Mineral Relative Abundance (wt%)		
	Uraninite	**Coffinite**	**Brannerite**
RX7253	6	91	3
RX7254	36	23	41
RX7255	2	16	82
RX7256	96	0	4
RX7257	93	7	0
RX7258	91	8	1
RX7259	83	14	3
RX7260	91	3	6
RX7261	1	5	94
RX7262	1	5	94
RX7263	100	0	0
RX7264	89	11	0
RX7265	5	13	82
RX7266	4	84	12
RX7267	89	8	3
RX7268	8	18	74
RX7269	70	17	13
RX7270	59	17	24
RX7271	0	44	56
RX7272	6	49	45
RX7273	1	46	53
RX7274	83	0	17
RX7275	24	1	75
RX7276	56	0	44

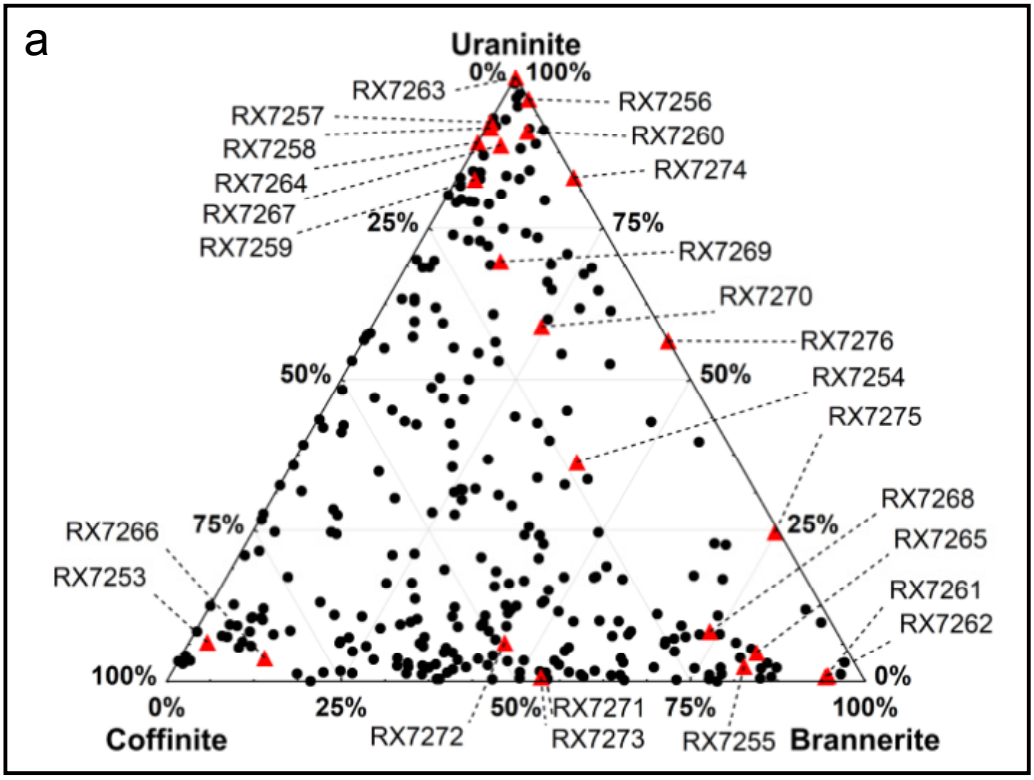

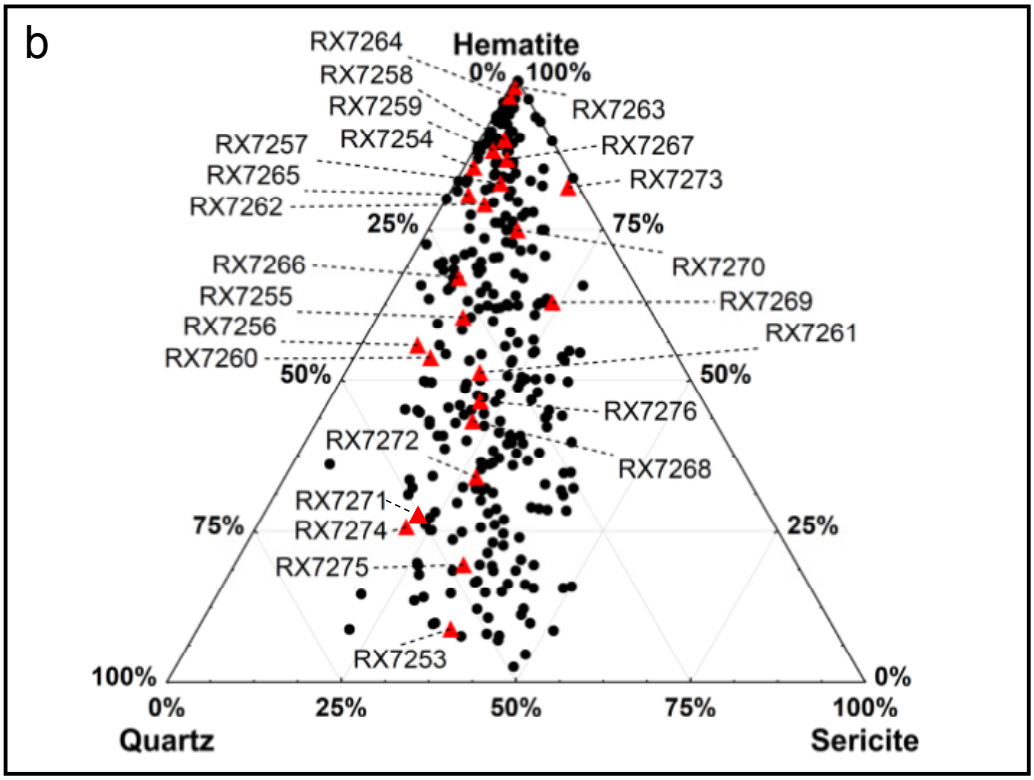

Figure 2.2: Ternary plots displaying mineralogical variability of samples selected for this study compared to typical OD ores. Data plotted are measured modal abundances (wt%) from MLA XMOD and SPL_Lite analysis, shown as relative proportions of: **(a)** uraninite, coffinite and brannerite (SPL_Lite data); **(b)** hematite, quartz and sericite (XMOD data). Image modified from Macmillan et al. (2016).

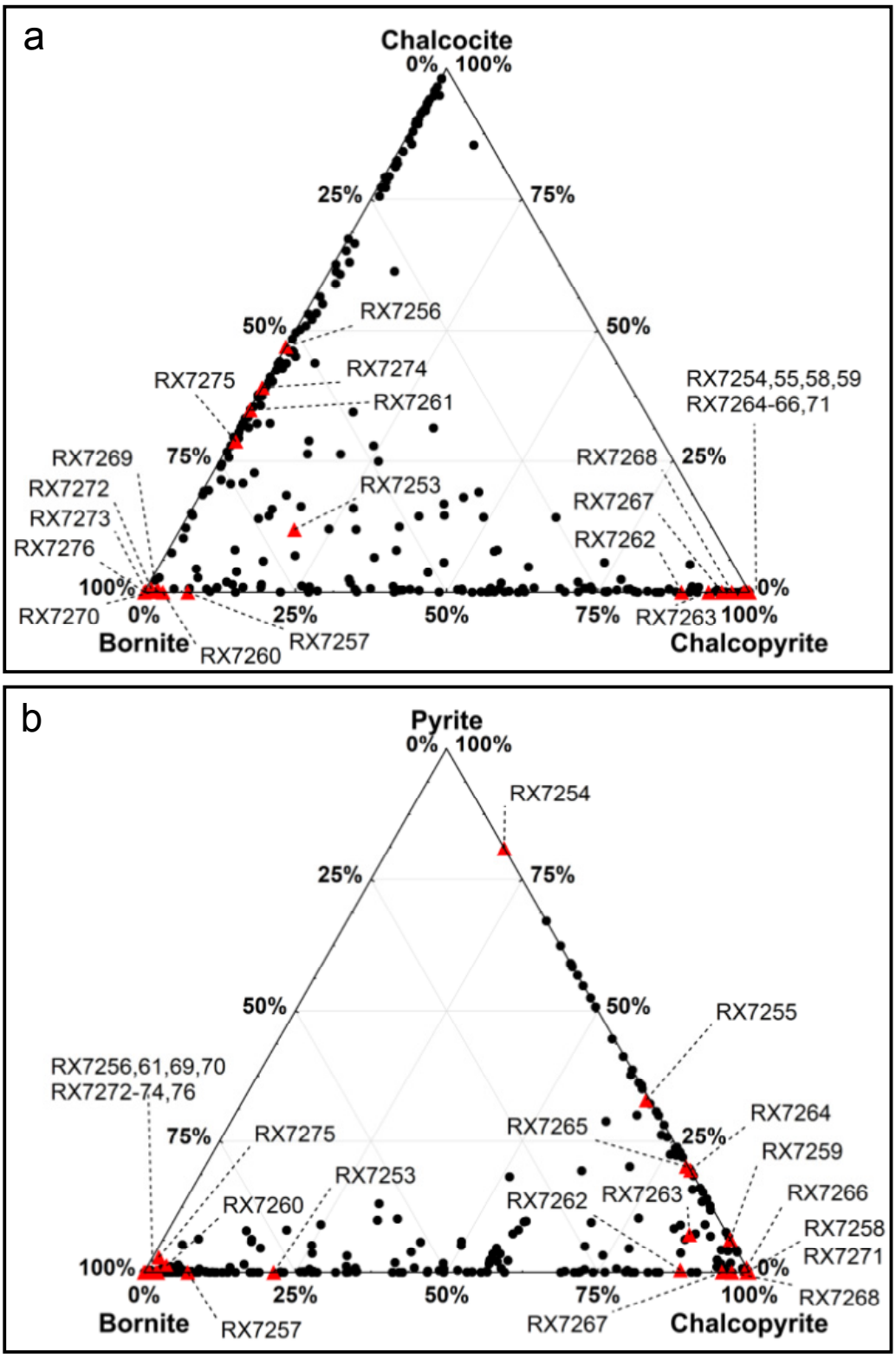

Figure 2.3: Ternary plots displaying mineralogical variability of samples selected for this study compared to typical OD ores. Data plotted are measured modal abundances (wt%) from MLA XMOD analysis, shown as relative proportions of: **(a)** chalcocite, bornite and chalcopyrite; **(b)** pyrite, bornite and chalcopyrite. Image modified from Macmillan et al. (2016).

2.2 Sample preparation

Diamond drill-core samples were cut and standard petrographic thin sections were prepared by Adelaide Petrographic Laboratories. Steps 1 to 3 are standard for all thin-section preparation, and Steps 4 and 5 are additional polishing/cleaning steps required only for samples that were to be analyzed using FIB-EBSD (reasons discussed in Section 2.6). Preparation steps included:

1. Impregnation of drill-core rock sample with araldite GY191 and Hardener HY951. Cure and then remove cured araldite from surface by sanding using 1200 grit fixed media (wet and dry sand paper).
2. Polish sample on ceramic lap with 6 µm diamond paste for 2 to 10 minutes as needed.
3. Polish sample using textmet (Buehler textmet 1500 8" PSA) cloth lap with 3 µm diamond paste for 30 – 60 minutes; with 1 µm diamond paste for 40 – 60 minutes; and with 1 or ¼ Kemet WP diamond solution for 30 – 60 minutes.
4. Final polish of sample using Struers MD Chem lap Kent polisher with Struers colloidal silica product (OP-S non Dry) for 2 hours.
5. As required, ultrasonic cleaning was used to avoid cross-contamination (especially important for the removal of colloidal silica).

2.3 Scanning electron microscopy (SEM)

Scanning electron microscopy (SEM) was conducted using a Quanta 450 field emission gun (FEG) SEM with silicon-drift detector (Adelaide Microscopy, University of Adelaide). This microscope can be operated in three different modes: environmental, low vacuum and high vacuum. For this study it was operated using the high vacuum mode. The operating conditions used included: 20 keV accelerating voltage, 60 Pa chamber pressure, 0° tilt, 10-11 mm working distance, with a spot size of 4-5. Detectors fitted include a secondary electron (SE)

detector, a backscattered electron (BSE) detector, and an EDAX® energy dispersive X-ray spectrometer (EDS). All of these detectors can be used for sample characterization. SE imaging was used to locate areas of interest for further analysis, and BSE imaging used to record all morphological and textural features observed within the samples. Each observed U-mineral texture was imaged using a range of magnifications, as well as different brightness and contrast settings to highlight internal heterogeneities which would otherwise not have been observed (Figure 2.4). Semi-qualitative chemical analyses were obtained using EDS. Prior to any analysis being conducted, samples were coated with ~15 nm-thick carbon film via thermal evaporation in a Quorum Q150TE vacuum evaporator. Samples were mounted on a 12 mm-diameter aluminium stub with double sided carbon tape before placing inside the SEM chamber ready for analysis.

All BSE images were assigned a unique ID (of the form RX72xx_yy, where xx=sample number and yy=grain number), and the locations of these regions were recorded on BSE image montages that were produced for each polished thin section from the Mineral Liberation Analyzer (MLA) 650 Environmental SEM (Central Science Laboratory, University of Tasmania). The location of all grains and areas of interest were therefore recorded, and this meant that if the same region of interest needed to be re-imaged or analyzed using different methods, it could easily be relocated.

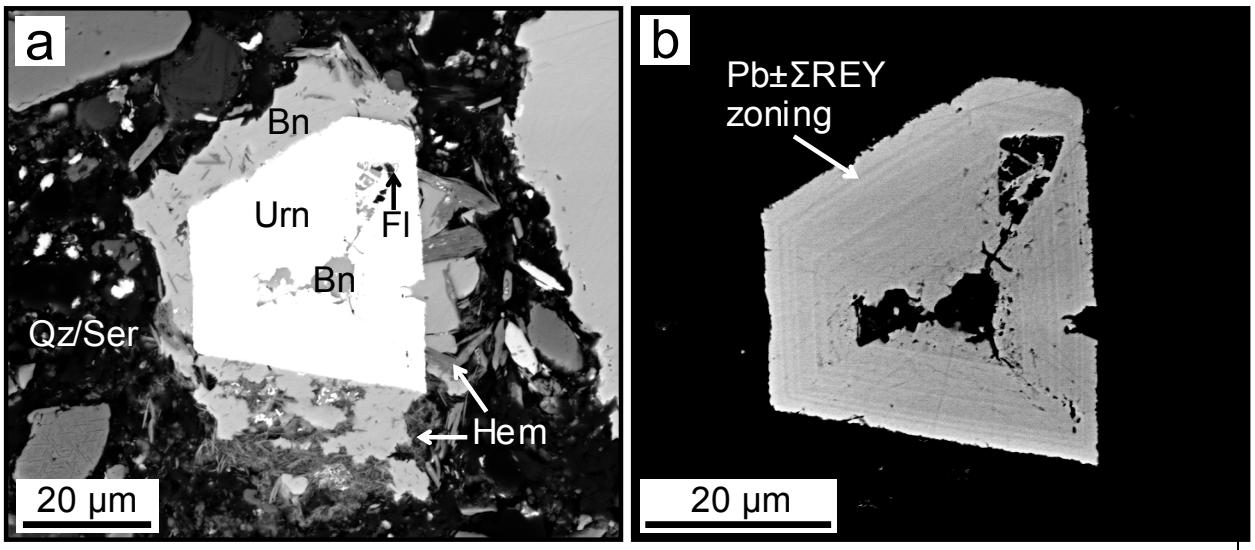

Figure 2.4: Back-scatter electron (BSE) images of a zoned uraninite (RX7269_37): **(a)** uraninite (Urn) grain contains bornite (Bn) and fluorite (Fl) inclusions and infilled cracks, and is surrounded by a bornite ± hematite (Hem) selvedge. Matrix minerals include quartz (Qz), sericite (Ser) and hematite; **(b)** reduced brightness and contrast settings to display otherwise unobservable chemical zoning of Pb and ΣREY.

2.4 Mineral Liberation Analysis (MLA)

Automated mineralogy was measured using a Mineral Liberation Analyzer (MLA) by staff at ALS Mineralogy, Brisbane. The MLA system consists of a SEM and special computer software which allows for the automated collection of mineralogy data. Numerous measurement and set-up modes, as documented by Gu (2003), can be used which are dependent on the type of samples being analyzed, as well as the type of data to be obtained. Measurement modes used for the current study were x-ray modal (XMOD) and sparse phase liberation mapping (SPL_Lite). The XMOD method (Figure 2.5a) is a basic point counting method and involves taking individual X-ray analyses at each counting point within a predefined grid. This method uses variation in BSE grey level to distinguish between minerals and only produces modal mineralogy data. Thus, the XMOD data collected for the current study was used to characterize the bulk modal abundances of all minerals (defined in Table

2.3) within each sample. The SPL_Lite method (Figure 2.5b) searches the sample BSE images for particles/areas of interest (i.e., U-bearing grains in this case) based on variation in BSE grey level. Each BSE image is collected and segmented to delineate mineral grain boundaries in each particle/area, and then each individual grain is analysed with one X-ray. Data is processed off-line to generate false colour mineral maps from the segmented data and x-ray spectra. Thus, the SPL_Lite method was used to specifically target the U-minerals and measure the relative abundances of U-minerals, their range of compositions, as well as details of all minerals found in contact with U-mineral grains. The association data obtained from the SPL_Lite method is calculated by measuring the length of the boundary between the U-mineral and any other mineral found touching it, and this is divided by the total length of the perimeter of the U-mineral grain. Thus, a relative proportion (in wt%) of each mineral found in contact with the U-mineral can be estimated, and this is recorded as the mineral association. The U-mineral relative abundance data, as obtained from the SPL_Lite method, was used to double check that all U-mineral types had been identified manually on the SEM. This ensured that the full gambit of U-mineral textures contained within all samples had been manually recognized.

Table 2.3: Detailed mineral list defined for all MLA analyses.

Mineral	**Formula**
Al_Hydroxide	$Al_2(SO_4)_3 \cdot 17(H_2O)$
Albite	$NaAlSi_3O_8$
Altaite	PbTe
Anhydrite	$CaSO_4$
Ankerite	$Ca(Fe,Mg,Mn)(CO_3)_2$
Apatite	$Ca_5(PO_4)_3F$
Barite	$BaSO_4$
Barite_Sr	$(Ba,Sr)SO_4$
Bastnäsite	$(Ce,La,Nd,Pr,Ca)(CO_3)F$
Bismuthinite	Bi_2S_3
Bornite	Cu_5FeS_4
Brannerite	$(U,Ca)(Ti,Fe)_2O_6$
Calcite	$(Ca,Mn)CO_3$
Carrollite	$CuCo_2S_4$
Cerussite	$PbCO_3$
Chalcocite	Cu_2S
Chalcopyrite	$CuFeS_2$
Chlorite_1	$(Mg,Fe,Al)_3(Al,Si)_4O_{10}(OH)_2$
Chlorite_2	$(Fe,Al)_3(Al,Si)_4O_{10}(OH)_2$
Chlorite_3	$Mg_2(Al,Fe)_3Si_3AlO_{10}(OH)_8$
Clausthalite	PbSe
Cobaltite	(Co,Fe)AsS
Coffinite-Si_7	$(U,Y,Ca,Ce,Nd,Fe)[(Si,Al)O_4,PO_4,(OH)_4]$
Coffinite-Si_9Y_7	$(U,Y,Ca,Ce,Nd,Fe)[(Si,Al)O_4,PO_4,(OH)_4]$
Coffinite-Si_9Y_9	$(U,Y,Pb,Fe,Er,Dy,Nd,Ce,La,Ca,K)[SiO_4,PO_4,(OH)_4]$
Coffinite-Si_{10}	$(U,Y,Ca,Ce,Nd,Fe)[(Si,Al)O_4,PO_4,(OH)_4]$
Coffinite-$Si_{10}Y_1$	$(U,Y,Pb,Fe,Nd,La,Ce,Ca,K)[(Si,Al)O_4,PO_4,(OH)_4]$
Coffinite-$Si_{10}Y_{10}$	$(U,Y,Ca,Ce,Nd,Fe)[(Si,Al)O_4,PO_4,(OH)_4]$
Coffinite-$Si_{12}Y_6$	$(U,Y,Pb,Fe,Nd,La,Ce,Ca,K)[(Si,Al)O_4,PO_4,(OH)_4]$
Corundum	$(Al,Fe)_2O_3$
Covellite	CuS
Crandallite_Grp	$(Ce,La,Nd,Ca,Sr)(Al,Fe)_3(SO_4,PO_4)_2(OH)_6$
Dolomite	$Ca(Mg,Fe,Mn)(CO_3)_2$
Domeykite	$(Cu,Fe)_3As$
FeO	Fe_2O_3
Florencite	$(Ce,La,Nd,Ca,Sr)(Al,Fe)_3(PO_4)_2(OH)_6$
Fluorite	CaF_2
Galena	PbS
Ilmenite	$(Fe,Mn)TiO_3$
Ilmenorutile	$(Ti,Nb,Fe,Mn)O_6$
Kaolinite	$Al_2Si_2O_5(OH)_4$

Mineral	**Formula**
Löllingite	$(Fe,Co,Ni)As_2$
Molybdenite	MoS_2
Monazite	$(Ce,La,Nd,Fe,Ca,Th)PO_4$
Native_Copper	Cu
Orthoclase	$KAlSi_3O_8$
Pyrite	FeS_2
Pyrrhotite	$Fe_{1-x}S$ (x=0.0-0.2)
Quartz	SiO_2
Rutile	TiO_2
Safflorite	$(Co,Fe)(As,S)_2$
Scheelite	$CaWO_4$
Schorl	$NaFe_3Al_6(BO_3)_3Si_6O_{18}(OH)_4$
Sellaite	MgF_2
Sericite	$K(Fe,Mg,Al)_2(AlSi_3O_{10})(OH,F)_2$
Siderite	$(Fe,Mn)CO_3$
Siderite_Mn	$(Fe,Mn,Ca)CO_3$
Sphalerite	(Zn,Fe)S
Synchysite	$Ca(Ce,Nd,La,Sm,Gd,Y,Fe)(CO_3)_2F$
Tellurobismutite	Bi_2Te_3
Tennantite	$(Ag,Cu,Zn,Fe)_{12}(As,Sb)_4S_{13}$
Thorite	$(Th,U,Fe,Y,P,Ca,Pb)SiO_4$
Topaz	$Al_2SiO_4(F,OH)_2$
Unknown	Un
Uraninite-Pb_5	$(U,Pb,Ce,Nd,Fe,Ca)O_2$
Uraninite-Pb_{10}	$(U,Pb,Y,Ce,Nd,Fe,Cu,Ca)O_2$
Uraninite-Pb_{15}	$(U,Pb,Ce,La,Nd,Sm,Gd,Y,Fe,Cu,Ca,K)O_2$
Uraninite-Pb_{20}	$(U,Pb,Fe,Nd,Ce,La,K,Y)O_2$
Uraninite_Si	$(U,Fe,Nd,Ce,La,Ca,K)(SiO_4,O_2)$
Uranothorite	$(U,Th,Y,P,Fe,Ca,Nd)SiO_4$
Xenotime	$(Y,Yb)PO_4$
Xenotime-U	$(Y,U,Dy,Nd,Sm,Gd,Fe)[(PO_4),(SiO_4)]$
Zircon	$ZrSiO_4$
Zircon-U	$(Zr,Hf,U,Ca,Fe,Fe,Dy,Er,Yb,Y)[(Si,Al)O_4]$

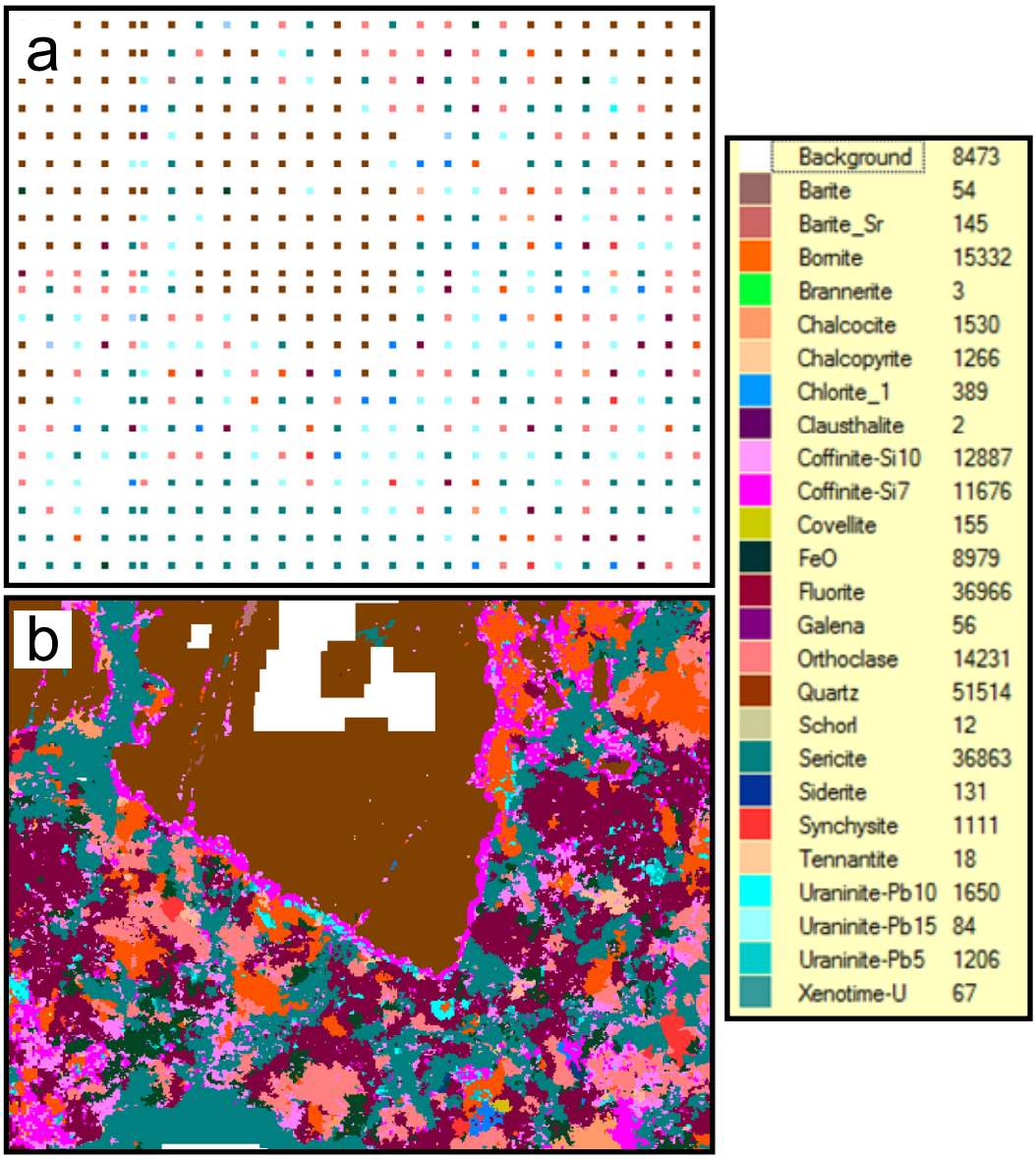

Figure 2.5: Examples of data collected by the MLA system: **(a)** point data attained from X-ray modal analysis (XMOD); **(b)** False colour map produced from sparse phase liberation mapping (SPL_Lite). Areas that are coloured white contained no U-minerals and were therefore not mapped.

2.5 Electron probe micro-analysis (EPMA)

Quantitative analysis of all U-minerals was obtained using a Cameca SX-Five electron probe micro-analyser (EPMA) at Adelaide Microscopy, University of Adelaide. This device is equipped with 5 tuneable wavelength-dispersive spectrometers (WDS), an energy dispersive X-ray spectrometer (EDS) and an optical microscope. The configuration of diffraction crystals available for use within the WDS spectrometers can be modified depending on the type of analysis being conducted, but for the current study these were setup with LPET (large area pentaerythritol) crystals for spectrometers 1, 4 and 5, a TAP (thallium hydrogen pthalate) crystal for spectrometer 2, and a LLIF (large area lithium fluoride) crystal for spectrometer 3. The Probe for EPMA software (Donovan, 2014) was used for data acquisition and processing.

For spot analyses, operating conditions included a 15 keV accelerating voltage, 100 nA beam current, 40° takeoff angle, with 0.5 to 1 μm-sized beam. A total of 28 elements were measured: U, Pb, Th, Na, Mg, Al, Si, P, S, K, Ca, Ti, Mn, Fe, Cu, As, Zr, Nb, Y, Ce, La, Pr, Nd, Sm, Gd, Sr, Ba, Te. The total acquisition time per point was 9 minutes 42 seconds. Details of the standards used and measured element X-ray lines for all spot analyses can be found in Tables 2.4 and 2.5.

For spot analyses, elements that may be affected by beam damage were measured first (e.g., P Kα, Pb Mβ, Na Kα, Mn Kα, K Kα) and intensity data was corrected for Time Dependent Intensity (TDI) loss (or gain) using a self-calibrated correction for these elements. The acquisition order was also adjusted to optimize spectrometer usage so that all spectrometers had approximately equal measurement times. Both unknown and standard intensities were corrected for dead-time, with standard intensities also being corrected for standard drift over time. The standards used for all analyses are listed in Table 2.4.

Table 2.4: Details of the element X-ray line measured, spectrometer/crystal type and standard used in calibration for all EPMA spot analyses.

Element X-ray Line	Spectrometer (Crystal)	Name of Primary Standard
U-Mβ	SP1 (LPET)	UO_2[a]
Pb-Mβ	SP1 (LPET)	Synthetic Pb Glass – K227[b]
Th-Mα	SP1 (LPET)	Huttonite[a]
Na-Kα	SP2 (TAP)	Albite[c]
Mg-Kα	SP2 (TAP)	Almandine Garnet[c]
Al-Kα	SP2 (TAP)	Almandine Garnet[c]
Si-Kα	SP2 (TAP)	Almandine Garnet[c]
P-Kα	SP5 (LPET)	Apatite[c]
S-Kα	SP5 (LPET)	Marcasite[c]
K-Kα	SP4 (LPET)	Sanidine[c]
Ca-Kα	SP4 (LPET)	Wollastonite[d]
Ti-Kα	SP4 (LPET)	Rutile[c]
Mn-Kα	SP3 (LLIF)	Rhodonite[c]
Fe-Kα	SP3 (LLIF)	Almandine Garnet[c]
Cu-Kα	SP3 (LLIF)	Chalcopyrite[d]
As-Lα	SP2 (TAP)	Gallium Arsenide[c]
Zr-Lα	SP5 (LPET)	Zircon[g]
Nb-Lα	SP5 (LPET)	Niobium Metal[c]
Y-Lα	SP5 (LPET)	Rare Earth Glass Standard – REE1[e]
Ce-Lα	SP1 (LPET)	Ce Glass[f]
La-Lα	SP1 (LPET)	La Glass[f]
Pr-Lβ	SP3 (LLIF)	Pr Glass[f]
Nd-Lβ	SP3 (LLIF)	Nd Glass[f]
Sm-Lβ	SP3 (LLIF)	Sm Glass[f]
Gd-Lβ	SP3 (LLIF)	Gd Glass[f]
Sr-Lα	SP2 (TAP)	Celestite[c]
Ba-Lα	SP4 (LPET)	Barite[c]
Te-Lα	SP4 (LPET)	Silver Telluride[d]

a) Standards from David Steele.
b) Synthetic Pb Glass standard from the National Institute of Standards and Technology (NIST), United States of America.
c) Standards from Astimex Standards Ltd.
d) Standards from P & H Developments, United Kingdom.
e) Rare Earth Glass Standard from (Drake and Weill, 1972)
f) Single element synthetic REE glasses from Edinburgh Materials and Microanalysis Centre, University of Edinburgh, United Kingdom
g) Standard from C.M. Taylor Company

Elemental mapping of 13 elements was also completed using PET and LPET crystals only. Set-up conditions included an accelerating voltage of 20 keV, beam current of 100 nA and beam-size of 1 μm. Element X-ray lines measured via WDS included: Ce Lα, P Kα, Ca Kα, Y Lα, and Pb Mα. In contrast, EDS were used to measure: Si Kα, Fe Kα, U Lα, S Kα, Cu Kα, La Lα, Nd Lα, and Ti Kα. Dwell time per point was 180 ms.

Three key steps required to attain accurate EPMA analysis, include: 1) the identification of all elements present in the phase(s) of interest; 2) the identification of any spectral interferences; and 3) selection of background positions which accommodate all elements present. Full wavelength spectrometer scans were therefore completed to identify all possible elements contained within the U-minerals. High-resolution wavelength scans were also conducted to target the specific wavelengths relevant for each identified element. This enabled selection of accurate background point positions which were not impacted by any interferences.

For the current study, U, Th and Pb were all important elements and were analysed using a LPET diffraction crystal (Table 2.5). The Th Mα peak is free from any interference, and was thus selected as an energy line to measure for analysis. Both U and Pb have numerous interferences on the Mα and Mβ emission lines, and thus selection of which line to use was more difficult. Using U as an example for the process involved in determining which emission line to measure, the identification of possible interferences with either the Mα or Mβ line, and the selection of background points will now be discussed. The U Mα line had a large overlap with the Th Mβ line, and was also near the large Ar K absorption edge (a major component of the P10 detector gas). Thus it was decided that the U Mα line was inappropriate to use for measurement of uranium. High-resolution wavelength scans of the U-minerals of interest (Figure 2.6) and selected standards (huttonite, Gd Glass, UO_2, sanidine and rhodonite; Figures 2.7 and 2.8) were conducted near the $Sin\Theta x10^5$ values of the U Mβ peak on

spectrometer 1. Emission lines identified within the SinΘx10^5 values of the U Mβ peak were: K $K\alpha_{1,2}$, Th $M\gamma_1$, Th $M_{4\text{-}02}$, Gd $L\beta_1$, K $SK\alpha_{3,4}$, and Mn $K\beta_{1,3}$ (Figures 2.7 and 2.8). The only emission lines identified from the selected U-mineral analysis points were U Mβ, K $K\alpha_{1,2}$, Th $M\gamma_1$ (Figure 2.6). But to account for any potential interferences, the location of all relevant emission lines as identified from the standards and unknowns have been considered in the selection of background point positions (point positions defined by dotted lines in Figures 2.7 and 2.8).

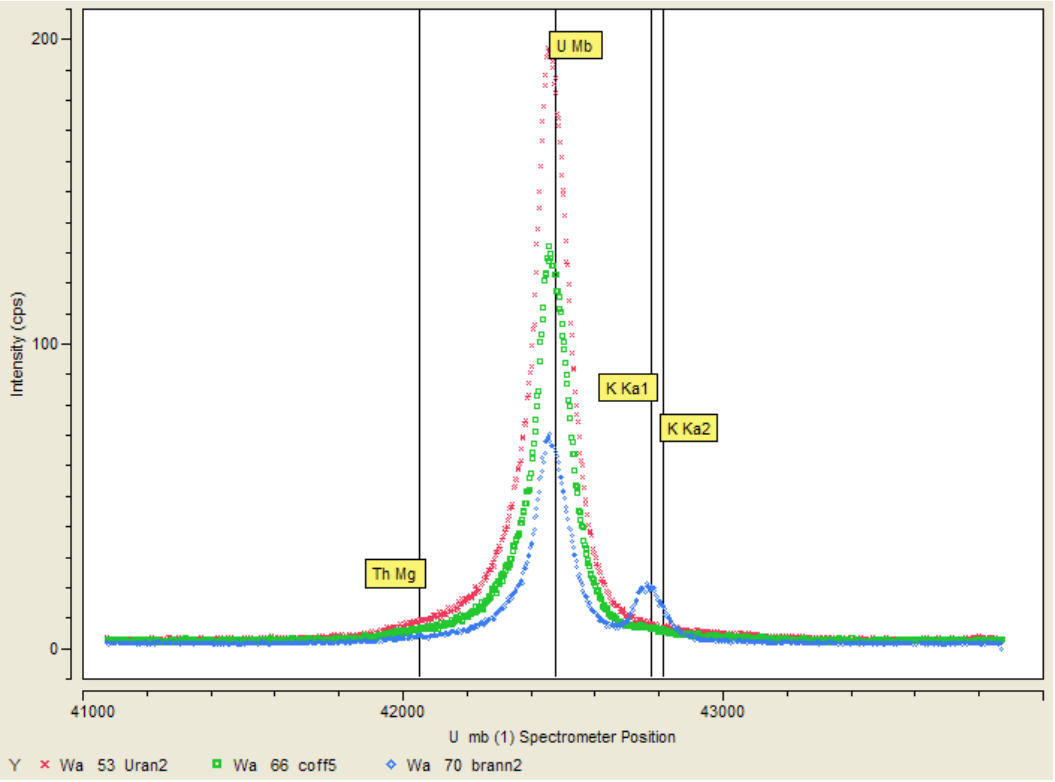

Figure 2.6: High-resolution wavelength scan for SinΘx10^5 values in the region of the U Mβ peak on spectrometer 1 for selected uraninite, coffinite and brannerite grains.

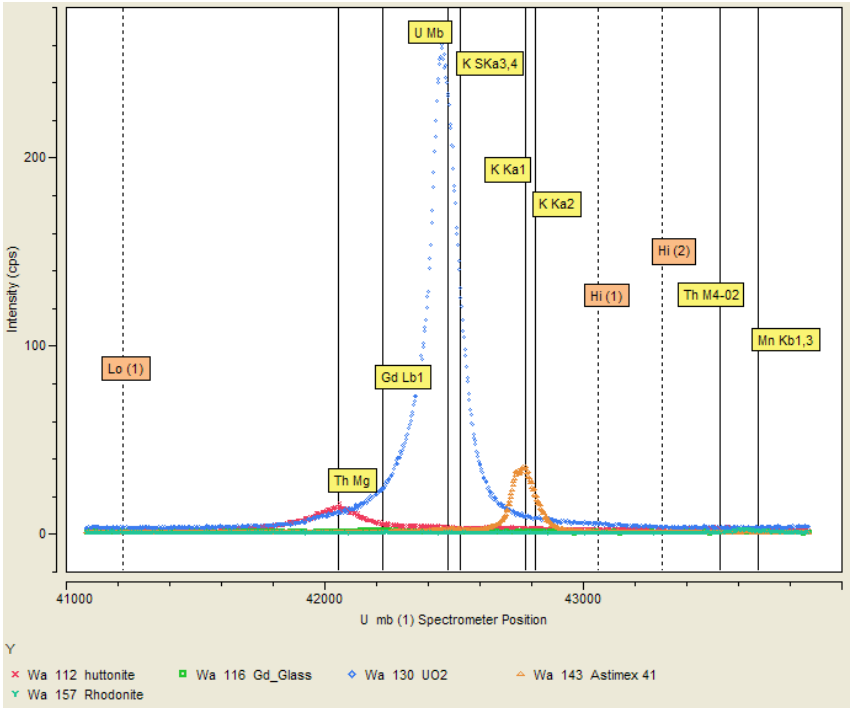

Figure 2.7: High-resolution wavelength scan for wavelengths in the region of the U Mβ peak on spectrometer 1 for selected standards (huttonite, Gd Glass, UO_2, sanidine and rhodonite).

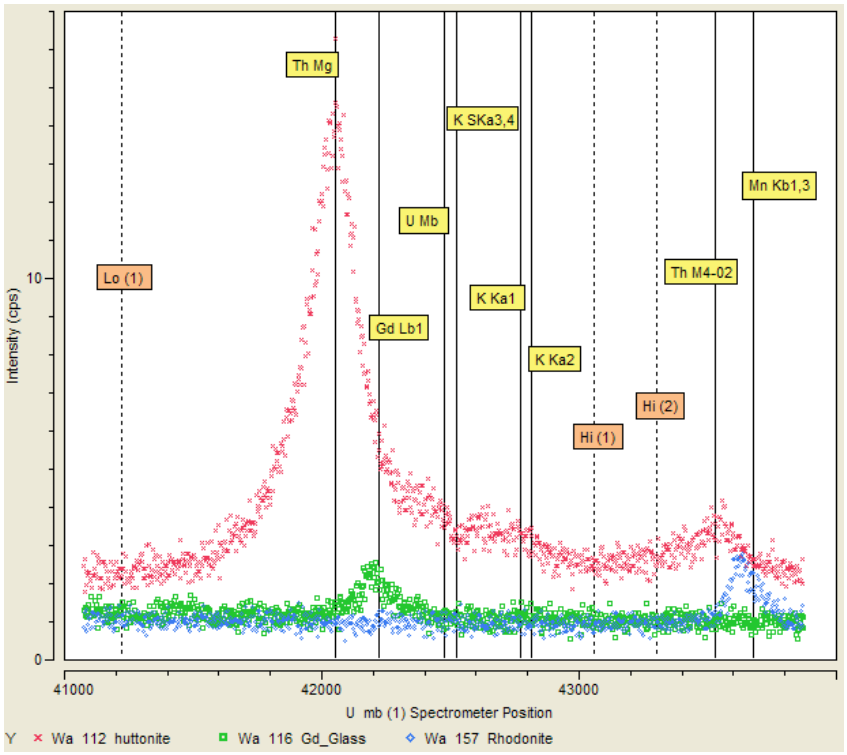

Figure 2.8: Close-up of high-resolution wavelength scan for wavelengths in the region of the U Mβ peak on spectrometer 1 for selected standards (huttonite, Gd Glass and rhodonite) to display numerous minor peaks which are otherwise masked due to lower count rates. Dotted lines show selected points for multi-point background determination.

Likewise, the choice of Pb Mα or Mβ emission line was constrained by numerous potential interferences, and although the Pb Mβ line was of slightly lower intensity, it had a cleaner spectrum and was therefore selected as the energy line to be measured. Potential interferences on the Pb Mβ line included: U $M\zeta_2$, S $K\beta_{1,3}$, S SKβ, Ba $L\beta_4$, Ce $L\alpha_1$, Nb $L\gamma_1$, as well as others in the vicinity of the peak. Thus, careful selection of the background point positions was vital in ensuring that none of these points coincided with any of the peak positions of these interferences.

Many of the U-minerals at OD also contain REY, and this often makes the selection of background positions challenging due to many cross-interferences (Donovan et al., 1993; Goemann, 2011). Typically, REY are measured on LIF or PET crystals (e.g., Pyle et al., 2002), with Pr, Nd, Sm, Gd and Dy often being measured via their Lβ emission lines, and Y, La, Ce, Er and Yb usually being measured via their Lα lines (e.g., Exley, 1980). The *d*-spacing of the PET and LIF crystals is usually $2d = 8.74$ nm and $2d = 4.02$ nm, respectively, and for higher mass REY the larger *d*-spacing found in the PET crystal dictates that these elements occur over a smaller $\text{Sin}\Theta x10^5$ range. The smaller $\text{Sin}\Theta x10^5$ range results in there being many more interference issues when analyzing REY with a PET crystal type. Moreover, the REY are often present in low concentrations, and thus often require long count times. To ensure all spectrometers were used optimally and to minimize count times, multiple spectrometers were therefore used to measure the REY elements. Wavelength scans were conducted on both LPET and LLIF crystals (the large area variants of PET and LIF crystals) for the Lα lines of both Ce and La. It was found that the counts were generally much greater on the LPET crystal than the LLIF crystal, and the peaks were much easier to identify. Furthermore, since a Ce correction is required for Pb Mβ, this also dictates the need for the Lα line of Ce to be measured on the same spectrometer as that used to analyse the Pb Mβ. For all of these reasons, Ce, La and Y were measured via their Lα lines on LPET crystals, and all

other REY were measured via their Lβ lines on the LLIF crystal. A summary of the crystal types, peak/off-peak count times and off-peak interference corrections methods applied for all measured element X-ray lines can be found in Table 2.5.

Table 2.5: Summary of set-up used for all U-mineral analyses on EPMA (element X-ray lines, on- and off-peak count times, and off-peak correction method used to correct for listed elemental interferences).

Element X-ray Line	On-Peak Count t (s)	Off-Peak High Count t (s)	Off-Peak Low Count t (s)	Interference with…	Off-Peak Correction
U-Mβ	50	25	12.5	K, Th	Multi-Point
Pb-Mβ	60	30	30	U, Ce, S, Y	Multi-Point
Th-Mα	50	12.5	12.5	-	Multi-Point
Na-Kα	20	5	10	U	Multi-Point
Mg-Kα	30	15	7.5	-	Multi-Point
Al-Kα	30	15	15	Ti	Multi-Point
Si-Kα	30	15	7.5	Y	Multi-Point
P-Kα	30	15	7.5	Ca, Cu	Multi-Point
S-Kα	20	10	5	Nd, La	Multi-Point
K-Kα	20	10	10	U	Multi-Point
Ca-Kα	30	15	15	-	Multi-Point
Ti-Kα	30	15	15	U	Multi-Point
Mn-Kα	10	5	5	As	Slope (Hi)
Fe-Kα	20	10	10	-	Multi-Point
Cu-Kα	20	10	10	-	Multi-Point
As-Lα	40	10	10	Sm, Nd	Multi-Point
Zr-Lα	20	20	20	Nd	Slope (Lo)
Nb-Lα	20	10	5	Mn	Linear
Y-Lα	50	25	25	-	Multi-Point
Ce-Lα	30	15	15	-	Linear
La-Lα	30	15	15	Nd	Slope (Lo)
Pr-Lβ	30	15	7.5	U	Multi-Point
Nd-Lβ	30	7.5	7.5	-	Multi-Point
Sm-Lβ	30	15	15	-	Multi-Point
Gd-Lβ	30	15	15	U	Multi-Point
Sr-Lα	30	15	7.5	-	Linear
Ba-Lα	20	10	5	Ti, U, Pr	Multi-Point
Te-Lα	20	10	10	Sm, U	Multi-Point

Another key factor in attaining accurate EPMA data is ensuring that points of analysis are carefully selected and are positioned directly over the phase of interest. For the U-minerals at OD, the size of the electron beam of the EPMA often approaches the size of the U-mineral being analysed. Moreover, the U-minerals are typically heterogeneous, may contain very fine intergrowths of various minerals, and are commonly chemically zoned. All of these factors make the attainment of clean spot analyses difficult, as the area analysed is often a mix of the U-mineral of interest with other intergrown or surrounding minerals. Thus, careful selection of analysis points was required, and all attained data was carefully filtered to remove any spurious results. The mean precision (based on 1σ) and typical minimum detection limits (mdl) values are reported in Table 2.6.

To track the reproducibility of the EPMA results, select standards (UO_2, K227, REE1 and almandine garnet) were run as unknowns, and elemental concentrations within these standards monitored. This highlighted the stability of the probe over time and also allowed for the removal of any data in cases of significant drift. The standard deviations (SD) for repeated analysis of these standards over a 4-month period were: 0.35 for U (n=44); 0.41 for Pb (n=41); 0.11 for Y (n=52); 0.10 for Si (n=46); and 0.18 for Fe (n=46).

Table 2.6: Minimum detection limits (wt%) and mean precision (wt%) based on 1σ for analyses of each U-mineral.

	Minimum Detection Limit (wt%)			**1σ Mean Precision (wt%)**		
	Brannerite	**Coffinite**	**Uraninite**	**Brannerite**	**Coffinite**	**Uraninite**
U	0.03	0.03	0.04	0.05	0.06	0.07
Pb	0.03	0.03	0.04	0.02	0.02	0.04
Th	0.03	0.04	0.04	0.01	0.02	0.02
Y	0.02	0.04	0.03	0.02	0.03	0.02
La	0.02	0.02	0.02	0.01	0.01	0.01
Ce	0.02	0.02	0.03	0.01	0.01	0.02
Pr	0.07	0.08	0.08	0.03	0.04	0.04
Nd	0.08	0.09	0.09	0.03	0.04	0.04
Sm	0.06	0.07	0.07	0.03	0.03	0.03
Gd	0.07	0.07	0.08	0.03	0.04	0.04
Na	0.02	0.02	0.02	0.01	0.01	0.01
Mg	0.01	0.01	0.01	0.004	0.004	0.004
K	0.01	0.01	0.01	0.003	0.004	0.003
Ca	0.005	0.005	0.01	0.01	0.01	0.01
Sr	0.02	0.02	0.02	0.01	0.01	0.01
Ba	0.02	0.03	0.03	0.01	0.01	0.01
Ti	0.01	0.01	0.01	0.02	0.003	0.004
Mn	0.03	0.03	0.03	0.01	0.02	0.02
Fe	0.02	0.02	0.02	0.02	0.02	0.01
Cu	0.03	0.03	0.04	0.02	0.02	0.02
Al	0.01	0.01	0.01	0.003	0.004	0.003
Si	0.01	0.01	0.01	0.01	0.01	0.005
P	0.01	0.01	0.01	0.004	0.01	0.004
S	0.01	0.01	0.01	0.004	0.01	0.01
As	0.02	0.02	0.03	0.01	0.01	0.01
Te	0.02	0.02	0.02	0.01	0.01	0.01
Nb	0.03	0.04	0.04	0.02	0.02	0.02
Zr	0.02	0.03	0.02	0.02	0.02	0.01

2.6 Focussed ion beam – scanning electron microscopy (FIB-SEM)

Nanoscale characterization of uraninite grains was carried out on a FEI Helios NanoLab 600 DualBeam™ FIB-SEM platform (Adelaide Microscopy, University of Adelaide) equipped with an energy dispersive X-ray spectroscopy (EDXS) detector, electron backscattered diffraction (EBSD) detector, and a solid-state scanning transmission electron microscopy (STEM) detector. Due to the vast number of analytical detectors and dual electron and ion beams, numerous analysis techniques can be employed on this device. These include: (1) secondary electron (SE) and backscattered electron imaging and mapping; (2) grain orientation and microstructural analysis using EBSD (refer Section 2.7); (3) the *in-situ* preparation and thinning of TEM foils (refer Section 2.8); (4) 3D 'slice and view' analysis; (5) compositional point analysis and mapping via EDXS; (6) STEM sub-micron mapping of TEM foils. The integrated use of all of these techniques and their application to micro- and nanoscale characterization of ore minerals is discussed by Ciobanu et al. (2011). Of relevance to the current study are EBSD analysis and the creation of TEM foils, and the particulars of these methods will now be discussed.

2.7 Focussed ion beam – electron backscattered diffraction (FIB-EBSD)

On the FIB-SEM platform mentioned above, EBSD data were collected using the EDAX-TSL™ EBSD system equipped with a Hikari camera. As discussed in Section 2.2, the thin-section samples to be analysed required additional polishing with colloidal silica to remove any surface damage generated during initial mechanical polishing, and to remove any surficial dust/oxide layers. EBSD is a surface sensitive technique and analysis is conducted in the top 10-50 nm region of the specimen (Wright et al., 2011), thus necessitating the need for such

rigorous sample preparation. Samples were also coated with a 1.5 to 2 nm thick carbon film using a Quorum Q150TE vacuum evaporator. The application of the carbon film is vital in the prevention of surface charging, but cannot be too thick, as otherwise only a weak electron diffraction pattern will be observed. Samples were mounted individually onto an aluminium analysis stub using Ag-Dag rather than traditional carbon-tape alone, as carbon-tape can melt during the long analysis times, causing the sample to move while being analysed. For EBSD analysis, the total sample tilt needs to be 70º. This was achieved by fitting the mounted sample on a 45º tilted sample holder, and then further tilting the specimen by 30º (refer Figure 2.9). EBSD patterns were collected at 20 kV and 2.7 nA with a working distance ranging between 10 and 13 mm. All data collection and processing parameters (i.e., gain, exposure etc.) were optimized to attain the best possible electron backscatter pattern (EBSP) for UO_2 rather than any other phase present in the mapped area (i.e., bornite, fluorite). Examples of some of these settings are given in Table 2.7. The OIM Data Collection (version 5.2) software was used for data collection, and the OIM Analysis (version 4.5) software was used for data analysis and interpretation.

For any EBSD analysis, the availability of crystallographic structure files for the materials being analysed is of critical importance. For the current study, minerals of interest included uraninite (UO_2), fluorite (CaF_2), bornite (Cu_5FeS_4) and chalcopyrite ($CuFeS_2$), and within the TSL structural database, structure files were available for these phases. Unfortunately, uraninite, fluorite and bornite are all often closely intergrown and all have similar cubic structures. This makes their identification by structural variation alone near impossible, so in addition to the structural data, energy-dispersive spectroscopy (EDS) data were simultaneously collected via a procedure similar to that outlined by Nowell and Wright (2004). Chemical Indexing (ChI-scan) could then be conducted, such that the measured EDS

element concentrations were used as inputs for Principal Component Analysis (PCA), and the components generated by this analysis assigned to individual mineral phases.

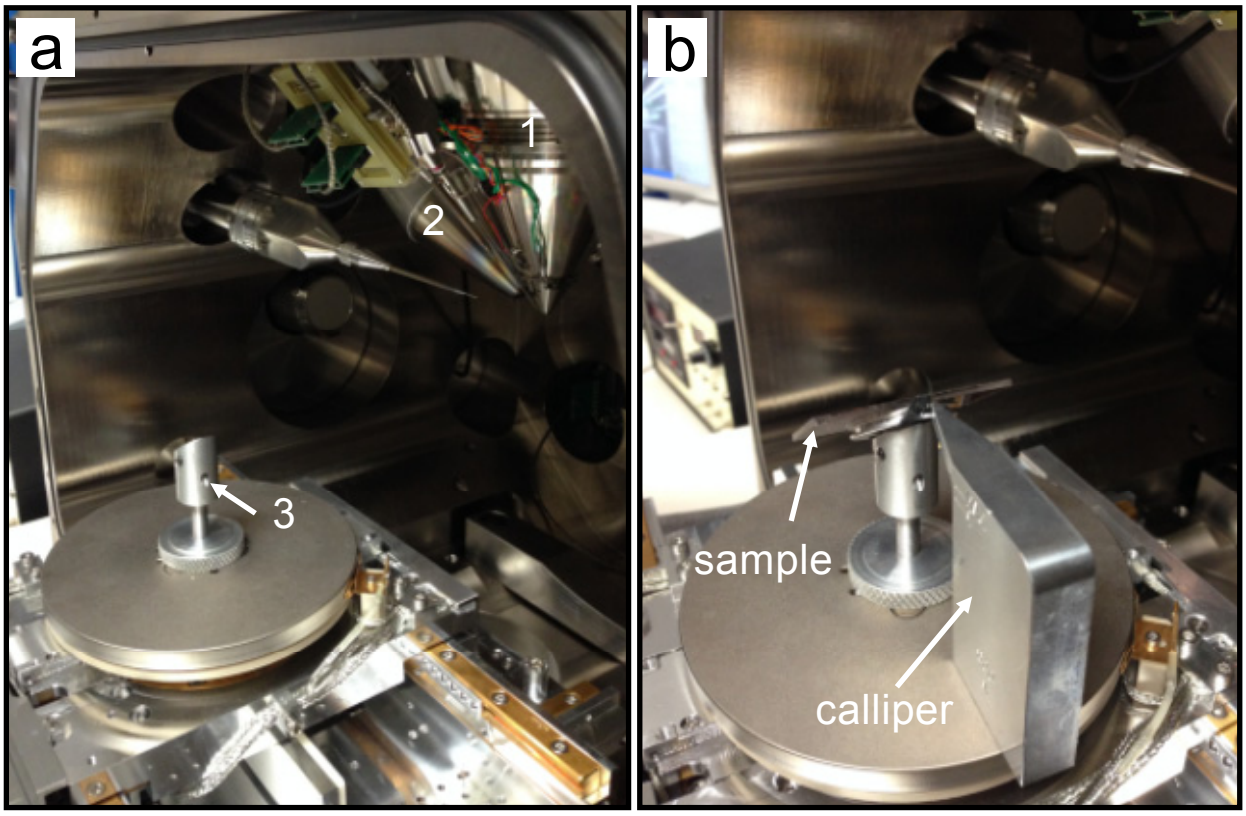

Figure 2.9: Photographs of inside the FIB-SEM platform at Adelaide Microscopy; **(a)** displays the field emission electron gun (1), gallium ion gun (2), and 45º tilted sample holder (3). The Hikari EBSD camera is not visible in this photograph; **(b)** displays a thin-section sample mounted onto the tilted sample holder. To ensure the mounted sample will not hit any of the detectors when inserted into the operating chamber, the sample height is measured using a calliper, prior to insertion into the chamber.

Table 2.7: Examples of EBSD data collection and processing settings used for selected uraninite-bornite crystals.

General Parameters	
Binned Pattern Size	96
Theta Step Size (degrees)	1
Rho Fraction	90%
Max Peak Count	7
Min Peak Count	3

Hough Parameters	
Hough Type	Classic
Resolution	Low
Convolution Mask	Medium (9x9)
Min Peak Magnitude	5
Min Peak Distance	25
Peak Symmetry	0.7

Data Processing Settings			
	RX7269_12	RX7270_19	RX7269_20
Grid Type	hexagonal	hexagonal	hexagonal
Working Distance (mm)	13	13	13
X Length (μm)	206.5	44.62	25.34
Y Length (μm)	194.6	40.63	34.31
Step Size (μm)	0.7	0.23	0.14
Total Points	95151	39873	51546
Number UO_2 Indexed Points	53875	8932	20770
Number Bornite Indexed Points	8074	19550	14775
Average UO_2 CI	0.91	0.73	0.39
Average bornite CI	0.22	0.37	0.14
UO_2 Average Fit (degrees)	1.68	1.3	2
Bornite Average Fit (degrees)	1.91	1.84	2.17

The collection of EBSD data involves matching the measured and theoretical EBSP bands (e.g., Figure 2.10) via automated indexing. There are typically several possible orientations which may satisfy any given pattern. To assess the reliability of the automated indexing process two methods are typically used: the Confidence Index (CI) or the 'fit' between the measured and theoretical bands. CI is a measurement of the probability of an orientation

solution based on using a voting scheme such that $CI = (V_1 - V_2)/V_{IDEAL}$, where V_1 and V_2 are the number of votes for the first and second solutions and V_{IDEAL} is the total possible number of votes from the detected EBSP bands (TexSEM, 2007). CI values range between 0 and 1, with lower values indicating a poor match. This can be misleading, as in many cases a low CI (~0.2) can be assigned to a pattern that is correctly indexed. Comparatively, the 'fit' parameter defines the average angular deviation between the theoretical EBSP bands and the measured EBSP bands based on the orientation obtained from the voting procedure.

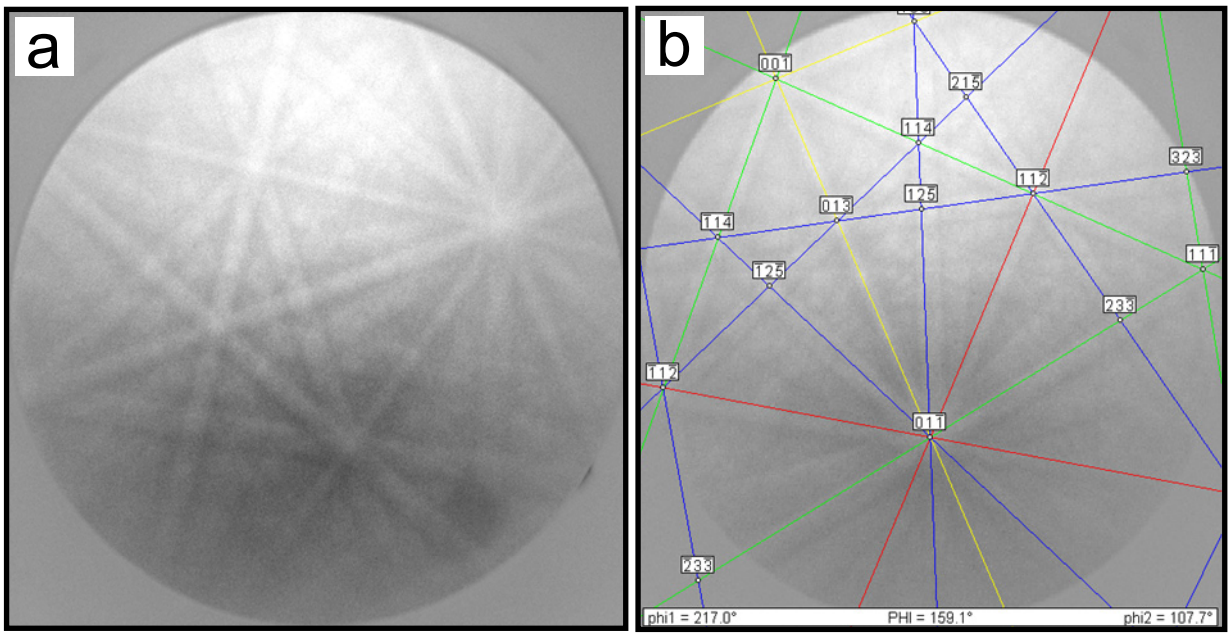

Figure 2.10: (a) an electron backscattered diffraction pattern for a selected point within a uraninite (UO_2) grain; **(b)** example of the indexing of the Kikuchi pattern using the UO_2 crystal structure as defined within the TSL database.

For the uraninite analysed as part of this study, the average CI ranged between 0.39 and 0.91 and the average band 'fit' for UO_2 ranged between 1.3º and 2º (refer Table 2.7). The 'fit' value (often reported as the Mean Angular Deviation) is generally used rather than CI when comparing the quality of EBSD data. Uraninite has not traditionally been analysed using EBSD, so comparison of this 'fit' value to other published uraninite works was not possible.

However, for comparison, some of the published zircon EBSD work have a 'fit' value of <1.7º for the data to be considered of adequate quality (e.g., Timms et al., 2006; Reddy et al., 2007; Nemchin et al., 2009; Moser et al., 2011). Thus the values obtained for analyses in the current study were considered to be satisfactory. All data collection and processing parameters were optimized for uraninite rather than bornite, thus bornite always has lower CI and 'fit' values than that of uraninite. Other possible reasons for the poorer quality of bornite indexing compared to UO_2 may be due to (Nowell and Wright, 2004): (1) differences in relief caused by different polishing rates for UO_2 and bornite, and (2) uraninite has a higher average atomic number than that bornite and therefore is likely to produce a stronger EBSP.

EBSD data often requires clean-up when there are isolated points that are not indexed or have been indexed incorrectly due to the presence of dust particles on the sample surface, surface roughness, or from overlapping patterns at boundaries. For these reasons, the OIM Analysis program offers several clean-up routines to try and minimize incorrect indexing. The 'Grain CI Standardization' and 'Grain Dilation' data clean-up methods were used for data collected as part of the current study. Both of these methods were set to have a grain tolerance angle of 5º and minimum grain size of 2 μm. Grain CI Standardization recovers a portion of the data with a low CI value but the correct orientation, and therefore maximizes the fraction of correctly indexed points. Grain Dilation modifies the orientations of points which do not belong to any grains but have neighbouring points which do belong to grains, and is particularly important at grain boundaries where the diffracting volume may be a combination of different crystal lattices. Thus, both of these methods maximize the number of points which are correctly indexed. Caution should be exercised with the use of any data clean-up procedure to avoid any unnecessary data smoothing, which may result in the loss of microstructural detail.

The data collected from the FIB-EBSD can be processed and displayed in numerous ways, including: EBSD pattern property maps, crystallographic orientation maps, inverse pole figure maps, pole figures, and misorientation maps. Details of some of these methods have been discussed within Chapters 4 and 5, and will therefore not be discussed here. Further details about the use of EBSD in the study of microstructures within rocks can be found in Prior et al. (1999).

2.8 Transmission electron microscopy (TEM)

Transmission electron microscopy (TEM) was used to attain electron diffraction patterns and high-resolution imaging of studied samples. The TEM used is a Philips 200CM instrument operated at 200 kV (Adelaide Microscopy), and is equipped with a double-tilt holder, a Gatan digital camera, and an energy dispersive X-ray (EDX) spectrometer. The EDX spectrometer allows for qualitative compositional data (scale of tens or hundreds of nanometres) to be attained. Measurements on the electron diffractions were performed using DigitalMicrograph™ 3.11.1. Indexing of minerals was checked by diffraction simulations using WinHREM™ 3.0 software and data from the American Mineralogist Crystal Structure Database (http://rruff.geo.arizona.edu/AMS/amcsd.php). Winwulff© 1.4.0 (JCrystalSoft) was also used to interpret electron diffraction patterns.

The FIB-SEM was used to prepare and lift-out carefully selected slices (termed TEM foils) of uraninite-bornite intergrowths (Figure 2.11). A special sample holder is used in the FIB-SEM so that the sample from which the TEM foil is extracted is within the FIB-SEM chamber at the same time as a TEM grid. This enables the foil to be cut and then placed directly onto the grid for subsequent analysis on the TEM. Ciobanu et al. (2011) comprehensively discuss the methodology in the integrated use of the FIB-SEM and TEM to make and analyze these foils. In brief:

1. The uraninite grain of interest is found and imaged with a working distance of approximately 4-5 mm.
2. Sample is tilted to 52° and a thin (1-2 μm) layer of platinum deposited on the area to be cut (Figure 2.11a).
3. Two parallel trenches on either side of the area of interest are then milled using the Ga ion beam at a high voltage (30 kV; Figure 2.11b).
4. The two surfaces which are generated on either side of the 'slice' are then cleaned using the ion beam with lower current and voltage, and cross-section imaging conducted.
5. The bottom and one side of the 'slice' is then also milled, leaving one side of the 'slice' still intact.
6. The specimen is de-tilted to 0° and a tungsten needle attached to the top of the 'slice' with a platinum weld.
7. The 'slice' is then cut free from the specimen, lifted and transported to the grid holder. It is then welded with platinum to the TEM grid with the tungsten needle still attached (Figure 2.11c). Once welding is complete, the needle is cut away leaving the 'slice' behind.
8. Further thinning of the 'slice' is then required so that it is thin enough (ideally <60-100 nm) for TEM analysis (Figure 2.11d). Thus, the 'slice' is re-tilted to 52° and sequentially thinned using decreasing currents and voltages. A smooth surface on each side of the 'slice' should thus be attained.
9. The TEM is subsequently used to attain diffraction data and conduct high-resolution imaging.

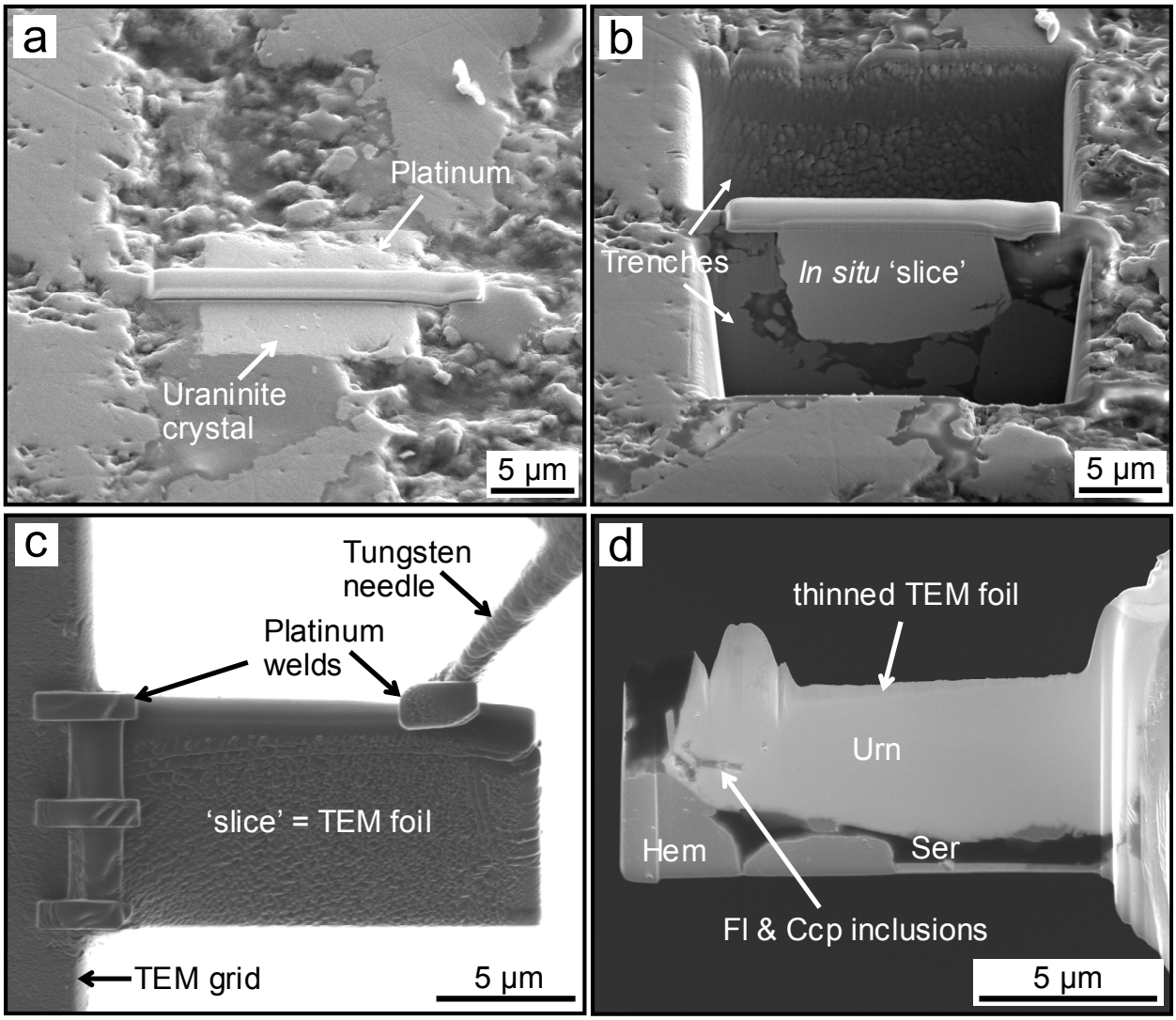

Figure 2.11: Secondary electron images of a primary uraninite crystal, displaying the: **(a)** uraninite crystal with deposited platinum layer; **(b)** resultant trenches created by milling using the Ga ion beam with *in-situ* 'slice' of sample; **(c)** sample 'slice' as displayed in (b) is lifted from the sample into a TEM grid with a tungsten needle. The 'slice' is welded to both the needle and TEM grid using platinum; **(d)** sample 'slice' is then further thinned using the Ga ion beam to form a TEM foil of adequate thinness. Abbreviations: Ccp = chalcopyrite, Fl= fluorite, Hem = hematite, Urn = uraninite, Ser = sericite.

CHAPTER 3

URANINITE FROM THE OLYMPIC DAM IOCG-U-AG DEPOSIT: LINKING TEXTURAL AND COMPOSITIONAL VARIATION TO TEMPORAL EVOLUTION

Edeltraud Macmillan[1,2], Nigel J. Cook[3], Kathy Ehrig[2], Cristiana L. Ciobanu[3], and Allan Pring[4]

[1]*School of Physical Sciences, The University of Adelaide, Adelaide, SA, 5000, Australia*

[2]*BHP Billiton Olympic Dam, Adelaide, SA, 5000, Australia*

[3]*School of Chemical Engineering, The University of Adelaide, Adelaide, SA, 5000, Australia*

[4]*School of Chemical and Physical Sciences, Flinders University, Bedford Park, SA, 5042, Australia*

Paper published in American Mineralogist

Statement of Authorship

Title of Paper	Uraninite from the Olympic Dam IOCG-U-Ag deposit: linking textural and compositional variation to temporal evolution.
Publication Status	☑ Published ☐ Accepted for Publication ☐ Submitted for Publication ☐ Unpublished and Unsubmitted w ork w ritten in manuscript style
Publication Details	Macmillan, E., Cook, N.J., Ehrig, K., Ciobanu, C.L. and Pring, A. (2016) Uraninite from the Olympic Dam IOCG-U-Ag deposit: linking textural and compositional variation to temporal evolution. American Mineralogist, 101, 1295-1320 <http://dx.doi.org/10.2138/am-2015-5411>.

Principal Author

Name of Principal Author (Candidate)	Edeltraud Macmillan
Contribution to the Paper	Devise plan for data collection and use of analytical methods, method/package development for various analytical methods, collected analytical data, processed and interpreted data, wrote manuscript, and acted as corresponding author.
Overall percentage (%)	85%
Certification:	This paper reports on original research I conducted during the period of my Higher Degree by Research candidature and is not subject to any obligations or contractual agreements with a third party that would constrain its inclusion in this thesis. I am the primary author of this paper.
Signature	Date 6/5/2016.

Co-Author Contributions

By signing the Statement of Authorship, each author certifies that:

i. the candidate's stated contribution to the publication is accurate (as detailed above);

ii. permission is granted for the candidate in include the publication in the thesis; and

iii. the sum of all co-author contributions is equal to 100% less the candidate's stated contribution.

Name of Co-Author	Nigel Cook
Contribution to the Paper	Supervised development of work, assisted in defining direction of research, helped with data interpretation and manuscript evaluation.
Signature	Date 1/6/2016

Name of Co-Author	Kathy Ehrig
Contribution to the Paper	Supervised development of work, assisted in defining direction of research, helped with sample selection, data interpretation and manuscript evaluation.
Signature	Date 6/5/2016

Name of Co-Author	Cristiana Ciobanu		
Contribution to the Paper	Helped with FIB and TEM data collection/analysis, data interpretation and manuscript evaluation.		
Signature		Date	2/06/2016

Name of Co-Author	Allan Pring		
Contribution to the Paper	Supervised development of work, assisted in defining direction of research, helped with data interpretation and manuscript evaluation.		
Signature		Date	16/5/16

Macmillan, E., Cook, N.J., Ehrig, K., Ciobanu, C.L. & Pring, A. (2016). Uraninite from the Olympic Dam IOCG-U-Ag deposit: linking textural and compositional variation to temporal evolution.
American Mineralogist, 101(6), 1295-1320.

CHAPTER 4

CHEMICAL ZONING AND LATTICE DISTORTION IN URANINITE FROM OLYMPIC DAM, SOUTH AUSTRALIA

Edeltraud Macmillan[1,2], Cristiana L. Ciobanu[3], Kathy Ehrig[2], Nigel J. Cook[3], and Allan Pring[4]

[1]*School of Physical Sciences, The University of Adelaide, Adelaide, SA, 5000, Australia*

[2]*BHP Billiton Olympic Dam, Adelaide, SA, 5000, Australia*

[3]*School of Chemical Engineering, The University of Adelaide, Adelaide, SA, 5000, Australia*

[4]*School of Chemical and Physical Sciences, Flinders University, Bedford Park, SA, 5042, Australia*

Paper accepted for publication in American Mineralogist (October 2016 edition)

Statement of Authorship

Title of Paper	Chemical zoning and lattice distortion in uraninite from Olympic Dam, South Australia.
Publication Status	☐ Published ☑ Accepted for Publication ☐ Submitted for Publication ☐ Unpublished and Unsubmitted w ork w ritten in manuscript style
Publication Details	Macmillan, E., Ciobanu, C.L., Ehrig, K., Cook, N.J., and Pring, A. (2016) Chemical zoning and lattice distortion in uraninite from Olympic Dam, South Australia. American Mineralogist <http://dx.doi.org/10.2138/am-2016-5753>.

Principal Author

Name of Principal Author (Candidate)	Edeltraud Macmillan
Contribution to the Paper	Devise plan for data collection, method/package development for EPMA and FIB-EBSD, collected analytical data, processed and interpreted data, wrote manuscript, and acted as corresponding author.
Overall percentage (%)	85%
Certification:	This paper reports on original research I conducted during the period of my Higher Degree by Research candidature and is not subject to any obligations or contractual agreements with a third party that would constrain its inclusion in this thesis. I am the primary author of this paper.
Signature	Date 6/5/2016

Co-Author Contributions

By signing the Statement of Authorship, each author certifies that:

i. the candidate's stated contribution to the publication is accurate (as detailed above);

ii. permission is granted for the candidate in include the publication in the thesis; and

iii. the sum of all co-author contributions is equal to 100% less the candidate's stated contribution.

Name of Co-Author	Cristiana Ciobanu
Contribution to the Paper	Provided assistance and training in use of FIB, assisted in identifying potential avenues for further work, helped with data interpretation and manuscript evaluation.
Signature	Date 2.06.2016

Name of Co-Author	Kathy Ehrig
Contribution to the Paper	Supervised development of work and helped with manuscript evaluation.
Signature	Date 6/5/2016

Name of Co-Author	Nigel Cook
Contribution to the Paper	Supervised development of work, helped with data interpretation and manuscript evaluation.
Signature	Date 1/6/2016

Name of Co-Author	Allan Pring
Contribution to the Paper	Supervised development of work, helped with data interpretation and manuscript evaluation.
Signature	Date 10/5/16

CHAPTER 4: CHEMICAL ZONING AND LATTICE DISTORTION IN URANINITE FROM OLYMPIC DAM, SOUTH AUSTRALIA

Abstract

Compositionally-zoned uraninite from the Olympic Dam iron oxide-copper-gold deposit is rarely preserved, but represents an early product of *in-situ* transformation of primary uraninite. Electron back-scatter diffraction data (Inverse Pole Figure, Image Quality and Grain Reference Orientation Deviation mapping) reveal formation of zoned uraninite to be the result of a sequence of superimposed effects rather than from primary growth mechanisms alone. This is the first known microstructural analysis of uraninite showing crystal-plastic deformation of uraninite via formation and migration of defects and dislocations into tilt boundaries. Defining grain-scale characteristics and microstructural features in radiogenically modified minerals like uraninite carries implications in better understanding the processes involved in their formation, highlights limitations in the use of uraninite for U-Pb chemical ages, as well as for constraining the incorporation and release of daughter radioisotopes, especially where zoning, porosity, fractures and microstructures are present.

Keywords: Uraninite, EBSD, chemical zoning, tilt boundaries, microstructures, Olympic Dam

4.1 Introduction

Compositional zoning is a common phenomenon in minerals (e.g., Shore and Fowler, 1996, and references therein). Such zoning has, however, only rarely been reported for uraninite (e.g., Alexandre et al., 2015; Macmillan et al., 2016) despite the frequently observed high concentrations of impurity elements including: Ca, Pb, REE+Y (hereafter ΣREY), Th, Fe, Si, P, Al, Mg, Mn, K, and many others (e.g., Finch and Murakami, 1999). The ~1590 Ma Olympic Dam (OD) iron-oxide copper gold deposit is unusually rich in uranium where uraninite (ideally UO_2) is one of three main U-minerals (the others are coffinite and

brannerite; Ehrig et al., 2012, and references therein). Two generations of uraninite, comprising four main textural classes are identified at OD (Macmillan et al., 2016): 1) 'primary', 2) 'zoned', 3) 'cob-web' and 4) 'massive'. Of relevance here are the 'early' generation (Classes 1-3), all characterized by Pb- and ΣREY-rich (up to 0.42 apfu collectively) single grains (tens to hundreds of μm in size). Differentiation between classes of 'early' uraninite is based on textural and chemical zonation patterns (Macmillan et al., 2016). The authors show that 'primary' uraninite represents the least-altered, most pristine, crystalline uraninite, whereas 'zoned' and 'cob-web' types have undergone chemical-textural modifications by *in-situ* alteration processes (i.e., single grains of 'primary' uraninite are progressively altered via solid-state diffusion followed by interaction with hydrothermal fluids to form 'zoned' through to 'cob-web' uraninite). The 'cob-web' class consists of rhythmic intergrowths of uraninite and sulfides from core to margin within any given grain. In contrast, changes in chemical zonation patterns relative to grain morphologies used to define 'zoned' uraninite as distinct from the 'primary' uraninite is less well constrained, and is the subject of the present study. The main question addressed here, is whether there is a link between the chemical zoning and microstructures within grains that show such modifications, and if so, could this provide clues in understanding the crystallization and alteration history of uraninite.

4.2 Background and rationale

Morphological changes between internal zoning and the margin outline as seen in grains from the 'zoned' class of uraninite (Macmillan et al., 2016) can result either from primary crystallization processes, during which rates and growth orientation change (e.g., in garnet; Allen and Buseck 1988), or from dynamic recrystallization in a broad range of geological environments (e.g., Urai et al., 1986; Steffen and Selverstone, 2006). The combined use of

electron back-scatter diffraction (EBSD) and orientation contrast (OC) imaging to study microstructures within minerals can be applied to any mineral at a range of scales (Prior et al., 1999). From EBSD and OC data it is possible to quantify microstructures empirically and constrain dislocation slip systems, and this coupled with other micro- and nanoscale observations can lead to a more rigorous understanding of the formation of the observed mineral textures. The presence of microstructures, boundaries and interfaces (i.e., slip systems, sub-grain boundaries) have been shown to be important in controlling alteration processes, and the formation of micro- and meso-textures (Prior et al., 1999 and 2002).

The use of microstructural data from EBSD and OC imaging has been the subject of numerous studies to quantify the formation of various mineral textures. In zircon, microstructural features may form as a result of a combination of primary growth characteristics, degree of radiation damage, and recovery from crystal-plastic deformation, e.g., formation of dislocations, low-angle grain boundaries, and movement of slip systems (e.g., Reddy et al., 2006). In other minerals (e.g., garnet, spinel) there are strong crystallographic preferred orientations and these microstructural features are shown to be linked to slip systems, dislocation creep and recovery (Boyle et al., 1998; Prior et al., 2002).

Defining grain-scale characteristics in radiogenically modified minerals like zircon or uraninite is important for constraining their geologic evolution or U-Pb ages, particularly when zoning, porosity, fractures and microstructures are present. Incorporation and release of daughter products of ^{235}U and ^{238}U decay such as ^{207}Pb and ^{206}Pb, respectively, depend upon the robustness of the crystal lattice to radiation damage (i.e., amorphization and healing rates), as well as external factors such as exposure to hydrothermal fluids. In contrast to zircon, healing rates are considered much faster for uraninite and the mineral does not suffer from amorphization due to radiation damage (e.g., Janeczek and Ewing, 1991).

There are three slip systems identified for UO_2: $\{001\}\langle 1\bar{1}0\rangle$, at room temperature and atmospheric pressure, and $\{110\}\langle 1\bar{1}0\rangle$ or $\{111\}\langle 1\bar{1}0\rangle$, at higher temperatures (Kelly et al., 2012). Any of these could be activated to generate microstructures during various processes, including concentration and/or release of minor/trace elements in uraninite. Here we employ EBSD analysis to study uraninite that has the necessary prerequisites to show relationships between minor element redistribution (modification of chemical zoning, fracture infill and mineral inclusions; Macmillan et al., 2016) and microstructures resulting from lattice distortion.

4.3 Analytical methodology

Quantitative analysis of uraninite was performed using a Cameca SX-Five Electron Probe Micro-Analyzer (EPMA; Adelaide Microscopy, University of Adelaide) equipped with 5 tunable wavelength-dispersive spectrometers (WDS). Twenty-eight elements were measured; methodologies for data collection/analysis are given in Macmillan et al. (2016) and Appendix 1. The EPMA was also used to generate WDS elemental maps including those for Pb (Mα) and Ce (Lα) in Figure 4.1a and b, respectively.

Electron back-scatter diffraction (EBSD) data were collected using the EDAX-TSL™ EBSD system on a FEI Helios NanoLab DualBeam™ FIB/SEM platform (Adelaide Microscopy). Analytical details are given in Appendix 1. Three data processing methods are applied: Inverse Pole Figure (IPF), Grain Reference Orientation Deviation (GROD) and Image Quality (IQ) mapping.

4.4 Results

The uraninite studied is zoned with respect to minor elements, with Pb and ΣREY (Ce is a proxy for LREE) having the highest concentrations, and these co-correlate with one another

(Figure 4.1a and b). The presence of discrete REY-minerals as minute inclusions can also be inferred from the Ce map (Figure 4.1b). This grain was chosen because the chemical patterns show two, (Pb+ΣREY)-poor, porous and fractured domains with equant-rhombic shape, aligned along the long axis of the planar section. One side of the section also displays edges parallel to the rhomb faces. Bornite and fluorite are also present as infill of fractures (Figure 4.1a). Such a zonation pattern relative to the morphology of the grain, could indicate a type of sector zoning during primary growth, or alternatively, relate to secondary processes involving minor element redistribution within the grain. Based on the color coding of the IPF map (Figure 4.1c and d), the grain orientation lies between the ⟨111⟩, ⟨001⟩ and ⟨101⟩ zone axes, and has been estimated as $\langle 11\bar{2} \rangle$ (based on simulation of pole figures in Figure A1, Appendix B.2). Face indexing of the grain is shown accordingly on Figure 4.1c.

The subtle gradational color variations on the IPF map (Figure 4.1c and d) indicate gradual changes in crystallographic orientation but no apparent relationships with the chemical zoning. The boundaries formed by a lattice rotation about the plane normal to several directions have been superimposed on the IPF and IQ maps, as have low-angle grain boundaries on the GROD map (Figures 4.1 to 4.3). This was appropriate to test if there was any relationship between these boundaries and the known slip systems for UO_2. Slip systems such as $\{111\}\langle 1\bar{1}0 \rangle$, with rotation about the $\langle 11\bar{2} \rangle$ direction, and which correspond to the present grain orientation, show only a few tilt boundary traces on the IPF map (Figure 4.1c), indicating little correlation between microstructures and chemical heterogeneity in the grain. In contrast, superimposed tilt boundaries formed by lattice rotation about $\langle 1\bar{1}0 \rangle$, normal to $\{001\}\langle 1\bar{1}0 \rangle$, but different to the present grain orientation, correlate with bornite ± fluorite infilled cracks, arrays of inclusions, and some of the chemical zonation boundaries on the IPF map (Figure 4.1d).

Intragranular orientation deviation as displayed by GROD mapping (Figure 4.2a) occurs as a response to deformation, or where there is stored strain (relative to a reference orientation) within a grain. There are variations in intragrain crystallographic orientations of up to 18°, although the majority of the grain has an orientation of between 3.5° and 7° (green) compared to the reference (blue, marked by a white cross). Moreover, the misorientation profile (Figure 4.2b) displays the range of orientations along the A-B profile delineated on the GROD map. Low-angle grain boundaries (<10°) are superimposed on the GROD map, and correlate with the tilt boundaries plotted on the IPF and IQ maps (Figures 4.1d and 4.3a). Areas that appear to have higher relative stored strain (yellow-red) are found in regions that have a higher concentration of, or are surrounded by, many low-angle grain boundaries (Figure 4.2a). When comparison is made between the tilt boundaries circled (black dotted lines on Figure 4.1d) and the compositional maps (Figure 4.1a and b), the shape of the concentration boundaries of (Pb+ΣREY) appear similar to that of some of the tilt boundaries.

The IQ map (Figure 4.3a) shows weak correlation with the chemical zonation pattern where zones of higher and lower IQ correlate with domains of elevated and lower (Pb+ΣREY), respectively. It is unclear whether observed variation in IQ is due to chemical variability alone, or to a combination of chemical variability and porosity/inclusion content, since the zones where IQ and chemical variability correlate also have higher porosity/inclusion content.

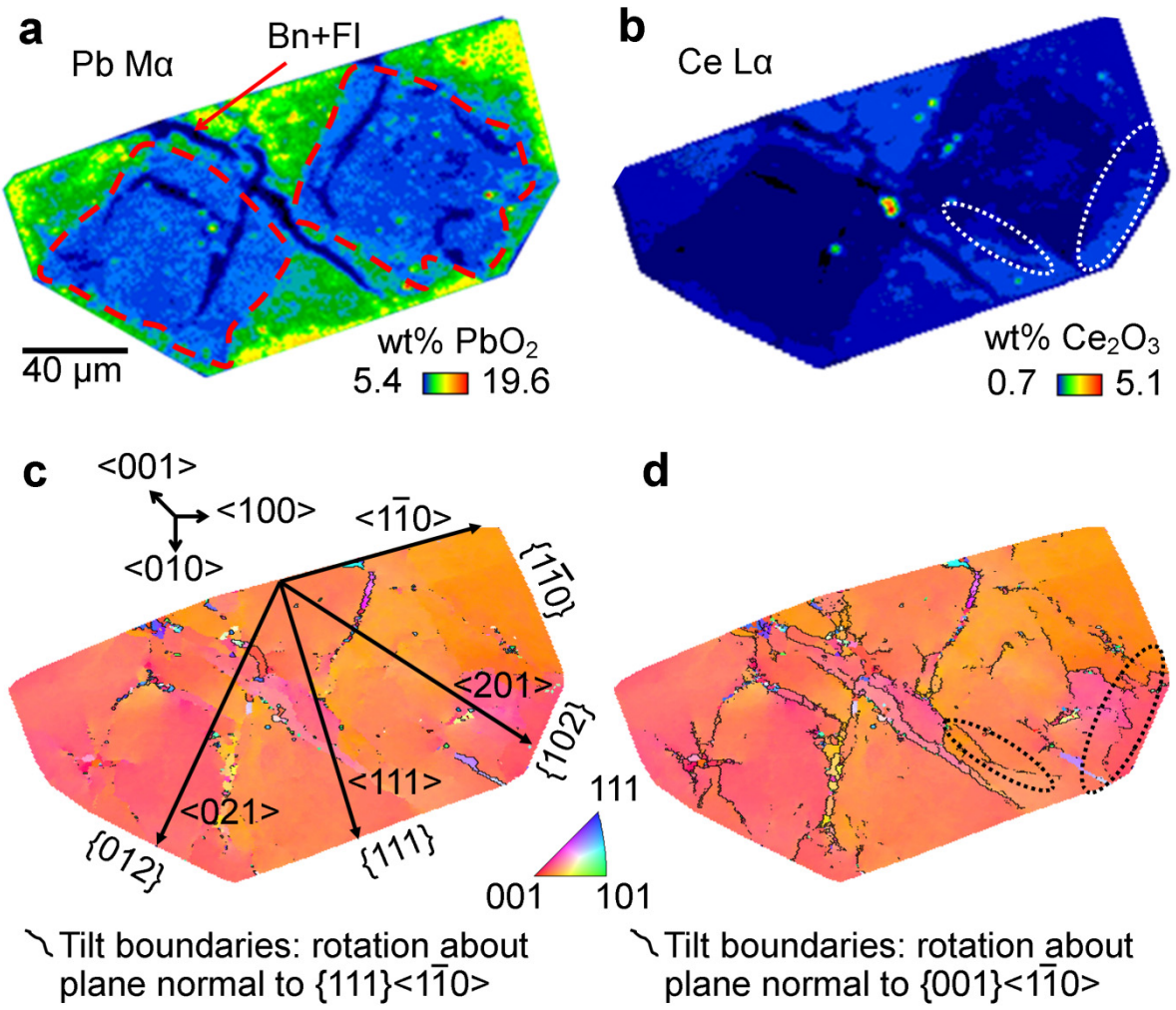

Figure 4.1: (a, b) EPMA-WDS maps showing Pb and Ce zonation in uraninite (Urn; adapted from Macmillan et al., 2016), with cracks infilled by bornite (Bn) and fluorite (Fl). Red-dotted lines demarcate (Pb+ΣREY)-poor sectors); **(c-d)** EBSD-derived ⟨001⟩ Inverse Pole Figure (IPF) map of UO_2 with superimposed tilt boundaries formed by a lattice rotation about the plane normal to {111}⟨1$\bar{1}$0⟩ in (c) and {001}⟨1$\bar{1}$0⟩ in (d). UO_2 is of one dominant orientation (close to ⟨11$\bar{2}$⟩ zone axis) and represents a single grain with some gradational color variation reflecting slight distortion of crystal lattice. White- and black-dotted circled areas highlight two examples of where the tilt boundaries correlate to Ce zonation boundaries (Figure 4.1b and d, respectively). Mean compositions (wt%) of low-Pb zones: 75.5 UO_2, 6.7 PbO_2, 3.4 CaO, 7.1 ΣREY_2O_3, 1.2 As_2O_3; high-Pb zones: 69.8 UO_2, 14.9 PbO_2, 1.6 CaO, 11.0 ΣREY_2O_3, 0.3 As_2O_3 (as reported in Macmillan et al., 2016).

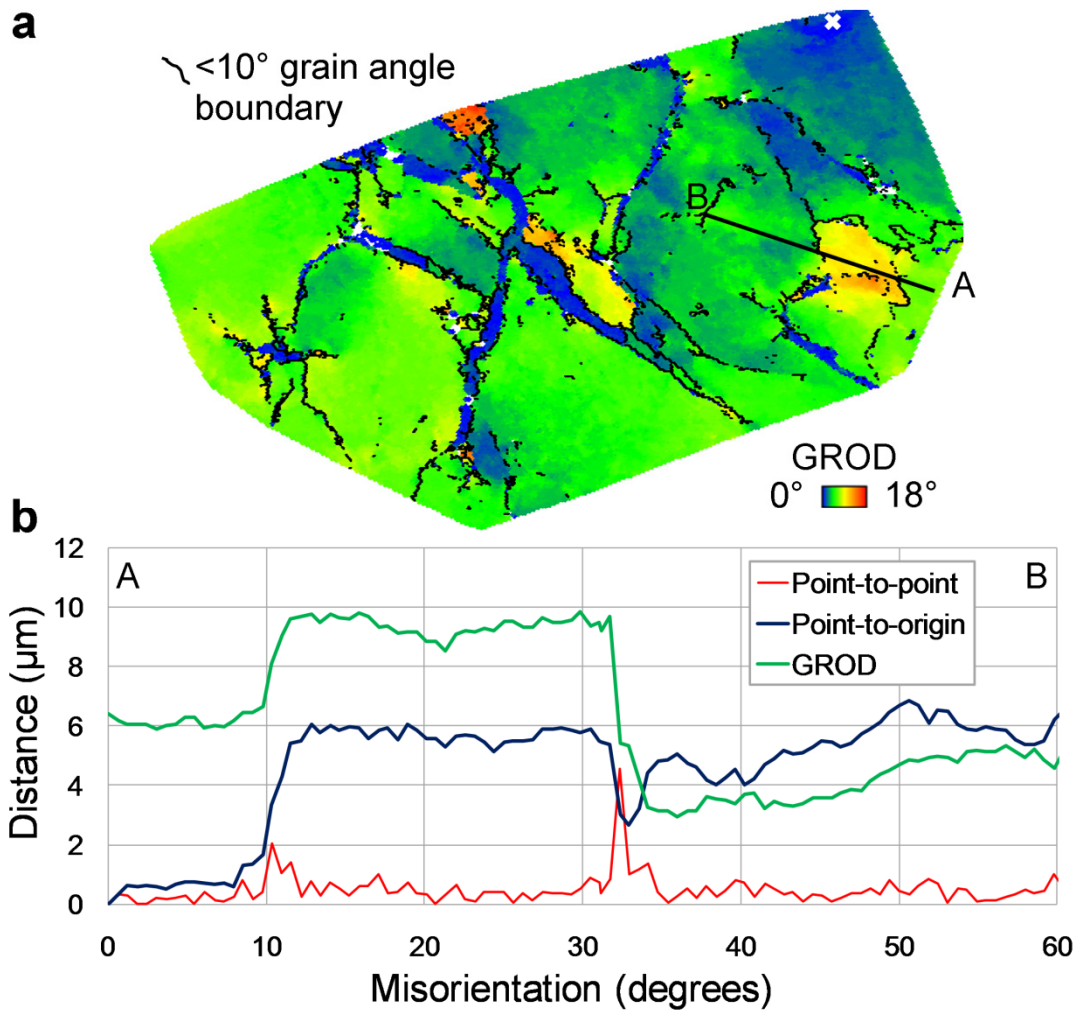

Figure 4.2: (a) EBSD-derived Grain Reference Orientation Deviation (GROD) map of UO_2 with superimposed <10° low-angle grain boundaries (solid black lines). Each pixel is colored from reference orientation (blue, defined by white cross) with misorientation of up to 18° (red). Misorientation profile (Figure 4.2b) plotted along section A-B; **(b)** EBSD-derived misorientation profile displaying the highest misorientation (~9°) correlates to zones of higher strain (yellow on Figure 4.2a).

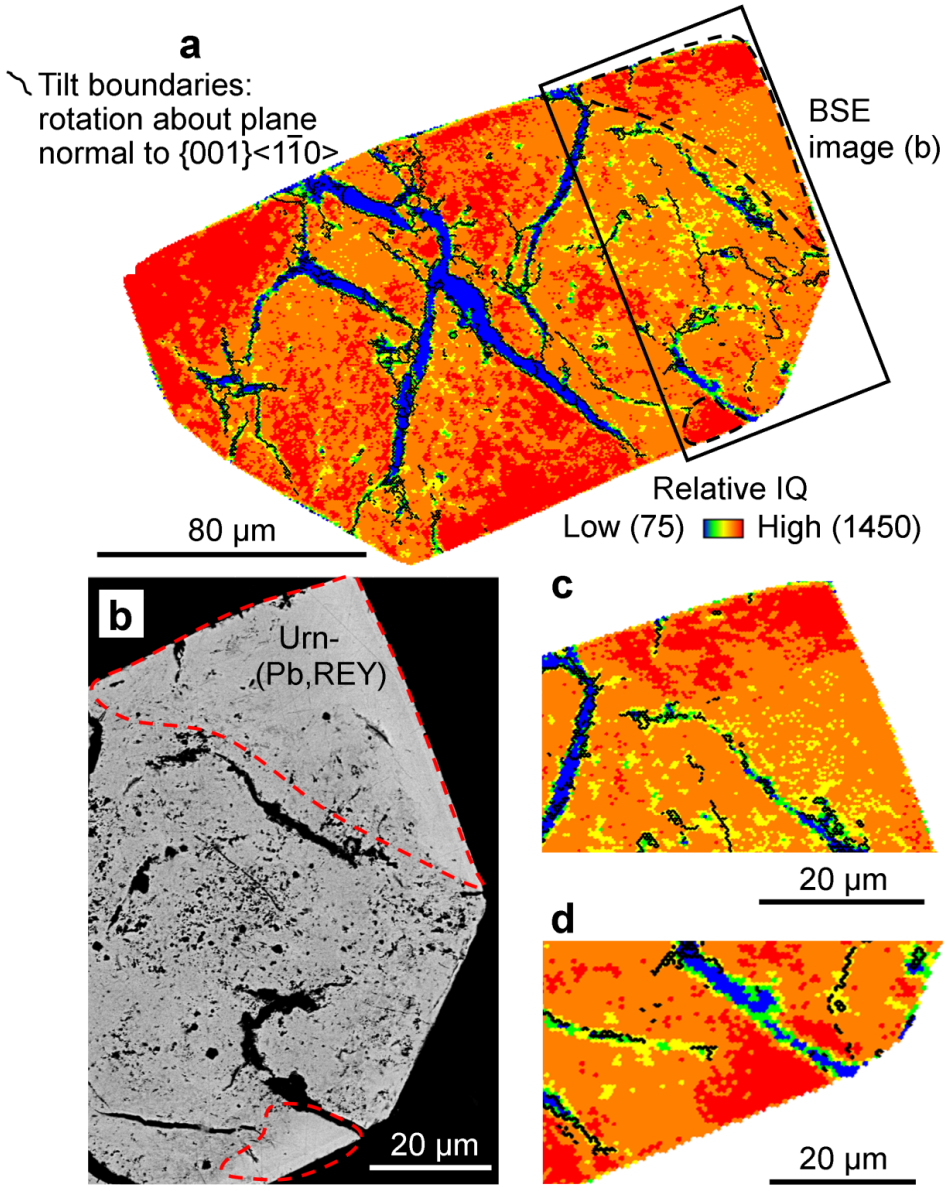

Figure 4.3: (a) EBSD-derived Image Quality (IQ) map of entire uraninite grain with superimposed tilt boundaries formed by a lattice rotation about the plane normal to $\{001\}\langle 1\bar{1}0\rangle$. Warmer colors (red-orange) represent areas of higher IQ (uraninite), and cooler colors (blue-green) represent areas of lower IQ (bornite and fluorite). Orange colored areas (uraninite) represent low-Pb uraninite with higher inclusion content whereas red colored areas represent high-Pb uraninite with lower inclusion content. Black dotted circled regions are further enlarged in (c) and (d), and area outlined with black rectangle is imaged in (b); **(b)** BSE image of uraninite grain with reduced brightness and contrast to highlight increased Pb/ΣREY and reduced porosity towards rim (red dashed lines); **(c-d)** EBSD-derived Image Quality (IQ) maps of UO_2 (colored as for (a)). The uraninite regions with lower porosity and elevated Pb±ΣREY have higher IQ (red) than zones with lower porosity (orange).

4.5 Discussion

4.5.1 Primary versus secondary minor/trace element patterns

The continual production of Pb as a result of radioactive decay, will cause some alteration to the chemistry and structure of uraninite and/or any other U-bearing minerals (Hazen et al., 2009, and references therein). An important, self-induced alteration phenomenon which affects all U-bearing minerals is the accumulation of long-term damage caused by α-decay events, or 'metamictization'. The most intense damage results in defect production and amorphization as, for example, has been shown for modelling of energetic uranium recoil damage within zircon (Devanathan et al., 2006). In contrast, uraninite is known to be quite resistant to α-recoil events because of relatively rapid annealing kinetics (Eyal and Fleischer, 1985; Janeczek and Ewing, 1991), and has the ability to self-heal radiation damage; the radioactive decay process can also induce redistribution of key elements such as Pb within a given grain (e.g., Hazen et al., 2009).

Incorporation of Pb and ΣREY within the crystal lattice was shown for 'primary', oscillatory-zoned uraninite which hosts the highest amounts of Pb (up to 0.2 apfu) and ΣREY (up to 0.2 apfu) and thus was defined as the earliest uraninite generation at OD (Macmillan et al., 2016). Although oxidation of U^{4+} to U^{6+} was calculated to compensate for substitutions and charge balance, no changes to crystal symmetry or lattice defects were found in such highly-substituted uraninite despite prediction of vacancies or other crystal structural modifications (Janeczek and Ewing, 1991). If all measured Pb is assumed as radiogenic, the oscillatory zoning with respect to Pb (and ΣREY) typical of primary uraninite at OD (Macmillan et al., 2016) is a self-induced diffusion patterning mechanism which traps daughter isotopes formed during α-recoil events. Weak oscillatory zoning with respect to (Pb+ΣREY) is also observed in the Th-U sector zoned uraninite from Mesoproterozoic pegmatite in Southern Norway,

where the sector zoning is attributed to primary growth (Alexandre et al., 2015).

Zones of comparable low-(Pb+ΣREY) concentrations with those discussed here for the square-shaped-sectors (< 0.1 apfu for Pb and ~ 0.1 apfu for ΣREY) in the 'zoned' type were also reported, but only as incipient sectorial zoning on $\langle h0l \rangle$ or equivalent directions in the 'primary' uraninite from OD (Macmillan et al., 2016). Also documented by these authors, were the presence of rare, fine particles of galena in parts of 'primary' uraninite grains affected by sub-μm fractures, infilled with bornite ± fluorite. Zonation patterns (of Pb) which are oscillatory, sectorial, or a combination thereof, can be the result of element redistribution during the same or sequential self-induced α-recoil 'dry' events, and/or as a result of the interaction with fluids of differing chemistry (Cu, S, F) to uraninite. Bornite ± fluorite inclusions and infill, are more abundant in the 'zoned' uraninite, and these can be used to elucidate fluid chemistry. Microstructural analysis is essential in being able to link the observed chemical patterns and heterogeneity with micro- and meso-scale lattice defects that could have assisted ingress of fluids during superimposed geological events.

4.5.2 Lattice distortion and chemical heterogeneity

The microstructural analysis of 'zoned' uraninite shows lattice rotation/dislocations tied to preferential slip systems, low-angle boundaries and areas of high-strain. All these microstructures correlate with directions/traces of chemical heterogeneity in the grain, i.e., (Pb+ΣREY)-zonation, pores, inclusions and (bornite ± fluorite)-infilled cracks. The correlation between lattice rotation about the $\langle 1\bar{1}0 \rangle$ direction on $\{001\}\langle 1\bar{1}0 \rangle$ slip system and the majority of tilt traces on the IPF map (Figure 4.1d) indicates that accumulation of dislocations and pile-up defects are attributable to the low-temperature slip system in UO_2 (Boyle et al., 1998; Kelly et al., 2012). Such a system is active during superimposed alteration since it is controlled by directions different to the grain orientation.

Lattice distortion, coincident with directions parallel to {201} and {021} faces of sector zoning (indicated by dashed lines on Figure 4.1d), and also with the orientation of infilled fractures, is highest in areas of high-stored strain accommodated by an increase in the abundance of low-angle boundaries (misorientation profile on the GROD map; Figure 4.2). Therefore, fracturing of uraninite could be considered the result of strain hardening by dislocation pile-up along chemical boundaries that impede dislocation glide and prohibit recovery. This is plausible since there is a considerable amount of strain energy stored in the region around a dislocation (Kelly et al., 2012).

Any distortions to the crystal lattice within the diffracting volume are recorded by IQ, and can be used as a qualitative indicator of sample microstructure (e.g., variable crystallographic orientations; grain boundaries; chemical variability; impurities; porosity; Reddy et al., 2007). Correlation between chemical heterogeneity and sample microstructure is observed from the diffuse patterns recorded from the (Pb+ΣREY)-low, high-U sectors on the IQ maps (orange regions in Figure 4.3). Such areas should display brighter patterns due to the higher atomic scattering effect produced by heavier elements (Wright and Nowell, 2006), but the presence of μm to sub- μm-scale inclusions/pores as dense fields instead induces diffuse diffraction patterns and thus lowers IQ.

All the above support the interpretation that the observed (Pb+ΣREY)-sector zoning is a result of the removal of these elements from pre-existing uraninite. Zones of structural weakness were formed as a result of the accumulation of defects and dislocations into tilt boundaries, which formed via lattice rotation about the plane normal to the active slip system in uraninite, permitting the ingress of a hydrothermal fluid into uraninite. Where dislocations and defects pile-up (i.e., along active slip systems), high-diffusivity pathways can be formed, aiding element mobility (Reddy et al., 2006). Replacement of uraninite by bornite ± fluorite occurred

along these planes, and these share common crystallographic orientations (both pink/orange in Figure 4.1c and d). The same fluids are likely responsible for the presence of other trace elements, such as Ca and As within the (Pb+ΣREY)-depleted sectors (Macmillan et al., 2016), as well as increased pore/inclusion content. The documentation of low-angle boundaries associated with high strain areas provides evidence for a dynamic rather than a static recovery process. Thus the ability for uraninite to progressively self-anneal radiation damage (in contrast to static temperature-driven annealing processes) may have modified the chemical zoning, but more importantly, the interaction between uraninite and ingressing fluids must have been pivotal in forming the modified zonation patterns observed in 'zoned' uraninites.

The results here are further evidence that the 'zoned' uraninite is a distinct, intermediate stage during *in-situ* transformation of uraninite from 'primary' to 'cob-web' stages (Macmillan et al., 2016). In the last stage (Figure A2, Appendix B.2) pseudomorphic sulfide replacement of uraninite is more intense and leads to extremely modified forms of 'zoned' type, with the microstructural features (i.e., GROD, IQ maps) for 'cob-web' uraninite being a variant of those displayed for 'zoned' uraninite (Figures 4.1 to 4.3).

4.6 Implications and outlook

Uraninite at OD has been exposed to a prolonged geologic history and has undergone multiple fluid-rock interaction events at variable flow rates, fluid-pressures, temperatures and rheologic contexts since early stage deposit formation at ~1590 Ma (Ciobanu et al., 2013). The interpretation of the evolution of uraninite is important in constraining mineralizing stages at OD and elsewhere. Future U-Pb uraninite geochronology requires a detailed knowledge of the inherent heterogeneity within these uraninites, since these dating methods assume chemical homogeneity at the scale of the microprobe beam. Thus, without combined microchemical and microstructural studies such as this, characterization of the heterogeneity

is not possible, and erroneous chemical ages may be attained. This type of work should be applied to other U-bearing minerals featuring comparable chemical-textural complexity such as hematite (Ciobanu et al., 2013), an intrinsic hydrothermal mineral in IOCG deposits.

4.7 Acknowledgements

This work forms part of the Ph.D. studies of EM and is supported by BHP Billiton. NJC, KE and AP acknowledge support from the ARC Research Hub for Australian Copper-Uranium. Staff at Adelaide Microscopy are thanked for instrument training. We appreciate insightful comments and suggestions from reviewers Mark Pearce, Alan Boyle and Paul Alexandre, and Editor Ian Swainson, which assisted us with revision of the manuscript.

CHAPTER 5

REPLACEMENT OF URANINITE BY BORNITE VIA COUPLED DISSOLUTION-REPRECIPITATION: EVIDENCE FROM TEXTURE AND MICROSTRUCTURE

Edeltraud Macmillan[1,2], Cristiana L. Ciobanu[3], Kathy Ehrig[2], Nigel J. Cook[3], and Allan Pring[4]

[1]*School of Physical Sciences, The University of Adelaide, Adelaide, SA, 5000, Australia*

[2]*BHP Billiton Olympic Dam, Adelaide, SA, 5000, Australia*

[3]*School of Chemical Engineering, The University of Adelaide, Adelaide, SA, 5000, Australia*

[4]*School of Chemical and Physical Sciences, Flinders University, Bedford Park, SA, 5042, Australia*

Paper submitted to The Canadian Mineralogist (in review)

Statement of Authorship

Title of Paper	Replacement of uraninite by bornite via coupled dissolution-reprecipitation: evidence from texture and microstructure.
Publication Status	☐ Published ☐ Accepted for Publication ☑ Submitted for Publication ☐ Unpublished and Unsubmitted w ork w ritten in manuscript style
Publication Details	Macmillan, E., Ciobanu, C.L., Ehrig, K., Cook, N.J., and Pring, A. (2016) Replacement of uraninite by bornite via coupled dissolution-reprecipitation: evidence from texture and microstructure. Submitted to The Canadian Mineralogist (in review at the time of thesis submission).

Principal Author

Name of Principal Author (Candidate)	Edeltraud Macmillan
Contribution to the Paper	Devise plan for data collection, method/package development for EPMA and FIB-EBSD, collected analytical data, processed and interpreted data, wrote manuscript, and acted as corresponding author.
Overall percentage (%)	90%
Certification:	This paper reports on original research I conducted during the period of my Higher Degree by Research candidature and is not subject to any obligations or contractual agreements with a third party that would constrain its inclusion in this thesis. I am the primary author of this paper.
Signature	Date 6/5/2016

Co-Author Contributions

By signing the Statement of Authorship, each author certifies that:

i. the candidate's stated contribution to the publication is accurate (as detailed above);

ii. permission is granted for the candidate in include the publication in the thesis; and

iii. the sum of all co-author contributions is equal to 100% less the candidate's stated contribution.

Name of Co-Author	Cristiana Ciobanu
Contribution to the Paper	Provided assistance and training in use of FIB, assisted in identifying direction for research and further work, helped with data interpretation.
Signature	Date 2.06.2016

Name of Co-Author	Kathy Ehrig
Contribution to the Paper	Supervised development of work and helped with manuscript evaluation.
Signature	Date 6/5/2016

Name of Co-Author	Nigel Cook
Contribution to the Paper	Supervised development of work, helped with data interpretation and manuscript evaluation.
Signature	Date 1/6/2016

Name of Co-Author	Allan Pring
Contribution to the Paper	Supervised development of work, assisted in identifying direction for research and further work, helped with data interpretation, and manuscript evaluation.
Signature	Date 10/5/16

CHAPTER 5: REPLACEMENT OF URANINITE BY BORNITE VIA COUPLED DISSOLUTION-REPRECIPITATION: EVIDENCE FROM TEXTURE AND MICROSTRUCTURE

Abstract

The occurrence and nature of rhythmically intergrown crystals of uraninite and bornite from the Olympic Dam iron oxide-copper-gold (IOCG)-U-Ag deposit of South Australia is reported. Distinct zones within primary, euhedral uraninite crystals have been replaced by bornite and minor fluorite leaving a skeleton of uraninite, in-filled with these minerals. The partially replaced uraninite crystals are always closely associated with locally abundant bornite and fluorite. The textural features of the intergrowth are consistent with partial replacement of uraninite by bornite via a coupled dissolution-reprecipitation reaction driven by a F-rich and Cu-Fe sulfide-bearing hydrothermal fluid rather than a form of oscillatory growth or exsolution from a U-Cu-Fe-S solid solution. The crystallographic relationship between the parent uraninite and the daughter bornite and fluorite were explored by Electron Back-Scatter Diffraction as all three minerals share common crystal structural features, despite their chemical diversity. Generally speaking, the crystallographic orientation of the uraninite parent is initially inherited by the replacing bornite, but later the orientation of bornite changes.

Keywords: uraninite, Cu-Fe-sulfides, Olympic Dam, epitaxial replacement, coupled dissolution-reprecipitation reaction

5.1 Introduction

The complex and often episodic processes leading to the formation of ore deposits can be unraveled by studying and understanding mineral textures and chemistries. Rhythmic intergrowths and banding between different minerals can form as a result of primary, co-

crystallization associated with either pooling of fluids in a small, closed-system within a larger fluid-rock interaction system, or by open interaction between the crystallizing mineral surface, and fluids which change their chemistry in a repetitive manner during the crystallization or deposition process (Ortoleva et al., 1987). For either of these cases disequilibrium conditions as well as the coupling of at least two of the active processes in the system need to occur to result in formation of the intergrowths and geochemical self-organization from an unpatterned to a patterned state or mineral texture (Nicolis and Prigogine, 1977).

Similar intergrown and banded mineral textures can also form via replacement. Mineral replacement reactions are common in many geological settings and particularly within hydrothermal ore deposits (e.g., Ramdohr, 1969; Augustithis, 1995). Mechanisms involved in these replacement reactions and their relationship to observed texture have been the subject of extensive empirical and experimental study (e.g., Putnis, 2009; Altree-Williams et al., 2015). Coupled dissolution-reprecipitation (CDR) reactions have been recognized in playing a vital role in replacement, and are at least as important as, solid state processes or hydrothermal leaching. All experimental studies to-date, have focused on mineral systems in which at least some of the chemical components are common to both the parent and the product mineral.

Macmillan et al. (2016) report chemical and textural relationships among distinct types of uraninite from the Olympic Dam (OD) deposit, South Australia. They identified two main generations – ‘early’ and ‘late’; the ‘early’ uraninite was sub-divided into 3 main classes (primary, zoned and cob-web) based on chemical and textural differences. Mechanisms involved in formation of ‘early’ uraninite were interpreted to follow an evolutionary trend where the same grain experiences cycles of *in-situ* growth, dissolution and recrystallization.

Observed replacement relationships are consistent, at least in-part to have formed by CDR reaction.

In this paper, we document the cob-web uraninite texture, and aim to understand the processes involved in formation of this texture, particularly with respect to the rhythmic intergrowth of uraninite and bornite. In all cases examined, small amounts of fluorite co-exist with uraninite and bornite.

Despite their chemical dissimilarity, all three minerals have fluorite-type structure, space group *Fm3m*, or closely related structures (Frondel, 1958; Vaughan and Craig, 1978; Anthony et al., 1990). The unit cell parameter *a* for uraninite (UO_2) is 5.4682 Å with a molar volume of 24.6 cm^3/mol, whereas bornite has a *Fm*3*m* subcell of 5.50 Å with a molar volume of 24.9 cm^3/mol and adopts an anti-fluorite-like structure (the cation + vacancy and anion positions are interchanged compared to the fluorite archetype). Fluorite has an *a* repeat of 5.4626 Å with a molar volume of 24.6 cm^3/mol. Uraninite, bornite and fluorite all exhibit penetration twinning on {111}, although it is less common with uraninite than in the other two minerals (Anthony et al., 1990). In reflected light, bornite often exhibits twin lamella which are inconsistent with the cubic symmetry of the subcell, indicating the development of twin domains associated with cation and vacancy ordering (Ramdohr, 1969). The known slip direction for UO_2 is $\langle 1\bar{1}0 \rangle$ (Kelly et al., 2012) and this direction is also common to bornite and fluorite.

In this study, textures were characterized using a scanning electron microscope (SEM) in back-scattered electron (BSE) imaging mode, the chemistry of the intergrowth was established by electron probe microanalysis (EPMA), and crystallographic orientations were identified using electron back-scatter diffraction (EBSD). Nanoscale characterization of the intergrowths by electron diffraction (ED) and transmission electron microscopy – energy-

dispersive spectroscopy (TEM-EDS) was carried out on a thinned foil prepared *in-situ* on a focused ion beam (FIB)-SEM platform.

5.2 Materials and methods

5.2.1 Sample characteristics

Samples studied are from the OD iron oxide-copper-gold (IOCG)-U-Ag deposit, the World's largest known economic uranium (U) resource. U-bearing minerals found within the deposit include uraninite, coffinite and brannerite (Ehrig et al., 2012). The first class of 'early' uraninites described by Macmillan et al. (2016) are the primary (Class 1) uraninites, and these are typically euhedral, display minimal alteration, and often exhibit zonation with respect to Pb, Σ(REE+Y, hereafter REY) and Th. Zoned (Class 2) uraninites are usually euhedral or subhedral in shape, display chemical zonation patterns, including elevated concentrations of Pb and ΣREY towards grain margins, often with reduced pore abundance/inclusion content within Pb-rich zones. Cob-web (Class 3) uraninites feature rhythmic intergrowths of uraninite with Cu-Fe-sulfides from core to margin (Figure 5.1), and display the greatest complexity in terms of habit, size and degree of grain rounding; intergrown or inclusions of fluorite are also common. The 'late' uraninites have been termed massive (Class 4) uraninites, and are characteristic of higher-grade ores and consist of fine-grained anastomosing-crustiform varieties as well as colloform and aphanitic varieties.

Primary, zoned and cob-web uraninites represent the same 'early' uraninite generation and are linked by similar elemental signatures (e.g., high Pb, Ce, Y and Nb). These are single uraninite crystals which have progressively been chemically and texturally altered, from the primary type through zoned and finally to cob-web types. Chemical zonation of Pb and ΣREY (higher concentrations at rims) for all 'early' uraninites can be attributed to solid-state diffusion, driven by radiation induced self-annealing and thermal events. In addition, some of

the 'early' uraninites (typically cob-web) also display variations in Ca ± Si contents and incipient formation of coffinite. The zoned and cob-web habits consist of uraninite which contains Cu-Fe-sulfide ± fluorite infilled cracks and inclusions, with cob-web types having rhythmic intergrowths and the highest abundance of these minerals. In some cases, the bornite lamellae are discontinuous and appear parallel to sub-parallel and form a cubic-type arrangement (Figure 5.1c), whereas in other examples there are concentric ringed intergrowths of uraninite and bornite, with fluorite inclusions and blebs (Figure 5.1d). Overall, cob-web uraninites display a higher degree of rounding, and 'swelling' of the margins, possibly due to multiple stages of uranium dissolution and reprecipitation and are thus the most texturally altered group of the 'early' uraninites. Constraining the formation of the cob-web (Class 3) uraninites is the focus of the current study.

EBSD analysis has been conducted on 8 selected crystals from two samples (S17 and S18) originally characterized by Macmillan et al. (2016). Two cob-web crystals were selected for detailed description here and illustrate the essential chemical and textural features (Figure 5.2a, c). The ED and TEM-EDS analysis was carried out on a foil from a different cob-web crystal in a separate sample (S15) as documented by Macmillan et al. (2016).

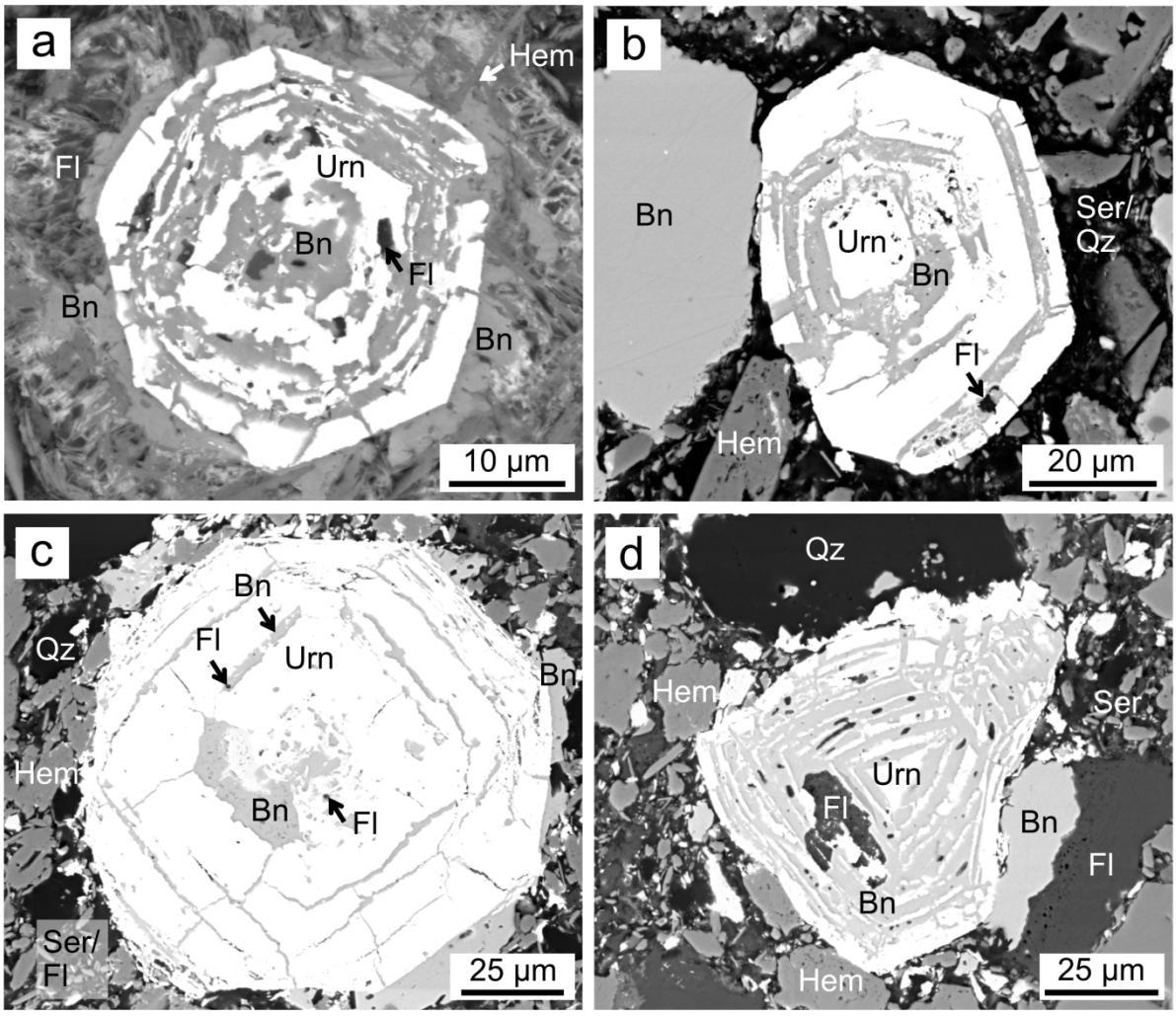

Figure 5.1: Back scattered-electron images of typical cob-web textures; **(a)** cob-web crystal S17.42 displaying rhythmic core-to-margin intergrowths of uraninite (Urn) and bornite (Bn) ± fluorite (Fl) inclusions and blebs. Grain is encompassed by selvedge of intergrown bornite, hematite (Hem) and fluorite; **(b)** broken cob-web crystal S17.61, again with intergrown uraninite, bornite and fluorite in a sericite (Ser) ± quartz (Qz) matrix with some larger surrounding grains of bornite and hematite; **(c)** cob-web crystal S18.18 with rhythmic intergrowths of bornite and inclusions of fluorite. The replacing bornite lamellae are discontinuous and appear parallel to sub-parallel and form a cubic-type arrangement, with thinner banding toward the rim of the grain. Some peripheral bornite, and matrix consists of sericite ± fluorite with quartz, hematite and bornite grains; **(d)** cob-web crystal S18.55 displaying concentric ringed intergrowths of uraninite and bornite, with fluorite inclusions and blebs. Surrounding larger grains of quartz, hematite, bornite and fluorite within a fine grained sericite/fluorite/quartz matrix.

5.2.2 Analytical methodology

A variety of micro-analytical and data processing techniques were employed (Appendix C). Nanoscale characterization and EBSD analysis was performed on a Dual Beam FIB-SEM FEI Helios Nanolab 600 platform (Adelaide Microscopy, University of Adelaide). Imaging was conducted in secondary electron (SE) mode and via the use of the solid-state scanning transmission electron microscopy (STEM) detector in bright field (BF) mode. EBSD patterns and maps were collected at 20 kV and 2.7 nA with a working distance ranging between 10 and 13 mm using a TSL^{TM} EBSD system equipped with a Hikari camera; data collection and processing settings are given in Table 5.1. Energy-dispersive spectroscopic (EDS) chemical data were also recorded concurrently with the EBSD patterns. This allowed for subsequent Chemical Indexing (ChI-scan) for phase identification, which was required since uraninite, bornite and fluorite have similar structures. Cob-web uraninite crystals are typically small (~20-50 μm) and contain mineral intergrowths extending well below the μm-scale, thus necessitating use of a FIB-EBSD rather than the SEM-EBSD system.

EBSD has been applied to study mineral textures in many different mineral systems at a range of scales (e.g., Prior et al., 1999). Numerous orientation contrast mapping methods are available to display the microstructures within minerals, but the key methods used in this study were: Confidence Index (CI), Image Quality (IQ), and Inverse Pole Figures (IPF). CI is a measure used to assess the reliability of the indexing process (see Appendix C) and was optimized to attain the best possible Electron Back-Scatter Pattern (EBSP) for UO_2 rather than for any other phase. For this reason, the CI of uraninite is typically much higher than that of bornite. IQ can be used to qualitatively identify variation in sample microstructure which is typically not observed in BSE images; e.g., crystallographic orientations, grain boundaries, surface topography, structural integrity, and porosity, to name a few (Reddy et al., 2007).

Grain orientation has been displayed via the use of IPF maps and pole figures. Adjacent grains of different color indicate the minerals of interest have differing orientations. Since uraninite crystallizes with fluorite-type structure, the [001], [101] and [111] crystallographic directions have been represented by the pole figures.

TEM work was performed on a Philips 200CM instrument operated at 200 kV, equipped with a double-tilt holder and Gatan digital camera. Investigation of FIB-prepared foils included high-resolution TEM (HR-TEM) imaging in BF mode, measurement of electron diffractions, and TEM energy-dispersive X-ray (EDX) spot analysis to identify micro- and nanoscale inclusions.

Table 5.1: EBSD data collection and processing settings.

General Parameters	
Binned Pattern Size	96
Theta Step Size (degrees)	1
Rho Fraction	90%
Max Peak Count	7
Min Peak Count	3

Hough Parameters	
Hough Type	Classic
Resolution	Low
Convolution Mask	Medium (9x9)
Min Peak Magnitude	5
Min Peak Distance	25
Peak Symmetry	0.7

	S18.19 Figure 5.2c	S17.20 Figure 5.2a
Grid Type	hexagonal	hexagonal
Working Distance (mm)	13	13
X Length (μm)	44.62	25.34
Y Length (μm)	40.63	34.31
Step Size (μm)	0.23	0.14
Total Points	39873	51546
Number UO_2 Indexed Points	8932	20770
Number Bornite Indexed Points	19550	14775
Average UO_2 CI	0.73	0.39
Average bornite CI	0.37	0.14
UO_2 Average Fit (degrees)	1.3	2
Bornite Average Fit (degrees)	1.84	2.17

5.3 Results

5.3.1 General microstructural observations

The two partially-replaced uraninite crystals analyzed using FIB-EBSD (Figure 5.2) are approximately 30 μm in diameter and have, in both cases, been sectioned at an oblique angle to [100]. It is nevertheless clear that the bands of uraninite and bornite are intergrown on the {110} and {100} faces. It is also apparent that in both cases, the outer rim of the crystal is

uraninite with inner irregularly spaced, parallel bands of bornite and uraninite. Within both crystals, there are small 1-2 μm sized grains of fluorite near their center and within some of the replacing bornite.

A visual comparison of CI for the two uraninite crystals is given as Figure 5.2b, d, and average CI and fit values are given in Table 5.1. In both cases, the CI values of uraninite are typically higher (warmer colors) than that of the bornite (cooler colors). Average CI values ranged from 0.73 to 0.39 for UO_2 and 0.37 and 0.14 for bornite. Fit values ranged between 1.3 and 2.0 for UO_2, and from 1.84 and 2.17 for bornite. The variation in CI and fit between UO_2 and bornite is partly expected since set-up was optimized based on EBSP bands for UO_2 rather than bornite, and optimization for different minerals often requires different exposure and gain settings (Appendix C). Both CI and "fit" values are relevant as these validate the quality of the indexing process, and are included here for this reason.

IQ maps for both cob-web uraninite crystals are displayed in Figure 5.3a, b. As with CI, IQ is higher for uraninite (yellow-red) than bornite (blue-green). The following key features are identified. Area (a) in Figure 5.3a highlights banding which is attributable to chemical zoning of Pb and ΣREY and the lack of inclusions (Macmillan et al., 2016). Some grain boundaries of bornite (blue/green) can be observed in areas (b, c-d) in Figure 5.3a and b, respectively. These grain boundaries are invisible on the BSE images (Figure 5.2a, c), but will be explored below when the IPF maps are discussed.

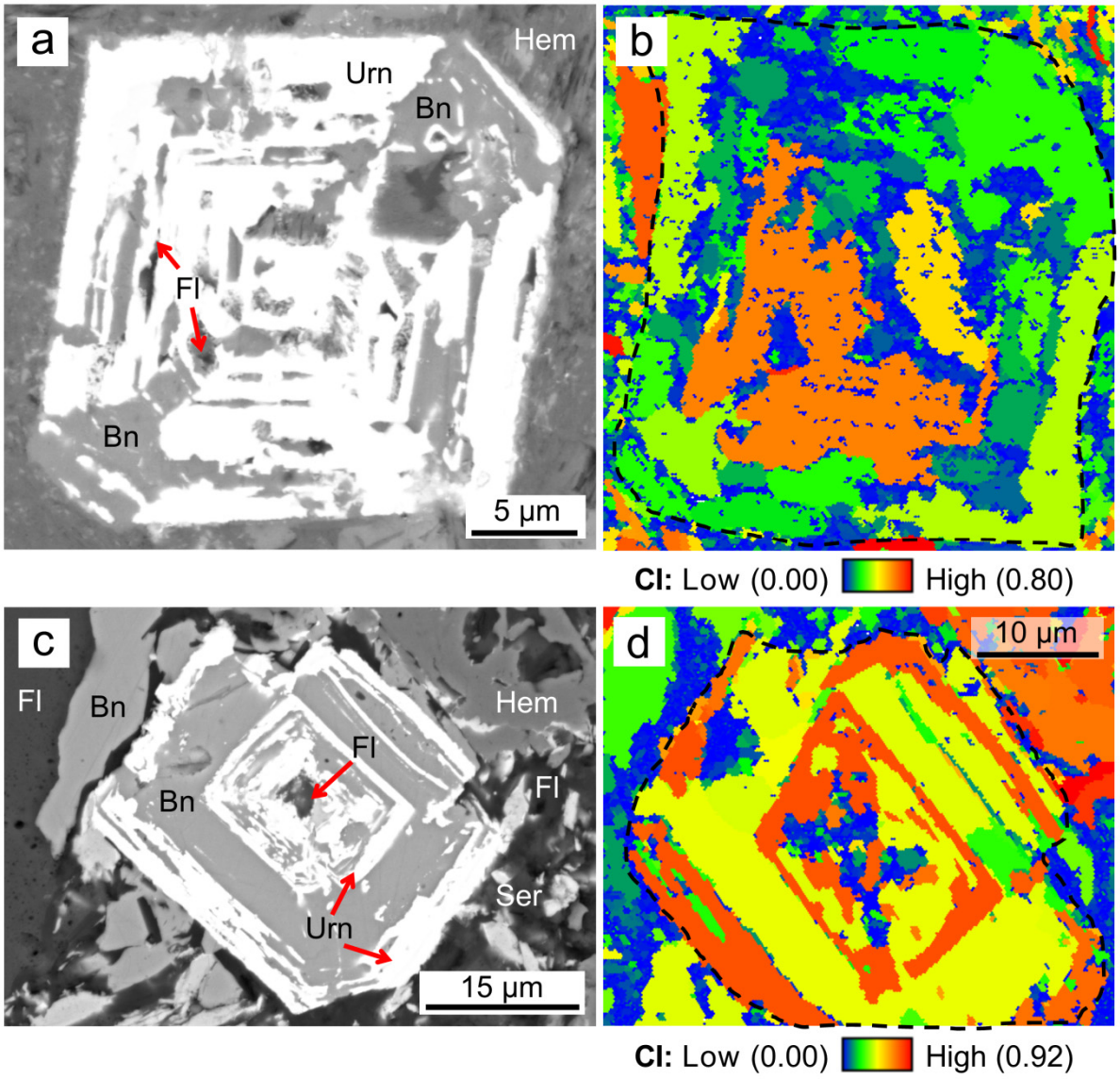

Figure 5.2: **(a)** Back scattered-electron image of cob-web crystal S17.20 with skeletal uraninite (Urn) intergrown with bornite (Bn), some fluorite (Fl) blebs, surrounded by finely intergrown hematite (Hem) and bornite; **(b)** EBSD-derived Confidence Index (CI) map of (a) with uraninite grain circled by black dashed line. CI values are higher for uraninite than bornite, with higher CI for less altered (i.e., central, colored yellow/orange) uraninite compared to more altered uraninite (i.e., rims, colored green). Matrix minerals (hematite, bornite ± fluorite) also with variable CI; **(c)** Back scattered-electron image of cob-web crystal S18.19 with bornite (Bn), surrounding minerals include fluorite (Fl), sericite (Ser), hematite (Hem); **(d)** EBSD-derived Confidence Index (CI) map of (c) with cob-web crystal circled by black dashed line. CI values range with cooler colors (blue-green) representing areas of lower CI and warmer colors (orange-red) representing areas of higher CI. UO_2 (red-orange) clearly has a higher CI than bornite (yellow-green).

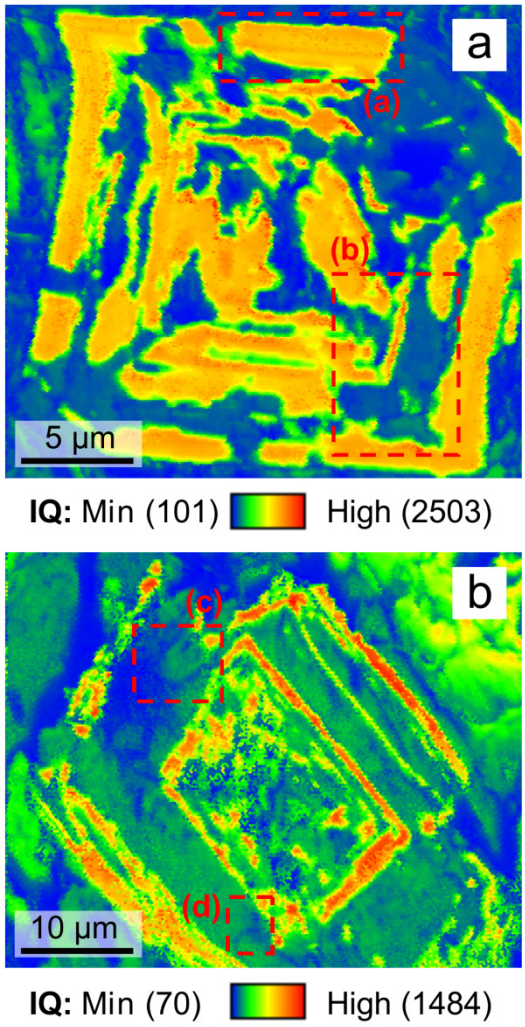

Figure 5.3: EBSD-derived Image Quality (IQ) map for cob-web crystals **(a)** S17.20 and **(b)** S18.19, warmer colors (red-orange) represent areas of higher IQ (uraninite), and cooler colors (blue-green) represent areas of lower IQ (bornite). IQ can be used to qualitatively display variation in sample microstructure. Areas (a-d) represent some of these microstructures: (a) highlights some banding which represents chemical variability (Pb, ΣREY) and inclusion content; (b-d) represent grain boundaries of bornite which are unobservable in the BSE images in Figure 5.2.

5.3.2 Crystallographic orientation of uraninite and bornite

Variation in crystallographic orientation within a crystal is displayed via IPF mapping, and shows whether a mineral represents a single or polycrystalline grain or aggregate. For both crystals (Figures 5.4a and 5.5a, respectively) uraninite is of a single crystallographic direction (between [111] and [001] for Figure 5.4a, and [101] for Figure 5.5a) and thus represents a single untwinned crystal. The slight gradational color variation shown Figure 5.4a, is attributable to alteration of uraninite and variation in chemical composition, an example of the latter is outlined in Area (a). This correlates with the observed variation in IQ (Figure 5.3a). However, if the orientation of bornite is considered, for one partially replaced uraninite crystal (Figure 5.4), the bornite consists of grains with differing crystallographic orientations (Figure 5.4b), and for the other crystal in Figure 5.5b, bornite is of two distinct orientations. If comparison is made between the respective IQ and IPF maps, the faintly observable bornite grain boundaries in area (b) on Figure 5.3a, are now clearly observable in Figure 5.4b. Likewise, the bornite boundaries in Figure 5.3b (areas c-d) are now also clearly observable in Figure 5.5b.

Visual comparison of the IPF maps and the pole figures for the uraninite and bornite forming the cob-web texture displayed in Figure 5.5 indicate that much of the bornite shares the orientation of the parent uraninite (green in Figure 5.5a-b). However, some of the bornite (pink in Figure 5.5b) is oriented at an angle of 45° from the uraninite and the other bornite. This indicates a second epitaxial relationship such that (110) bornite is parallel to (100) uraninite. It is notable that for a crystal with two orientations of bornite, that there are grains of bornite outside the crystal top left (pink) and bottom left (green), that are crystallographically coherent with the bornite replacing the crystal. This seems to represent bornite overgrowths on the parent uraninite.

The foil representing a cob-web crystal (Figure 5.6a) was cut through the side of a third crystal in such a way as to preserve the geometrical outline of the parent crystal, but avoids the complex intergrowths of Cu-Fe-sulfides and fluorite with uraninite on the other side of the crystal. TEM imaging of the foil shows a trail of inclusions near the uraninite-fluorite interface and these highlight a network of thin, interconnecting fractures (Figure 5.6b). Two of the largest inclusions (a few hundred nm in diameter) represent examples of typical multicomponent inclusions containing chalcopyrite-bornite-galena (Figure 5.6c), and fluorite-bornite (Figure 5.6d).

Orientation relationships between uraninite and sulfides were confirmed by ED patterns obtained for the larger inclusions (Figure 5.6b-d). The satellite reflections that are present on selected-area-electron-diffraction (SAED) patterns obtained for chalcopyrite are attributed to intergrowths with bornite (Figure 5.7a). The bornite is identified as being intermediate bornite with 4*a* superstructure (e.g., Ding et al., 2005; Figure 5.7b). Epitaxial relationships between bornite and uraninite are along [100] (Figure 5.7b). A slight offset is observed between the uraninite [100]* and [112]* in chalcopyrite (Figure 5.7a). SAEDs obtained from the margin between galena and uraninite show these to be coherent intergrowths along [100] which are slightly offset from one another (Figure 5.7c) due to galena's larger unit cell (a=5.93 Å). The intergrowth plane between uraninite [001] and chalcopyrite down [110] is shown by a SAED (Figure 5.7d) obtained on the margin between the chalcopyrite and uraninite (Figure 5.6c). SAED patterns (Figure 5.7e, f) from the bornite and uraninite associated with fluorite from one of the inclusions (Figure 5.6d) confirms polycrystallinity and the epitaxial relationship between these minerals.

5.3.3 Chemistry of replacement

Macmillan et al. (2016) document the chemistry and texture of different uraninites from OD, including a small number of primitive, seemingly unaltered crystals with mean composition $(U_{0.56}Pb_{0.19}Th_{0.07}REY_{0.19}Ca_{0.04})O_2$. Comparatively, the mean composition of the partially-replaced cob-web uraninites are compositionally less homogeneous, with compositions falling into two distinct groups based primarily on Pb content: a typically high-Pb group $(U_{0.63}Pb_{0.17}REY_{0.18}Ca_{0.06})O_2$; and a typically low-Pb group $(U_{0.67}Pb_{0.07}REY_{0.13}Ca_{0.11}Na_{0.02})O_2$ (see Macmillan et al., 2016 for EPMA data). The principal compositional difference between the primitive uraninites and the parts of the cob-web crystals that remain after replacement is a lack of measurable Th and the addition of Ca.

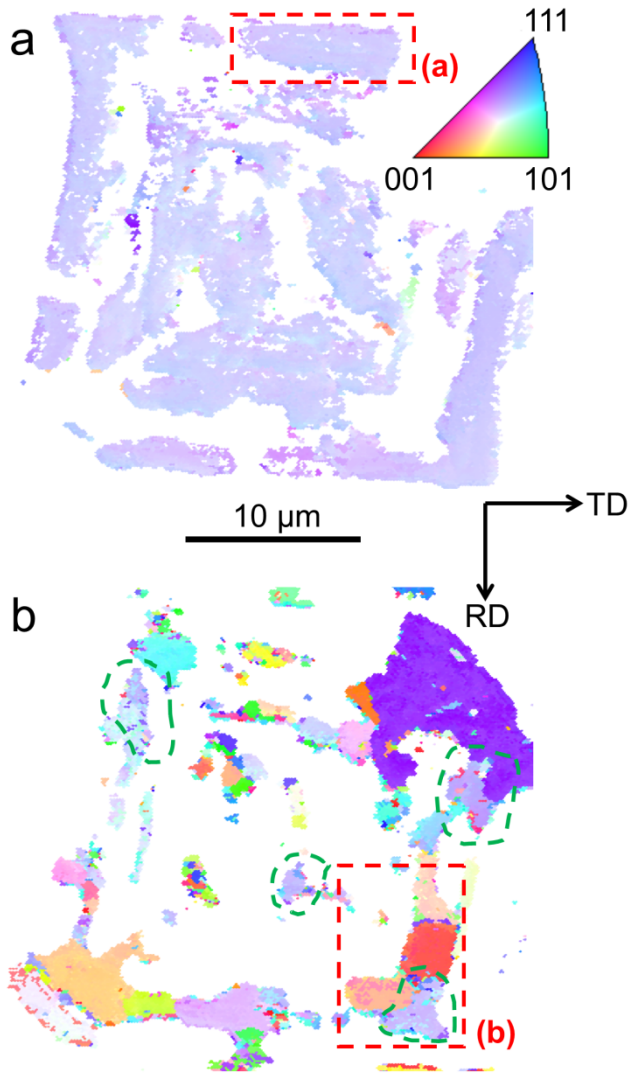

Figure 5.4: (a) EBSD-derived Inverse Pole Figure-Normal Direction (IPF-ND) map of UO_2 from cob-web crystal S17.20. Uraninite has one dominant (between [111] and [001]) orientation and represents a single crystal which precipitated at one time. Gradational color variation (outlined by red-dashed box (a)) reflects slight distortion of the crystal lattice due to chemical variability (Pb, ΣREY) and pore/inclusion content; **(b)** EBSD-derived IPF-ND map of bornite from cob-web crystal S17.20. Mosaic of bornite grains which display multiple orientations that differ to UO_2. Area outlined by red-dashed box (b) corresponds to area marked in Figure 5.3a (IQ variability) and confirms that bornite consists of multiple grains. Regions circled by green dashed lines appear to have similar orientation to that of uraninite (i.e., between [111] and [001]).

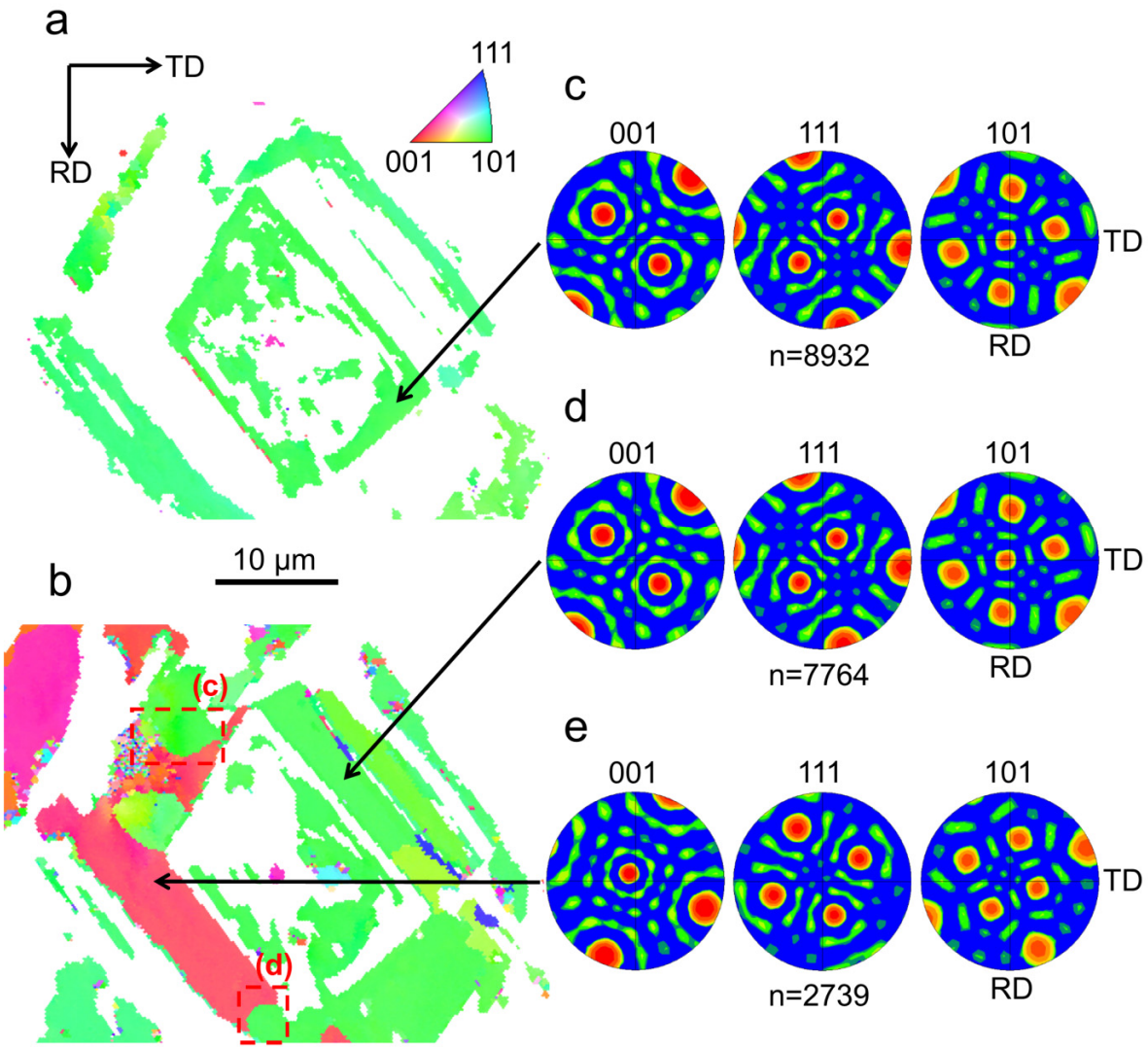

Figure 5.5: Selected images for cob-web crystal S18.19; **(a)** EBSD-derived Inverse Pole Figure-Normal Direction (IPF-ND) map of UO_2. UO_2 is of one dominant orientation [101] and represents a single crystal; **(b)** EBSD data derived IPF-ND map of bornite. Some bornite appears to be epitaxial with uraninite (i.e., UO_2 and bornite share the same orientation, colored green), whilst the other bornite has a 45° difference in orientation (colored pink, [001]). Areas (c) and (d) correspond to areas marked in Figure 5.3b and confirm that the IQ variability is due to grain boundaries within bornite; **(c)** Stereographic projections (colored using a logarithmic scale) of crystallographic poles {001}, {110} and {111} of UO_2 for the EBSD data shown in (a); **(d)** Stereographic projections (colored using a logarithmic scale) of crystallographic poles {001}, {110} and {111} for bornite for the EBSD data shown in (b) which shares the same orientation as UO_2 (colored green); **(e)** Stereographic projections (colored using a logarithmic scale) of crystallographic poles {001}, {110} and {111} for bornite for the EBSD data shown in (b) which has a differing orientation to UO_2 (colored pink).

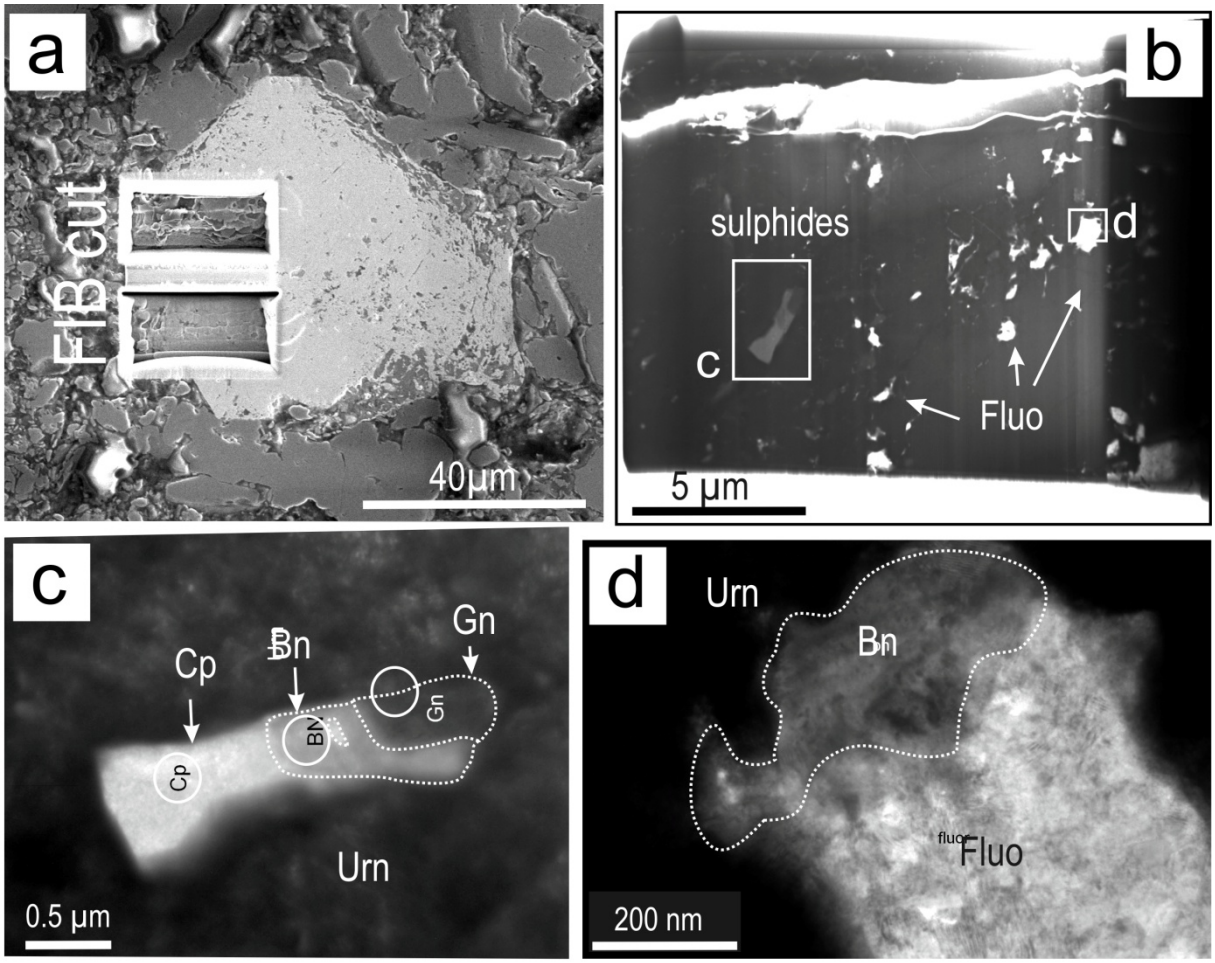

Figure 5.6: Secondary Electron image (a), STEM Bright Field image (b), and TEM images (c-d) showing uraninite (S15.60) hosting micron- to nanoscale inclusions of sulfides and fluorite; **(a)** Location of FIB cut across the half of the grain that preserves the geometrical outline of the parent crystal, but avoids the complex intergrowths of Cu-Fe-sulfides and fluorite with uraninite on the other side of the crystal; **(b)** TEM foil prepared from cut in (a) showing trails of inclusions as marked; **(c, d)** Some of the largest, composite inclusions as marked in uraninite. Abbreviations: Bn=bornite; Cp=chalcopyrite; Gn=galena; Fluor=fluorite; Urn= uraninite.

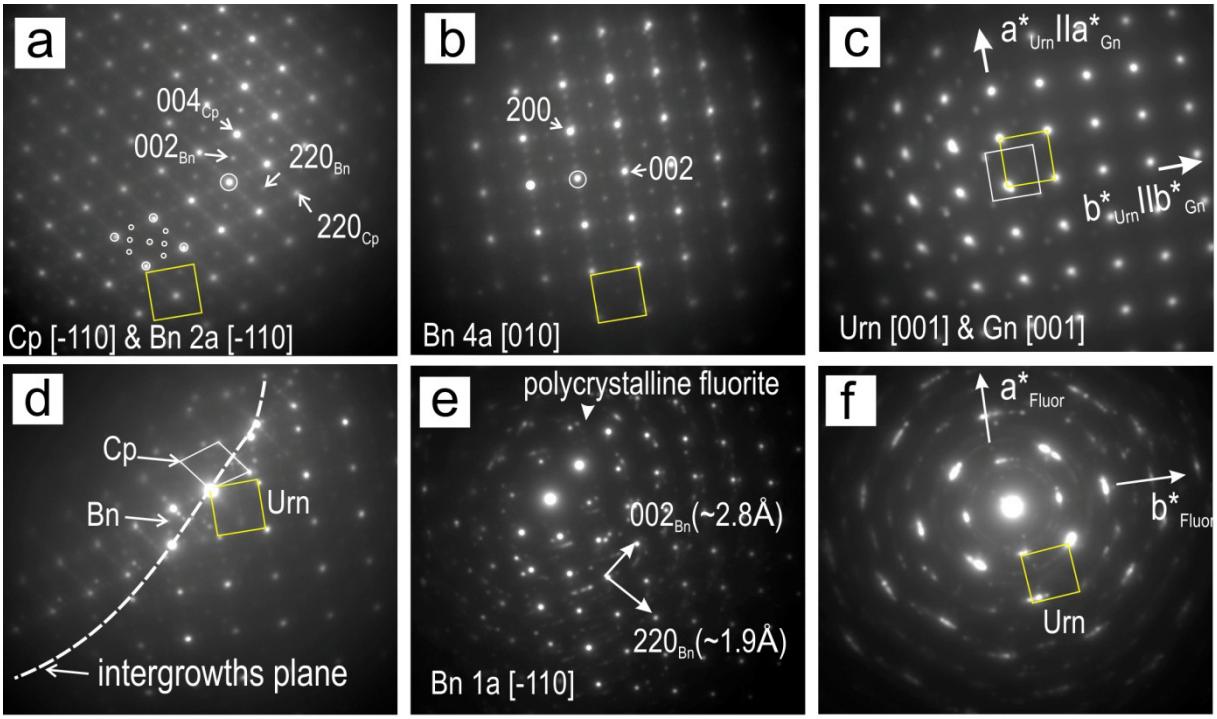

Figure 5.7: Selected-area-electron-diffractions (SAEDs) showing the orientation relationships between mineral inclusions and host uraninite. The zone axis marked represents orientation of each mineral when specimen tilted down to [001] zone axis of uraninite (main motif marked by the yellow square). All SAEDs, except in (f) were obtained from inclusions in Figure 5.6c-d; **(a)** Coherent intergrowths between chalcopyrite and bornite down to [-110] of both minerals. Bornite shows satellite reflections (small circles) indicating a 2*a* superstructure; **(b)** Epitaxial intergrowths between bornite and uraninite along the cube axes. Note bornite shows satellite reflections attributable to a 4*a* superstructure; **(c)** Slight offset between galena and uraninite on [001] zone axis; **(d)** SAED obtained across the boundary (marked by the dashed line) between uraninite and sulfides in (a). This shows *(h.k.2l)** chalcopyrite ~ parallel to *b** uraninite (slight offset as seen from the mismatch between the rhomb and square outlines; **(e)** Polycrystalline fluorite and bornite; note the absence of satellite reflections indicating the primitive cell (1*a* bornite; indexed using space group *F23*); **(f)** Polycrystalline fluorite epitaxial with uraninite.

5.4 Discussion

We propose that the cob-web uraninite crystals from OD have formed as a result of CDR reaction where uraninite is being partially replaced by bornite. Features which are characteristic of textures formed via CDR reactions and observed in this case and include: preservation of the original uraninite crystal shape; sharp boundary between uraninite and bornite; epitaxial growth of bornite on uraninite; presence of porosity within the parent and product phases; amalgamation and annealing of porosity and inclusions at the uraninite-bornite interface (i.e., coarsening).

5.4.1 Epitaxial growth and ease of nucleation

The first observable feature of the cob-web texture is that based on IPF data, uraninite has been shown to represent one dominant crystallographic direction (Figures 5.4a and 5.5a). This supports the hypothesis that these are single uraninite crystals which have subsequently undergone an *in-situ* modification process rather than rhythmic reworking and recrystallization. However, bornite appears to be slightly more complex, in some cases it has identical orientation as uraninite, but also in a second crystallographic relationship related by a 45° rotation (Figure 5.4b) such that $\{100\}_{uraninite}$ is parallel to $\{110\}_{bornite}$. The epitaxy between these planes is of lower energy than a random orientation, which may explain why replacement occurred along these planes.

From SAED patterns (Figure 5.7) it was shown that bornite, fluorite and galena contained within inclusions in uraninite were epitaxial to uraninite, the slight offset observed between the uraninite and chalcopyrite cube axis and [112]* direction in chalcopyrite (Figure 5.7a) was due to the presence of a penetration twin. Thus, both EBSD (Figure 5.5) and TEM (Figure 5.7) data confirm an epitaxial relationship between some sulfides (bornite) and

uraninite. In contrast, formation of the fluorite was not interface coupled, as it is polycrystalline and does not always share an interface with the parent uraninite.

The epitaxial relationship between uraninite and bornite indicate that the replacement is pseudomorphic with an interface-coupled dissolution-reprecipitation mechanism (ICDR reaction). For an ICDR replacement, dissolution and precipitation processes need to be spatially coupled as the reaction front advances through the original crystal, and the dissolution step of the reaction needs to be rate limiting (Xia et al. 2009a, b). If preservation occurs on the nanoscale, so that the replacing mineral crystallographic orientation is inherited from the parent mineral, this will result in pseudomorphism (Putnis et al., 2005; Putnis, 2009). Here we also observe bornite in a second epitaxial relationship to the parent uraninite (i.e., Figure 5.5b, e), but there is no break in the spatial separation between the dissolution and reprecipitation so the replacement is still consistent with ICDR and is not non-perfect replacement (Putnis et al., 2005). In the crystal in Figure 5.5b, with the two orientations on bornite, it is notable that there is evidence of overgrowths of bornite on the outside of the uraninite crystals. This indicates that the replacement reaction may have initiated at two sites in the crystal, one of which nucleated such that $\{100\}_{\text{uraninite}}$ is parallel to $\{100\}_{\text{bornite}}$ and the other where $\{100\}_{\text{uraninite}}$ is parallel to $\{110\}_{\text{bornite}}$. Understanding how the replacement processes interact is difficult as we can only see the replacement texture on a single 2-dimensional slice of what is clearly a 3-dimensional process.

Ultimately, the nature of the texture formed by CDR replacement is controlled by the local supersaturation at the replacement interface, since this dictates the nature of nucleation and subsequent growth of the product phase. A summary of typical growth mechanisms and nucleation can be found in Altree-Williams et al. (2015). Initially the product phase must nucleate at the outside surface of the parent crystal and there is an activation energy barrier

which exists and limits product nucleation. The activation energy barrier defines a threshold supersaturation for either epitaxial nucleation or heterogeneous nucleation and defines points at which the rate of nucleation increases sharply via either nucleation type. When the supersaturation is above the threshold value, any new product formed is dominated by nucleation, whilst below this value crystal growth defines new product formation. For the case of bornite replacing uraninite (Figure 5.5), it is therefore likely that initially there was epitaxial replacement of uraninite by bornite, and the concentration of Cu, Fe, S etc. at the reaction interface must have been above the threshold epitaxial supersaturation as bornite replaced uraninite and grew in a single orientation. In this case it appears that at a second point on the surface there was a second site for epitaxial nucleation in a different orientation with {100} bornite parallel to {110} uraninite. Thus the {100} bornite (pink, Figure 5.5b) grew as did the {110} bornite (green) and the two reaction fronts eventually met within the parent crystal.

5.4.2 Porosity and inclusion formation

An abundance of pores and nanoscale inclusions were observed within the uraninite crystals using the TEM. Porosity is always formed as part of CDR replacement reactions. It has been shown that when Cu-Fe-sulfides such as bornite and chalcopyrite are formed by mineral replacement reactions, these are initially porous, facilitating transport to and from the reaction interface (Xia et al. 2014; Zhao et al. 2014a, b; Li et al. 2015). The generation of both porosity and new grain boundaries during CDR replacement is important in allowing for continued replacement. Increased surface energy is required to generate these grains and pores, which further drives the need for the product to reequilibrate (Altree-Williams et al., 2015). Where there is supersaturation of the local solution at the replacement interface mineral inclusions of the supersaturated phases may form within the CDR generated porosity. Thus coarsening of

porosity or inclusions (termed Ostwald ripening; Ratke and Voorhees, 2002) occurs whereby there is dissolution of small inclusions or amalgamation of nano-scale inclusions, and subsequent growth of larger inclusions or porosity. Thus, porosity is a transient feature and could coarsen to reduce the free energy of the system and produce a texturally stable product (Putnis, 2009).

Closure of porosity by coarsening may trap the fluids that were in the pores and thus fluid and mineral inclusions may form and be the only remnants that such an alteration occurred (e.g., Putnis and Putnis, 2007). This can therefore elucidate some of the conditions at the time of closure, but care needs to be taken with interpretation as the trapped fluids represent the composition of the bulk fluid responsible for driving the mineral replacement reaction, overprinted with compositional characteristics of the parent mineral, rather than the bulk fluid composition alone. Since fluorite, chalcopyrite and bornite are often present as inclusions within the parent uraninite it can be assumed that the fluid at the reaction front must have been a F-rich, Cu-Fe sulfide-bearing hydrothermal fluid. The fluorite found within the bornite-uraninite crystals is probably formed as the porosity in the bornite disappears during annealing, and the fluorite and other inclusions crystallize from the trapped hydrothermal fluid. The nature of the other inclusions reflects the composition of the fluid.

The generation of porosity alone will not permit fluid flow unless the pores are interconnected to form a permeable network. Thus another requirement for replacement to proceed is establishing access pathways for fluid into the replaced mineral. Pathways may include: twin boundaries/crystal faces/cleavage planes (Putnis and Putnis, 2007; Pearce et al., 2013), grain boundaries (Engvik et al., 2009; Etschmann et al., 2014), and fractures (Jamtveit et al., 2009). Such features are advantageous since nucleation may occur on these boundaries which already have a surface energy and hence nucleation is easier than within the crystal lattice

(Pearce et al., 2013). The rotation axis boundaries of uraninite that has been replaced by bornite (Figure 5.5) correlate to the $\langle 1\bar{1}0 \rangle$ slip direction. It is therefore likely that replacement has occurred along this known slip system.

5.4.3 The replacement reaction

Evidence of partial replacement of uraninite crystals by bornite and fluorite, together with the local abundance of bornite and fluorite generally found within the samples, indicate that the replacement was driven by a F-rich hydrothermal fluid that was also enriched in Cu, S, Fe and Ca. Unfortunately, there is little published experimental data on the properties of such F-rich hydrothermal fluids but it is known that F-rich hydrothermal solutions will preferentially strip Th over U and will also dissolve Th and U in their tetravalent states (Keppler and Wyllie, 1990).

It is difficult to write exact chemical equations for the replacement process due to the lack of common chemistry between the parent uraninite and the bornite ± fluorite. Since the parent uraninite and the product bornite and fluorite all share a common structural archetype (and almost identical molecular volumes), the potential replacement reaction may be represented by:

Uraninite + (F^-, Cu^+, Fe^{3+}, S^{2-}, Ca^{2+} -bearing)-hydrothermal fluid $\rightarrow$

bornite ± chalcopyrite + fluorite + skeletal uraninite

The ICDR replacement of uraninite and bornite is unusual compared to many such replacements (see Putnis 2009; Altree-Williams et al. 2015) in that there are no common chemical constituents between the parent uraninite and the product bornite. The volume of fluid at the reaction interface in a ICDR reaction is very small making high levels of supersaturation possible, thus in the situation where one or more chemical components are

common to both the parent and daughter phases, it is easy to understand how the daughter phase would nucleate and grow, being fed by chemical components from the bulk solution and the dissolution of the parent phase. In the case discussed here, with no common chemical components, all of the Cu, Fe and S must come from the bulk solution and with the restricted volume at the reaction interface, one would expect that this might serve to increase the level of supersaturation with respect to bornite crystallization, inhibiting the process. Since the reaction clearly proceeds, one must conclude that the products of the uraninite dissolution (i.e., U, O, REE etc.) change the interface fluid chemistry such that it favors bornite precipitation and growth. It seems likely that it is a change in the fO_2 that favors the precipitation of bornite.

Li et al. (2015) attempted to replace uraninite crystals with bornite/chalcopyrite using hydrothermal conditions (which did not contain any F, but did contain the other essential elements: Cu, Fe and S), and found that the uraninite was more soluble than the bornite/chalcopyrite. Instead thin stringers of uraninite were observed growing at the original parent bornite or chalcopyrite grain surface, and there was no epitaxial relationship between the sulfides and the over growing uraninite. While these experiments were unsuccessful in producing the cob-web style uraninite textures, they are consistent with the proposition that the reactions in nature are driven by F-rich, Cu-Fe sulfide-bearing hydrothermal fluids.

5.4.4 Conceptual model - evolution of 'early' uraninite

A conceptual model for the evolution of the 'early' uraninites (summarized in Figure 5.8) involves:

1. A uranium mineralizing event occurs, during which cubic, crystalline uraninite is precipitated (forming primary uraninites, Figure 5.8a). Fluctuations in solution chemistry during growth, as well as controlled crystallographic uptake of certain elements (e.g., Alexandre et al., 2015) may have led to the formation of the initial concentric and oscillatory chemical zoning of the crystal. Subsequent solid-state diffusion which was driven by radiation induced self-annealing and other thermal/geological events modify the chemical zoning within these uraninites (forming zoned uraninites, Figure 5.8b).
2. A F-rich Cu-Fe sulfide-bearing hydrothermal fluid is introduced into the system. The driving force for replacement is related to the presence of F, which is known to preferentially strip Th over U and will also dissolve both Th and U in their tetravalent states. Parts of the uraninite are thus preferentially dissolved and there is pseudomorphic replacement of single crystal uraninite by bornite via CDR reaction (Figure 5.8c). Replacement occurs along chemical zones within the primary uraninites which are preferentially dissolved, and act as fluid pathways into the crystal. These also correlate to the $\langle 1\bar{1}0 \rangle$ slip direction in uraninite. The reaction interface between the uraninite and bornite is sharp. It is thought that uraninite is being replaced by bornite since the uraninite contains sulfide-fluorite inclusions which contain no observable nano- or microscopic uraninite inclusions. If uraninite was replacing the Cu-Fe-sulfides, there would also be uraninite inclusions

contained within the Cu-Fe-sulfides and fluorite, which are not observed. This marks the start of the formation of cob-web texture.

3. The replacement process stalled when the fluid no longer had access to the reaction front or conditions changed (i.e., fluid conditions changed and prevented uraninite solubility). The replacement is only recognizable when the reaction front is "fossilized" due to there being insufficient fluid to complete replacement (Putnis, 2002). This is what we are seeing by the remaining skeletal uraninite within the cob-web texture.
4. Ostwald ripening occurred to minimize the free energy and allowed for the amalgamation of porosity and inclusions that were formed during the CDR replacement process.
5. Remaining 'early' uraninites are thus a mix of the primary, zoned and cob-web uraninites. Not all 'early' uraninites underwent the same degree of replacement possibly since a hydrothermal fluid may have been unable to access all parts of the rock containing these uraninites equally due to differing local variation in mineral assemblage and pore density.

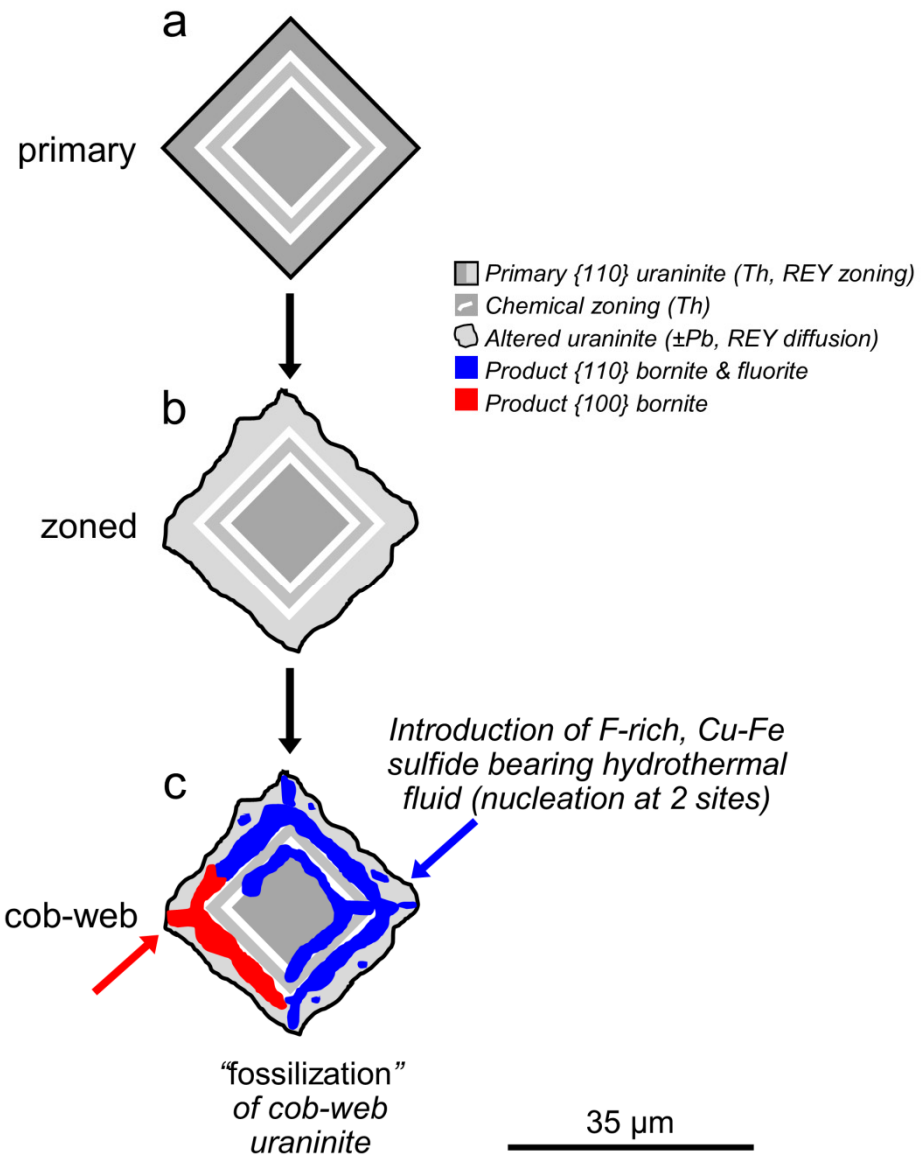

Figure 5.8: Schematic representation of the evolution of 'early' uraninites: **(a)** Precipitation of euhedral, cubic uraninite (primary) with concentric and sectorial zonation of Pb, Th and ΣREY; **(b)** Chemical zoning is altered due to solid-state diffusion driven by radiation-induced self-annealing and other thermal/geological events (forming zoned uraninite); **(c)** Influx of F-rich and Cu-Fe sulfide-bearing hydrothermal fluid which preferentially dissolves uraninite along certain chemical zones (Th-rich and correlating to $\langle 1\bar{1}0 \rangle$ slip direction) of uraninite. Epitaxial replacement of uraninite with bornite ensues via interface-coupled dissolution-reprecipitation mechanisms, forming the cob-web texture. Replacement stops and 'fossilization' of the cob-web uraninite texture occurs when there is insufficient fluid at the reaction front.

5.5 Conclusions

Processes involved in formation of 'early' uraninites at OD have been constrained by coupled EBSD and TEM data. It has been revealed that grain-scale replacement of uraninite by bornite occurs via CDR reaction, and replacement is controlled by the inherent chemical zoning within the uraninite crystal. This study has shown that the 'early' uraninites are generally of single grain orientation and represent a progressive *in-situ* alteration process of primary through zoned and cob-web uraninites. This work expands on the work of Macmillan et al. (2016) in better constraining the evolution of the uraninite at OD, so that a robust genetic model for the evolution of the U-mineralization within such IOCG deposits may be developed. Further work will address both the chemistry of the dissolved uraninite, and that of the fluid. Experimental work may help to resolve some of these ambiguities. Also, understanding the replacement process is difficult from a single 2-dimensional slice of a crystal, thus further work is required on the FIB and TEM to try and document the replacement process in 3-dimensions.

Uraninite is known to have rapid annealing kinetics (e.g., Janeczek and Ewing, 1991) where uraninite self-heals any radiation damage, and it was thus initially thought that the use of EBSD analysis on such a mineral may have limited applicability. Much of the published EBSD work has been conducted on zircon, for which fracture healing and recrystallization take place at far slower rates than in uraninite (Hazen et al., 2009). This study has demonstrated, however, that EBSD can be used to provide evidence for the processes involved in generating the complex cob-web uraninite textures visible at OD, and probably also in many other U-rich IOCG deposits.

Furthermore, in terms of studies which consider CDR-driven replacement of minerals, typically the parent and daughter phases have some similar chemical constituents. In this case

the parent uraninite and daughter bornite are chemically different and share no common constituents. This study is therefore important in highlighting that it is possible to have CDR-driven replacement between phases with no chemical commonality.

5.6 Acknowledgements

This work forms part of the Ph.D. studies of E.M. and is supported by BHP Billiton. Staff at Adelaide Microscopy, notably Angus Netting, Benjamin Wade, Ken Neubauer and Animesh Basak, are thanked for instrument access and training. Dr Kan Li is thanked for undertaking the preliminary unsuccessful hydrothermal experimental study of the replacement of uraninite by bornite.

CHAPTER 6

CHEMICAL AND TEXTURAL INTERPRETATION OF LATE STAGE COFFINITE AND BRANNERITE FROM THE OLYMPIC DAM IOCG-AG-U DEPOSIT

Edeltraud Macmillan[1,2], Nigel J. Cook[3], Kathy Ehrig[2], and Allan Pring[4]

[1]*School of Physical Sciences, The University of Adelaide, Adelaide, SA, 5000, Australia*

[2]*BHP Billiton Olympic Dam, Adelaide, SA, 5000, Australia*

[3]*School of Chemical Engineering, The University of Adelaide, Adelaide, SA, 5000, Australia*

[4]*School of Chemical and Physical Sciences, Flinders University, Bedford Park, SA, 5042, Australia*

Paper submitted to Mineralogical Magazine (in review)

Statement of Authorship

Title of Paper	Chemical and textural interpretation of late-stage coffinite and brannerite from the Olympic Dam IOCG-Ag-U deposit.
Publication Status	☐ Published ☐ Accepted for Publication ☑ Submitted for Publication ☐ Unpublished and Unsubmitted w ork w ritten in manuscript style
Publication Details	Macmillan, E., Cook, N.J., Ehrig, K., and Pring, A. (2016) Chemical and textural interpretation of late-stage coffinite and brannerite from the Olympic Dam IOCG-Ag-U deposit. Submitted to Mineralogical Magazine (in review at the time of thesis submission).

Principal Author

Name of Principal Author (Candidate)	Edeltraud Macmillan
Contribution to the Paper	Devise plan for data collection and use of analytical methods, method/package development for various analytical methods, collected analytical data, processed and interpreted data, wrote manuscript.
Overall percentage (%)	95%
Certification:	This paper reports on original research I conducted during the period of my Higher Degree by Research candidature and is not subject to any obligations or contractual agreements with a third party that would constrain its inclusion in this thesis. I am the primary author of this paper.
Signature	Date 6/5/2016.

Co-Author Contributions

By signing the Statement of Authorship, each author certifies that:

i. the candidate's stated contribution to the publication is accurate (as detailed above);

ii. permission is granted for the candidate in include the publication in the thesis; and

iii. the sum of all co-author contributions is equal to 100% less the candidate's stated contribution.

Name of Co-Author	Nigel Cook
Contribution to the Paper	Supervised development of work, helped with data interpretation and manuscript evaluation.
Signature	Date 1/6/2015

Name of Co-Author	Kathy Ehrig
Contribution to the Paper	Supervised development of work and helped with manuscript evaluation.
Signature	Date 6/5/2016

Name of Co-Author	Allan Pring
Contribution to the Paper	Supervised development of work and helped with manuscript evaluation.
Signature	Date 10/5/16

CHAPTER 6: CHEMICAL AND TEXTURAL INTERPRETATION OF LATE-STAGE COFFINITE AND BRANNERITE FROM THE OLYMPIC DAM IOCG-AG-U DEPOSIT

Abstract

The Olympic Dam iron-oxide copper-gold-silver-uranium deposit, South Australia, contains three dominant U-minerals: uraninite; coffinite; and brannerite. Microanalytical and petrographic observations provide evidence for an interpretation in which brannerite and coffinite largely represent the products of U mineralising events after initial deposit formation at 1.6 Ga. The marked chemical and textural differences between the various types of brannerite and coffinite highlight the role of multiple stages of U dissolution and reprecipitation.

Based on petrographic characteristics (size, habit, textures and mineral associations) and compositional variation, brannerites are divided into four distinct groups (brannerite-A, -B, -C and -D), and coffinite into three groups (coffinite-A, -B and -C). Brannerite-A ranges in composition from what is effectively a uraniferous rutile to stoichiometric brannerite, and has elevated (Mg+Mn+Na+K) and (Fe+Al) compared to the other brannerite types. It displays the most diverse range of morphologies, and includes complex irregular-shaped aggregates, replacement bands, and discrete elongate seams. 'Randomly-oriented hair-like needles to blades' best describes the internal structure exhibited by brannerite-A. Brannerite-B (<5 μm in size) is generally prismatic in shape, similar to that of rutile prisms. It is typically associated with barite and REY-minerals (REE+Y=REY). Brannerite-C and -D are both associated with Cu-(Fe)-sulfides and typically comprise of irregular masses and blebs (10-50 μm in size). These have a more uniform or massive internal structure. Brannerite-D is distinct from -C as it always contains inclusions of galena. Brannerite-B to -D all contain elevated ΣREY, with brannerite-B and -C having elevated As, and brannerite-D having elevated Nb.

All coffinite is typically globular (each globule is 2-10 μm in size) to collomorphic in appearance. Coffinite-A ranges from discrete globules to collomorphic bands which completely encompass quartz grains. Coffinite-B is always found with uraninite, and includes collomorph coffinite which is enveloped by massive uraninite, as well as aureoles of coffinite on the margins of individual uraninite crystals. Coffinite-C is associated with brannerite and REY-minerals. In some cases, individual coffinite globules contain needles of chlorite and/or sericite. The majority of coffinite is chemically heterogeneous and exhibits zones enriched in Si ± P which occur within the coffinite closest to adjacent quartz. There are also zones with enriched ΣREY and Ca. Coffinite-B contains high-Ca, but lower ΣREY and (P+As+Nb) than coffinite-A and -C. Coffinite-C has the highest ΣREY, whereas coffinite-A displays the largest variability in composition.

Estimates of the structural formulae for the various groupings of brannerite and coffinite, as well as the mean of all data collected for each mineral are presented. Within brannerite, the dominant A-site substitutions include Ca^{2+} and REY^{3+} replacing U^{4+} and/or U^{6+}, and in the B-site, typical substitution of Ti^{4+} occurs with Si^{4+}, Na^{+} and Fe^{3+}. For coffinite, U^{4+} and/or U^{6+} within the A-site are typically replaced by Ca^{2+}, Fe^{2+} and REY^{3+}, and in the B-Site, Ti^{4+} is replaced by P^{5+}.

Based on textural observations, supported by chemical composition, it has been concluded that brannerite and coffinite have precipitated as part of a late-stage U-event at OD, which may have involved the dissolution and/or reprecipitation of earlier precipitated uraninite, or may represent the products of a later U-mineralizing event. Evidence which supports formation of late-stage coffinite and brannerite includes: (1) the low-Pb contents of both brannerite and coffinite (i.e., experienced minimal radioactive decay or radiogenic Pb has been mobilized from these minerals); (2) coffinite is often found on the edges of uraninite,

thus implying this process occurred after deposition of uraninite; (3) coffinite is often found on the edge of brannerite aggregates, which is suggestive that brannerite precipitation occurred before coffinite. Moreover, there are many features (e.g., banding, scalloped edges, alteration rinds, variable compositions etc.) which have been observed for all U-minerals, and these are typically formed as a result of hydrothermal alteration processes. Based on inclusions contained within, and minerals associated with both brannerite and coffinite, it is likely that the hydrothermal fluid/s contained F, Cu, Fe, S, Si and Ca, as well as Na and K from the partial dissolution and alteration of feldspars.

Keywords: uranium; coffinite; brannerite; Olympic Dam; IOCG deposits

6.1 Introduction

The most important U^{4+} minerals found in nature, based on abundance and economic value, are uraninite [UO_2], coffinite [$U(SiO_4)_{1-x}(OH)_{4x}$] and brannerite [$U(Ti,Fe)_2O_6$] (Finch and Murakami, 1999). Although most U^{4+} minerals occur as accessory minerals in granitic, pegmatitic or aluminous metamorphic rocks, coffinite and brannerite appear largely restricted to systems where uranium has been mobilized and subsequently reprecipitated as these minerals.

Transport of U can occur in both reducing and oxidizing environments (Finch and Murakami, 1999). Under reducing conditions, U can typically be transported only fractions of a cm, however if either F^- or Cl^- ligands are available, these can stabilize the U^{4+} in solution, and the transport distance may be much further (Keppler and Wyllie, 1990). In contrast, under oxidizing conditions, the uranyl ion (UO_2^{2+}) and related complexes can allow for U migration up to many km from source until the solution chemistry changes sufficiently to allow for precipitation of U minerals (Finch and Murakami, 1999). When the uranyl ion comes into contact with more reducing conditions like organic matter or sulfides, the U is subsequently

reduced and may allow for precipitation of other U-minerals. Coffinite, for example, is usually only found in deposits formed by low-temperature processes, and is often an alteration product of an earlier uraninite that has been altered under reducing conditions (Janeczek and Ewing, 1992a; Plant et al., 1999). Thus, in some cases U-minerals may already have precipitated within a deposit from an earlier mineralizing event, and if exposed to later fluids, the U may be remobilized and then reprecipitated as the same or different U-mineral/s.

A 'recycling' of uranium minerals is considered applicable to the Olympic Dam (OD) deposit, South Australia, the World's largest uranium resource. There are 3 dominant U-minerals at OD: uraninite, coffinite and brannerite, and petrographic study provides extensive evidence of multiple stages of U dissolution and reprecipitation (e.g., Reeve et al., 1990; Ehrig et al., 2012; Kirchenbaur et al., 2016; Macmillan et al., 2016). There have been at least two uraninite mineralizing events at OD, an early one at ca. 1590 Ma, and a superimposed, younger event. Both events generated texturally and chemically distinct uraninites (Macmillan et al., 2016). The presence of brannerite and coffinite at OD has long been acknowledged, but no mineralogical study has been published before now. The key objectives here are therefore to determine the chemical and textural variability of brannerite and coffinite at OD, and to suggest possible mechanisms of formation and alteration of these minerals.

6.2 Background and geological context

Both brannerite and coffinite are texturally diverse and display wide compositional ranges, as a result of formation in wide-ranging geological settings. The key crystal chemical features of both minerals are discussed below, followed by a brief introduction to uranium mineralogy at OD.

6.2.1 Brannerite

The ideal chemical formula of brannerite is UTi_2O_6. The mineral crystallizes in the monoclinic system, with space group *C*2/*m* (Szymanski and Scott, 1982) and is isostructural with thorutite, $ThTi_2O_6$ (Ruh and Wadsley, 1966). Stoichiometric brannerite theoretically contains 62.8 wt% UO_2 and 37.2 wt% TiO_2 (Frondel, 1958). Like many uranium minerals, however, brannerite is commonly non-stoichiometric, and has been shown to have a complex and variable chemical composition (e.g., Frondel, 1958; Ferris and Ruud, 1971; Szymanski and Scott, 1982; Saager and Stupp, 1983; Smith, 1984; Lumpkin et al., 2012). The general formula is best described to be AB_2O_6, where A is U and commonly also Pb, Ca, Fe, Th, REE+Y (hereafter, ΣREY), and B typically contains Ti, which can be replaced by Si, Al, or Fe. Brannerite has also been reported to contain Ba, Sr, Ni, Bi, Sn, Ta, Nb, Sc, P, He and Zr. The A-site is octahedral (six-coordinated), and the B-site is also octahedral, but the octahedra share corners and/or edges to form a structural framework (Szymanski and Scott, 1982). One attempt at a more accurate formula is given by Szymanski and Scott (1982): $(U, Pb, Ca)_{0.6x}Ti_x(Si, Fe, Al, V)_{3.36-1.65x}O_6$, where 1.2<x<1.8. Brannerite is also typically oxidized, and often contains both U^{4+} and U^{6+} (Finch and Murakami, 1999). The related mineral orthobrannerite is hydrated and has the formula $(U^{4+}, U^{6+})(Ti, Fe)_2O_6(OH)$ (Singh et al., 1990; Gaines et al., 1997).

All natural brannerite is metamict (Smith, 1984), and due to radioactive decay via α-particle emission, is typically amorphous (Lumpkin et al., 2014). The metamict nature of brannerite may explain why it is able to incorporate large amounts of impurities into its structure, including Pb from the radioactive decay of U. Brannerite is found in a number of different geological environments, including placer deposits, veins, metasomatic-hydrothermal veins and replacements, pegmatites, and in disseminated copper and molybdenum deposits (Ferris

and Ruud, 1971). The first detailed description and photomicrographs of brannerite were provided by Ramdohr (1957), who described the often delicate and complex internal network of blades and intergrowths of brannerite aggregates.

6.2.2 Coffinite

Coffinite, nominally $USiO_4.nH_2O$, $I4_1/amd$ and Z=4, is a tetragonal orthosilicate with U^{4+} coordinated by eight O atoms in the form of a distorted cube-like polyhedron (Fuchs and Gebert, 1958). Ideal hydrated coffinite contains 73.75 wt% UO_2, 16.41 wt% SiO_2 and 9.84 wt% H_2O, whereas ideal anhydrous coffinite contains 81.80 wt% UO_2 and 18.20 wt% SiO_2 (Janeczek and Ewing, 1992a, 1996). There are a large number of possible element substitutions: U^{6+}, Zr^{4+}, Th^{4+}, Hf^{4+}, Ca^{2+}, Fe^{2+} and REY^{3+} in the A-site (U^{4+}); and P^{5+}, As^{5+}, V^{5+}, W^{6+} and S^{6+} in the B-site (Si^{4+}). F^- may exchange with $(OH)^-$, and there can also be potential vacancies in the tetrahedral site (Stieff et al., 1956; Pointer et al., 1988; Hansley and Fitzpatrick, 1989; Janeczek and Ewing, 1992a; Förster, 2006). An extensive range of limited or complete solid solutions between coffinite and isostructural minerals are thus possible. These include, but are not restricted to the relative common solid solutions between coffinite [$USiO_4$], zircon [$ZrSiO_4$], thorite [$ThSiO_4$] and xenotime [$(Y,REE)PO_4$] (e.g., Speer, 1980; Pointer et al., 1988; Finch and Hanchar, 2003; Förster, 2006). Hansley and Fitzpatrick (1989) and Janeczek and Ewing (1996) show coffinite-xenotime solid solution is complete and widespread in natural samples. With respect to some of the extended range of elements reported in coffinite, some may clearly be contained as fine-grained intergrowths or inclusions within coffinite rather than incorporated in the lattice. The typically fine-grained (<10 μm) and intergrown character of coffinite can make accurate and unambiguous microanalysis difficult (Hansley and Fitzpatrick, 1989; Finch and Murakami, 1999).

Coffinite occurs in a variety of different uranium deposit types, including granitic systems and those where uranium has been remobilized via hydrothermal or meteoric waters. It is commonly associated with sandstone uranium and/or low-temperature U deposits (Stieff et al., 1956; Dahlkamp, 1978; Ludwig and Grauch, 1980). Coffinite can also be formed in reducing conditions via alteration of uraninite in Si-rich systems (Janeczek and Ewing, 1992a), and from hydrothermal and supergene processes in granitic environments (Leroy and Turpin, 1988; Förster, 2006). Smits (1989) described coffinite as a component of the Witwatersrand gold deposits, South Africa, where it occurs in paleoplacer conglomerates and replaces detrital uraninite grains through uptake of silica.

6.2.3 Geological context

The Olympic Dam iron-oxide copper-gold (IOCG)-silver-uranium deposit is located 520 km NNW of Adelaide, South Australia. The geological setting and mineralogy of the OD deposit have been described in detail elsewhere (e.g., Reeve et al., 1990; Ehrig et al., 2012), so only specific features pertaining to the U-minerals are discussed here. IOCG deposits often contain significant amounts of U, including OD (Reeve et al., 1990) and Ernest Henry, east of Mt. Isa, Queensland (Ryan, 1998), but little mineralogical data has been published about the textural and chemical variability of the U-minerals within these deposits. Initial U-mineral work at OD focused predominantly in the higher-grade, central parts of the deposit where massive uraninite textures are typical (Trueman et al., 1986; Oreskes and Einaudi, 1990; Johnson, 1993). More recently, due to the improved geological knowledge from the extensive drillhole and mineralogical database, a greater awareness of the U-mineral variability and mineral association has been ascertained. Ehrig et al. (2012) describe how the proportion of uraninite relative to coffinite and brannerite increases with total Fe content throughout the deposit. The average relative proportions of brannerite, coffinite and uraninite across the entire deposit are

31, 56, and 13 wt%, respectively; however local mineralogical variation throughout the deposit impacts upon which U-mineral is most abundant. Typically, uraninite is more strongly associated with hematite and sulfides, but coffinite and brannerite tend to be more closely associated with gangue (quartz, sericite, chlorite, or hematite).

Macmillan et al. (2016) outline uraninite mineralogy at OD, and identify at least two main uraninite mineralizing events with evidence of multiple stages of U dissolution and reprecipitation. There are crystalline and sparsely preserved early uraninites, and late uraninites which tend to be stringer-like, massive, or aphanitic. Textural and chemical differences between these uraninites, as well as differences in the Pb/U ratios (based on electron microprobe analyses), distinguish the two types. Both show evidence of hydrothermal alteration, but there may also have been additional influxes of U-bearing fluids which allowed precipitation of brannerite and coffinite. It has been proposed (e.g., Oreskes and Einaudi, 1992; Ehrig et al., 2012; Kirchenbaur et al., 2016) that the uranium minerals have a complex history with repeated cycles of precipitation, dissolution and reprecipitation. Kirchenbaur et al. (2016) suggest that the uranium is likely sourced from upper crustal lithologies; the $\delta^{238}U$ values are consistent with those of hydrothermal deposits with U sourced from high-temperature granitoid/volcanic/volcanogenic rocks. Moreover, no elevated $\delta^{238}U$ signatures were identified (typical of U deposits formed under low-temperature conditions), and thus these authors suggest that there is no evidence for involvement of a low-temperature fluid in the formation of the U-mineralization at OD. It is, however, possible that post- or re-depositional processes destroyed any evidence of high $\delta^{238}U$. These authors also identified a lack of fission fragment contributions, and this was explained by more recent U deposition (i.e., post the initial ~1.6 Ga age of mineralization), or episodic development of the U ores with repeated fractionation of U. Thus, the results presented by Kirchenbaur et al. (2016) support the notion of a gradual addition of U in several stages over >1000 Ma which

occurred at elevated temperatures during mineralization, and highlights the prolonged and complex processes involved in U-mineral formation at OD. This study therefore aims to document the chemical and textural variability of both coffinite and brannerite, and to interpret the results to further refine understanding of the protracted U mineralization processes involved in formation of the OD deposit.

6.3 Analytical methods

A total of 23 representative samples were analyzed, and polished thin-sections examined by scanning electron microscopy (SEM), using a Quanta 450 field emission gun (FEG) SEM with silicon-drift detector (Adelaide Microscopy, University of Adelaide). Qualitative variation in chemistry of the U-minerals was determined using SEM-energy dispersive spectroscopy (EDS).

Assays were measured to determine the bulk concentration of various elements in each sample (Macmillan et al., 2016); U_3O_8 values (Table 6.1) are of significance here. Samples selected for this study contained a range of U_3O_8 grades, as it was thought this provided the best chance of obtaining variation in the relative abundances of U-minerals. Subsequent characterization of modal mineralogy using a Mineral Liberation Analyzer (MLA) system (ALS Mineralogy, Brisbane; Appendix D and Table A1) was conducted (Macmillan et al., 2016). Bulk modal mineralogy was measured using the X-ray modal (MLA XMOD) technique. Sparse phase liberation mapping (MLA SPL_Lite) was used to specifically target U-minerals and provide information on the relative abundances of uraninite, coffinite and brannerite (Table 6.1), as well as details of all minerals found in contact with U-mineral grains (Appendix D, Table A2).

Quantitative compositional data for both brannerite and coffinite were obtained using a Cameca SX-Five electron probe micro-analyzer (EPMA) equipped with 5 tunable

wavelength-dispersive spectrometers (Adelaide Microscopy, University of Adelaide). Operating conditions were 15 keV accelerating voltage, 100 nA beam current, 40° takeoff angle, with 0.5 to 1 μm-sized beam. A total of 28 elements were measured: U, Pb, Th, Na, Mg, Al, Si, P, S, K, Ca, Ti, Mn, Fe, Cu, As, Zr, Nb, Y, Ce, La, Pr, Nd, Sm, Gd, Sr, Ba and Te. 'Probe for EPMA' software (Donovan, 2014) was used for data processing. Standards, X-ray lines, count times, mean precision and typical minimum detection limits (mdl) values are reported in the Appendix D.

Table 1.1: Sample details (ID, depth, U_3O_8 grade) with summary of coffinite and brannerite textures and relative proportions of U-minerals in each sample.

Sample ID	Sample No.	Hole ID	Depth (m)	U_3O_8 Grade (ppm)	U-Mineral Relative Abundance (wt%) [a]			Breccia Type [b]	Brannerite Group	Coffinite Group	Coffinite/Brannerite Texture Description
					Uraninite	Coffinite	Brannerite				
S1 [d]	RX7253	RD1303	471.9	21326	6	91	3	GRNH	-	A1 & B	Coffinite (collomorphic) rimming quartz, often enveloped by massive uraninite; coffinite has variable P/Y, Si, Ca (speckled); laths of bornite sometimes protrude into coffinite globules
S2 [d]	RX7254	RD1304	890.1	781	36	23	41	HEMH	C	A1	Brannerite associated with chalcopyrite and hematite; coffinite globules often discrete
S3 [c]	RX7255	RD1305	691.0	364	2	16	82	GRNL	A	A1	Needle-like brannerite often as an overgrowth on rutile grains and intergrown with fluorite/sericite/chlorite; disseminated globules of coffinite associated with siderite/hematite/quartz, in some cases these coffinite globules nucleate on chalcopyrite into quartz grains
S4 [c]	RX7256	RD1988	880.8	6914	96	0	4	HEMH	A & B	-	Bladed brannerite found surrounding rutile within sericite; blebs of brannerite with barite often found near REY-minerals (zircon/monazite)
S5	RX7257	RD1988	1618.9	597	93	7	0	HEM	-	B	Coffinitisation of uraninite crystals; fine grained "dusting" of U-minerals (in hematite)
S6	RX7258	RD1988	1768.8	408	91	8	1	HEM	-	B	Coffinitisation of uraninite crystals; fine grained "dusting" of U-minerals (in hematite)
S7	RX7259	RD1988	1808.9	369	83	14	3	HEM	-	A1 & C2	Coffinite globules found on edges of xenotime and as discrete globules nucleating on hematite in quartz; fine grained "dusting" of U-minerals (in hematite)
S8 [d]	RX7260	RD2080	479.7	1686	91	3	6	GRNL	A	A1 & C2 & C3	Coffinite globules often rimming quartz, some contain bright banding and globules often very mottled in appearance; Brannerite with sericite and hematite
S9 [c,d]	RX7261	RD3000W1	936.3	387	1	5	94	HEMH	A & C	A1 & C1	Mixture of needle-like to bladed brannerite masses in sericite and brannerite blebs associated with bornite/chalcocite/hematite; coffinite globules found on rims of brannerite masses and as discrete globules on the edge of quartz grains
S10 [c,d]	RX7262	RD3000W1	948.2	382	1	5	94	HEMH	A	C1 & C2	Needle-like to bladed brannerite masses and irregular aggregates with replacement bands; minor coffinite on edges brannerite masses; coffinite intergrown with REY-minerals
S11	RX7264	RD3002	472.4	119	89	11	0	HEM	-	A1	Fine grained discrete coffinite globules on edge quartz grains and "dusting" of U-minerals in hematite
S12	RX7265	RD3022	921.6	2244	5	13	82	HEM	A	C1	Coffinite and brannerite intimately intergrown with sericite/chlorite
S13 [d]	RX7266	RD3022	968.2	731	4	84	12	HEM	A	A1 & A2	Coffinite globules and collomorphic textures rimming quartz; in some cases galena crystals found near coffinite; some coffinite display radiating growth pattern; brannerite disseminated and associated with quartz, hematite and siderite
S14	RX7267	RD3035	675.5	1293	89	8	3	HEMH	-	A1 & B	Coffinitisation of uraninite crystals; some discrete coffinite globules on rims quartz grains in hematite
S15	RX7268	RD3035	876.8	638	8	18	74	HEM	A	A1 & C1	Coffinite rimming quartz, appears altered and is usually within sericite; disseminated coffinite globules and irregular masses of brannerite in sericite/quartz/hematite/fluorite bands
S16	RX7269	RD3035	970.5	1605	70	17	13	HEMF	A	B	Coffinitisation of uraninite crystals; brannerite in sericite/quartz/hematite/fluorite bands
S17	RX7270	RD3307	1092.8	1153	59	17	24	HEM	A	B	Coffinitisation of uraninite crystals; brannerite in sericite/quartz/hematite/fluorite bands
S18 [d]	RX7271	RD3554	455.9	424	0	44	56	GRNH	A & C	A1 & A2 & C1	Disseminated coffinite globules in quartz/sericite, sometimes associated with chalcopyrite or galena; minor coffinite globules on edges brannerite masses; needle-like to bladed brannerite masses associated with hematite and sericite; some brannerite blebs in chalcopyrite
S19 [d]	RX7272	RD3554	494.4	425	6	49	45	GRNH	A	A1 & C1	Coffinite globules in sericite/fluorite/carbonates, often nucleating on edge bornite and/or quartz; coffinite and brannerite intergrowths; fine grained REY-phosphates often near coffinite
S20	RX7273	RD3554	498.2	139	1	46	53	GRNH	C	A1	Disseminated coffinite in hematite, bornite and sericite; irregular, patches of brannerite in bornite; fine grained "dusting" of U-minerals in hematite
S21 [c]	RX7274	RD3560	716.3	11259	83	0	17	GRNL	A & D	-	brannerite blebs in hematite containing galena, hematite, bornite/chalcocite and anatase (?); some brannerite in sericite/quartz/hematite bands
S22	RX7275	RD3560	719.6	494	24	1	75	GRNL	A & D	-	Brannerite masses in sericite/quartz/hematite/fluorite bands; some brannerite blebs inside bornite
S23	RX7276	RD3560	726.7	408	56	0	44	GRNL	A & B & D	-	Brannerite masses in sericite/quartz/hematite/fluorite bands; some brannerite blebs inside bornite; brannerite blebs found along rutile lamellae in hematite (with REY-minerals; i.e., bastnasite)

Note: where <5% relative abundance of a U-mineral identified by MLA, not possible to assign U-mineral to textural group as counting statistics are too low.

a) Relative proportions of coffinite/brannerite/uraninite as determined from MLA sparse phase liberation mapping (SPL_Lite) data.

b) Breccia types: GRNH = Roxby Downs Granite (RDG; 90-70%) with some hematite (10-30%) breccia, matrix contains hematized sericite, quartz; GRNL = RDG (70-40%) with hematite (30-60%) breccia, granitic clasts with hematite-rich matrix; HEMH = Hematite (60-90%) with RDG (40-10%) breccia, hematite-rich matrix supported breccia with hematitic clasts; HEM = Hematite (>90%) with RDG (<10%) breccia, hematite-rich matrix and clasts with strong hematite alteration; HEMF = Hematite with GRV clasts, often porphyritic with chloritized phenocrysts.

c) EPMA data for this sample used for compositional range estimates of brannerite (Table 6.2).

d) EPMA data for this sample used for compositional range estimates of coffinite (Tables 6.3a and 6.3b).

6.4 Petrography

Samples were selected to ensure coverage of the broadest possible range of U-mineral associations throughout the deposit, and thus targeted a range of U_3O_8 grades and mineralogies. The samples analyzed are the same as those described in Macmillan et al. (2016).

The heterogeneous and poorly stoichiometric nature of brannerite and variability in U and Ti content, has led to the interchangeable use of the terms uraniferous anatase, -rutile, -leucoxene (and variants thereof, including uraniferous titanite and -ilmenite) by some authors (e.g., Saager and Stupp, 1983). For the purposes of consistency, the terms rutile (TiO_2-rich) and uraniferous rutile (increasing U content) are used here, since without crystal structural data, it is impossible to distinguish between the TiO_2 polymorphs and other Ti-bearing phases.

Brannerite occurrence varies from complex irregularly-shaped aggregates and anastomosing bands of uraniferous rutile-brannerite with an internal structure of randomly orientated hair-like needles and blades (Figure 6.1), to irregular masses and blebs of brannerite with more uniform-massive internal structure (Figures 6.2 and 6.3). Regardless of fabric, all brannerite is intimately intergrown with a mixture of rutile, hematite, Cu-(Fe)-sulfides, sericite, chlorite, fluorite, REY-minerals and quartz.

Coffinite also displays a broad range of textural associations although its morphology is typically globular to collomorphic. In many cases, coffinite globules completely rim quartz grains (Figure 6.4a-c), or are found nucleating onto sulfides (Figure 6.4e, f). Coffinite is also found in association with uraninite, which may include collomorphic coffinite which rims quartz and is enveloped by massive uraninite (Figure 6.5a-c); or individual early uraninite crystals which display incipient coffinitization with an aureole of coffinite around the uraninite (Figure 6.5d). In other cases, coffinite globules occur on the edge of rutile-bornite-

brannerite-sericite aggregates or are associated with REY-minerals (Figure 6.6a-d). Commonly, coffinite is found nucleating onto grain boundaries, particularly on the edges of quartz and/or sulfides. It is frequently associated with quartz, sericite, hematite and sulfides, as well as brannerite and uraninite.

Brannerite is here categorized into four distinct groups, and coffinite into three groups on the basis of petrographic characteristics (size, habit, textures and mineral associations), as well as differences in composition.

6.4.1 Brannerite petrography and textural classes

Brannerite is classified into four texturally distinct groups (hereafter, brannerite-A, -B, -C and -D). The first, brannerite-A, is variable in size (tens to hundreds of μm) and ranges in composition from what is effectively uraniferous rutile to stoichiometric brannerite. Brannerite-A displays a diverse range of morphology, including complex irregular-shaped aggregates (Figure 6.1a, b), replacement bands (Figure 6.1c), and discrete elongate seams (Figure 6.1d). The internal structure of brannerite-A ranges from randomly-orientated hair-like needles and blades to a mix of massive or bleb-like irregular masses (Figure 6.1d-f). In some cases, hematite and rutile are replaced by an anastomosing band of uraniferous rutile-brannerite (e.g., Figure 6.1c). A U-concentration gradient may be observed, with rims of higher U surrounding zones of lower U content. Likewise, some irregular aggregates of brannerite (Figure 6.1a) have fine dispersions of uraniferous rutile in the center with lower U content grading into U-rich brannerite on the rim. Fine-grained minerals commonly intergrown with brannerite-A include rutile, hematite, sericite, chlorite, fluorite and quartz (e.g., Figure 6.1). Cu-(Fe)-sulfides, hematite and rutile are often dispersed throughout the brannerite aggregates (Figure 6.1b).

Brannerite-B is generally finer grained (<5 μm) and intimately associated with barite and REY-minerals (e.g., florencite, crandallite and monazite). The barite typically contains fine disseminations of Cu-(Fe)-sulfides and also a fine dusting of galena. Blebs of brannerite-B can be found on the margins of Ti-rich hematite and TiO_2 lamallae (Figure 6.2a-c). In some cases, the brannerite has a prismatic shape similar to that of individual rutile prisms, suggesting pseudomorphic replacement (Figure 6.2c).

Brannerite-C and -D represent more irregular masses and blebs, are generally 10-50 μm in size and tend to have a more uniform or massive internal structure. These are distinct from one another but both display some association with Cu-(Fe)-sulfides. Brannerite-C is generally massive and surrounded by an alteration rim where brannerite contains elevated Si, Fe, Cu and S (based on SEM-EDS spectra; Figure 6.2d). These are either contained completely within Cu-(Fe)-sulfides (Figures 6.2d and 6.3a), or are found on the edges of Cu-(Fe)-sulfide grains (Figure 6.3b). Some Bi-sulfides (Figure 6.3a) and Ag-tellurides (Figure 6.3b) have been identified in close proximity to brannerite-C. In all cases, brannerite-C is found in association with fine-grained sericite, fluorite, chlorite and quartz (Figures 6.2d and 6.3a-b). Brannerite-D is distinct in that it is the only brannerite which contains visible inclusions of galena (Figure 6.3c-f). Neighboring hematite may, in some cases, also contains galena (Figure 6.3c, d). Irregular-shaped blebs of brannerite-D typically contain rutile clusters (possibly anatase?), patches of bornite, and hematite grains. The edges of the larger brannerite-D masses consist of more lath-like brannerite intimately intergrown with sericite/chlorite (Figure 6.3e, f).

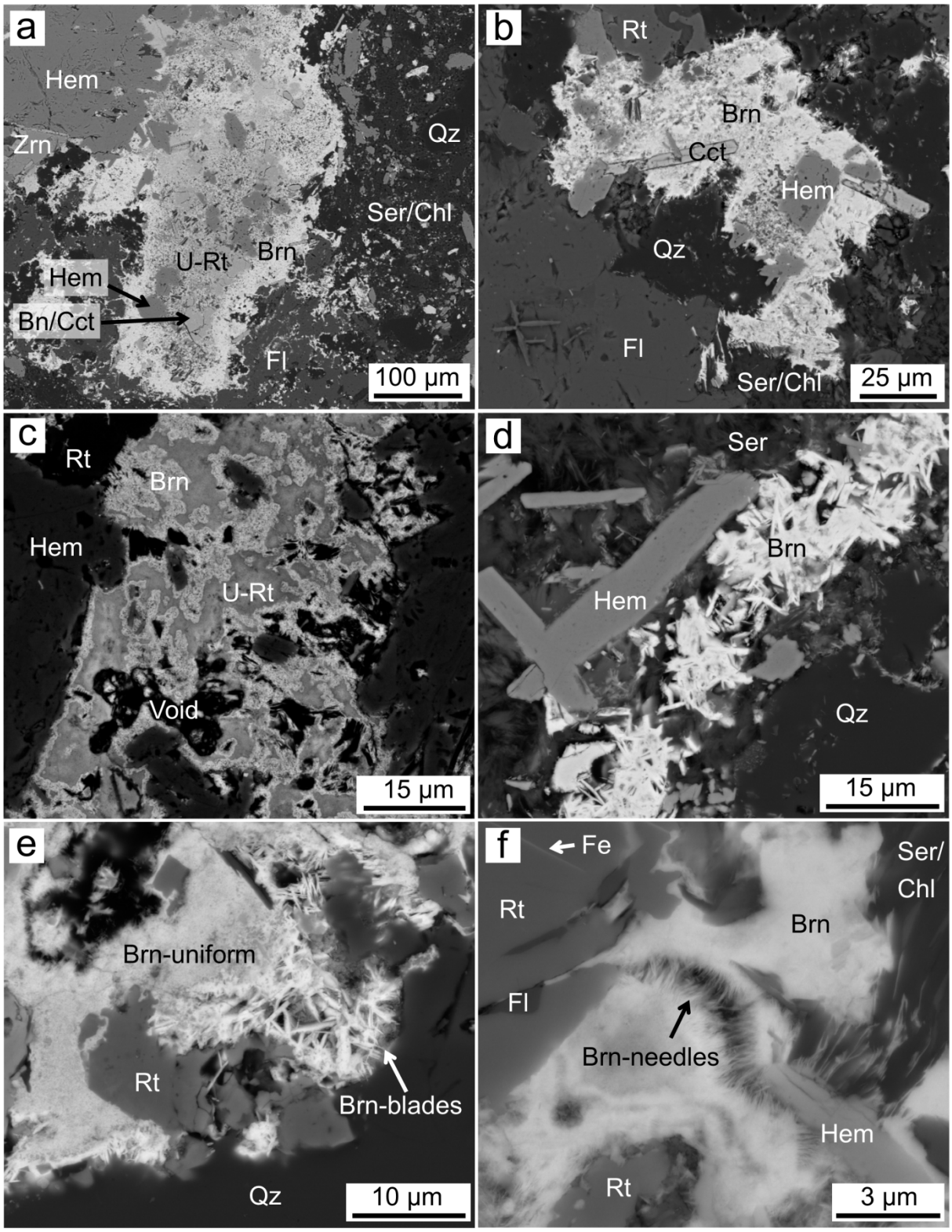

Figure 6.1: Back-scatter electron (BSE) images of brannerite-A; **(a)** irregular aggregate of brannerite (Brn, S9.91) consisting of fine dispersions of uraniferous rutile (U-Rt; central) grading to brannerite on the rim. There is an enrichment of uranium (bright) on the periphery of the aggregate. Fine-grained rutile (Rt), fluorite (Fl), sericite (Ser) and chlorite (Chl) are intergrown within the uraniferous rutile/brannerite. Grains of chalcocite (Cct),

bornite (Bn) and hematite (Hem) are contained within the aggregate. The aggregate occurs on the edge of a larger hematite mass containing fluorite and zircon (Zrn), and within a matrix of finely intergrown sericite, chlorite and fluorite, and grains of quartz (Qz), hematite and bornite; **(b)** irregular needle- to blade-shaped network of brannerite (S9.73) containing chalcocite laths, Ti-bearing hematite (Hem), and fine-grained dispersions of rutile, fluorite, sericite and chlorite. Brannerite mass is surrounded by rutile, quartz, fluorite, sericite and chlorite; **(c)** anastomosing band of uraniferous rutile-brannerite (S9.61) replacing Ti-bearing hematite which contains fine-grained sericite, chlorite and Fe-Ti phases and some unfilled cavities/holes. The reduced brightness and contrast displays a mottled U-concentration gradient, with rims of higher U content (light grey) surrounding zones of lower U content (dark grey); **(d)** network of randomly orientated needle- to blade-shaped brannerite (S9.30) within a matrix of fine-grained sericite, quartz and hematite, and some larger hematite laths and quartz grains; **(e)** needle- to blade-shaped network of brannerite (S9.79) grading into more massive brannerite, typically found on edges of irregular brannerite aggregates (like (a)); **(f)** fine hair-like needles of brannerite (S3.24) growing into a void on the edge of a Fe-bearing rutile grain. Brannerite is intimately intergrown with fluorite, sericite, chlorite and hematite.

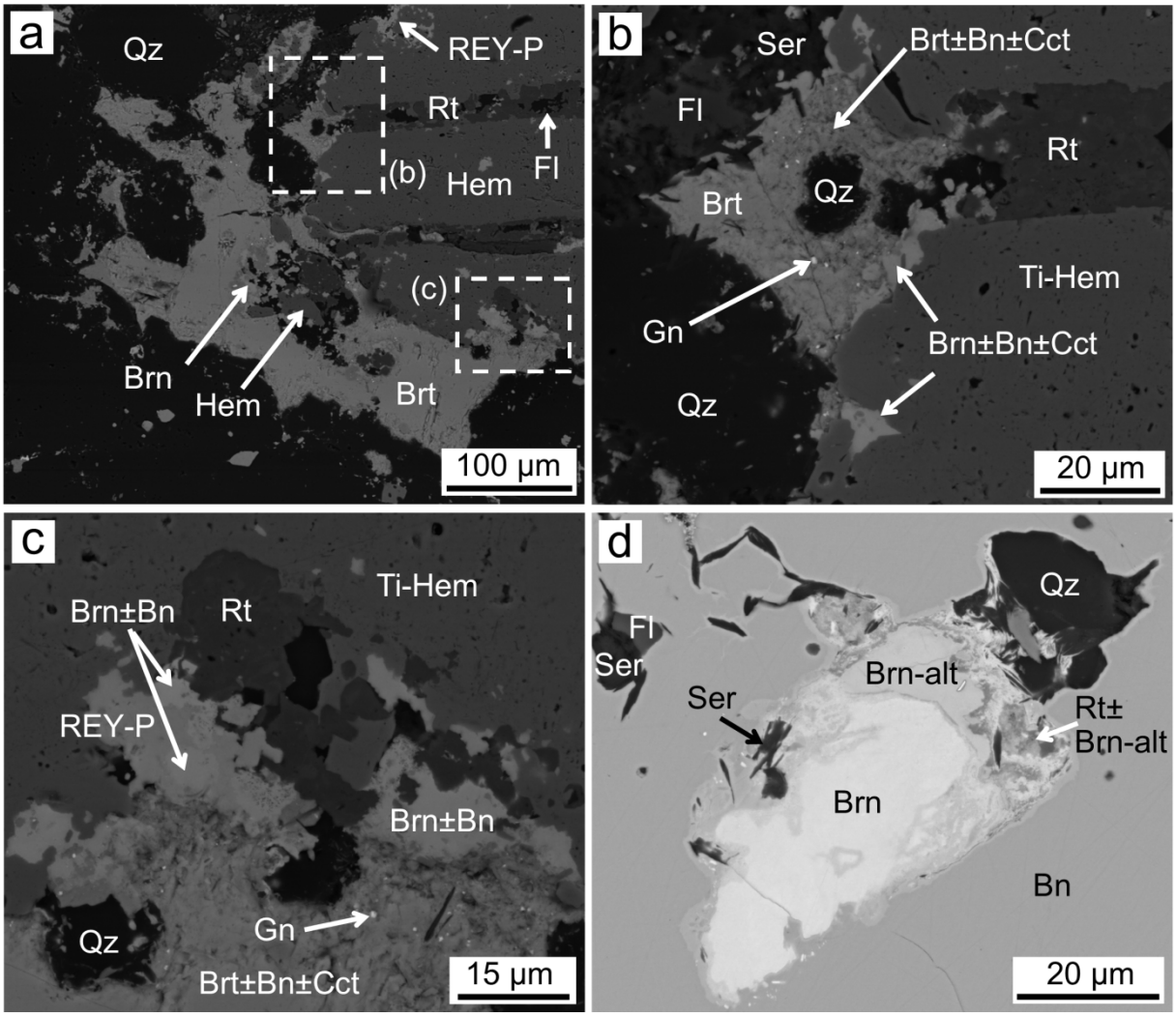

Figure 6.2: BSE images of brannerite-B and -C; **(a)** fine-grained blebs of brannerite-B (Brn, S4.33) intergrown with barite (Brt) on the edge of a hematite (Hem) grain containing rutile (Rt) lamellae. Areas outlined by white dotted boxes are enlarged in (b) and (c); **(b)** blebs of brannerite-B (S4.44) growing on margins of Ti-rich hematite (Ti-Hem) and rutile lamellae. Brannerite is intergrown with barite, bornite (Bn) and chalcocite (Cct), and there is a fine dusting of galena (Gn); **(c)** blebs of brannerite-B (S4.53) intergrown with a REY-phosphate (REY-P; florencite/crandallite?) on the edge of prismatic-grained rutile clusters. The morphology of brannerite appears to mimic the prismatic shape of some individual rutile grains. Adjacent barite contains fine-grained dusting of Cu-(Fe)-sulfides and galena (based on EDS spectra); **(d)** irregular-shaped bleb of brannerite-C (S9.23) contained within a mass of bornite/chalcocite. Cracks containing fine-grained sericite, fluorite, chlorite and quartz are found within bornite/chalcocite. An alteration rim (Brn-alt) surrounds more uniform central brannerite, where brannerite contains elevated amounts of Si, Fe, Cu and S (based on SEM-EDS spectra).

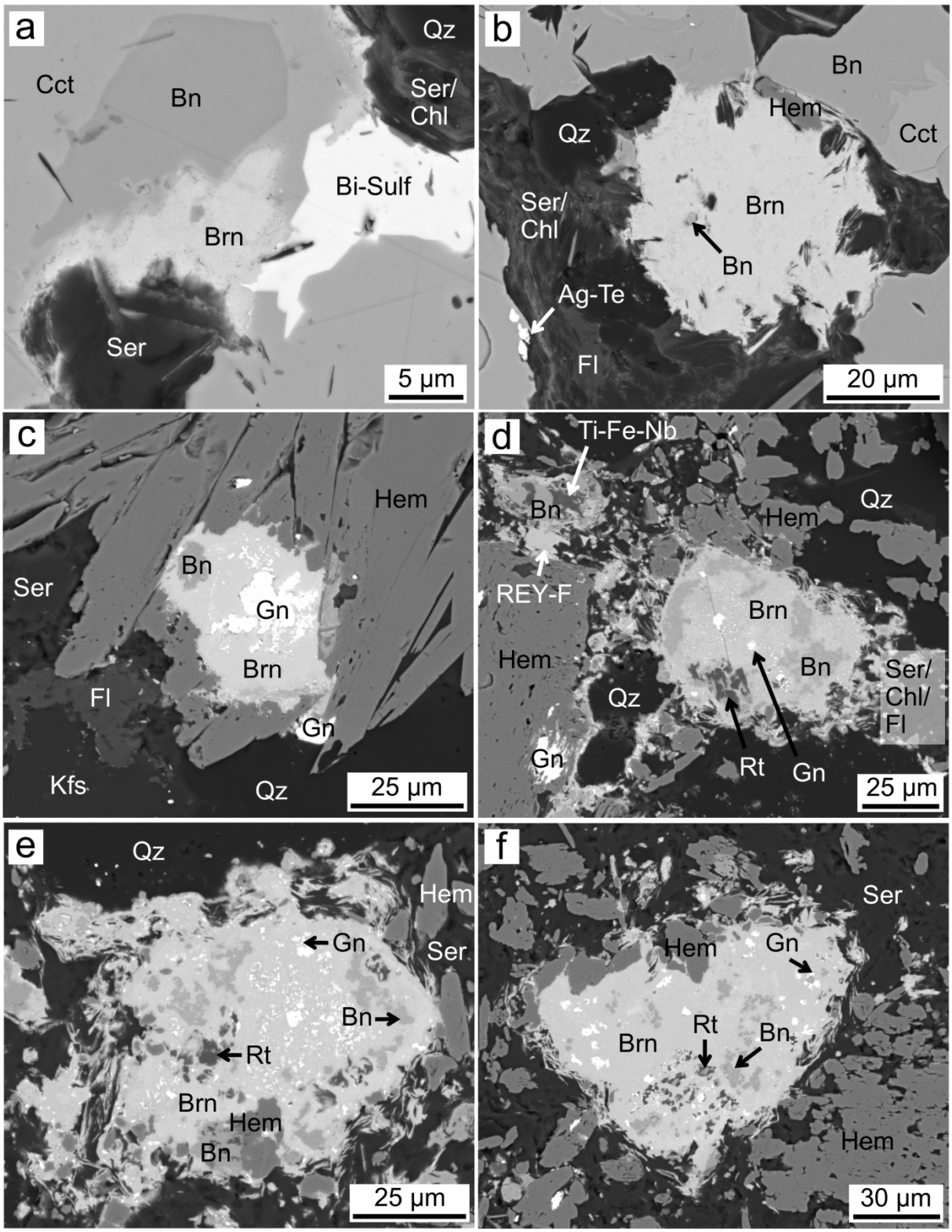

Figure 6.3: BSE images of brannerite-C and -D; **(a)** irregular-shaped bleb of brannerite-C (Brn, S9.6) found within a mass of bornite/chalcocite (Bn/Cct) and adjacent to a Bi-bearing sulfide (Bi-Sulf). The edges of brannerite appear altered (mottled appearance) and is again associated with a sericite/chlorite (Ser/Chl) mass; **(b)** irregular-shaped mass of brannerite-C (S9.15) growing on the edge of a bornite/chalcocite grain. Brannerite is within a fine-

grained sericite, chlorite, fluorite (Fl) matrix which contains quartz (Qz) grains. Silver-tellurides (Ag-Te) are also found nearby; **(c)** irregular-shaped bleb of brannerite-D (S21.92) within aggregated laths of hematite (Hem). Brannerite-D contains inclusions of galena (Gn) and bornite. Galena is also observed within the hematite laths. Surrounding minerals include: sericite, fluorite, K-feldspar (Kfs) and quartz; **(d)** irregular-blebs of brannerite-D (S21.110) found within a band of intergrown sericite, chlorite and fluorite. Brannerite contains rutile and hematite clusters, as well as patches of bornite. There are numerous patches and specks of galena within both the brannerite and neighboring hematite; **(e)** an irregular-bleb of brannerite-D (S21.114) containing peripheral bornite and hematite grains. Galena is present in the form of larger inclusions and as a fine-dusting within the brannerite. Rutile clusters (possibly anatase?) and patches of bornite can also be seen within brannerite. The edges of the larger brannerite mass consist of more lath-like brannerite which is intimately intergrown with sericite/chlorite; **(f)** irregular mass of brannerite-D (S21.98) again containing patches of bornite, rutile clusters and inclusions of galena. The edges of the main brannerite mass consist of lath-like brannerite which is intergrown with chlorite/sericite, and there are some larger grains of hematite.

6.4.2 Coffinite petrography and textural classes

Coffinite is classified into three distinct groups (hereafter, coffinite-A, -B and -C). There are a number of distinct mineral association and textural differences within these broader groups. These are identified in the following by a numbered suffix (i.e., A1, A2, C1, C2 and C3). All coffinite is found in association with quartz (i.e., often grows on the periphery of quartz) and hematite, and is typically globular to collomorphic in appearance.

The majority of identified coffinite belong to groups -A, and -B. Coffinite-A ranges from discrete globules to collomorphic bands which completely encompass quartz grains (Figure 6.4a-c). Individual coffinite-A globules are 2-10 μm in size, and the collective collomorphic coffinite-A + quartz aggregates range in size from 20 to 100 μm (Figure 6.4a-c). The coffinite-A1 subtype is always associated with or nucleating onto Cu-(Fe)-sulfides (Figure

6.4e), whereas subtype A2 is found with galena (Figure 6.4c, d and f). Globules of coffinite-A are chemically heterogeneous (mottled appearance) and usually contain Si-rich bands of coffinite closest to the quartz grain into which they grow (Figure 6.4b).

Coffinite-B is always found in association with uraninite, and includes collomorph coffinite rimming quartz, which is in turn enveloped by massive uraninite (Figure 6.5a-c), and also aureoles of coffinite surrounding individual uraninite crystals with incipient coffinitization (Figure 6.5d). Collomorph coffinite-uraninite intergrowths are typically hundreds of μm in size, with individual coffinite globules 2-10 μm in diameter. The enveloping massive uraninite typically is speckled with high-Pb uraninite (Figure 6.5b-c). Bornite needles and grains can be found within both coffinite and uraninite. Coffinite-B displays compositional heterogeneity; darker (on BSE images), more uniform, Si±P-enriched zones generally occurring along the rims of quartz grains and where the coffinite is fractured. The brighter coffinite-B is more mottled in appearance than the Si-rich coffinite; the higher U content considered responsible for this difference in contrast. The other main sub-type of coffinite-B is found on the edges of uraninite crystals where incipient coffinitization has occurred (Figure 6.5d). The coffinite is usually found in patches or as an aureole on the rim of the uraninite-bornite grains.

Coffinite-C includes three subtypes -C1, -C2, and -C3. Broadly, coffinite-C is defined as being associated with brannerite or REY-minerals, with individual globules typically 2-10 μm in diameter. In some cases, coffinite-C globules coalesce forming a string of almost collomorphic coffinite (Figure 6.6a). Coffinite-C1 is defined as being associated with, or nucleating onto brannerite, and grows between the edge of rutile-bornite-brannerite-sericite aggregates and quartz (Figure 6.6a, b). Globules of coffinite-C1 often contain needles of chlorite and/or sericite (Figure 6.6c). In some cases, discrete globules of coffinite-C1 are

found at the peripheries of larger brannerite-A aggregates (Figure 6.1a). Coffinite-C2 and -C3 are both associated with REY-minerals (Figure 6.6d), with -C2 often exhibiting finger-like growth into REY-minerals, whereas -C3 contains distinct bright banding when the brightness and contrast of the BSE image are reduced.

Generally, the rounded edge of individual coffinite grains is typically found within quartz, and the flattened edge of the globule is always found along the grain boundary of quartz or any mineral (i.e., sulfide, brannerite, or uraninite) onto which the coffinite nucleates (e.g., Figures 6.4d, e and 6.5c). Moreover, individual coffinite globules often appear to have a radiating-fibrous internal structure, and growth appears to occur into quartz grains (Figure 6.4d).

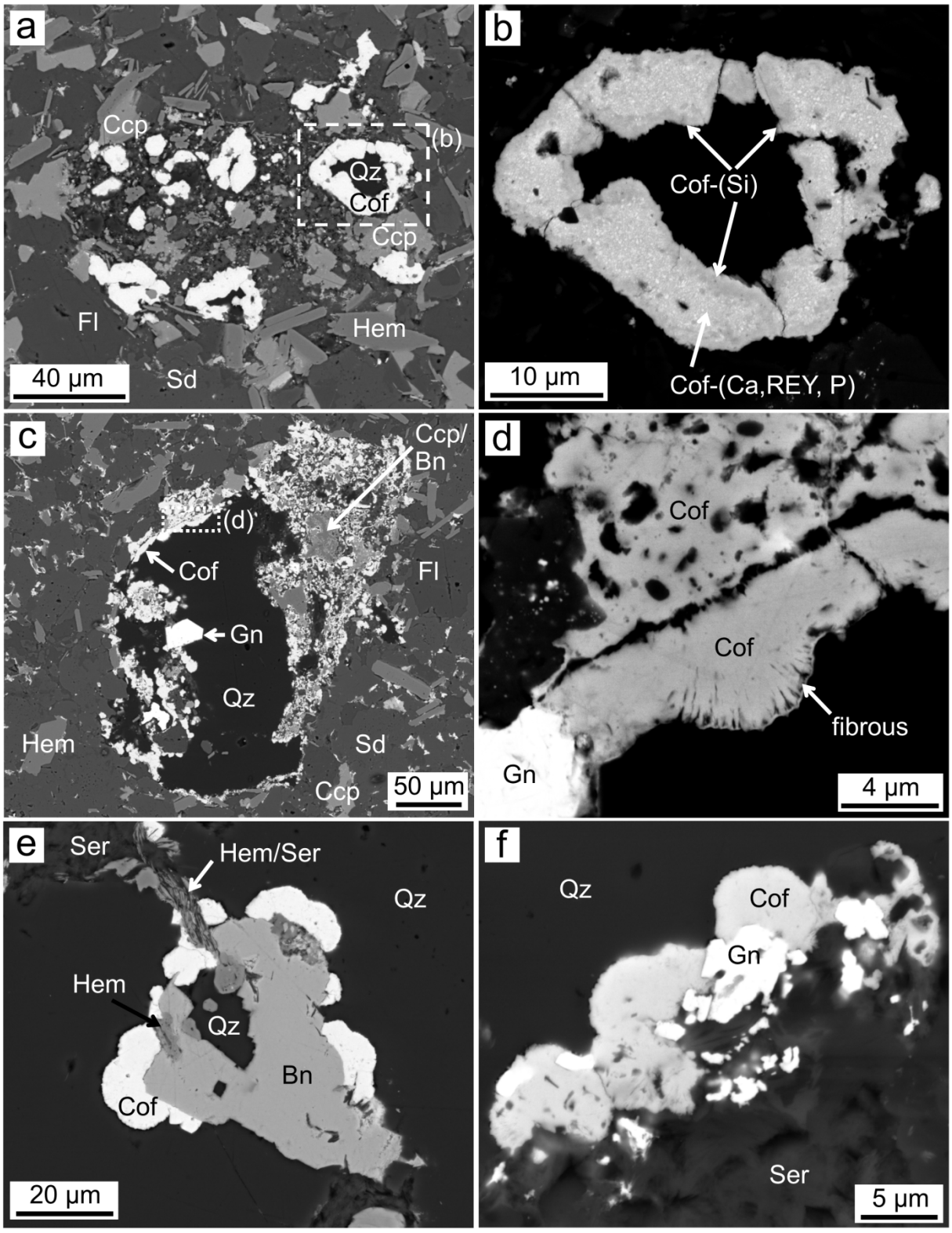

Figure 6.4: BSE images of coffinite-A subtypes; **(a)** coffinite-A1 (Cof; S13.8) rimming quartz (Qz) in a matrix of siderite (Sd), fluorite (Fl), chalcopyrite (Ccp) and hematite (Hem). Area outlined by white dotted box is enlarged in (b); **(b)** coffinite-A1 (S13.9) rimming quartz with reduced brightness and contrast to display chemical heterogeneity (mottled appearance) within coffinite globules and Si-rich coffinite (Coff-(Si); duller)

closest to quartz grain and Ca/REY/P-rich coffinite [Cof-(Ca,REY,P); brighter]; **(c)** coffinite-A2 (S13.15) globules and dendrites with galena (Gn), hematite and chalcopyrite grains rimming quartz. Surrounding minerals include: fluorite, siderite and hematite. Area outlined by white dotted box is enlarged in (d); **(d)** enlargement of coffinite-A2 globules (S13.29) and galena grains with reduced brightness and contrast to display more uniform appearance of coffinite and radiating-fibrous internal structure of individual coffinite grain. It appears that growth of coffinite has occurred into the quartz grain; **(e)** globules of coffinite-A1 (S19.105) nucleating onto the edges of a bornite grain into quartz. Some fine-grained brannerite-sericite contained on edges of bornite grain. The flattened edge of the coffinite-A1 globules on the periphery of the bornite grain implies nucleation onto the sulfide, and growth into the quartz grain; **(f)** coffinite-A2 globules associated with galena (S18.43) growing along the boundary of quartz-sericite (Ser).

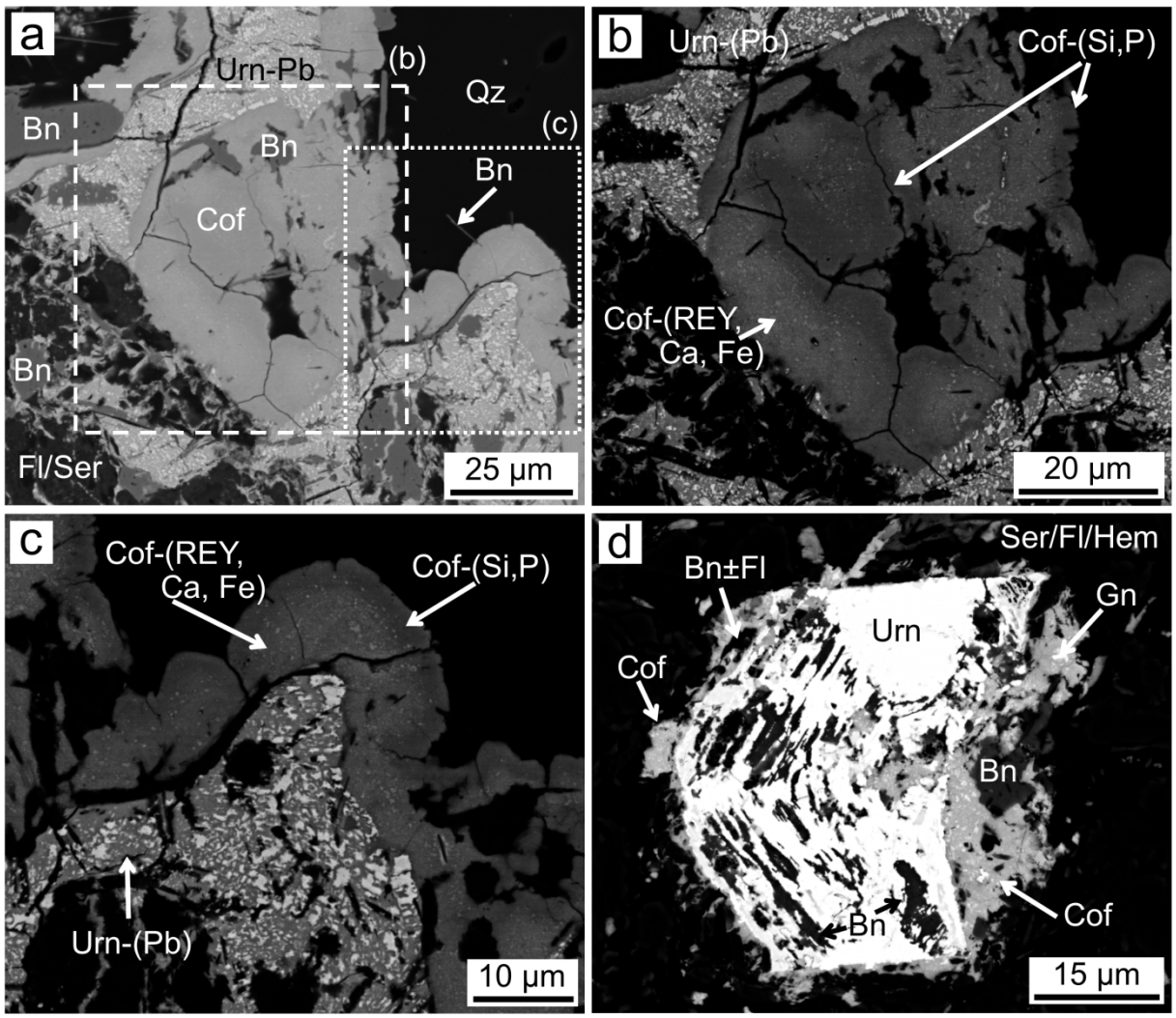

Figure 6.5: BSE images of coffinite-B; **(a)** collomorphic coffinite-B (Cof; S1.5) rimming quartz (Qz) grains. Coffinite-B is encompassed by massive uraninite enriched in Pb (Urn-(Pb)). Bornite (Bn) needles and grains found within both coffinite and uraninite. Matrix material consists of fluorite (Fl), siderite (Sd) and sericite (Ser). Areas outlined by white dotted boxes are enlarged in (b) and (c); **(b)** close-up of collomorphic coffinite-B (S1.6) with reduced brightness and contrast to display compositional variability within coffinite-B and uraninite. Bright regions in uraninite are Pb-rich. Darker, more uniform zones within coffinite are unusually enriched in Si and P (Cof-(Si,P)). Some of the brighter coffinite (Cof-(REY,Ca,Fe)) is more mottled in appearance and has higher ΣREY, Ca and Fe than the Si-rich coffinite; **(c)** close-up of collomorphic coffinite-B (S1.9) again with reduced brightness and contrast to highlight that the coffinite enriched in Si and P (darker) generally occurs along the rims of quartz grains and where the coffinite is cracked; **(d)** aureole of coffinite-B around uraninite-bornite crystal (S17.37) contained in a matrix of

hematite (Hem), quartz and sericite grains. Coffinite appears mottled in appearance and contains some specks of galena (Gn).

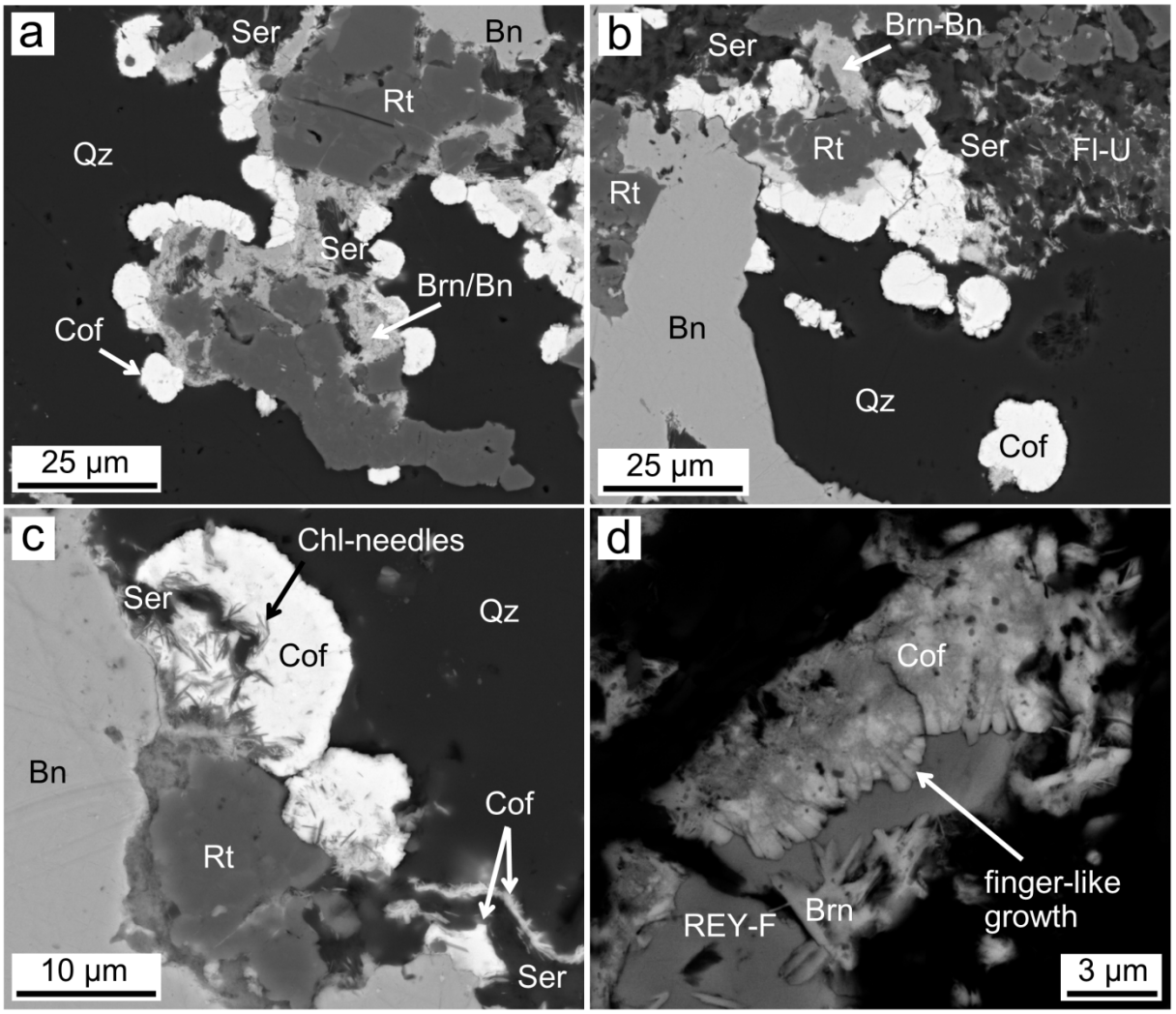

Figure 6.6: BSE images of coffinite-C subtypes; **(a)** discrete coffinite-C1 globules (Cof, S19.103) growing between the edge of a rutile-bornite-brannerite-sericite (Rt-Bn-Brn-Ser) aggregate and quartz (Qz) grain; **(b)** coffinite-C1 globules (S19.96) nucleating onto brannerite-rutile aggregates, bornite and holes within quartz. Brannerite is intimately intergrown with bornite ± fluorite (Fl) ± sericite; **(c)** close-up of an individual coffinite-C1 globule (S19.97) nucleating onto bornite-brannerite-rutile-sericite aggregate. Needles of chlorite (Chl) and/or sericite are enclosed within the coffinite-C1 globule; **(d)** coffinite-C2 globules (S10.40) intimately associated with a REY-fluoride mineral (REY-F; bastnäsite/synchysite). Reduced brightness and contrast reveals internal chemical heterogeneity and radiating finger-like structure.

6.4.3 Associations and distribution of coffinite and brannerite

A total of 23 samples were analyzed in this study; each sample contains different relative abundances of uraninite, coffinite and brannerite (Table 6.1). Samples which contained the most brannerite (94%) relative to all U-minerals were typically dominated by brannerite-A. The latter was identified in 15 samples, whereas brannerite-B, -C and -D were found in only 2, 4 and 3 samples, respectively. Thus brannerite-A occurs within the broadest range of samples in terms of depth, rock type and grade (Table 6.1). Comparatively, the most coffinite contained in any one sample was 91% of all U-minerals, with coffinite-A being dominant (occurs within 13 samples). Coffinite-C1 and -B were found in 6 samples each, with coffinite-C2 and C3 only occurring in a minority of samples.

MLA data can be used to understand what minerals are found in association with either brannerite or coffinite. For example, where a wt% value is given for mineral-A found in association with brannerite, this represents the wt% of mineral-A found in association with the total surface wt% of brannerite. Overall, the minerals found in direct contact with either brannerite or coffinite do not change among the sample suite, but the relative proportions of individual components within the associations can be used to highlight some differences between the different groupings (Figures 6.7 and 6.8; Appendix D, Table A2). The dominant minerals found in association with brannerite are hematite (29-38 wt%), sericite/chlorite (21-31 wt%) and quartz (10-24 wt%). Brannerite-A is also commonly associated with carbonate, fluorite, Ti-minerals and sulfides (5 wt% each). Brannerite-B has the highest association with quartz and sericite/chlorite (combined total of 55 wt%) of all brannerite groups. The highest association of any brannerite group with sulfides is for brannerite-C (24 wt%), and brannerite-D has the highest association (7 wt%) with Pb-minerals (dominantly galena but also minor

cerussite, clausthalite and altaite). The relative proportion of other U-minerals (coffinite and uraninite) found in grain contact with brannerite is usually fairly low (up to 1.5 wt%).

Coffinite was predominantly associated with hematite (28-45 wt%), quartz (12-30 wt%), and sericite/chlorite (9-22 wt%). The association of coffinite with sulfides is reasonably consistent between groups (approximately 4-7 wt%). Coffinite-B has the highest relative association with fluorite (13 wt%) and K-feldspar (7 wt%) of any coffinite group, and coffinite-A has the highest association with carbonates (7 wt%). The relative proportion of other U-minerals (brannerite and uraninite) found in contact with coffinite is often high (up to 5 wt% brannerite and 2 wt% uraninite), highlighting the fact that coffinite is often found peripheral to, and replacing, other U-minerals.

The distribution of brannerite and coffinite shows no discernable zonation trend with lithology or sulfide zoning. Both minerals can be found at any depth within the deposit (i.e., brannerite/coffinite can be found in both shallow and deep samples; Table 6.1). They can be found within a single drillhole, but their abundance and type does vary with depth. For example, in one of the deepest drillholes (RD1988; Table 6.1), brannerite-A and -B is found in the shallowest sample (S4, ~880 m), coffinite-B is found at depths between 1620 to 1770 m (S5 and S6), and coffinite-A1 and -C2 are found in the deepest (~1800 m) sample (S7). In another drillhole (RD3035), coffinite-A1 and -B are found at a depth of ~375 m (S14), and the two deeper samples (S15 and S16) contain both brannerite-A and a mixture of coffinite-A1, -B and -C1.

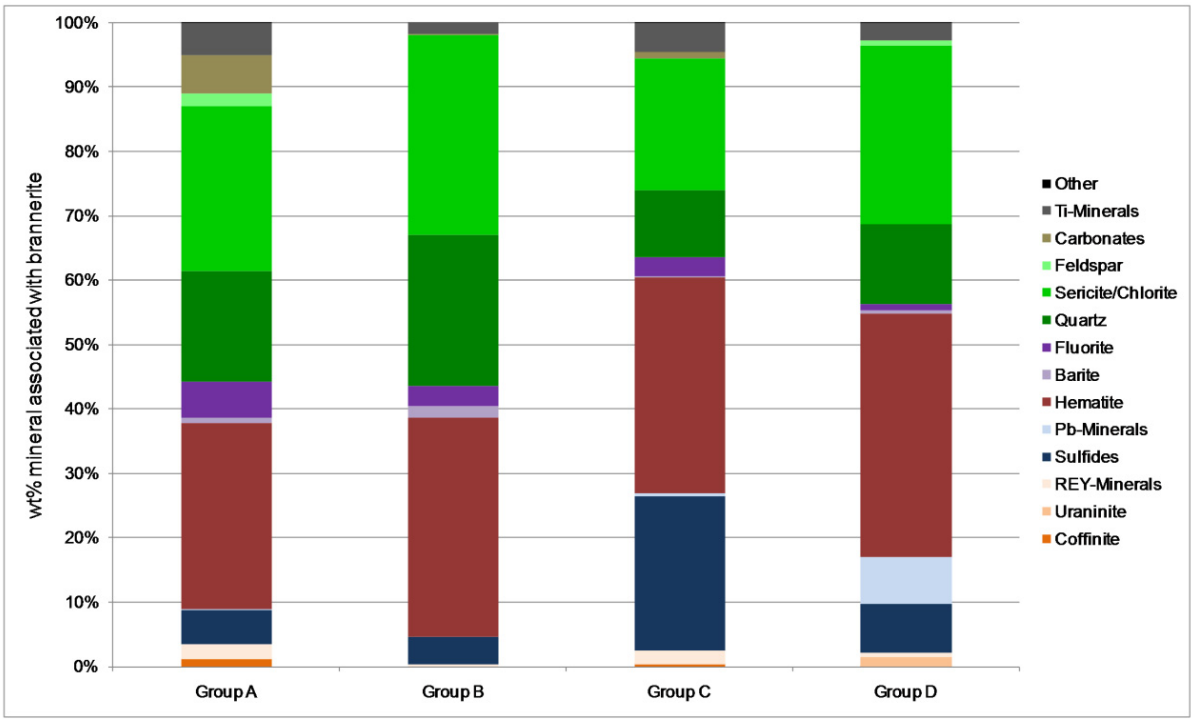

Figure 6.7: Column chart displaying wt% of various minerals in association with brannerite (MLA data; Appendix D, Table A2). The association data for each brannerite group have been averaged for all samples containing that particular brannerite as identified in Table 6.1.

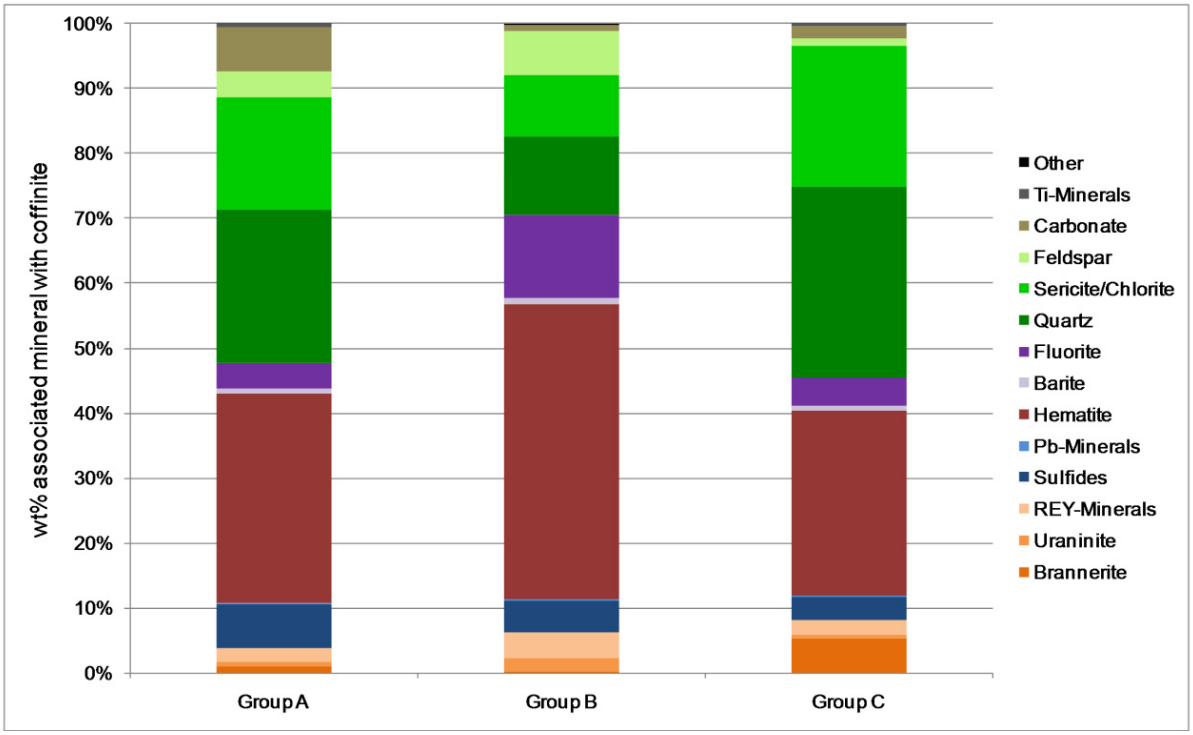

Figure 6.8: Column chart displaying wt% of various minerals in association with coffinite (MLA data; Appendix D, Table A2). The association data for each coffinite group have been averaged for all samples containing the particular coffinite as identified in Table 6.1.

6.5 Compositional data

6.5.1 Data presentation and formulae calculation

All 23 samples were analyzed by SEM and EPMA. Data filtering was undertaken to remove individual analyses which did not correspond to compositionally homogenous brannerite or coffinite. For brannerite, points which had >50 wt% TiO_2, >10 wt% Fe_2O_3 or SiO_2, >5 wt% CaO, >4 wt% Cu_2O and >2 wt% ZrO_2, BaO, SO_3, PbO or P_2O_5 were excluded, as were those with <25 wt% TiO_2 or <30 wt% UO_2. A similar filtering process was used for coffinite analyses, where points which had >25 wt% SiO_2, >10 wt% Fe_2O_3, >5 wt% CaO, >4 wt% Cu_2O, BaO or SO_3, >2 wt% PbO or Al_2O_3, and >1 wt% TiO_2, were excluded, as were those with <45 wt% UO_2 or <10 wt% SiO_2. Anomalous concentrations of these components are attributable to mineral impurities and fine-grained intergrowths or inclusions with various minerals.

Clean spot analysis proved difficult to obtain. The main factors contributing to data rejection were: i) brannerite and/or coffinite was too fine-grained; ii) brannerite and coffinite were finely intergrown; iii) brannerite/coffinite grains contained inclusions of REY-minerals, galena, hematite, rutile, Cu-(Fe)-sulfides, barite or various silicates; and iv) grains had incipient branneritization or coffinitization, or had partially altered rims. Grains displaying one or more of these features yielded poor analytical totals (typically <85%), and these analyses were rejected. Moreover, for both brannerite and coffinite, variability in analytical totals is likely due to a combination of metamictization, amorphization and/or hydration (Lumpkin et al., 2012). A total of 395 brannerite analyses and 380 coffinite analyses were however deemed acceptable. Means, standard deviations and minimum/maximum values are reported in Tables 6.2, 6.3a and 6.3b.

Selection of compositionally homogeneous areas for EPMA analysis proved difficult, not only due to the fine-grained nature of the minerals themselves but also since there is chemical heterogeneity within individual grains. This heterogeneity is highlighted by significant variation in grey-scale within brannerite (Figures 6.1a,c and 6.2d), and coffinite (Figures 6.4b and 6.5b-c).

A variety of different methods were employed to discriminate between different brannerite/coffinite groups, and included comparison based solely on chemistry, where cluster analysis was used to distinguish different groups. Although this proved moderately successful, it did not take any of the valuable textural data into account. Thus, discrimination of different groups of brannerite and coffinite was made based on their mode of occurrence (habit, associated minerals etc.) and any key distinguishing features (e.g., internal banding). EPMA data has been reported as mean analyses (Tables 6.2, 6.3a and 6.3b) for the entire population, and also as mean analyses for key identified textural groups. Since each group occupies a compositional range, minimum, maximum and standard deviation values are included in the tables. In some cases, concentrations of one or more elements were <mdl in individual spot analyses. A value of half the individual spot analysis mdl was utilized for calculation of the mean, for all subsequent statistical analysis, *apfu* calculations and data plotting.

The *apfu* calculations for brannerite require several critical assumptions: i) a basis of 6 O atoms and AB_2O_6 stoichiometry; ii) cation valencies and site allocations (A vs. B) given in Table 6.2 are correct; iii) S^{6+}, Cu^{+}, P^{5+} are omitted since these elements are probably restricted to nanoscale inclusions; iv) 74% of U is present as U^{6+} (see below); v) Fe, As are present in oxidized form i.e., as Fe^{3+} and As^{5+}; vi) Fe^{3+} and REY^{3+} are assumed to be contained in brannerite and no correction has been made for any Fe present within Cu-(Fe)-sulfide

inclusions or REY hosted by REY-mineral inclusions; and vii) any anion substitution (e.g., F^-, $(OH)^-$ or $(CO_3)^{2-}$ for O^{2-}) is insignificant. To highlight the chemical variability between brannerite groups, total cations, as well as A- and B-site cation totals have been included in the tables.

For coffinite, the key *apfu* calculation assumptions included: i) a basis of 4 O atoms and a mineral stoichiometry of ABO_4; ii) cation valencies and site allocations (A vs B) given in Tables 6.3a and 6.3b are correct; iii) Cu^+ is omitted since it is probably restricted to nanoscale inclusions of Cu-(Fe)-sulfides; iv) 43.6% of U is present as U^{6+} (see below); v) Fe is present as Fe^{2+} since it likely occupies the A-site and there are known charge balance mechanisms which use Fe^{2+} rather than Fe^{3+} (see below); vi) S^{6+} and Fe^{2+} are assumed to be contained in coffinite, and no correction has been made for any S or Fe contained within Cu-(Fe)-sulfides; and vii) any anion substitution (e.g., F^-, $(OH)^-$ or CO_3^{2-} for O^{2-}) is insignificant. To highlight the chemical variability between coffinite groups, in addition to the total cations and A- and B-site cation totals, values for A/B, ΣREY and (P+As+Nb) are included in the tables. When discussing compositional variability of brannerite or coffinite below, Y is combined with the other REE (ΣREY), but in the case of coffinite, where Y is typically much higher, the REE and Y contents have sometimes been separated.

6.5.2 Chemical composition of brannerite

Table 6.2 gives means and compositional ranges for each brannerite class. The mean composition for all brannerite analyzed in this study (n=395) is 41.13 wt% UO_2, 34.34 wt% TiO_2, 4.14 wt% SiO_2, 1.96 wt% CaO, 4.83 wt% Fe_2O_3, 0.69 wt% Na_2O, 0.77 wt% Nb_2O_5, 2.85 wt% ΣREY_2O_3 and 0.40 wt% PbO, with a mean analytical total of 94.90 wt%.

Calculated formulae were initially derived by normalization to 6 O atoms, but cation totals typically ranged between 2.85 and 3.24, rather than the ideal 3.0. Only 122 of 395 analyses

had a cation total in the range 2.95-3.05. A method was thus devised to see whether allocation, by iteration, of some U^{4+} to U^{6+} might improve these cation totals. It was found that if 74% of total U was assumed to be U^{6+}, then 73% of analyses (291 of 395) would have cation totals within an acceptable range. This assumption seems plausible given that brannerite compositional analyses by wet chemical methods (e.g., Pabst, 1954; Whittle, 1954) yield approximately 75% U as UO_3, with the remainder as UO_2. More recently, multiple U valencies (U^{4+}, U^{5+} and U^{6+}) have been identified in brannerite (e.g., Finnie et al., 2003; Vance et al., 2015), further supporting the validity of the multiple U valence assumption.

In terms of site occupancy for brannerite, the A-site typically contains 0.37-0.71 *apfu* U^{4+}+U^{6+}, and up to 0.46 *apfu* other cations, which includes a maximum of 0.32 *apfu* Ca^{2+} and 0.24 *apfu* ΣREY^{3+} (Table 6.2). Similarly, the B-site typically contains 1.23-2.04 *apfu* Ti^{4+}, and up to 1.16 *apfu* other B-site cations, including a maximum of 0.52 *apfu* Si^{4+}, 0.43 *apfu* Fe^{3+}, 0.23 *apfu* Na^{+}, 0.13 *apfu* Al^{3+} and 0.12 *apfu* Mg^{2+}. The A-site cation totals range between 0.46-1.01 *apfu*, with a mean of 0.79 *apfu*; whereas the B-site cation totals range between 2.01-2.58 *apfu*, with a mean of 2.23 *apfu*. However, total cations (A+B) tend to range between 2.92-3.30 *apfu*, with a mean of 3.02. The marked deviation from ideal 1.0 *apfu* A-site and 2.0 *apfu* B-site totals indicates there is significant replacement within both sites, with charge compensation and possibly, also vacancies (see below). For each brannerite class, an empirical formula can be given based on mean composition (Table 6.2):

Brannerite-A: $[U_{0.56}Ca_{0.12}REY_{0.05}M^{*}_{0.01}]_{0.75}[Ti_{1.58}Si^{*}_{0.26}Fe^{*}_{0.27}Nb^{*}_{0.03}N^{*}_{0.15}]_{2.29}O_6$

Brannerite-B: $[U_{0.61}Ca_{0.16}REY_{0.08}M^{*}_{0.02}]_{0.86}[Ti_{1.58}Si^{*}_{0.21}Fe^{*}_{0.20}Nb^{*}_{0.05}N^{*}_{0.06}]_{2.10}O_6$

Brannerite-C: $[U_{0.61}Ca_{0.11}REY_{0.06}M^{*}_{0.02}]_{0.81}[Ti_{1.56}Si^{*}_{0.26}Fe^{*}_{0.23}Nb^{*}_{0.03}N^{*}_{0.07}]_{2.14}O_6$

Brannerite-D: $[U_{0.54}Ca_{0.14}REY_{0.14}M^{*}_{0.04}]_{0.86}[Ti_{1.55}Si^{*}_{0.30}Fe^{*}_{0.20}Nb^{*}_{0.04}N^{*}_{0.04}]_{2.13}O_6$

where M^* = Σ(Sr,Ba,Pb,Th), Si^* = Σ(Si,Zr), Fe^* = Σ(Fe,Al), Nb^* = Σ(Nb,As) and N^* = Σ(Mg,Mn,K,Na). The mean formula for all analyses can be given as:

$$[U_{0.56}Ca_{0.13}REY_{0.08}M^*_{0.02}]_{0.79}[Ti_{1.57}Si^*_{0.27}Fe^*_{0.25}Nb^*_{0.03}N^*_{0.11}]_{2.23}O_6$$

In comparison with this average, brannerite-B and -C (Figures 6.2 and 6.3a-b) contain the highest U (0.61 *apfu*). The highest M^* and ΣREY values of 0.04 and 0.14 *apfu*, respectively, are noted for brannerite-D (Figure 6.3c-f). Ca is highest in brannerite-B (0.16 *apfu*; Figure 6.2a-c) Thus, brannerite-B and -D have the highest A site totals (both 0.86 *apfu*). The ideal A-site total is 1.0 *apfu*, therefore these low A-site totals highlight a deficiency in A-site cations. All brannerite types have similar Ti contents (1.55-1.58 *apfu*), with the highest Si^* content for brannerite-D (0.30 *apfu*), and lowest for brannerite-B (0.21 *apfu*). All other B-site cations for the different brannerite types contain variable amount of other impurities; Fe^* and N^* are highest in brannerite-A (0.27 and 0.15 *apfu*, respectively), and Nb^* the highest for brannerite-B (0.05 *apfu*). B-site totals deviate from the ideal 2.0, ranging between 2.10 (brannerite-B) to 2.29 (brannerite-A), highlighting that B-site cation totals are commonly in excess.

Table 6.2: Electron probe microanalytical data for brannerite.

Type	All data				A				B				C				D			
Valid N (analyses)	395				250				22				9				114			
(wt%)	Mean	Min	Max	SD	Mean	Min	Max	SD	Mean	Min	Max	SD	Mean	Min	Max	SD	Mean	Min	Max	SD
UO_2	41.13	30.50	48.74	4.44	41.58	30.50	48.74	5.16	43.11	40.19	44.28	0.93	43.83	36.38	45.98	3.34	39.54	35.05	43.97	2.20
TiO_2	34.34	25.95	49.94	3.91	34.79	25.95	49.94	4.84	33.25	32.49	33.92	0.35	33.41	32.57	35.11	0.77	33.66	31.07	35.23	0.72
Na_2O	0.69	0.05	1.88	0.45	0.96	0.26	1.88	0.33	0.33	0.09	0.83	0.17	0.35	0.06	0.62	0.22	0.19	0.05	0.50	0.09
MgO	0.11	<mdl	1.37	0.15	0.16	0.03	1.37	0.17	0.03	0.02	0.04	-	0.07	<mdl	0.13	0.05	0.02	<mdl	0.04	-
Al_2O_3	0.35	0.05	2.08	0.26	0.38	0.14	2.08	0.31	0.11	0.05	0.25	0.05	0.25	0.12	0.73	0.18	0.34	0.20	0.86	0.07
SiO_2	4.14	2.01	8.40	1.07	4.01	2.46	8.26	0.96	3.11	2.01	5.69	0.88	3.99	2.01	6.80	1.49	4.65	3.07	8.40	1.08
P_2O_5	0.08	<mdl	1.70	0.15	0.13	<mdl	1.70	0.17	<mdl	<mdl	<mdl	-	0.05	<mdl	0.11	0.04	<mdl	<mdl	0.09	-
SO_3	0.09	<mdl	1.76	0.18	0.05	<mdl	1.00	0.11	0.39	<mdl	1.76	0.50	<mdl	<mdl	0.10	0.03	0.12	<mdl	0.78	0.12
K_2O	0.13	<mdl	0.78	0.12	0.18	0.05	0.78	0.12	0.03	<mdl	0.09	0.02	0.08	<mdl	0.12	0.05	0.03	<mdl	0.10	0.02
CaO	1.96	0.59	4.81	0.75	1.85	0.66	4.81	0.83	2.34	1.21	3.00	0.37	1.70	0.59	2.44	0.57	2.15	0.80	3.33	0.56
MnO	0.21	0.05	0.48	0.06	0.20	0.06	0.48	0.05	0.25	0.16	0.31	0.04	0.21	0.14	0.27	0.04	0.23	0.05	0.41	0.07
Fe_2O_3	4.83	2.39	9.89	1.30	5.41	2.39	9.89	1.25	4.12	2.79	7.23	1.03	4.45	3.36	6.07	0.77	3.74	3.10	4.84	0.37
Cu_2O	1.21	<mdl	3.77	0.85	1.56	0.24	3.77	0.79	0.91	0.29	1.67	0.31	2.17	1.06	3.22	0.89	0.44	<mdl	2.43	0.38
As_2O_5	0.28	<mdl	1.21	0.25	0.30	<mdl	1.21	0.17	0.99	0.67	1.19	0.11	0.55	0.31	1.03	0.30	0.10	<mdl	0.18	-
SrO	0.13	<mdl	0.42	0.09	0.08	<mdl	0.42	0.04	0.10	0.06	0.30	0.05	0.05	<mdl	0.07	-	0.24	0.09	0.36	0.06
ZrO_2	0.49	0.10	1.96	0.28	0.45	0.10	1.96	0.24	0.30	0.20	0.37	0.04	0.47	0.16	0.79	0.29	0.60	0.18	1.53	0.35
Nb_2O_5	0.77	0.30	1.65	0.33	0.58	0.41	1.20	0.14	0.50	0.30	0.58	-	0.51	0.39	0.60	-	1.23	0.87	1.65	0.12
BaO	0.40	<mdl	1.99	0.34	0.20	<mdl	1.99	0.15	0.44	0.26	1.29	0.23	0.56	0.13	1.30	0.44	0.83	0.51	1.55	0.22
Y_2O_3	1.22	0.36	3.75	0.95	0.76	0.36	3.29	0.58	0.93	0.84	1.02	-	0.91	0.48	2.08	0.48	2.30	1.11	3.75	0.86
La_2O_3	0.17	0.11	0.79	-	0.16	0.11	0.79	-	0.23	0.19	0.27	-	0.15	0.12	0.18	-	0.18	0.15	0.25	-
Ce_2O_3	0.63	0.23	1.49	0.26	0.46	0.23	1.24	0.10	1.05	0.86	1.47	0.14	0.59	0.50	0.74	0.09	0.93	0.74	1.49	0.14
Pr_2O_3	<mdl	<mdl	0.23	-	<mdl	<mdl	<mdl	-	<mdl	<mdl	0.19	-	<mdl	<mdl	<mdl	-	<mdl	<mdl	0.23	-
Nd_2O_3	0.38	<mdl	1.07	0.26	0.22	<mdl	0.63	-	0.44	0.34	0.55	-	0.33	<mdl	0.71	-	0.72	0.39	1.07	-
Sm_2O_3	0.15	<mdl	0.60	0.16	<mdl	<mdl	0.33	-	<mdl	<mdl	0.19	-	<mdl	<mdl	0.39	-	0.36	<mdl	0.60	-
Gd_2O_3	0.30	<mdl	1.13	0.32	<mdl	<mdl	1.13	0.19	<mdl	<mdl	0.24	-	0.23	<mdl	0.80	0.22	0.65	0.19	1.12	0.31
PbO	0.40	<mdl	1.93	0.50	0.08	<mdl	0.14	-	0.42	0.28	0.79	0.12	0.28	0.13	0.72	0.19	1.11	0.47	1.93	0.34
ThO_2	0.22	<mdl	1.38	0.17	0.22	<mdl	1.38	0.21	0.12	0.10	0.17	-	0.21	0.12	0.36	0.07	0.23	0.05	0.34	0.05
TOTAL Ox	94.90	85.09	99.90	2.17	95.03	85.09	99.90	2.61	93.87	92.65	96.72	1.15	95.63	94.47	96.63	0.82	94.74	92.68	97.44	0.92
Brannerite Formula (apfu) - based on 6 O																				
U^{4+}	0.146	0.096	0.184	0.019	0.147	0.096	0.184	0.022	0.158	0.146	0.164	0.005	0.158	0.126	0.170	0.016	0.140	0.118	0.156	0.008
U^{6+}	0.415	0.275	0.524	0.054	0.418	0.275	0.524	0.063	0.449	0.416	0.466	0.013	0.449	0.358	0.483	0.045	0.399	0.335	0.444	0.023
Ca^{2+}	0.129	0.037	0.320	0.050	0.121	0.040	0.320	0.055	0.159	0.079	0.203	0.026	0.114	0.037	0.167	0.039	0.141	0.051	0.222	0.038
Sr^{2+}	0.004	0.000	0.015	0.003	0.003	0.000	0.015	0.001	0.004	0.002	0.011	0.002	0.002	0.000	0.003	0.001	0.009	0.003	0.013	0.002
Ba^{2+}	0.010	0.000	0.045	0.008	0.005	0.000	0.045	0.004	0.011	0.007	0.032	0.006	0.014	0.003	0.030	0.011	0.020	0.012	0.036	0.005
Y^{3+}	0.040	0.010	0.122	0.031	0.025	0.010	0.108	0.019	0.031	0.028	0.034	0.002	0.030	0.015	0.066	0.015	0.075	0.036	0.122	0.028
La^{3+}	0.004	0.002	0.019	0.001	0.004	0.002	0.019	0.001	0.005	0.005	0.006	0.000	0.004	0.003	0.004	0.000	0.004	0.003	0.005	0.000
Ce^{3+}	0.014	0.005	0.034	0.006	0.010	0.005	0.029	0.002	0.024	0.020	0.034	0.003	0.013	0.012	0.017	0.002	0.021	0.017	0.032	0.003
Pr^{3+}	0.002	0.001	0.005	0.001	0.001	0.001	0.004	0.001	0.003	0.001	0.004	0.001	0.002	0.001	0.003	0.001	0.003	0.001	0.005	0.001
Nd^{3+}	0.008	0.001	0.024	0.006	0.005	0.001	0.013	0.002	0.010	0.008	0.012	0.001	0.007	0.004	0.015	0.003	0.016	0.009	0.024	0.004
Sm^{3+}	0.003	0.000	0.013	0.003	0.001	0.000	0.007	0.001	0.002	0.001	0.004	0.001	0.003	0.001	0.008	0.002	0.008	0.003	0.013	0.003
Gd^{3+}	0.006	0.001	0.024	0.006	0.003	0.001	0.024	0.004	0.003	0.002	0.005	0.001	0.005	0.001	0.016	0.004	0.013	0.004	0.023	0.006
Pb^{2+}	0.003	0.000	0.016	0.004	0.001	0.000	0.001	0.000	0.004	0.002	0.007	0.001	0.002	0.001	0.006	0.002	0.009	0.004	0.016	0.003
Th^{4+}	0.003	0.000	0.019	0.002	0.003	0.000	0.019	0.003	0.002	0.001	0.002	0.000	0.003	0.002	0.005	0.001	0.003	0.001	0.005	0.001
Total A-site cations	0.787	0.459	1.010	0.104	0.745	0.459	1.010	0.107	0.864	0.779	0.904	0.032	0.805	0.647	0.918	0.085	0.861	0.727	0.928	0.043
Total A-site cations (excluding U)	0.226	0.076	0.462	0.088	0.181	0.076	0.462	0.068	0.258	0.188	0.329	0.027	0.198	0.125	0.265	0.054	0.322	0.199	0.390	0.050
Ti^{4+}	1.574	1.230	2.042	0.133	1.584	1.230	2.042	0.163	1.582	1.529	1.619	0.027	1.561	1.521	1.587	0.020	1.551	1.392	1.615	0.040
Si^{4+}	0.253	0.128	0.516	0.064	0.244	0.134	0.516	0.059	0.196	0.128	0.347	0.053	0.246	0.128	0.406	0.084	0.284	0.191	0.501	0.062
Na^{+}	0.082	0.006	0.232	0.054	0.114	0.029	0.232	0.041	0.040	0.011	0.098	0.021	0.042	0.008	0.075	0.027	0.023	0.006	0.057	0.010
Mg^{2+}	0.010	0.000	0.120	0.013	0.014	0.003	0.120	0.015	0.003	0.002	0.004	0.000	0.007	0.000	0.012	0.005	0.001	0.000	0.004	0.001
Al^{3+}	0.025	0.004	0.133	0.018	0.027	0.010	0.133	0.022	0.008	0.004	0.018	0.004	0.018	0.009	0.050	0.012	0.024	0.015	0.061	0.005
K^{+}	0.010	0.000	0.060	0.009	0.014	0.004	0.060	0.009	0.003	0.001	0.007	0.002	0.006	0.000	0.009	0.004	0.002	0.000	0.008	0.002
Mn^{2+}	0.011	0.003	0.024	0.003	0.010	0.003	0.024	0.003	0.014	0.008	0.017	0.002	0.011	0.007	0.015	0.002	0.012	0.003	0.022	0.004
Fe^{3+}	0.221	0.126	0.434	0.056	0.246	0.126	0.434	0.053	0.196	0.128	0.334	0.047	0.207	0.160	0.268	0.030	0.172	0.142	0.224	0.017
As^{5+}	0.009	0.000	0.041	0.008	0.009	0.000	0.041	0.006	0.033	0.022	0.040	0.004	0.018	0.010	0.034	0.010	0.003	0.000	0.006	0.001
Zr^{4+}	0.015	0.003	0.058	0.008	0.013	0.003	0.058	0.007	0.009	0.006	0.011	0.001	0.014	0.005	0.024	0.009	0.018	0.005	0.046	0.010
Nb^{5+}	0.021	0.009	0.043	0.009	0.016	0.011	0.031	0.004	0.014	0.009	0.016	0.002	0.014	0.011	0.016	0.002	0.034	0.024	0.043	0.003
Total B-site cations	2.230	2.009	2.582	0.125	2.293	2.075	2.582	0.112	2.096	2.052	2.184	0.042	2.144	2.009	2.307	0.105	2.125	2.061	2.281	0.038
Total B-site cations (excluding Ti)	0.656	0.422	1.163	0.131	0.709	0.463	1.163	0.127	0.515	0.436	0.653	0.065	0.584	0.422	0.759	0.116	0.574	0.468	0.802	0.069
Total cations	3.017	2.920	3.301	0.055	3.038	2.929	3.301	0.057	2.961	2.939	3.006	0.021	2.949	2.920	3.014	0.028	2.985	2.932	3.021	0.022

Note: Average minimum detection limit (mdl) per element for 99% confidence interval (wt%): U≈0.03, Pb≈0.03, Th≈0.03, Na≈0.02, Mg≈0.01, Al≈0.01, Si≈0.01, P≈0.01, S≈0.01, K≈0.01, Ca≈0.005, Ti≈0.01, Mn≈0.03, Fe≈0.02, Cu≈0.03, As≈0.02, Zr≈0.02, Nb≈0.03, Y≈0.02,Ce≈0.02, La≈0.02, Pr≈0.07, Nd≈0.08, Sm≈0.06, Gd≈0.07, Sr≈0.02, Ba≈0.02.

6.5.3 Chemical composition of coffinite

The mean and compositional range for each coffinite group are given in Tables 6.3a and 6.3b. The mean composition for all analyzed coffinite (n=380) is 58.44 wt% UO_2, 15.79 wt% SiO_2, 3.05 wt% P_2O_5, 2.19 wt% CaO, 1.81 wt% FeO, 0.11 wt% As_2O_5, 4.78 wt% Y_2O_3, 0.84 wt% Nb_2O_5, 4.20 wt% ΣREE_2O_3, with a mean analytical total of 93.99 wt%.

Initially, the chemical formula of coffinite was calculated by normalization to 4.00 O atoms, but cation totals were all above the ideal 2.0 (2.05 to 2.34). Using a similar method to that derived for brannerite, we varied the amount of U^{4+} and U^{6+} to see if this could improve the cation totals to a more acceptable range (1.95-2.05). It was found that if 43.6% of total U was assumed to be U^{6+}, then 85% (i.e., 296/380) of analyses had cation totals in the acceptable range. As with brannerite, the U content of coffinite in most published work is reported as a single oxide, but U^{6+} is recognized in coffinite (e.g., Goldhaber et al., 1987). The likelihood that both U^{4+} and U^{6+} are present within coffinite is also strengthened by the possible substitution of Ca^{2+}, and involving both U cations (see below). The addition of H^+ (protons) in the form of H_2O, or $(OH)^-$ in lieu of, or in addition to the presence of U^{6+} could also aid charge balance, thus providing another mechanism to support the presence of U^{6+}.

For coffinite of the form ABO_4, the A-site typically contains 0.39-0.85 *apfu* U^{4+}+U^{6+}, and up to 0.74 *apfu* other A-site cations, including a maximum of 0.23 *apfu* Ca^{2+}, 0.33 *apfu* Fe^{2+}, 0.14 *apfu* Mg^{2+}, 0.10 *apfu* Na^+, and 0.61 *apfu* ΣREY^{3+} (Tables 6.3a and 6.3b). Similarly, the B-site typically contains 0.44-1.03 *apfu* Si^{4+}, and up to 0.54 *apfu* other B-site cations, including a maximum of 0.41 *apfu* P^{5+}, 0.14 *apfu* Nb^{5+}, 0.11 *apfu* S^{6+}, 0.10 *apfu* Al^{3+}. The A-site cation totals range between 0.79-1.30 *apfu*, with a mean of 1.07 *apfu*; whereas the B-site cation totals range between 0.70-1.20 *apfu*, with a mean of 0.94 *apfu*. Cation totals tend to range between 1.94-2.21 *apfu*, with a mean of 2.01. The deviations from the ideal 1.0 *apfu* A-

and B-site totals indicates there is some replacement within both the A- and B-sites of coffinite; exchange mechanisms are discussed below. The A/B ratios are mostly >1 (ranging between 0.66 and 1.87) and with a mean of 1.16 for all coffinite data. Typically, A>B for all coffinite groups except coffinite-C1 and -C3. For each coffinite grouping an estimate of the chemical formula based on the mean composition (Tables 6.3a and 6.3b) can therefore be made:

Coffinite-A1: $[U^*_{0.61}Ca^*_{0.14}REY_{0.24}Na^*_{0.04}]_{1.04}[Si_{0.78}P_{0.13}Nb^*_{0.01}M^*_{0.04}]_{0.96}O_4$

Coffinite-A2: $[U^*_{0.62}Ca^*_{0.24}REY_{0.17}Na^*_{0.03}]_{1.06}[Si_{0.77}P_{0.10}Nb^*_{0.04}M^*_{0.05}]_{0.96}O_4$

Coffinite-B: $[U^*_{0.77}Ca^*_{0.25}REY_{0.12}Na^*_{0.05}]_{1.19}[Si_{0.67}P_{0.09}M^*_{0.05}]_{0.81}O_4$

Coffinite-C1: $[U^*_{0.50}Ca^*_{0.12}REY_{0.33}Na^*_{0.05}]_{1.00}[Si_{0.79}P_{0.19}M^*_{0.04}]_{1.03}O_4$

Coffinite-C2: $[U^*_{0.46}Ca^*_{0.25}REY_{0.28}Na^*_{0.04}]_{1.03}[Si_{0.52}P_{0.36}M^*_{0.10}]_{0.98}O_4$

Coffinite-C3: $[U^*_{0.50}Ca^*_{0.23}REY_{0.20}Na^*_{0.04}]_{0.97}[Si_{0.62}P_{0.28}Nb^*_{0.01}M^*_{0.11}]_{1.02}O_4$

where U^*= Σ(U,Th,Zr), Ca^* = Σ(Ca,Fe,Mg,Mn,Sr,Pb,Ba), Na^* = Σ(Na,K), Nb^* = Σ(Nb,As), and M^* = Σ(Ti,Al,S). The average formulae for coffinite (all 380 analyses) is:

$$[U^*_{0.63}Ca^*_{0.20}REY_{0.19}Na^*_{0.04}]_{1.07}[Si_{0.75}P_{0.12}Nb^*_{0.02}M^*_{0.05}]_{0.94}O_4$$

From the estimated chemical formula for the different coffinite groups compared to the average, coffinite-B (coffinite associated with uraninite; Figure 6.5) contains the most U^* (0.77 *apfu*), and Ca^* (0.25 *apfu*), lowest ΣREY (0.12 *apfu*), and has the highest A-site totals (1.19 *apfu*). Conversely, it has the lowest P content (0.09 *apfu*) and B-site totals (0.81 *apfu*) of all coffinite types. Coffinite-C1 (coffinite associated with brannerite; Figure 6.6a-c) has the highest ΣREY content (0.33 *apfu*), lowest Ca^* content (0.12 *apfu*), an A-site total close to

parity, and Si content (0.79 *apfu*) the highest of all coffinite. Some brannerite is found in close proximity to REY-bearing minerals (i.e., Figure 6.2a-c) and often contains some ΣREY. Coffinite-C2 and -C3 have the highest M^* content; 0.10 and 0.11, respectively. Coffinite-A does not contain a unique concentration of any particular element, but represents the majority of coffinite analyzed, although coffinite-A2 does have the highest Nb^* content (0.04 *apfu*), albeit this value is low compared to the more dominant substituents.

Table 6.3a: Electron probe microanalytical data for coffinite-A and -B.

Type	All data				A1				A2				B			
Valid N (analyses)	380				122				180				52			
(wt%)	Mean	Min	Max	SD	Mean	Min	Max	SD	Mean	Min	Max	SD	Mean	Min	Max	SD
UO_2	58.44	45.14	70.02	5.66	57.06	47.57	69.00	5.33	58.45	49.35	65.64	3.48	66.41	58.53	70.02	2.44
SiO_2	15.79	10.38	24.69	2.78	16.35	10.89	24.69	2.66	16.32	11.45	24.47	2.28	13.09	10.58	21.37	2.18
Na_2O	0.34	<mdl	1.20	0.25	0.37	<mdl	1.08	0.24	0.30	<mdl	1.20	0.27	0.42	0.19	1.00	0.16
MgO	0.10	0.01	2.14	0.15	0.05	0.02	0.18	0.02	0.09	0.01	0.73	0.09	0.12	0.09	0.26	0.03
Al_2O_3	0.55	<mdl	1.86	0.35	0.53	0.06	1.73	0.25	0.62	0.18	1.81	0.39	0.32	0.21	0.55	0.07
P_2O_5	3.05	0.63	11.43	1.82	3.27	1.54	5.39	0.88	2.55	0.63	6.18	1.03	2.04	1.37	3.75	0.45
SO_3	0.34	<mdl	3.31	0.61	0.14	<mdl	3.31	0.41	0.25	<mdl	3.23	0.50	0.72	0.09	2.10	0.44
K_2O	0.11	<mdl	0.74	0.10	0.14	<mdl	0.62	0.11	0.08	<mdl	0.74	0.09	0.07	0.04	0.17	0.02
CaO	2.19	0.57	4.59	0.90	1.70	0.62	3.40	0.71	2.12	0.80	4.59	0.75	3.36	2.96	3.80	0.19
TiO_2	0.13	<mdl	0.90	0.11	0.14	<mdl	0.90	0.11	0.14	0.07	0.41	0.04	0.03	<mdl	0.28	0.05
MnO	0.09	<mdl	0.51	0.10	0.05	<mdl	0.39	0.07	0.06	<mdl	0.51	0.06	0.26	0.08	0.41	0.09
FeO	1.81	0.22	8.41	1.57	0.96	0.22	5.18	0.80	2.72	0.36	8.41	1.77	0.94	0.51	1.68	0.21
Cu_2O	0.36	<mdl	3.78	0.41	0.41	<mdl	3.78	0.55	0.33	<mdl	1.67	0.31	0.44	<mdl	1.70	0.34
As_2O_5	0.11	<mdl	1.05	0.17	0.09	<mdl	0.65	0.17	0.14	<mdl	0.56	0.14	<mdl	<mdl	<mdl	-
SrO	<mdl	<mdl	0.18	-	<mdl	<mdl	0.10	-	0.03	<mdl	0.18	0.03	<mdl	<mdl	0.04	-
ZrO_2	0.21	<mdl	1.44	0.19	0.24	<mdl	1.44	0.28	0.20	<mdl	0.75	0.10	0.15	0.05	0.29	0.05
Nb_2O_5	0.84	<mdl	6.11	0.96	0.16	<mdl	0.93	0.21	1.65	<mdl	6.11	0.82	<mdl	<mdl	<mdl	-
BaO	0.20	<mdl	0.62	0.15	0.15	<mdl	0.49	0.11	0.30	0.04	0.62	0.11	<mdl	<mdl	<mdl	-
Y_2O_3	4.78	0.37	15.60	3.06	7.05	1.12	11.94	2.75	3.30	0.37	7.66	1.45	2.09	1.48	2.53	0.30
La_2O_3	0.27	0.16	2.30	0.16	0.24	0.17	0.39	-	0.26	0.16	2.30	0.22	0.40	0.32	0.53	0.06
Ce_2O_3	1.12	0.30	5.06	0.44	0.94	0.30	1.38	0.24	1.27	0.84	5.06	0.53	1.23	1.01	1.79	0.19
Pr_2O_3	0.22	<mdl	0.70	-	<mdl	<mdl	0.32	-	0.26	<mdl	0.70	-	0.21	<mdl	0.34	-
Nd_2O_3	1.29	0.33	2.76	0.42	1.00	0.33	1.82	0.29	1.66	1.24	2.76	0.21	0.99	0.73	1.31	-
Sm_2O_3	0.48	<mdl	0.86	0.18	0.37	<mdl	0.74	-	0.62	0.27	0.86	-	0.29	0.16	0.41	-
Gd_2O_3	0.81	0.19	1.82	0.29	0.87	0.31	1.26	0.20	0.81	0.19	1.02	-	0.36	0.19	0.51	-
PbO	0.20	<mdl	1.97	0.30	0.11	<mdl	1.03	0.20	0.24	<mdl	1.97	0.37	0.31	0.14	0.84	0.17
ThO_2	0.12	<mdl	3.61	0.37	0.30	<mdl	3.61	0.61	<mdl	<mdl	0.52	0.08	<mdl	<mdl	<mdl	-
TOTAL Ox	93.99	86.28	100.00	2.16	92.88	86.51	100.00	2.58	94.84	90.92	99.06	1.39	94.34	93.24	96.21	0.77
Coffinite Formula (apfu) - based on 4 O																
U^{4+}	0.354	0.218	0.477	0.054	0.345	0.262	0.466	0.048	0.349	0.254	0.431	0.035	0.430	0.316	0.477	0.036
U^{6+}	0.273	0.168	0.369	0.042	0.267	0.203	0.360	0.037	0.270	0.196	0.334	0.027	0.333	0.244	0.369	0.028
Th^{4+}	0.001	0.000	0.039	0.004	0.003	0.000	0.039	0.006	0.000	0.000	0.005	0.001	0.000	0.000	0.000	0.000
Zr^{4+}	0.005	0.000	0.032	0.004	0.005	0.000	0.032	0.006	0.005	0.000	0.017	0.002	0.004	0.001	0.007	0.001
Mg^{2+}	0.007	0.001	0.138	0.010	0.004	0.002	0.012	0.002	0.007	0.001	0.049	0.006	0.009	0.006	0.017	0.002
Ca^{2+}	0.114	0.030	0.234	0.050	0.089	0.030	0.194	0.043	0.109	0.038	0.234	0.041	0.186	0.141	0.220	0.018
Mn^{2+}	0.004	0.000	0.019	0.004	0.002	0.000	0.018	0.003	0.003	0.000	0.019	0.003	0.012	0.003	0.019	0.004
Fe^{2+}	0.072	0.009	0.334	0.061	0.039	0.009	0.205	0.031	0.107	0.013	0.334	0.068	0.041	0.020	0.072	0.010
Sr^{2+}	0.001	0.000	0.005	0.001	0.001	0.000	0.003	0.001	0.001	0.000	0.005	0.001	0.000	0.000	0.001	0.000
Pb^{2+}	0.003	0.000	0.024	0.004	0.001	0.000	0.014	0.003	0.003	0.000	0.024	0.005	0.004	0.002	0.012	0.002
Ba^{2+}	0.004	0.000	0.012	0.003	0.003	0.000	0.010	0.002	0.006	0.001	0.012	0.002	0.000	0.000	0.000	0.000
Y^{3+}	0.120	0.009	0.377	0.075	0.178	0.032	0.300	0.070	0.083	0.009	0.180	0.033	0.058	0.036	0.071	0.010
La^{3+}	0.005	0.002	0.041	0.003	0.004	0.003	0.008	0.001	0.005	0.002	0.041	0.004	0.008	0.006	0.010	0.001
Ce^{3+}	0.020	0.005	0.089	0.008	0.017	0.005	0.026	0.004	0.022	0.013	0.089	0.009	0.023	0.020	0.030	0.003
Pr^{3+}	0.004	0.001	0.012	0.001	0.003	0.001	0.006	0.001	0.005	0.002	0.012	0.001	0.004	0.002	0.006	0.001
Nd^{3+}	0.022	0.005	0.047	0.007	0.017	0.005	0.035	0.006	0.028	0.019	0.047	0.004	0.018	0.014	0.022	0.002
Sm^{3+}	0.008	0.002	0.014	0.003	0.006	0.002	0.014	0.002	0.010	0.004	0.014	0.002	0.005	0.002	0.007	0.001
Gd^{3+}	0.013	0.003	0.026	0.004	0.014	0.006	0.020	0.003	0.013	0.003	0.016	0.002	0.006	0.003	0.009	0.001
Na^{+}	0.032	0.001	0.103	0.023	0.034	0.001	0.101	0.022	0.027	0.001	0.103	0.024	0.042	0.017	0.102	0.016
K^{+}	0.006	0.000	0.042	0.006	0.008	0.000	0.033	0.006	0.005	0.000	0.042	0.005	0.005	0.003	0.011	0.002
Total A-site cations	1.066	0.790	1.301	0.101	1.041	0.813	1.277	0.092	1.056	0.885	1.279	0.081	1.187	0.911	1.301	0.095
Total A-site cations (excluding U)	0.439	0.291	0.744	0.068	0.429	0.291	0.604	0.049	0.437	0.296	0.744	0.076	0.424	0.340	0.494	0.036
Si^{4+}	0.752	0.437	1.032	0.104	0.779	0.584	1.032	0.092	0.771	0.601	1.022	0.080	0.669	0.572	0.918	0.073
Ti^{4+}	0.005	0.000	0.033	0.004	0.005	0.000	0.033	0.004	0.005	0.002	0.016	0.002	0.001	0.000	0.011	0.002
P^{5+}	0.121	0.027	0.410	0.064	0.132	0.068	0.211	0.032	0.102	0.027	0.231	0.039	0.088	0.063	0.145	0.015
As^{5+}	0.003	0.000	0.023	0.004	0.002	0.000	0.018	0.005	0.004	0.000	0.015	0.004	0.000	0.000	0.001	0.000
Nb^{5+}	0.018	0.000	0.138	0.021	0.004	0.000	0.022	0.005	0.035	0.001	0.138	0.018	0.001	0.000	0.001	0.000
Al^{3+}	0.031	0.001	0.098	0.018	0.030	0.003	0.086	0.013	0.034	0.011	0.098	0.020	0.019	0.013	0.034	0.003
S^{6+}	0.012	0.000	0.112	0.021	0.005	0.000	0.112	0.014	0.009	0.000	0.109	0.017	0.027	0.004	0.080	0.016
Total B-site cations	0.942	0.698	1.202	0.101	0.957	0.726	1.161	0.093	0.960	0.769	1.176	0.076	0.806	0.698	1.090	0.089
Total B-site cations (excluding Si)	0.190	0.096	0.544	0.068	0.178	0.111	0.283	0.034	0.189	0.129	0.324	0.030	0.137	0.096	0.216	0.026
Total cations	2.007	1.940	2.205	0.042	1.998	1.951	2.076	0.025	2.016	1.940	2.205	0.053	1.994	1.966	2.048	0.015
A/B	1.157	0.658	1.865	0.246	1.110	0.700	1.753	0.226	1.112	0.758	1.639	0.169	1.500	0.836	1.865	0.257
ΣREY	0.191	0.081	0.421	0.066	0.240	0.115	0.356	0.063	0.165	0.081	0.250	0.031	0.122	0.095	0.140	0.010
P+As+Nb	0.142	0.050	0.411	0.060	0.138	0.068	0.226	0.032	0.141	0.085	0.233	0.030	0.089	0.064	0.146	0.015

Note: Average minimum detection limit (mdl) per element for 99% confidence interval (wt%): U≈0.03, Si≈0.007, Na≈0.02, Mg≈0.008, Al≈0.006, P≈0.009, S≈0.01, K≈0.007, Ca≈0.005, Ti≈0.007, Mn≈0.03, Fe≈0.02, Cu≈0.03, As≈0.02, Sr≈0.02, Y≈0.04, Zr≈0.03, Nb≈0.04, Ba≈0.03, La≈0.02, Ce≈0.02, Pr≈0.08, Nd≈0.09, Sm≈0.07, Gd≈0.07, Pb≈0.03, Th≈0.04.

Table 6.3b: Electron probe microanalytical data for coffinite-C.

Type	C1				C2				C3			
Valid N (analyses)	11				9				6			
(wt%)	Mean	Min	Max	SD	Mean	Min	Max	SD	Mean	Min	Max	SD
UO_2	47.98	45.14	50.64	1.82	48.21	45.48	50.60	1.73	51.74	46.32	64.87	6.91
SiO_2	17.03	12.25	22.36	3.91	12.22	10.38	15.03	1.55	15.12	10.55	22.32	4.93
Na_2O	0.50	0.31	0.90	0.18	0.37	0.05	0.77	0.25	0.29	<mdl	1.01	0.37
MgO	0.06	0.02	0.09	0.02	0.65	0.10	2.14	0.62	0.51	0.24	0.66	0.18
Al_2O_3	0.56	<mdl	1.56	0.52	0.69	0.07	1.86	0.67	0.84	0.30	1.43	0.42
P_2O_5	5.16	1.26	10.58	4.33	9.93	7.71	11.43	1.26	7.96	3.38	10.12	2.61
SO_3	<mdl	<mdl	0.05	-	1.98	<mdl	2.82	0.81	2.21	1.02	2.80	0.65
K_2O	0.10	0.02	0.31	0.08	0.19	0.07	0.36	0.12	0.29	0.10	0.50	0.15
CaO	1.47	0.57	2.38	0.80	3.44	1.49	3.98	0.75	3.33	2.75	3.83	0.45
TiO_2	0.34	0.11	0.87	0.25	0.15	0.01	0.86	0.27	0.13	<mdl	0.26	0.11
MnO	<mdl	<mdl	0.08	-	0.08	<mdl	0.13	-	0.14	0.09	0.28	0.07
FeO	1.12	0.32	2.98	0.77	1.21	0.56	3.44	1.02	1.10	0.60	1.87	0.48
Cu_2O	0.41	0.13	0.98	0.26	<mdl	<mdl	0.12	-	0.14	<mdl	0.47	0.16
As_2O_5	0.12	<mdl	0.26	0.12	0.13	<mdl	0.57	0.17	0.55	<mdl	1.05	0.42
SrO	<mdl	<mdl	<mdl	-	<mdl	<mdl	<mdl	-	<mdl	<mdl	0.05	-
ZrO_2	0.23	0.04	0.71	0.21	0.33	0.08	0.84	0.28	0.37	0.19	0.69	0.21
Nb_2O_5	<mdl	<mdl	<mdl	-	<mdl	<mdl	<mdl	-	<mdl	<mdl	<mdl	-
BaO	0.18	0.14	0.23	0.03	0.04	<mdl	0.18	0.05	<mdl	<mdl	0.03	-
Y_2O_3	11.47	7.84	14.90	2.55	9.59	6.99	15.60	2.42	6.60	2.46	8.18	2.08
La_2O_3	0.18	0.16	0.21	-	0.24	0.21	0.28	-	0.28	0.23	0.38	0.05
Ce_2O_3	0.50	0.47	0.55	-	0.87	0.49	1.05	0.16	1.05	0.92	1.16	0.08
Pr_2O_3	<mdl	<mdl	<mdl	-	<mdl	<mdl	0.21	-	<mdl	<mdl	0.19	-
Nd_2O_3	0.54	0.47	0.65	-	0.83	0.37	0.97	-	0.86	0.60	0.95	-
Sm_2O_3	0.24	0.17	0.30	-	0.53	0.19	0.67	-	0.49	0.27	0.56	-
Gd_2O_3	1.30	0.82	1.72	0.34	1.65	1.40	1.82	-	1.33	0.55	1.63	0.39
PbO	<mdl	<mdl	<mdl	-	0.25	<mdl	0.81	0.29	0.15	<mdl	0.77	0.30
ThO_2	0.20	<mdl	0.83	0.26	0.06	<mdl	0.24	0.08	<mdl	<mdl	<mdl	-
TOTAL Ox	89.85	86.28	93.64	2.69	93.85	91.35	95.84	1.33	95.67	93.87	97.79	1.80
Coffinite Formula (apfu) - based on 4 O												
U^{4+}	0.279	0.229	0.319	0.027	0.257	0.237	0.268	0.009	0.276	0.218	0.416	0.072
U^{6+}	0.216	0.177	0.247	0.021	0.199	0.184	0.207	0.007	0.213	0.168	0.322	0.056
Th^{4+}	0.002	0.000	0.009	0.003	0.001	0.000	0.003	0.001	0.000	0.000	0.000	0.000
Zr^{4+}	0.005	0.001	0.017	0.005	0.007	0.002	0.017	0.006	0.008	0.003	0.014	0.005
Mg^{2+}	0.004	0.001	0.006	0.001	0.041	0.007	0.138	0.040	0.031	0.014	0.042	0.010
Ca^{2+}	0.071	0.031	0.115	0.036	0.156	0.072	0.179	0.033	0.149	0.118	0.173	0.023
Mn^{2+}	0.001	0.000	0.003	0.001	0.003	0.001	0.005	0.001	0.005	0.003	0.012	0.003
Fe^{2+}	0.043	0.013	0.119	0.030	0.043	0.020	0.124	0.038	0.039	0.021	0.064	0.019
Sr^{2+}	0.000	0.000	0.000	0.000	0.000	0.000	0.000	0.000	0.000	0.000	0.001	0.000
Pb^{2+}	0.000	0.000	0.000	0.000	0.003	0.000	0.009	0.003	0.002	0.000	0.008	0.003
Ba^{2+}	0.003	0.002	0.005	0.001	0.001	0.000	0.003	0.001	0.000	0.000	0.000	0.000
Y^{3+}	0.280	0.191	0.350	0.053	0.218	0.160	0.377	0.063	0.144	0.067	0.184	0.041
La^{3+}	0.003	0.003	0.004	0.000	0.004	0.003	0.004	0.000	0.004	0.003	0.006	0.001
Ce^{3+}	0.009	0.007	0.010	0.001	0.013	0.008	0.017	0.002	0.016	0.013	0.020	0.002
Pr^{3+}	0.001	0.001	0.002	0.001	0.002	0.001	0.003	0.001	0.002	0.001	0.003	0.001
Nd^{3+}	0.009	0.007	0.011	0.001	0.013	0.006	0.015	0.003	0.013	0.011	0.014	0.001
Sm^{3+}	0.004	0.003	0.005	0.001	0.008	0.003	0.010	0.002	0.007	0.005	0.008	0.001
Gd^{3+}	0.020	0.012	0.025	0.004	0.023	0.020	0.026	0.002	0.018	0.009	0.022	0.005
Na^{+}	0.045	0.027	0.083	0.018	0.030	0.004	0.064	0.021	0.026	0.001	0.100	0.037
K^{+}	0.006	0.001	0.019	0.005	0.010	0.004	0.019	0.006	0.016	0.005	0.029	0.010
Total A-site cations	1.001	0.859	1.072	0.074	1.031	0.956	1.189	0.072	0.970	0.790	1.263	0.162
Total A-site cations (excluding U)	0.507	0.404	0.613	0.083	0.575	0.484	0.736	0.072	0.481	0.404	0.530	0.048
Si^{4+}	0.789	0.542	1.022	0.195	0.519	0.437	0.617	0.067	0.621	0.445	0.829	0.157
Ti^{4+}	0.012	0.004	0.029	0.009	0.005	0.000	0.029	0.009	0.004	0.000	0.008	0.003
P^{5+}	0.194	0.050	0.396	0.159	0.356	0.296	0.410	0.040	0.277	0.146	0.359	0.083
As^{5+}	0.003	0.000	0.006	0.003	0.003	0.000	0.013	0.004	0.012	0.000	0.023	0.009
Nb^{5+}	0.000	0.000	0.001	0.000	0.000	0.000	0.001	0.000	0.000	0.000	0.001	0.000
Al^{3+}	0.031	0.001	0.088	0.029	0.034	0.004	0.095	0.034	0.041	0.014	0.071	0.019
S^{6+}	0.000	0.000	0.002	0.001	0.063	0.001	0.090	0.026	0.068	0.039	0.089	0.018
Total B-site cations	1.030	0.944	1.141	0.078	0.981	0.940	1.057	0.040	1.023	0.784	1.202	0.143
Total B-site cations (excluding Si)	0.241	0.111	0.409	0.135	0.462	0.335	0.503	0.053	0.402	0.219	0.544	0.124
Total cations	2.032	2.000	2.107	0.029	2.012	1.946	2.138	0.056	1.993	1.958	2.047	0.029
A/B	0.981	0.753	1.131	0.140	1.055	0.909	1.254	0.105	0.986	0.658	1.610	0.334
ΣREY	0.325	0.225	0.401	0.057	0.281	0.224	0.421	0.057	0.204	0.118	0.248	0.046
P+As+Nb	0.198	0.050	0.403	0.162	0.360	0.300	0.411	0.038	0.289	0.149	0.377	0.091

Note: Average minimum detection limit (mdl) per element for 99% confidence interval (wt%): U≈0.03, Si≈0.007, Na≈0.02, Mg≈0.008, Al≈0.006, P≈0.009, S≈0.01, K≈0.007, Ca≈0.005, Ti≈0.007, Mn≈0.03, Fe≈0.02, Cu≈0.03, As≈0.02, Sr≈0.02, Y≈0.04, Zr≈0.03, Nb≈0.04, Ba≈0.03, La≈0.02, Ce≈0.02, Pr≈0.08, Nd≈0.09, Sm≈0.07, Gd≈0.07, Pb≈0.03, Th≈0.04.

6.6 Discussion

6.6.1 Compositional trends for brannerite

Chemical variability in terms of substitution into sites A and B is summarized in Figures 6.9 and 10. Potential A-site substituents are plotted against total U (Figure 6.9), and for the total A-site cations excluding U (Figure 6.9a) no clear trend is discernable. However, if selected A-site substituents are plotted individually, several trends are evident. There is a strong negative correlation between ΣREY and total U for brannerite with elevated ΣREY (brannerite-B to -D), with the slope of the line-of-best fit = -0.92. Plotting Pb against total U (Figure 6.9c) gives the same strong negative correlation for brannerite-B to -D. Brannerite-A has the least ΣREY, Pb and other A-site substituents when compared to other brannerite groups. Addition of other divalent cations (Ca, Sr and Ba) to Pb does not change the negative correlation with U (Figure 6.9d). Although Ca is the second most abundant A-site cation (0.13 *apfu* for all analyses), there is no discernable relationship when plotted against U (Figure 6.9d). Thus, as suggested by Lumpkin et al. (2012), coupled substitutions involving Ca and B-site cations, or oxygen and hydroxyl groups may explain the observed patterns.

B-site substitutions are plotted against Ti (Figure 6.10). In most cases, a negative correlation between a particular element and Ti is observed, indicative of substitution for that element. The same negative correlation is seen between total B-site cations (excluding Ti) with Ti (Figure 6.10a). There are, however, two distinct trends, with brannerite-A typically having a broader range of both Ti values and total B-site cation contents than brannerite-B to -D. The slope of the trend for brannerite-A is also shallower (c.f. -0.57 versus -1.68). The total B-site occupancies for brannerite-B to -D are also closer to the ideal (2.0) than brannerite-A, highlighting the fact that brannerite-A has greater levels of B-site substitution than the other groups, or that brannerite-B to -D represents purer examples of brannerite.

Considering the key elements involved in B-site substitution, the trends for total B-site (excluding Ti) vs. Ti (Figure 6.10a), and for Si vs. Ti (Figure 6.10b), are similar. Brannerite-A displays a shallower slope (-0.57 and -0.24, respectively) than the trend for brannerite-B to -D (-1.68 and -1.54, respectively). All brannerite shows a broad range of Si content (0.13-0.52 *apfu*). The role of Si in brannerite is unclear. Lumpkin et al. (2012) suggest it occupies the B-site, but admit this is questionable since they only found a weak correlation between Si and Ti.

The divalent cations Mg and Mn are combined with monovalent Na and K *apfu* contents and plotted against Ti (Figure 6.10c). The trends are analogous if each element is plotted individually. These four elements typically reflect lower temperature hydrothermal alteration, and are thus sensibly combined onto a single plot. The (Mg+Mn+Na+K) content of brannerite-A varies (line-of-best fit slope -0.19), but has a negative trend; whereas for brannerite-B to -D, there is no apparent trend and the data cluster together. Brannerite-A contains more (Mg+Mn+Na+K) than the other brannerite groups.

The trivalent cations Fe and Al have also been combined and plotted against Ti (Figure 6.10d). The negative trend is less discernable than for the above, however brannerite-A still appears to have a negative correlation (line-of-best fit with slope -0.13). On average, brannerite-A contains more (Fe+Al) than brannerite-B to -D. Observed scatter in this plot may be due to the presence of both Fe^{2+} and Fe^{3+}, or could indicate the simultaneous presence of these elements in the A- and B-sites.

Elevated Nb^{5+} occurs within brannerite-D (Figure 6.10e), whereas As^{5+} is elevated within brannerite-B and -C (Figure 6.10f). For both elements, the data appear to cluster rather than form a trend. However, the brannerite-A data exhibit a slight negative trend for As, even if As contents are low (usually <0.013 *apfu*).

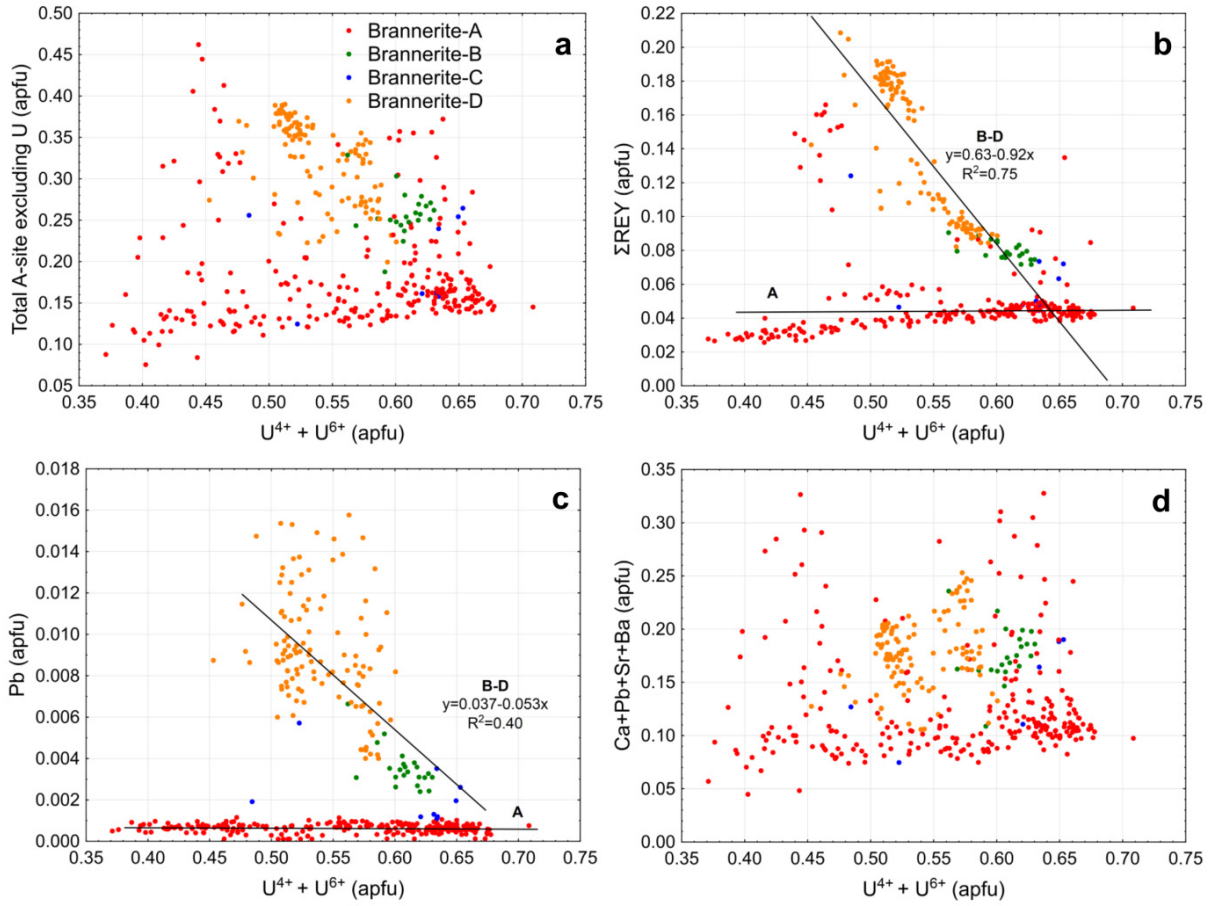

Figure 6.9: Scatterplots of selected A-site cations versus total U content of brannerite in atoms per formula unit (*apfu*); **(a)** Total A-site cations excluding U^{4+} and U^{6+} (i.e., Ca^{2+}, Sr^{2+}, Ba^{2+}, ΣREY^{3+}, Pb^{2+}, Th^{4+}) display no discernable trend with total U; **(b)** ΣREY show a negative correlation with total U, especially for brannerite-B to -D. Brannerite-A has a lower ΣREY content, so line-of-best fit is almost horizontal; **(c)** Pb has a negative correlation with total U, especially for brannerite-B to -D. Again, the low-Pb content of brannerite-A yields a horizontal line-of-best fit; **(d)** the addition of Ca, Sr and Ba to Pb content causes more scatter and provides less information than that gained by (c).

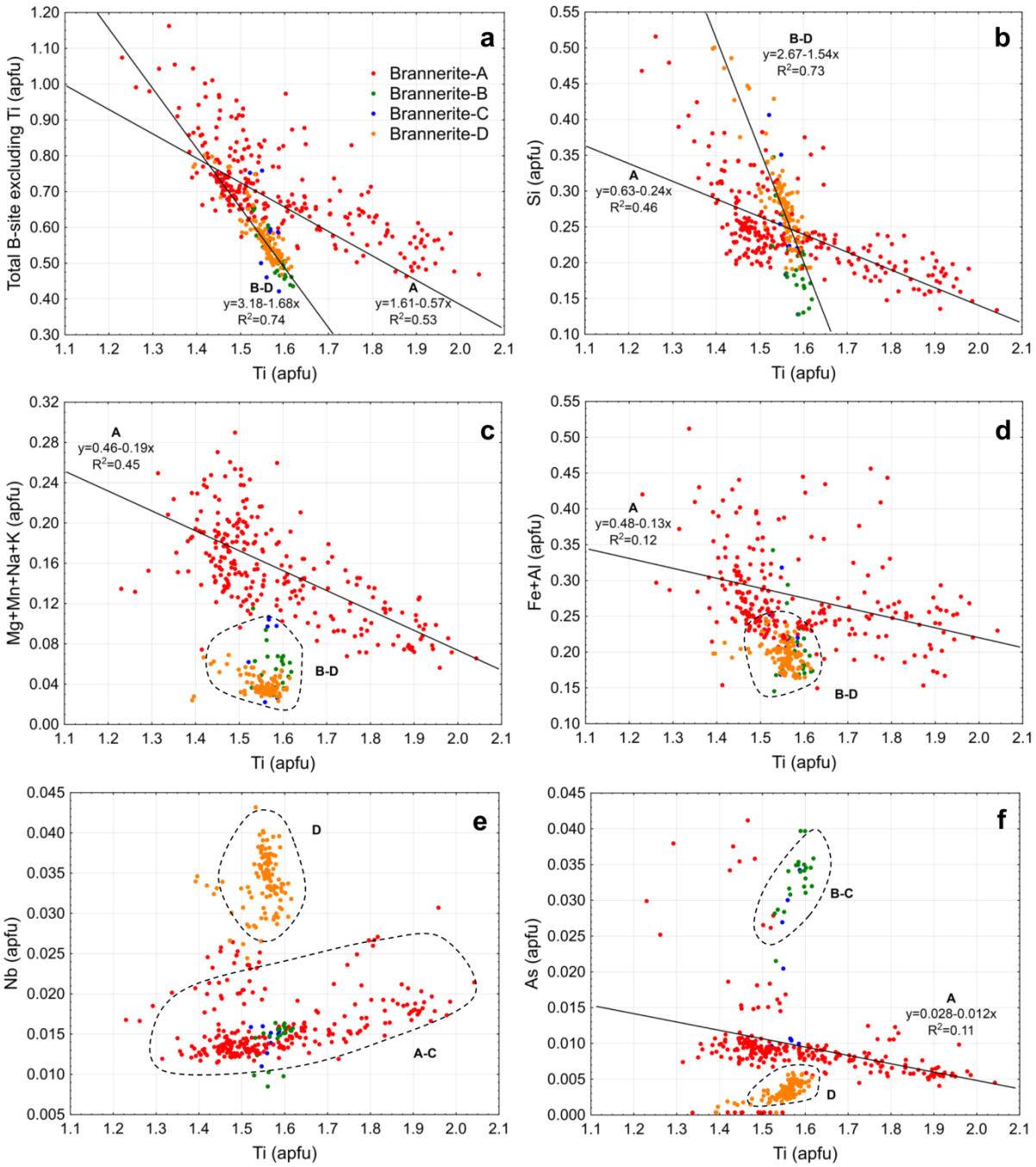

Figure 6.10: Scatterplots of selected B-site cations versus Ti content of brannerite (*apfu*); **(a)** total B-site cations excluding Ti^{4+} (i.e., Si^{4+}, Na^{+}, Mg^{2+}, Al^{3+}, K^{+}, Mn^{2+}, Fe^{3+}, As^{5+}, Zr^{4+}, Nb^{5+}) display two clear negative correlations. Brannerite-A appears to span a greater Si and Ti range compared to brannerite-B to -D; **(b)** Si has a negative correlation with Ti, again with data for brannerite-B to -D having a steeper line-of-best fit compared to data for brannerite-A; **(c)** divalent Mg and Mn with monovalent Na and K have a negative correction with Ti, especially for brannerite-A as shown by line-of-best fit. Brannerite-B to -D data cluster (circled by dashed line) beneath the line-of-best fit; **(d)** trivalent Fe and Al only display a weak negative correlation with Ti. Brannerite-B to -D data cluster (circled

by dashed line) beneath the line-of-best fit; **(e)** Nb data tend to cluster (circled by dashed lines) rather than form trends with Ti, with brannerite-D having the highest Nb content; **(f)** As data also tend to cluster (circled by dashed lines) rather than form trends with Ti, However, there is a negative correlation for brannerite-A and brannerite-B and-C have the highest As contents.

6.6.2 Trace element substitution into brannerite

Our results demonstrate the highly variable composition of brannerite at OD. Uranium is clearly replaced by significant, though variable amounts of Ca and ΣREY with up to 32% and 24%, respectively, of the A-site occupied by these substituents. These results are concordant with Lumpkin et al. (2012), who found that the A-site may contain appreciable Ca, Th, and ΣREY (up to 50-60% of the total A-site substituents). Mechanisms responsible for their incorporation into the A-site are poorly documented, but are most likely to be:

$$Ca^{2+} + U^{6+} \rightarrow 2U^{4+} \qquad \text{[b1]}$$

$$(REY)^{3+} + U^{5+} \rightarrow 2U^{4+} \qquad \text{[b2]}$$

Both coupled substitutions are plausible and would account for the observed correlations. Other cations for which mechanism [b1] may be relevant include Sr^{2+}, Ba^{2+} and Pb^{2+}. Diffuse reflectance spectroscopy and X-ray photoelectron spectroscopy (e.g., Vance et al., 2001; Finnie et al., 2003), has shown that synthetic brannerite contains U^{5+}, aiding charge balance to facilitate incorporation of Ca and ΣREY.

The Ti content of brannerite also varies, but appears less variable than U, with approximately 20% of the B-site occupied by substituents (Si, Fe, Na, Al, Nb, Zr, Mn, Mg, K, and As),

concordant with Lumpkin et al. (2012). Coupled B-site substitution of potential applicability here is:

$$(Fe, Al)^{3+} + Nb^{5+} \rightarrow 2Ti^{4+} \qquad \text{[b3]}$$

Niobium is, however, not always present and mechanism [b3] may only partly explain Fe and Al substitution. For OD brannerite, As^{5+} is also present in some brannerite and could readily join Nb^{5+} in mechanism [b3]. Arsenic-for-Ti exchange is plausible, although it has not been previously documented in brannerite. Charge balance for cations with lesser valencies than 4+ introduced into the B-site (i.e., Fe^{3+}, Mn^{2+}, Mg^{2+}, Na^{+} and K^{+}), could also be achieved by the addition of $(OH)^{-}$, i.e.:

$$Fe^{3+} \rightarrow Ti^{4+} + OH^{-} \qquad \text{[b4]}$$

$$(Mn, Mg)^{2+} + (Na, K)^{+} \rightarrow Ti^{4+} + OH^{-} \qquad \text{[b5]}$$

Substitutions [b4] and [b5] are, however, speculative and require confirmation by Raman infrared spectroscopy. Natural radiation-damaged brannerite can contain appreciable H_2O (up to 7.4 wt% at Crocker's Well; Ludwig and Cooper, 1984), thus supporting charge compensation by $(OH)^{-}$.

Silicon displays a negative correlation with Ti (Figure 6.10b) but it is unclear whether Si can directly substitute for Ti. It is known that Si is unlikely to substitute for Ti in octahedral coordination above trace levels at low pressures, and is thus thought to occupy interstitial rather than structural sites (Lumpkin et al., 2012). Detailed characterization at the nanoscale is required to ascertain whether Si is an interstitial and/or a structural component of brannerite.

Figure 6.11 and Table 6.2 clearly show there is generally a surplus of B-site occupancy (i.e., above ideal 2.0 *apfu*) and a corresponding deficit in the A-site (i.e., below ideal 1.0 *apfu*).

This observation supports a coupling of substitutions across the two sites. Furthermore, there is less variability of total A- and B-site values for brannerite-B to -D (circled with dashed line on Figure 6.11).

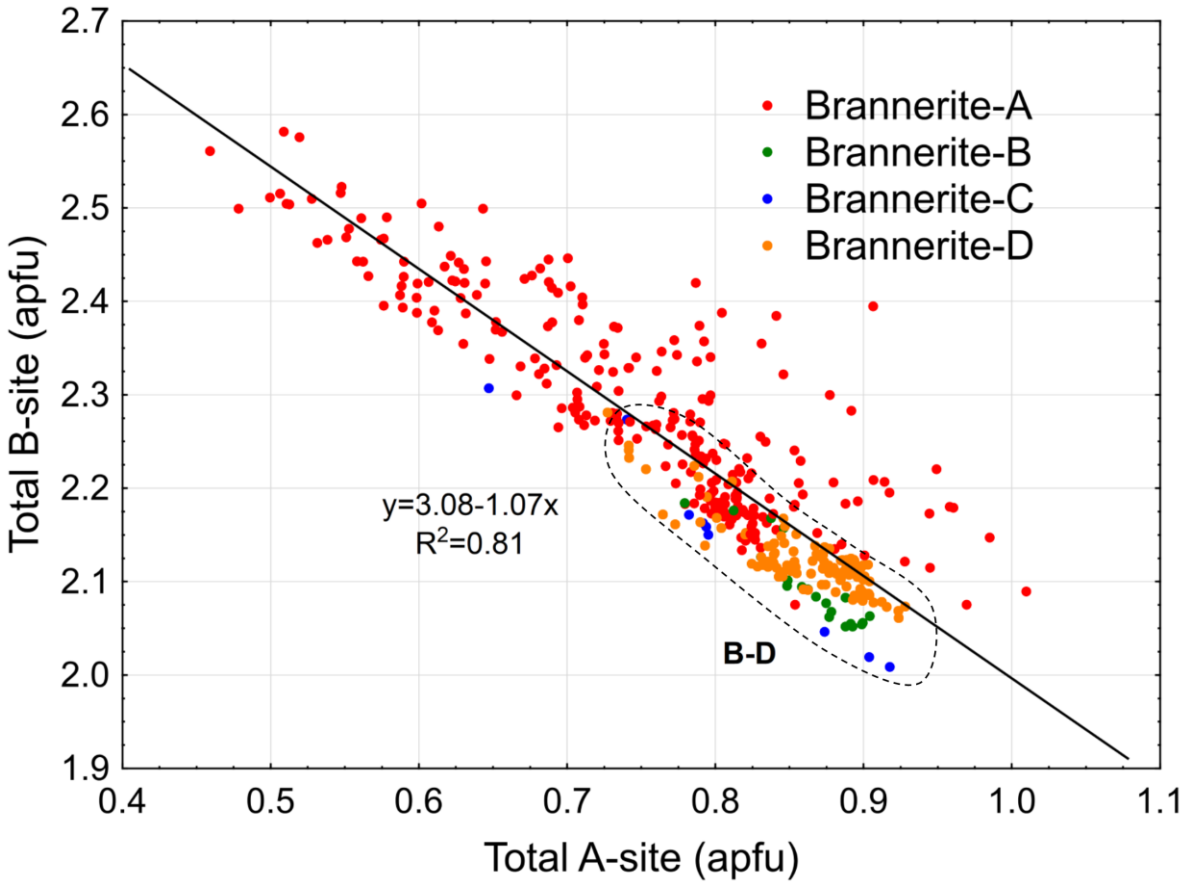

Figure 6.11: Scatterplot of total B-site cations versus total A-site cations for brannerite (*apfu*). There is generally a surplus of B-site charge (i.e., values above the ideal 2.0) and a deficit of A-site charge (i.e., values below the ideal 1.0). Data circled by dashed line represent brannerite-B to -D which have totals closest to ideal.

6.6.3 Brannerite formation

Formation of brannerite is generally linked to decomposition of ilmenite in the presence of U-bearing hydrothermal fluids, and the subsequent adsorption of U onto the surface of decomposing ilmenite (e.g., Ferris and Ruud, 1971). This process was originally described by

Ramdohr (1957), who suggested brannerite forms *in situ* via the 'Pronto reaction' where uranium migrates to Ti-rich phases, or titanium to uraninite, forming U-titanite:

$$UO_2 + 2 - 3TiO_2 \rightarrow UTi_{2-3}O_{6-8} \qquad \text{(1, Pronto reaction)}$$

The reaction results in the formation of 'uraninite ghosts': fine-grained brannerite splinters rimming the peripheries of abraded uraninite. Brannerite thus pseudomorphs rutile laths which are, in turn, originally derived from ilmenite. The 'Pronto reaction' (1) is thought to occur under hydrothermal conditions at temperatures of ~225 °C (Schidlowski, 1966).

Ramdohr (1957) and Schidlowski (1966) relate rutile to the decomposition of ilmenite but do not directly relate brannerite textures to those of ilmenite; however, this is covered by Ferris and Ruud (1971). Ilmenite is known to alter in stages so that any given grain may contain variable stringers, lamellae, patches and rims of material which differ, both crystallographically and chemically, from the original ilmenite (Lynd, 1960). This results in a mineral aggregate which has multiple Ti-bearing phases and leads to differential uptake of U. Iron is always removed.

OD brannerite often displays variable chemical composition and in some cases, displays evidence of further geochemical alteration by the presence of alteration rims (Figures 6.2d and 6.3a). Incorporation of Si, Ca, Na, ΣREY, Fe, Nb, As etc., substituting for U and Ti, are all potentially sourced from interactions with hydrothermal fluid(s). The variable U content of OD brannerite may be due to limited and/or variable supply of uranium to the sites of decomposing ilmenite, or alternatively due to oversupply of Ti and other elements. The compositional diversity observed may also reflect alteration of pre-existing brannerite. This may be particularly important for brannerite-C (Figures 6.2d and 6.3a) which shows evidence of marginal alteration. Notably, all OD brannerite has low-Th content (<mdl-1.38 wt% ThO_2).

It is known that uraninite formed at lower temperatures (<250 °C) characteristically contains less Th than if formed at >350 °C (e.g., Hazen et al., 2009). Sodium content is also commonly used to reflect low-temperature hydrothermal alteration. The Na content of all OD brannerite is fairly constant (0.05-1.88 wt% Na_2O).

A key observation for OD brannerite is that those with the highest U, typically occur on the margins of the brannerite-rutile-hematite aggregates (e.g., Figure 6.1a), and this grades into uraniferous rutile with lesser U toward the aggregate center. Ferris and Ruud (1971) explained this phenomenon using absorption of U onto titanogels. Titanogels and titanium oxyhydroxides are known to have high sorptive capacities for weak uranium solutions (Davies et al., 1964; Yermolayev, 1971). The transformation of ilmenite into various Ti-rich phases may have occurred progressively from the outside inward, one surface layer at a time, forming a titanogel or analogous compound. Thus as replacement progressed, rutile was formed from ilmenite in the presence of a U-bearing solution, and TiO_2 incorporated U within each layer that crystallized. The rate of formation of rutile or the precursor titanogel and the concentration of U in solution would ultimately control the composition(s) of the precipitating brannerite, and where little or no U was available, only rutile (or anatase) would form. Such a process accounts for the observed textural variability, where within brannerite containing aggregates there is a mix of brannerite laths, and partially replaced uraniferous rutile. The mix of brannerite and rutile layers can be explained in terms of fluctuating U content in the fluid.

Replacement of ilmenite by rutile in an acidic environment was explored by Janssen et al. (2010), invoking coupled dissolution-reprecipitation (CDR) reaction (Putnis, 2002). Janssen et al. (2010) found that alteration begins at the original ilmenite crystal surface and moves inward along fractures generated by the volume changes associated with ilmenite dissolution, and there is simultaneous reprecipitation of rutile (i.e., pseudomorphic replacement of the

original ilmenite with rutile). This may also be applicable to brannerite, with the key difference being the presence of U within a hydrothermal fluid. Geisler et al. (2005a) showed clear evidence that alteration of crystalline pyrochlore-type ceramics $[(Ca,Na,Sr)_2(Ta,Nb,Ti,Si)_2O_6F)]$ is CDR-controlled rather than a function of diffusion-controlled leaching.

To explain the association of brannerite with sulfides, Ferris and Ruud (1971) use the work of Gruner (1959) to show that H_2S-saturated fluids will react with ilmenite to form rutile and pyrite at >220 °C:

$$FeTiO_3 + H_2S \rightarrow TiO_2 + FeS + H_2O \qquad (2)$$

$$FeS + H_2S \rightarrow FeS_2 + H_2 \qquad (3)$$

Adams et al. (1974) alternatively suggest that alteration of magnetite and ilmenite by O_2-deficient groundwaters can occur at Eh<-0.2 and pH<7. Pyrite and uraninite would be preserved but the reaction still allows for decomposition of both magnetite and ilmenite as temperatures decrease. This may be applicable to OD brannerite, which typically is associated with sulfides and barite.

Another key parameter to be considered in the formation and alteration of brannerite is the role of radiation damage. In older brannerite which displays substantial radiation damage, the Pb content is expected to be higher, assuming that lead has not migrated from the parent mineral. Lead may serve as a network modifier, particularly when accompanied by elevated Si, since the Ti-Si-O framework allows for retention of radiogenic Pb (Lumpkin et al., 2012). However, losses of significant amounts of radiogenic Pb from brannerite (~40%; Lumpkin et al., 2012) have also been reported, and in these cases brannerite often contains abundant fine

galena particles. This has been attributed to local trapping of Pb, whereby brannerite has been exposed to fluids containing S (e.g., Lumpkin et al., 2012, and references therein).

Overall, OD brannerite contains low concentrations of Pb (<mdl-1.93 wt% PbO), thus either indicating that the various types of brannerite are young (i.e., insufficient time for significant production of radiogenic Pb), or that Pb has been mobilized out of brannerite. The only brannerite at OD found in close proximity to galena is brannerite-D. There are three possible explanations for the spatial association of galena and brannerite. Firstly, galena may be non-radiogenic and trapped within brannerite during initial mineralization, an interpretation supported by the abundant co-existing sphalerite within these samples. Alternatively, brannerite-D may represent an older generation of brannerite from which radiogenic Pb has not migrated from the parent mineral but instead formed galena. This is supported by the distinctive trace element signature of brannerite-D, with higher ΣREY than all other brannerite types. A final possibility is that the abundance of contained galena in brannerite-D relates to decay or replacement of pre-existing uraninite.

6.6.4 Compositional trends for coffinite

To further understand element variability within the different coffinite groups, the most strongly correlating elements in the A- or B-sites are plotted (Figures 6.12 and 6.13). In some cases, the data for coffinite-B have distinct trend lines which differ to those of the overall coffinite dataset, highlighting key chemical differences. Firstly, some of the A-site substitutions are considered: Ca vs. total U (Figure 6.12a); and ΣREY vs. total U (Figure 6.12b). Calcium correlates positively with U whereas ΣREY shows a broadly negative correlation with U. The line-of-best fit for coffinite-B data (Figure 6.12a) is offset to that of the bulk of the coffinite analyses, indicating that coffinite-B contains more Ca than the other coffinite types. A positive correlation between Ca and U is expected since, as shown by

varying the brightness and contrast of some of the coffinite globules (Figures 6.4b and 6.5b-c), the brighter coffinite always contains more Ca and U than the duller coffinite, which is instead elevated in Si. The ΣREY content of coffinite-B (Figure 6.12b) is lower than in the majority of coffinite analyses, but there is nevertheless a slight positive correlation between ΣREY and total U for coffinite-B, contrasting with the negative correlation seen for the majority of analyses.

A-site Ca is plotted against B-site Si on Figure 6.12c, exposing a negative correlation. Again the line-of-best fit for coffinite-B appears offset to that of the other coffinite types, but the trends are similar. Pentavalent P, As and Nb plotted against Si (Figure 6.12d) shows a broadly negative correlation, except for coffinite-B for which there is a slight positive correlation. Clear differences in brightness and contrast were observed on BSE images of individual coffinite globules of coffinite-B (Figure 6.5a-c). These were attributed to higher Si and P (duller coffinite), or higher ΣREY, Ca and Fe content (brighter coffinite). The positive correlation between Si and P is unusual, and only applies to coffinite-B. An inverse relationship would be expected if Si and P contents were directly coupled.

Plotting ΣREY against Σ(P,As,Nb) (Figure 6.12e) shows a positive correlation, but if coffinite analyses with the greatest ΣREY or Σ(P,As,Nb) contents are removed, there is no apparent relationship. This implies that these two variables alone do not control element substitution patterns.

As expected, B-site Si content (Figure 6.12f) has a negative correlation with A-site Σ(U,Th,Ca). To achieve charge balance, coffinite with the highest U content would be expected to have the lowest Si content and *vice versa*.

Overall, a negative correlation between total B-site cations versus total A-site cations is observed (Figure 6.13a). The ideal totals for both the A- and B-site totals are 1, and hence for

comparison the 1:1 line is superimposed on the figure. Our data closely fit the 1:1 relationship, although A-site totals often exceed B-site totals causing the slope of the line to shift slightly downwards (slope of -0.91).

All analyses for the A-site cations plot near the U apex on a U-ΣREY-Ca ternary plot (Figure 6.13b). Two distinct trends are, however, identifiable: 1) coffinite-C appear to have elevated ΣREY; and 2) coffinite-B contain the least ΣREY, but the most Ca. This may indicate formation of coffinite from fluids of differing local chemistries.

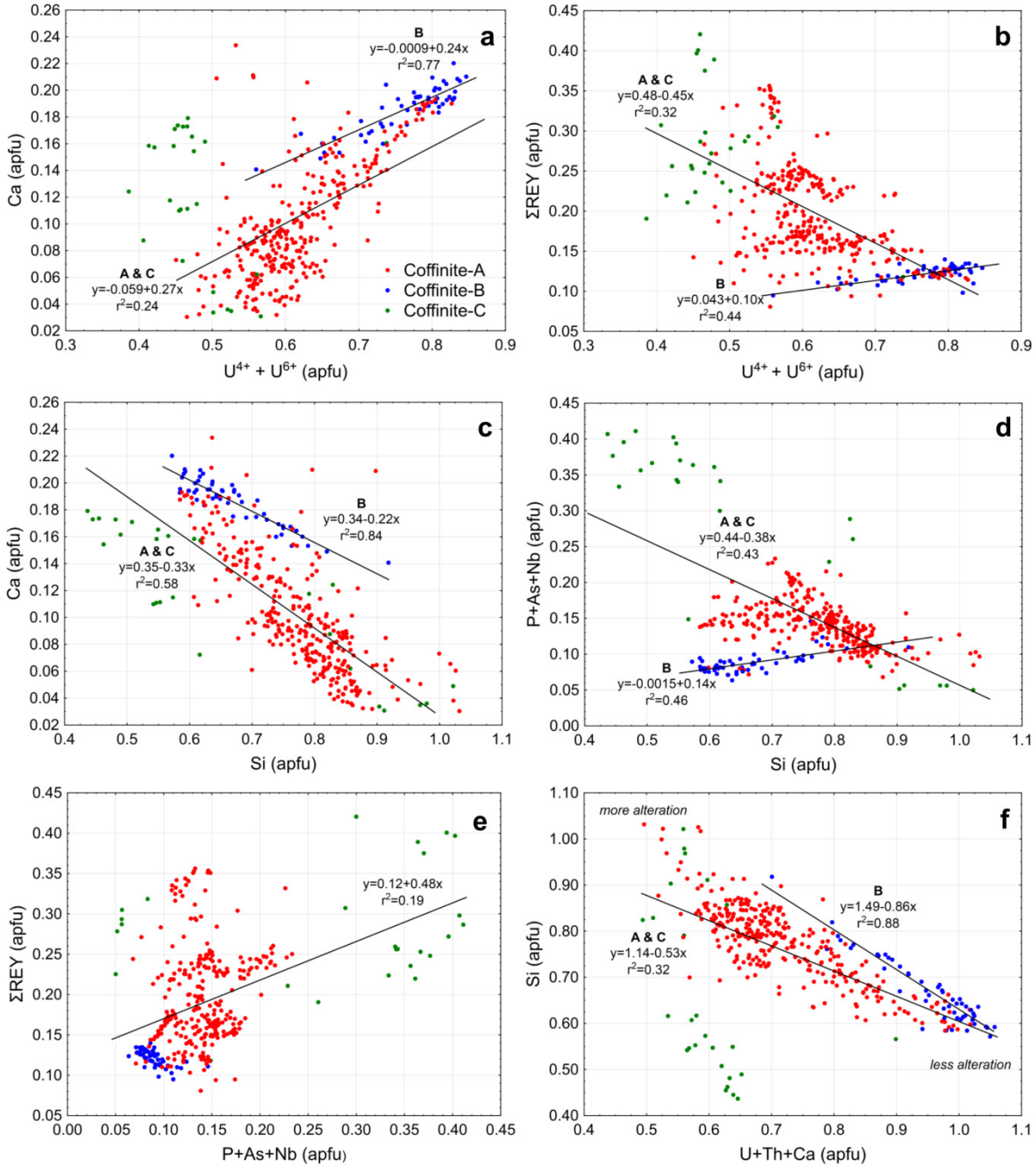

Figure 6.12: Scatterplots of selected A- and B-site cations for coffinite (*apfu*); **(a)** Ca vs. total U shows a positive correlation; **(b)** ΣREY vs. total U has an overall negative correlation, with the low ΣREY content of coffinite-B causing the line-of-best fit to be almost horizontal; **(c)** Ca vs. Si has a negative correlation; **(d)** Σ(P,As,Nb) versus Si has a negative correlation for all coffinite types except coffinite-B; **(e)** ΣREY vs. Σ(P,As,Nb) has an overall positive correlation; **(f)** Si vs. Σ(U,Th,Ca) has a negative correlation.

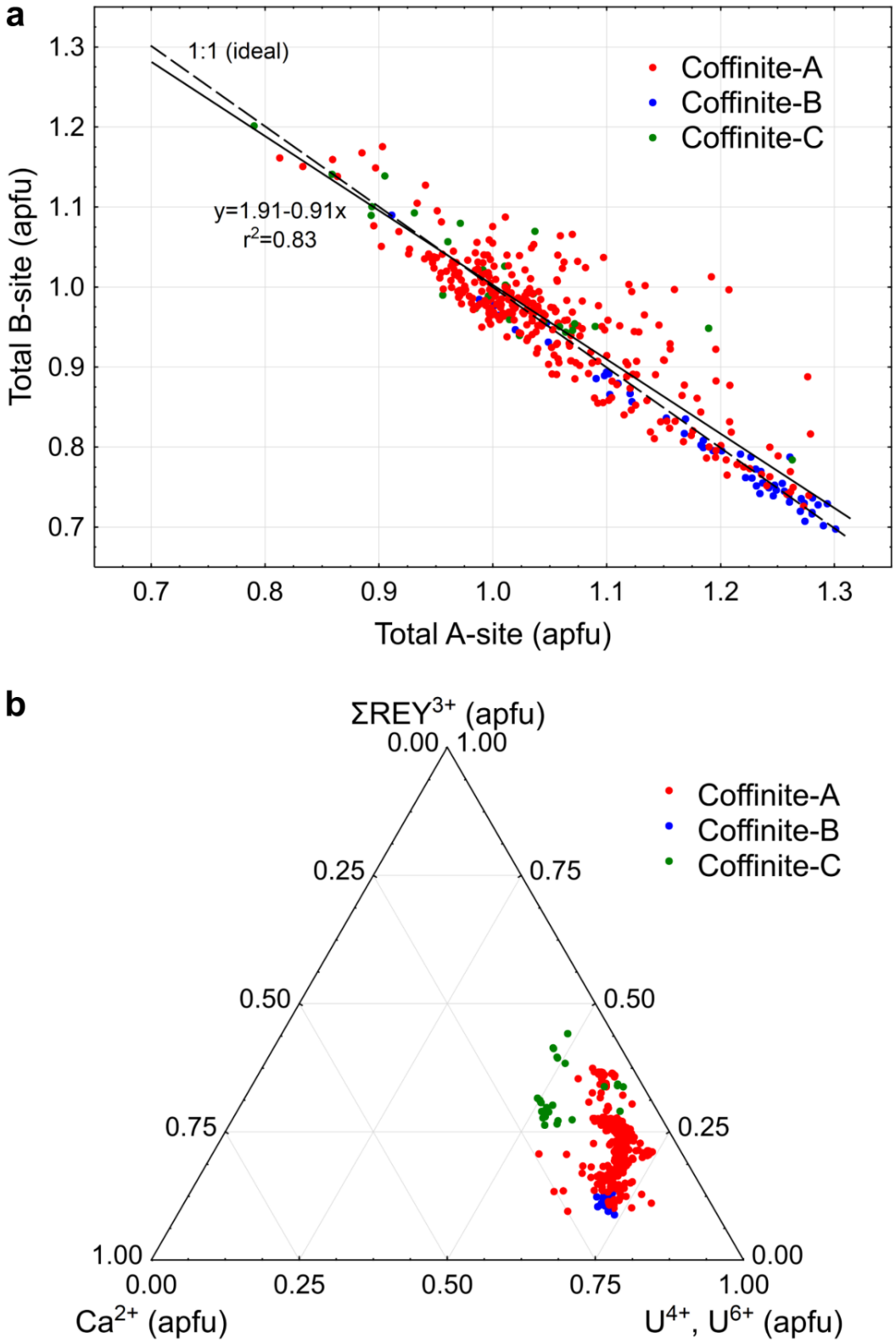

Figure 6.13: (a) Scatterplot of total B-site cations versus total A-site cations for coffinite (*apfu*). There is a negative correlation close to the expected 1:1; **(b)** Ternary plot of ΣREY^{3+} vs. $U^{4+}+U^{6+}$ and Ca^{2+}. The majority of coffinite-A and -C cluster together and form a trend toward increasing ΣREY^{3+}. Coffinite-B cluster together toward the $U^{4+}+U^{6+}$ apex, whereas coffinite-C form their own cluster with elevated ΣREY^{3+}.

6.6.5 Trace element substitution into coffinite

Several substitution mechanisms are reported to occur in coffinite to balance charge (Hansley and Fitzpatrick, 1989; Janeczek and Ewing, 1996; Förster, 2006; Deditius et al., 2008 and references therein). These include:

$$(REY)^{3+} + P^{5+} \leftrightarrow U^{4+} + Si^{4+} \quad [c1]$$

$$Ca^{2+} + U^{6+} \leftrightarrow 2U^{4+} \quad [c2]$$

$$2Ca^{2+} + 0.8P^{5+} + 0.2^{IV}[\quad] \leftrightarrow U^{4+} + Si^{4+} \quad [c3]$$

$$2Ca^{2+} + P^{5+} + (OH)^{-} \leftrightarrow U^{4+} + Si^{4+} \quad [c4]$$

$$2(REY)^{3+} + (Ca, Fe)^{2+} \leftrightarrow 2(U, Th, Zr)^{4+} \quad [c5]$$

$$(REY)^{3+} + (As, Nb, P)^{5+} \leftrightarrow U^{4+} + Si^{4+} \quad [c6]$$

$$Ca^{2+} + (As, Nb, P)^{5+} \leftrightarrow REY^{3+} + Si^{4+} \quad [c7]$$

$$P^{5+} + Al^{3+} \leftrightarrow 2Si^{4+} \quad [c8]$$

$$U^{4+} + Si^{4+} \leftrightarrow U^{6+} + \left[2(OH)^{-}, 0.5[\quad]\right] \quad [c9]$$

$$Ca^{2+} + S^{6+} \leftrightarrow U^{4+} + Si^{4+} \quad [c10]$$

$$2Y^{3+} + U^{6+} \leftrightarrow 3U^{4+} \quad [c11]$$

Mechanisms [c1] to [c5] probably all contribute to the element substitutions in OD coffinite, although their relative roles vary from one coffinite group to the next. In terms of the marked P and Y enrichment in some coffinite, coupled xenotime-type substitution [c1] (Hansley and Fitzpatrick, 1989) involves ΣREY^{3+} incorporation into octahedral A-sites, and charge balance

via P^{5+} substitution in the tetrahedral B-site. Janeczek and Ewing (1996), however, warn that mechanism [c1] alone cannot explain the composition of some high-Ca coffinite where the ΣREY content is too low, and P content too high. These authors explained the formation of high-Ca coffinite via limited solid solution with ningyoite, $(U,Ca,Ce)(PO_4)_2 \bullet 1\text{-}2H_2O$, thereby allowing for the substitution of Ca and P for U, and Si (i.e., mechanisms [c2]-[c4]). The $^{IV}[\ ]$ represents tetrahedral-site vacancies in the coffinite structure, which would allow for cation deficiencies in the tetrahedral site. A deficiency in silica (i.e., A>B) is identified in analyses of Bangombé coffinite (Janeczek and Ewing, 1996), and this deficiency is also observed for OD coffinite. Mechanisms [c3] and [c4] may help explain this phenomenon. Substitution [c2] yields a positive correlation between Ca^{2+} and U^{6+}, whereas substitutions [c3] to [c5] would yield negative correlations between Ca^{2+} and U^{4+}. Substitution [c5] (Förster, 2006) only involves A-site elements and may also be important. Moreover, a similar substitution to [c1] is the substitution of As^{5+} and Nb^{5+}, in addition to P^{5+}, into the A-site, allowing for chernovite [$YAsO_4$]-type substitution [c6] (Janeczek and Ewing, 1996), but Ca^{2+} and ΣREY^{3+} may compete for charge compensation via [c7] (Deditius et al., 2008). It is likely that P^{5+} plays an important role in coupled substitution since it is present in moderate quantities (mean 0.12 *apfu*). The main substituting cations in OD coffinite are Ca^{2+}, Fe^{2+} and ΣREY^{3+}, which substitute for U^{4+} in the A-site, and P^{5+} which substitutes for Si^{4+} in the B-site.

Another possible substitution mechanism is Al^{3+} substitution [c8] for both the A- and B-sites within thorite (Förster, 2006), and this may also be applicable here. However, due to the fairly low Al content of OD coffinite (mean ~0.03 *apfu*), and the fact that aluminosilicates have been identified within coffinite (e.g., Figure 6.6c), we have decided not to consider this type of substitution any further.

As discussed above, a negative correlation between total cations in the A- and B-sites is observed (Figure 6.13a), with the slope of the line-of-best-fit being -0.91 (i.e., A-site totals typically exceed B-site totals). We have assumed the presence of U^{6+} when calculating structural formulae, which may explain the higher A-site values. To compensate for the excess positive charge from U^{6+}, either $(OH)^-$, or vacancies in the Si position (mechanism [c9]) may be present, which may be in turn be linked to mechanism [c2]. Likewise, the presence of excess Ca^{2+} and ΣREY^{3+} may lead to higher A-site totals.

Another mechanism, [c10] that may play a significant role is S-for-Si substitution, resulting in enhanced incorporation of P and ΣREY (Jensen and Ewing, 1998; Deditius et al., 2009). The presence of S reduces the number of vacancies needed in the coffinite structure, in turn aiding charge balance and allowing incorporation of less abundant elements (Tables 6.3a and 6.3b). Coffinite-C2 and -C3 contain the most P (0.36 and 0.28 *apfu*, respectively) and also have the highest levels of S (0.063 and 0.068 *apfu*, respectively), inferring that mechanism [c10] is of importance, especially for the most P-rich coffinite.

The maximum Y content measured in coffinite was 15.6 wt% Y_2O_3 (0.38 *apfu*), and this contributes to some of the high A-site totals. Yttrium is typically accommodated by elevated P levels (coffinite-xenotime solid solution [c1]; Figure 6.12e). An alternative mechanism [c11] involves Y^{3+} and U^{6+} substitution for U^{4+} (Pointer et al., 1988). This may also be relevant for the OD coffinite, since to balance charge, the presence of U^{6+} has been assumed.

The key interdependencies among various cations (Figures 6.12 and 6.13) were discussed above, but in light of the different coupled substitutions, the following points should also be raised. The negative correlation between Si and Ca (Figure 6.12c) and positive correlation between U and Ca (Figure 6.12a) may indicate that Ca^{2+} incorporation results in Si^{4+} loss from the B-site. P^{5+} also generally shows a negative correlation with Si^{4+} (Figure 6.12d), thus

supporting mechanisms [c3] and [c4]. The negative correlation between ΣREY and U (Figure 6.12b) strongly indicates competition between ΣREY and U for A-site occupancy during crystallization.

6.6.6 Coffinite formation

Coffinite can be found in a variety of environments, but typically results from low-temperature processes. In some cases, coffinite formation involves alteration of previously precipitated uraninite through the uptake of silica (coffinitization). When this occurs, it usually happens at the margins of uraninites, or in domains that show signs of alteration (Janeczek and Ewing, 1995). Alternatively, coffinite may form as a result of changing redox, $a SiO_2$, pH, temperature, or pressure conditions, which induce coffinite precipitation. For example, the concentration of $H_4SiO_{4(aq)}$ in groundwater is controlled by the presence of Al-silicates and quartz (Robit-Pointeau et al., 2006). Also, in the presence of sulfides, and with sufficient Si concentration, coffinite will be precipitated in preference to uraninite (Janeczek and Ewing, 1992a; Fayek et al., 1997). This may suggest that coffinite is more stable than uraninite in reducing, Si-rich environments.

To precipitate any mineral from solution, local conditions need to change to allow precipitation to take place. In terms of the precipitation of oxidized U, one possible mechanism to induce precipitation of U^{4+}-minerals is the presence of a reductant. Coffinite commonly displays a close association with sulfides or organic matter; these will retard migration and subsequently reduce U^{6+} in solution to U^{4+} (e.g., Goldhaber et al., 1987; Hansley and Fitzpatrick, 1989). For both coffinite (e.g., Figure 6.4e-f) and brannerite (Figures 6.1b, 6.2d and 6.3a-f) at OD, the close association with Cu-(Fe)-sulfides is ubiquitous, and these are the most likely reductants. An additional observation for coffinite is the presence of chlorite inside individual coffinite globules (Figure 6.6c), as well as intergrowths of chlorite

and sericite with brannerite (Figure 6.6a-b). Reduced Fe is present in aluminosilicates such as chlorite, and these have been shown to be the principal reductants of oxidized uranium from some hydrothermal fluids (Komninou and Sverjensky, 1996; Gregory et al., 2005). Destruction of the Fe-rich silicates releases Fe^{2+} and causes reduction of solution U^{6+}. Thus, as the hydrothermal fluids interact with aluminosilicates, these begin to dissolve, releasing Si, Fe, Ti etc., which may then be incorporated into the precipitating U-minerals.

The concentration of Th in coffinite is typically below mdl (e.g., Hansley and Fitzpatrick, 1989; Deditius et al., 2008), and this is also true for OD coffinite. Thorite precipitates at 200-400 °C, whereas coffinite usually precipitates at far lower temperatures (100-140 °C; Goldhaber et al., 1987; Janeczek and Ewing, 1992a; Förster, 2006). Thus the absence of Th is expected in coffinite, especially if the mineral forms as an alteration product of uraninite under Si-rich, low-temperature, reducing conditions (e.g., Janeczek and Ewing, 1992a).

6.6.7 Evolution of brannerite and coffinite at Olympic Dam

The distinct chemistries of the different brannerite groups may indicate that the local conditions that formed brannerite-A were different to those that formed brannerite-B to -D, or that they formed at different times. Brannerite-A, typically has elevated (Mg+Mn+Na+K) and (Fe+Al) concentrations (Figure 6.10c and d, respectively), but lower ΣREY, Pb and other A-site substituents (Figure 6.9) compared to brannerite-B to -D. There is also a difference in pentavalent B-site substitution, with elevated Nb in brannerite-D, and As in brannerite-B and -C, possibly resulting from the greater availability of these cations via breakdown of phases initially containing them. Alternatively, the low-ΣREY content of brannerite-A may suggest that ΣREY may have precipitated into another mineral (i.e., REY-minerals) in preference to brannerite.

Based on the needle- and lath-like internal structure of brannerite (especially brannerite-A), it is likely that formation involved decomposition of ilmenite/leucoxene in the presence of a Cu-U-bearing fluid. U in solution combined with titania to form uraniferous rutile grading into brannerite, and the leached iron from ilmenite decomposition combined with sulfur and metals in the hydrothermal fluid to form sulfides. The presence of S may have aided alteration of ilmenite and stabilized partially leached uraninite. Brannerite-B to -D have a more massive-uniform internal structure but also show evidence of lath-like textures on their margins, suggesting formation via an analogous mechanism. These brannerite types appear to have replaced Ti-rich hematite, or rutile in close association with hematite. Irrespective of the replaced mineral, the chemistry of replacement is considered similar.

Coffinite exhibits variable chemistry (Figures 6.12 and 6.13); coffinite-B is especially distinct from the other groups. Coffinite-B has more Ca, but less ΣREY replacing U, and typically lower (P+As+Nb) contents than the other groups. Coffinite-C has elevated ΣREY, whereas coffinite-A shows the broadest range of substituents. In two examples (e.g., Figure 6.12b and d) coffinite-B displays a positive trend, whereas coffinite-A and -C exhibit negative trends, further highlighting that substitution mechanisms for coffinite-B likely differ to those for coffinite-A and -C.

Since coffinite-B is associated with massive uraninite, it is likely that these formed as a result of remobilization of U from uraninite or from direct replacement of that mineral. Massive uraninites also contain significant Ca and have lower ΣREY contents than crystalline uraninites (Macmillan et al., 2016). The higher ΣREY and (P+As+Nb) contents of coffinite-C (Figure 6.12b and d, respectively), may indicate that these precipitated from fluids carrying elevated concentrations of these elements. This is not unexpected since these coffinite types

are found in association with brannerite (Figure 6.6a-b) or REY-minerals (Figure 6.6d), both of which contain ΣREY.

Textural observations and chemical differences allow us to conclude that brannerite and coffinite precipitated as part of a late-stage U-event at OD. This may have involved dissolution and/or reprecipitation of earlier uraninite, or may have involved a fresh influx of U. Key observations which support late-stage formation include: 1) low-Pb contents of both brannerite and coffinite, indicating these minerals experienced little radioactive decay and/or that radiogenic Pb was mobilized from these minerals; 2) coffinitization is often evident on the edges of uraninite crystals (Figure 6.5d), thus implying this process occurred after uraninite deposition; 3) coffinite in contact with massive uraninite (Figure 6.5a-c) occurs on the edges of these masses, and this uraninite contains much higher Pb than coffinite; 4) where brannerite and coffinite are found in close association (i.e., Figure 6.6a-b), the coffinite occurs on the margins of brannerite, suggesting brannerite pre-dates coffinite.

Other key observations include the fact that brannerite sometimes touches coffinite but is rarely found touching uraninite (Figure 6.7). Three hypotheses may explain this: 1) brannerite formation was not the result of dissolution of earlier uraninite, but formed from another source of U; 2) brannerite did not form as a result of direct replacement of earlier precipitated uraninite; or 3) any U that has been remobilized from earlier precipitated uraninite has been transported away from the site of initial dissolution and subsequently precipitated elsewhere as brannerite. Uraninite is chemically active, readily dissolved and mobilized in the presence of fluids. It therefore exchanges elements and reprecipitates easily during fluid circulation and mineral replacement (Grandstaff, 1976; Kotzer and Kyser, 1993; Alexandre and Kyser, 2005). The solubility of uraninite increases with temperature and with increased concentrations of F, Cl and/or CO_2 (Keppler and Wyllie, 1990). It is only sparingly soluble in reducing

groundwaters under normal pH conditions (e.g., Parks and Pohl, 1988). Furthermore, the migration of U in reducing groundwaters is aided by the stability of U^{4+}-fluoride complexes at pH<4 (Finch and Murakami, 1999).

Conversely, coffinite is often found touching both uraninite and brannerite (Figure 6.8), or on the periphery of these minerals. It is therefore logical that fluids reacted with previously precipitated uraninite and/or brannerite, mobilized U from these minerals, and subsequently precipitated coffinite. The fluid must have had sufficient SiO_2 content to precipitate coffinite rather than uraninite.

Precipitation of both brannerite and coffinite from solution, whether oxidizing or reducing, requires a nucleation site. It has been mentioned above that in most cases, both brannerite and coffinite are intimately associated with either sulfides, or Fe^{2+}-bearing aluminosilicates (notably chlorite). It is thus likely that the hydrothermal fluid contained oxidized uranium, and the sulfides and/or chlorite acted as reductants, reducing uranyl species from solution.

Both brannerite and coffinite are most strongly associated with hematite, sericite/chlorite, quartz and fluorite (Figures 6.7 and 6.8). It is common to see both brannerite and coffinite within bands of sericite, chlorite and/or fluorite. The permeability of such intervals is likely greater than those dominated by quartz or hematite. The presence of brannerite/coffinite within these bands may reflect penetration by hydrothermal fluid, and precipitation of these minerals (+ fluorite) from that fluid. From observed mineral inclusions contained within brannerite and surrounding minerals, it is likely that the fluid/s contained F, Cu, Fe, S, Si and Ca, as well as Na and K derived from partial dissolution and alteration of feldspars (Kontonikas-Charos et al., in review).

6.7 Future work and concluding remarks

The evolution of uranium minerals at OD over the past 1.6 billion years is complex and difficult to reconstruct unequivocally. Microanalytical and petrographic observations nevertheless provide evidence for an interpretation in which brannerite and coffinite largely represent the products of later U mineralizing events. Together with new data for uraninite (Macmillan et al., 2016), these observations highlight the role of multiple stages of U dissolution and reprecipitation. The cyclic nature of these events is reflected in marked chemical and textural differences between the various types of brannerite and coffinite.

We suggest that dominant substitutions within brannerite include Ca^{2+} and REY^{3+} in the A-site (replacing U^{4+} and/or U^{6+}), and Si^{4+}, Na^{+} and Fe^{3+} in the B-site, replacing Ti^{4+}. For coffinite, dominant substitutions include Ca^{2+}, Fe^{2+} and REY^{3+} in the A-site (replacing U^{4+} and/or U^{6+}), and P^{5+} in the B-site, replacing Si^{4+}. Further work is required to either validate these substitutions into the A- and B-sites of brannerite and coffinite, or to determine if these elements occur within interstitial sites. This could be done, for example, by nanoscale chemical mapping of foils prepared *in-situ* by FIB-SEM. The valency state of U also impacts on assumptions made for derivation of structural formulae, so attempts to ascertain whether multiple valencies of U are present, e.g., by X-ray absorption spectroscopy (XAS), are warranted. The presence of structural water or $(OH)^{-}$ within both brannerite and coffinite has also been documented in many studies, and could be explored via Raman infrared spectroscopy.

Integrating the chemical and textural results reported here with those reported elsewhere (e.g., Kirchenbaur et al., 2016; Macmillan et al., 2016) expands understanding of the sequence of events that generated the uranium mineralization at Olympic Dam. The work represents a

critical step towards development of a paragenetic sequence for U-mineralization and a genetic model for the deposit.

6.8 Acknowledgements

This work forms part of the Ph.D. studies of E.M. and is supported by BHP Billiton. Ken Neubauer, Angus Netting and Benjamin Wade (Adelaide Microscopy) are thanked for SEM and EPMA training, respectively. Nicole Allen is thanked for her assistance with EPMA.

CHAPTER 7

CONCLUSIONS & RECOMMENDATIONS

CHAPTER 7: CONCLUSIONS & RECOMMENDATIONS

Olympic Dam is the largest economic uranium resource in the world, but the characterization of the U-minerals and processes involved in their formation have only recently been understood and documented. Uranium displays a complex and highly variable paragenesis, with multiple stages of U dissolution and reprecipitation readily recognizable. This study has advanced our knowledge of the U-minerals contained within the OD deposit, and has provided detailed chemical and textural data to help define the diverse range of complex U-mineral textures observed at this deposit. Extensive analysis of uraninite has revealed that there are two distinct generations, and that Pb is both lattice-bound and inclusion-hosted within uraninite, thereby necessitating a revision of the commonly-used structural formula for uraninite proposed by Janeczek and Ewing (1992c) to suit the heterogeneity of uraninite at OD.

Suggestions have been made about the processes involved in the formation and modification of chemical zoning within certain types of uraninite. Some of the individual uraninite crystals display rhythmic intergrowths with Cu-(Fe)-sulfides, and it has been shown that coupled dissolution-reprecipitation reactions were responsible for at least partial replacement of uraninite crystals by bornite and fluorite. Replacement was likely driven by a F-rich hydrothermal fluid that was also enriched in Cu, S, Fe and Ca. Hydrothermal fluids have played a pivotal role in forming the mineral textures that are observed today. Their likely composition(s) remain speculative, however, the presence of fluorite within or around many of the intergrown U-mineral textures is suggestive that a F-rich fluid was involved. The other significant contribution to the understanding of the U-minerals made by this research is a detailed characterization of the chemical and textural heterogeneity of brannerite and coffinite, which likely formed late in the evolution of the deposit.

7.1 The evolution of uraninite

The seminal research that formed the foundation of much of the subsequent research carried out within the project, was the characterization of the chemical and textural variability of uraninite from OD. Initial work combined microanalytical data, petrographic observations, and nanoscale characterization of individual uraninite grains to show that there were at least two main uraninite mineralizing events at OD, and multiple stages of U dissolution and reprecipitation. Of these two generations of uraninite, four main textural classes were identified: 1) primary, 2) zoned, 3) cob-web and 4) massive. The primary to cob-web uraninites represent the early generation, and are characterized by Pb- and ΣREY-rich single-grains (tens to hundreds of μm). In contrast, the texturally later massive uraninites consist of Pb- and ΣREY-poor, often Ca-rich fine-grained (~1-3 μm) massive aggregates. Furthermore, an evolutionary trend for primary to cob-web uraninites is recognized, in which the same grain experiences cycles of *in-situ* growth, dissolution and recrystallization.

Trace and minor-element trends, as well as textural observations aided in identification of this cycle. Inclusion-hosted Pb (as galena), as well as regions of high- and low-Pb content (lattice-bound, oscillatory-zoned domains) were identified, especially for primary to cob-web uraninites. The variable Pb deportment may indicate that some of the Pb^{4+} has been converted to Pb^{2+} via auto-reduction. Due to the relative incompatibility of Pb^{2+}, it is forced out of the uraninite structure. Alternatively, radiation damage to uraninite (i.e., fission tracks, metamict domains, regions impacted by release of He and/or Rn) may have formed amorphous regions which allowed for Pb diffusion and/or percolation of fluids into uraninite. These however, heal over time due to the rapid annealing kinetics of uraninite. The discovery of lattice-bound Pb and ΣREY within uraninite prompted revision of the structural formula for uraninite. Calculations for the oxidation state [$U^{6+}/(U^{4+}+U^{6+})$] of the early and late uraninite populations

were also made and point to different conditions at the time of formation. It is likely that all late uraninites formed at significantly lower-temperatures (T<250 °C). The early uraninites are thought to have formed from higher-temperature, granite-derived hydrothermal fluids, with later hydrothermal alteration of the zoned and cob-web types (these have elevated Na, Mn, Ca, Si).

Identification of zoned uraninites and their unusual zonation patterns prompted further work to characterize their formation and subsequent development. The primary uraninite has a cubic habit with core-to-margin oscillatory and sectorial zoning of Pb and ΣREY, which is consistent with primary growth mechanisms. In contrast, zoned uraninite is often prismatic in habit and zonation shows no correlation with the morphology of the grain. Microstructural analysis was conducted via the use of EBSD, and this was the first study that sought to apply EBSD techniques to the formation of microstructures within uraninite. It was shown that formation of zoned uraninite is the result of a sequence of superimposed effects rather than from primary growth mechanisms alone. Chemical zonation is a consequence of the alteration of initial oscillatory zoning, whereby radioactive decay (e.g., increased Pb content and annealing of radiation damage), and the interaction between uraninite and ingressing fluids along zones of structural weakness (e.g., tilt boundaries) have modified the internal zonation pattern of these uraninites.

Another unusual and striking textural feature identified was that of the cob-web uraninites, which consist of rhythmic intergrowths of uraninite, Cu-(Fe)-sulfides and fluorite. The crystallographic relationship between uraninite, bornite and fluorite were explored using EBSD. It was revealed that grain-scale replacement of uraninite by bornite occurred via CDR reaction, and replacement was controlled by the inherent chemical zoning (of Th) within the uraninite crystal. The crystallographic orientation of the uraninite parent is initially inherited

by the replacing bornite, but later the orientation of bornite changes. Partial replacement of uraninite crystals by bornite and fluorite, the presence of Cu-(Fe)-sulfide and fluorite inclusions within the parent uraninite, as well as the local abundance of bornite and fluorite found within the samples, indicates that replacement was likely driven by a F-rich hydrothermal fluid that was also enriched in Cu, S, Fe and Ca. In CDR-driven replacement of minerals, the parent and daughter phases typically have some similar chemical constituents. This study is therefore important in highlighting that it is possible to have CDR-driven replacement between phases with no common chemical constituents, but which nevertheless share common crystal structural features.

Overall, few previous studies have linked textural and compositional changes in uraninite grains to micro- and nanoscale observations. The collation and analysis of a dataset such as this highlights the power of combining numerous analytical methods to attain both chemical and microstructural data to unravel the story behind some complex mineral textures. This kind of detailed analysis is required if further understanding of the U-mineralization process which occurred at OD is to be completely understood. There are still numerous unanswered questions about the evolution of uraninite at OD; these are discussed in Section 7.4.

7.2 Coffinite and brannerite

The full story of uranium at OD cannot be understood without study of the abundant coffinite and brannerite. Previously, these were assumed to only be present in minor amounts, but as shown by Ehrig et al. (2012), coffinite and brannerite actually represent a significant proportion of the U-minerals within the deposit. Also, many studies mention the numerous cycles of U dissolution and reprecipitation that have occurred at OD, but none have tried to quantify this statement. Although the work conducted as part of this project by no means quantifies the degree or amount of U dissolution and reprecipitation which has occurred

within the deposit, nor consider U that has been added or lost to the system over time, it does provide detailed textural and chemical data pertaining to the uranium minerals, which may help to further explore this hypothesis. Since both coffinite and brannerite are known to form in low-temperature hydrothermal environments, it is likely these minerals will play an important role in understanding the dissolution and reprecipitation of U within the deposit.

Based on petrographic characteristics (size, habit, textures and mineral associations), as well as compositional variation, brannerite has been grouped into four distinct groups, and coffinite into three groups. Estimates of the structural formulae for each of these groupings have been suggested, and predictions about possible elemental substitution mechanisms made. It has been concluded that brannerite and coffinite have precipitated as part of a late-stage U-event at OD, which may have involved the dissolution and/or reprecipitation of earlier precipitated uraninite, or may have involved a fresh influx of U. Evidence which supports formation of late-stage coffinite and brannerite includes: (1) the low-Pb contents of both brannerite and coffinite (i.e., experienced minimal radioactive decay or radiogenic Pb has been mobilized from these minerals); (2) coffinite is often found on the edges of uraninite, thus implying this process occurred after deposition of uraninite; (3) coffinite is often found on the edge of brannerite aggregates, which is suggestive that brannerite precipitation occurred before coffinite. There are also many features (e.g., banding, scalloped edges, alteration rinds, variable compositions etc.) which have been observed for all U-minerals, and these can only be formed by processes which occur after initial deposition of the mineral on which they occur, and are typical of interaction with hydrothermal fluids. It is unlikely that a single fluid could precipitate all of these minerals at one time as the conditions and chemical components required to form each of these minerals differs significantly. Thus, although it is unclear whether the coffinite and brannerite form as a direct result of the alteration of uraninite, the numerous chemical and textural observations strongly suggest that most

uraninite in the deposit likely pre-dates both coffinite and brannerite. Those brannerites which contain galena inclusions, however, may also have formed early in the evolutionary history of the deposit, and the galena contained within them is a result of radioactive decay.

7.3 Synopsis of the U-mineralogy at Olympic Dam

Based on the key findings of this work, some of the hypotheses made by others have been reaffirmed, and additional conclusions drawn. A brief synopsis of the U-minerals and processes involved in U-mineralization at Olympic Dam can be summarized as follows:

1. Confirmed that the distribution of U-minerals is not zoned at the deposit scale.
2. Affirmed that uraninite tends to dominate in samples which contain >500 ppm U_3O_8, and coffinite and brannerite are more abundant where U_3O_8 grades are <500 ppm U_3O_8.
3. Uraninite, coffinite and brannerite can co-exist within the scale of a thin-section (i.e., within a few hundred micrometres), but brannerite is rarely found touching uraninite, and coffinite can be found touching both brannerite and uraninite.
4. On average, uraninite is more associated with sulfides and hematite (~80 wt% total) than both coffinite and brannerite (~40 wt% each). Other minerals which are associated with both coffinite and brannerite are quartz, sericite/chlorite and carbonates.
5. The Olympic Dam uraninites have very high-ΣREY contents compared to many of the other uraninites around the World. TEM data revealed that the ΣREY were both lattice-bound, and for recrystallized uraninite, contained within REY-mineral (e.g., synchysite, monazite, bastnäsite, florencite) inclusions.
6. The crystalline uraninites (Classes 1 to 3) form a continuum and represent the progressive *in-situ* alteration of primary uraninite, through zoned to cob-web types.

These uraninites are distinct from the Class 4 uraninites, which appear to represent a later mineralization event.

7. Class 4 uraninites are probably older than coffinite and brannerite. This might suggest a change in the alteration and mineralization processes in more recent times.

7.4 Future work

The research conducted as part of this project has raised numerous unanswered questions and issues, and it is hoped that some of these will spur research projects in the future. A list of possible future ideas to be investigated is given here:

1. Validate oxidation states of both U and Pb in uraninite to support the revised structural formula. This carries with it implications for the deportment and mobilization of radionuclides within the deposit, and their behaviour during mineral processing. X-ray absorption spectroscopy (XAS) is a possible method which could be used to measure oxidation state.

2. Further refinement of the structural formulae for both brannerite and coffinite is also required. This includes validation of the oxidation state of U, possibly using XAS as mentioned above. Also, work is required to verify whether the assumed elemental substitutions into the structural A- and B-sites of brannerite and coffinite are valid, or whether these elements are found within interstitial sites or nanoscale inclusions. This could be done via the integrated use of FIB-SEM and HRTEM and/or XAS. Furthermore, structural water (and/or OH^-) has been documented by many to be present in uraninite, coffinite and brannerite, so it is proposed that detailed Raman/Infrared spectroscopy be used to try and ascertain if this is applicable at OD.

3. Monitor the exchangeability of ^{18}O with ^{16}O within the low-Pb coffinite and brannerite mineral structures using Raman/Infrared spectroscopy by immersion in ^{18}O enriched water. This may provide insight into whether the coffinite and brannerite structures are chemically open (i.e., have ^{18}O readily exchanging for ^{16}O) or closed. Ultimately this may reveal the release and/or retention mechanisms of Pb within these minerals. If the structures are found to be open, then it is possible that any radiogenic lead has been mobilized from within these minerals. Conversely, if these minerals are found to be closed, then this may provide proof that these minerals are indeed geologically young (i.e., have not experienced significant radioactive decay), and confirm their place in the paragenetic sequence.

4. Conduct additional nanoscale chemical mapping on FIB-prepared foils to determine if there is any evidence of superstructuring within uraninite (i.e., presence of U_4O_9 or U_3O_8). Density functional theory (DFT) conducted by others (e.g., Desgranges et al., 2009 and 2011, Andersson et al., 2013) may provide the basis for some of this structural information. If superstructures are identified, the newly identified structures could then be input into the TSL database and used for subsequent EBSD analysis, which may provide more microstructural information about the uraninites.

5. Conduct CDR experiments to test if replacement of uraninite by Cu-(Fe)-sulfides is possible and identify the conditions under which this replacement occurs. Li et al. (2015) have already attempted to replace uraninite crystals with bornite/chalcopyrite using hydrothermal conditions (fluid contained Cu, Fe, S, but no F). Unfortunately, the uraninite was more soluble than the bornite/chalcopyrite in these experiments, and thin stringers of uraninite were observed growing at the original parent bornite or chalcopyrite grain surface which were not epitaxial to the uraninite. New experiments

could be designed which also contain F within the hydrothermal fluid. If successful, this would confirm the premise that the reactions in nature are driven by F-rich, Cu-Fe sulfide-bearing hydrothermal fluids. Furthermore, experiments which use uraninite crystals that contain oscillatory zonation, particularly of Th, Pb and ΣREY as the starting material for replacement may resolve some of the uncertainties regarding the composition of uraninite prior to replacement.

6. Investigate the possibility of CDR replacement of ilmenite/rutile aggregates with brannerite using F-rich, Cu-Fe sulfide-bearing hydrothermal fluids. Much of the previous work (e.g., Ramdohr, 1957; Ferris and Ruud, 1971) suggests that brannerite forms from the replacement of ilmenite via an 'adsorption process'. Some suggest that the transformation of ilmenite forms titanogels or titanium oxyhydroxides which are known to have high sorptive capacities for weak uranium solutions (Laskorin et al., 1958; Davies et al., 1964; Yermolayev, 1971). The transformation proceeds progressively from the outside inward (i.e., only one surface layer at a time) thus allowing each layer of titania to only adsorb U available at that time. Thus, where little or no U is available, only rutile or anatase results, forming the commonly observed brannerite/rutile aggregates. With the advancement in understanding of CDR replacement reactions, particularly with respect to hydrothermal alteration of pyrochlore (Geisler et al. 2005a, 2005b), it may be possible to experimentally show that the formation of brannerite occurs from a replacement process rather than adsorption processes.

7. The current study identified the replacement process of uraninite with bornite based on single 2-dimensional slices of crystals, but this makes understanding the 3-dimensional replacement process difficult. Traditional X-ray and neutron tomography

methods lack the resolution to study this problem. Thus, further work is required on the FIB-SEM and TEM to try and document the replacement process in 3-dimensions on samples which have been well characterized by EBSD, before extracting and thinning on FIB-SEM.

8. Obtain trace element patterns and chondrite-normalized ΣREY fractionation trends for the all U-minerals using laser ablation inductively coupled plasma mass spectroscopy (LA-ICPMS). Likewise, analyses which target the Pb isotope signatures within both the U-minerals and the associated Pb-minerals could be conducted to determine whether Pb is radiogenic (i.e. ^{206}Pb, ^{207}Pb and ^{208}Pb), or non-radiogenic crustal lead (^{204}Pb). These analyses may help to further refine some of the classification schemes, and may also provide additional 'fingerprinting' mechanisms if unique signatures and/or isotopic ratios are identified.

9. Conduct uranium isotopic studies on the mineral scale to expand on the whole-rock U isotopic work conducted by Kirchenbaur et al. (2016). Uraninite, coffinite and brannerite should all be targeted, as well as grain-scale heterogeneity within individual U-minerals to see if U-isotopic fractionation can be identified. This may also contribute to the development of a paragenetic sequence of U-mineralization at OD.

10. Use the chemical and textural features of the individual U-minerals as documented within this thesis, plus those from past and ongoing research projects to formulate an updated genetic model and paragenetic sequence of U-mineralization for the OD deposit. In particular, this may involve using the latest findings about the heterogeneity of individual uraninite grains and the various classes to obtain some detailed uraninite geochronology on very small sample volumes (e.g., by SHRIMP). Also, due to the chemical and textural heterogeneity of the U-minerals, most studies to

date have looked at each mineral in isolation. Thus, now that the fundamentals of these minerals and their mutual relationships have been established and documented (some of which is contained in this thesis), it should be possible to try to understand how all of these observations can be linked together into a broader deposit-wide context.

11. Investigate other U-bearing minerals in the deposit to help in the development of the U-mineralization paragenetic sequence. The study of U in hematite has already been completed by Ciobanu et al. (2013), but further work could be conducted on other minerals like florencite, monazite, synchysite, bastnäsite, fluorapatite, zircon, xenotime, pyrite, chalcopyrite, bornite, and chalcocite, which have all been documented to contain minor (0.1-1 wt%) or trace (<0.1 wt%) amounts of U (Ehrig et al., 2012; Kirchenbaur et al., 2016). Moreover, a study of the U-content in minerals which have not previously been documented to contain U (like fluorite, barite, carbonates) could be initiated, to provide even more data about the deportment of U within the deposit.

CHAPTER 8

REFERENCES CITED

CHAPTER 8: REFERENCES CITED

Adams, S.S., Curtis, H.S. and Hafen, P.L. (1974) Alteration of detrital magnetite-ilmenite in continental sandstones of the Morrison Formation, New Mexico. In: Formation of Uranium Deposits, p. 219-253. International Atomic Energy Agency, Vienna.

Agangi, A., Kamenetsky, V. and McPhie, J. (2010) The role of fluorine in the concentration and transport of lithophile trace elements in felsic magmas: Insights from the Gawler Range Volcanics, South Australia. Chemical Geology, 273, 314-325.

Alexandre, P. and Kyser, T.K. (2005) Effects of cationic substitutions and alteration in uraninite, and implications for the dating of uranium deposits. The Canadian Mineralogist, 43, 1005-1017.

Alexandre, P., Peterson, R. and Joy, B. (2015) Sector zoning in uraninite. The Canadian Mineralogist, 53, 1-11.

Allen, F.M. and Buseck, P.R. (1988) XRD, FTIR, and TEM studies of optically anisotropic grossular garnet. American Mineralogist, 73, 568-584.

Allen, G.C. and Holmes, N.R. (1995) A mechanism for the UO_2 to α-U_3O_8 phase transformation. Journal of Nuclear Materials, 223, 231-237.

Allen, S.R., McPhie, J., Ferris, G. and Simpson, C. (2008) Evolution and architecture of a large felsic igneous province in western Laurentia: The 1.6 Ga Gawler Range Volcanics, South Australia. Journal of Volcanology and Geothermal Research, 172, 132-147.

Altree-Williams, A., Pring, A., Ngothai, Y. and Brugger, J. (2015) Textural and compositional complexities resulting from coupled dissolution-reprecipitation reactions in geomaterials. Earth-Science Reviews, 150, 628-651.

Andersson, D.A., Baldinozzi, G., Desgranges, L., Conradson, D.R. and Conradson, S.D. (2013) Density functional theory calculations of UO_2 oxidation: Evolution of UO_{2+x}, U_4O_{9-y}, U_3O_7, and U_3O_8. Inorganic Chemistry, 52, 2769-2778.

Anthony, J.W., Bideaux, R.A., Bladh, K.W. and Nichols, M.C. (1990) Handbook of mineralogy. Mineral Data Publishing, Mineralogical Society of America, Virginia.

Apukhtina, O., Kamenetsky, V., Ehrig, K., Kamenetsky, M., McPhie, J., Maas, R., Meffre, S., Goemann, K., Rodemann, T., Cook, N.J. and Ciobanu, C.L. (2016) Postmagmatic magnetite-apatite assemblage in mafic intrusions: A case study of dolerite at Olympic Dam, South Australia. Contributions to Mineralogy and Petrology, 171.

Augustithis, S.P. (1995) Atlas of the textural patterns of ore minerals and metallogenic processes. de Gruyter, Berlin.

Barton, M.D. (2014) Iron oxide(-Cu-Au-REE-P-Ag-U-Co) systems. In: Holland H.D. and K.K. Turekian, Eds., Treatise on Geochemistry, 2nd Edition, Volume 11, Chapter 23, p. 515-541. Elsevier Ltd.

Bourdon, B., Henderson, G.M., Lundstrom, C.C. and Turner, S.P. (2003) Introduction to U-series geochemistry. In: B. Bourdon, G.M. Henderson, C.C. Lundstrom and S.P. Turner, Eds., Uranium-Series Geochemistry, 52, p. 1-21. Reviews in Mineralogy and Geochemistry, Mineralogical Society of America, Chantilly, Virginia.

Bowles, J.F.W. (1978) Quantitative microprobe analysis of uranium minerals. The Microscope, 26, 55-67.

Boyle, A.P., Prior, D.J., Banham, M.H. and Timms, N.E. (1998) Plastic deformation of metamorphic pyrite: new evidence from electron backscatter diffraction and forescatter orientation contrast imaging. Mineralium Deposita, 34, 71-81.

Burns, P.C. and Finch, R.J. (1999) Wyartite; crystallographic evidence for the first pentavalent-uranium mineral. American Mineralogist, 84, 1456-1460.

Chernyshev, I.V., Golubev, V.N., Chugaev, A.V. and Baranova, A.N. (2014) $^{238}U/^{235}U$ isotope ratio variations in minerals from hydrothermal uranium deposits. Geochemistry International, 52, 1059-1078.

Ciobanu, C.L., Cook, N.J., Utsunomiya, S., Pring, A. and Green, L. (2011) Focussed ion beam–transmission electron microscopy applications in ore mineralogy: Bridging micro- and nanoscale observations. Ore Geology Reviews, 42, 6-31.

Ciobanu, C.L., Wade, B.P., Cook, N.J., Schmidt Mumm, A. and Giles, D. (2013) Uranium-bearing hematite from the Olympic Dam Cu–U–Au deposit, South Australia: A geochemical tracer and reconnaissance Pb–Pb geochronometer. Precambrian Research, 238, 129-147.

Creaser, R.A. and Cooper, J.A. (1993) U-Pb geochronology of middle Proterozoic felsic magmatism surrounding the Olympic Dam Cu-U-Au-Ag and Moonta Cu-Au-Ag deposits, South Australia. Economic Geology, 88, 186-197.

Cuney, M. (2009) The extreme diversity of uranium deposits. Mineralium Deposita, 44, 3-9.

Cuney, M. and Kyser, K. (2009) Chapter 7: Hydrothermal uranium deposits related to igneous rocks. In: M. Cuney and K. Kyser, Eds., Recent and Not-so-Recent Developments in Uranium Deposits and Implications for Exploration, Mineralogical Association of Canada, Short Course Series, Volume 39, p. 1-14.

Dahlkamp, F.J. (1978) Classification of uranium deposits. Mineralium Deposita, 13, 83-104.

Davies, R.V., Kennedy, J., McIlroy, R.W., Spence, R. and Hill, K.M. (1964) Extraction of uranium from sea water. Nature, 203, 1110-1115.

Deditius, A.P., Utsunomiya, S. and Ewing, R.C. (2007) Fate of trace elements during alteration of uraninite in a hydrothermal vein-type U-deposit from Marshall Pass, Colorado, USA. Geochimica et Cosmochimica Acta, 71, 4954-4973.

—— (2008) The chemical stability of coffinite, $USiO_4 \cdot nH_2O$; $0<n<2$, associated with organic matter: A case study from Grants uranium region, New Mexico, USA. Chemical Geology, 251, 33-49.

Deditius, A.P., Utsunomiya, S., Wall, M.A., Pointeau, V. and Ewing, R.C. (2009) Crystal chemistry and radiation-induced amorphization of P-coffinite from the natural fission reactor at Bangombé, Gabon. American Mineralogist, 94, 827-837.

Depiné, M., Frimmel, H.E., Emsbo, P., Koenig, A.E. and Kern, M. (2013) Trace element distribution in uraninite from Mesoarchaean Witwatersrand conglomerates (South Africa) supports placer model and magmatogenic source. Mineralium Deposita, 48, 423-435.

Desgranges, L., Baldinozzi, G., Rousseau, G., Nièpce, J.-C. and Calvarin, G. (2009) Neutron diffraction study of the in situ oxidation of UO_2. Inorganic Chemistry, 48, 7585-7592.

Desgranges, L., Baldinozzi, G., Siméone, D. and Fischer, H.E. (2011) Refinement of the α-U_4O_9 crystalline structure: New insight into the $U_4O_9 \rightarrow U_3O_8$ transformation. Inorganic Chemistry, 50, 6146-6151.

Devanathan, R., Corrales, L.R., Weber, W.J., Chartier, A. and Meis, C. (2006) Molecular dynamics simulation of energetic uranium recoil damage in zircon. Molecular Simulation, 32, 1069-1077.

Ding, Y., Veblen, D.R. and Prewitt, C.T. (2005) High-resolution transmission electron microscopy (HR-TEM) study of the 4a and 6a superstructure of bornite Cu_5FeS_4. American Mineralogist, 90, 1256-1264.

Donovan, J.J., Snyder, D.A. and Rivers, M.L. (1993) An improved interference correction for trace element analysis. Microbeam Analysis, 2, 23-28.

Donovan, J.J. (2014) Probe for EPMA: Acquistion, automation and analysis. Ver. 10.3.5 Xtreme Edition, Probe Software, Inc., Oregon, United States of America.

Drake, M.J. and Weill, D.F. (1972) New rare earth element standards for electron microprobe analysis. Chemical Geology, 10, 179-181.

Ehrig, K., McPhie, J. and Kamenetsky, V. (2012) Geology and mineralogical zonation of the Olympic Dam Iron Oxide Cu-U-Au-Ag deposit, South Australia. Special Publication

Number 16 - Geology and Genesis of Major Copper Deposits, Society of Economic Geologists, 237-267.

Engvik, A.K., Golla-Schindler, U., Berndt, J., Austrheim, H. and Putnis, A. (2009) Intragranular replacement of chlorapatite by hydroxy-fluor-apatite during metasomatism. Lithos, 112, 236-246.

Etschmann, B., Brugger, J., Pearce, M.A., Ta, C., Brautigan, D., Jung, M. and Pring, A. (2014) Grain boundaries as microreactors during reactive fluid flow: experimental dolomitization of a calcite marble. Contributions to Mineralogy and Petrology, 168, 1-12.

Evins, L.Z., Jensen, K.A. and Ewing, R.C. (2005) Uraninite recrystallization and Pb loss in the Oklo and Bangombé natural fission reactors, Gabon. Geochimica et Cosmochimica Acta, 69, 1589-1606.

Ewing, R.C., Meldrum, A., Wang, L.M., Weber, W.J. and Corrales, L.R. (2003) Radiation effects in zircon. In: J.M. Hanchar and P.W.O. Hoskin, Eds., Zircon: Reviews in Mineralogy and Geochemistry, 53, p. 387-425. Mineralogical Society of America, Geochemical Society, Washington D.C.

Exley, R.A. (1980) Microprobe studies of REE-rich accessory minerals: implications for Skye granite petrogenesis and REE mobility in hydrothermal systems. Earth and Planetary Science Letters, 48, 97-110.

Eyal, Y. and Fleischer, R.L. (1985) Timescale of natural annealing in radioactive minerals affects retardation of radiation-damage-induced leaching. Nature, 314, 518-520.

Fanning, C.M., Blissett, R.B., Parker, A.J., Ludwig, K.R. and Blissett, A.H. (1988) Refined Proterozoic evolution of the Gawler Craton, South Australia, through U-Pb geochronology. Precambrian Research, 40-41, 363-386.

Fanning, C.M., Reid, A. and Teale, G. (2007) A geochronological framework for the Gawler Craton, South Australia. South Australian Geological Survey Bulletin, 55, p. 258.

Fayek, M., Janeczek, J. and Ewing, R.C. (1997) Mineral chemistry and oxygen isotopic analyses of uraninite, pitchblende and uranium alteration minerals from the Cigar Lake Deposit, Saskatchewan, Canada. Applied Geochemistry, 12, 549-565.

Fayek, M. and Kyser, T.K. (1997) Characterization of multiple fluid-flow events and rare-earth-element mobility associated with formation of unconformity-type uranium deposits in the Athabasca Basin, Saskatchewan. The Canadian Mineralogist, 35, 627-658.

Fayek, M., Burns, P., Guo, Y.X. and Ewing, R.C. (2000) Micro-structures associated with uraninite alteration. Journal of Nuclear Materials, 277, 204-210.

Fayek, M. (2013) Chapter 4: Uranium ore deposits: A review. In: P. Burns and G.E. Sigmon, Eds., Uranium: Cradle to Grave, Mineralogical Association of Canada, Short Course Series, Volume 43, p. 121-146.

Ferris, C.S. and Ruud, C.O. (1971) Brannerite: its occurrences and recognition by microprobe. Colorado School of Mines Quarterly, 66, 1-35.

Field, D.P., Magid, K.R., Mastorakos, I.N., Florando, J.N., Lassila, D.H. and Morris, J.W. (2010) Mesoscale strain measurement in deformed crystals: A comparison of X-ray micro-diffraction with electron backscatter diffraction. Philosophical Magazine, 90, 1451-1464.

Finch, R.J. and Ewing, R.C. (1992) The corrosion of uraninite under oxidizing conditions. Journal of Nuclear Materials, 190, 133-156.

Finch, R.J. and Murakami, T. (1999) Systematics and paragenesis of uranium minerals. In: P.C. Burns and R.J. Finch, Eds., Uranium: Mineralogy, Geochemistry and the Environment, 38, p. 91-179. Reviews in Mineralogy and Geochemistry, Mineralogical Society of America, Chantilly, Virginia.

Finch, R.J. and Hanchar, J.M. (2003) Structure and chemistry of zircon and zircon group minerals. In: J.M. Hanchar and P.W.O. Hoskin, Eds., Zircon: Reviews in Mineralogy and

Geochemistry, 53, p. 1-26. Mineralogical Society of America, Geochemical Society, Washington D.C.

Finnie, K.S., Zhang, Z., Vance, E.R. and Carter, M.L. (2003) Examination of U valence states in the brannerite structure by near-infrared diffuse reflectance and X-ray photoelectron spectroscopies. Journal of Nuclear Materials, 317, 46-53.

Fleischer, M. and Mandarino, J.A. (1995) Glossary of mineral species. Mineralogical Record Inc, Tucson, Arizona.

Flint, R.B., Blissett, A.H., Conor, C.H., Cowley, W.M., Cross, K.C., Creaser, R.A., Daly, S.J., Krieg, G.W., Major, R.B., Teale, G.S. and Parker, A.J. (1993) Mesoproterozoic. In: J.F. Drexel, W.V. Preiss and A.J. Parker, Eds., The Geology of South Australia: The Precambrian, 1, Bulletin 54, p. 106-169. Geological Survey of South Australia, Adelaide.

Foden, J., Elburg, M., Dougherty-Page, J. and Burtt, A. (2006) The timing and duration of the Delamerian Orogeny: Correlation with the Ross Orogen and implications for Gondwana assembly. The Journal of Geology, 114, 189-210.

Förster, H.J. (1999) The chemical composition of uraninite in Variscan granites of the Erzgebirge, Germany. Mineral Magazine, 63.

—— (2006) Composition and origin of intermediate solid solutions in the system thorite–xenotime–zircon–coffinite. Lithos, 88, 35-55.

Fraser, G., McAvaney, S., Neumann, N., Szpunar, M. and Reid, A. (2010) Discovery of early Mesoarchean crust in the eastern Gawler Craton, South Australia. Precambrian Research, 179, 1-21.

Frimmel, H.E., Schedel, S. and Brätz, H. (2014) Uraninite chemistry as forensic tool for provenance analysis. Applied Geochemistry, 48, 104-121.

Frondel, C. (1958) Systematic mineralogy of uranium and thorium. U.S. Geological Survey Bulletin.

Fryer, B.J. and Taylor, R.P. (1987) Rare-earth element distributions in uraninites: Implications for ore genesis. Chemical Geology, 63, 101-108.

Fuchs, L.H. and Gebert, E. (1958) X-ray studies of synthetic coffinite, thorite and uranothorites. American Mineralogist, 43, 243-248.

Gaines, R.V., Skinner, H.C.W., Foord, E.E., Mason, B., Rosenzweig, A., King, V.T. and Dowty, E. (1997) Dana's new mineralogy. 8th ed., Wiley & Sons, New York.

Gauthier-Lafaye, F., Holliger, P. and Blanc, P.-L. (1996) Natural fission reactors in the Franceville basin, Gabon: A review of the conditions and results of a "critical event" in a geologic system. Geochimica et Cosmochimica Acta, 60, 4831-4852.

Geisler, T., Pöml, P., Stephan, T., Janssen, A. and Putnis, A. (2005a) Experimental observation of an interface-controlled pseudomorphic replacement reaction in a natural crystalline pyrochlore. American Mineralogist, 90, 1683-1687.

Geisler, T., Seydoux-Guillaume, A.M., Poeml, P., Golla-Schindler, U., Berndt, J., Wirth, R., Pollok, K., Janssen, A. and Putnis, A. (2005b) Experimental hydrothermal alteration of crystalline and radiation-damaged pyrochlore. Journal of Nuclear Materials, 344, 17-23.

Geisler, T., Schaltegger, U. and Tomaschek, F. (2007) Re-equilibration of zircon in aqueous fluids and melts. Elements, 3, 43-50.

Giles, C.W. (1988) Petrogenesis of the Proterozoic Gawler Range Volcanics, South Australia. Precambrian Research, 40–41, 407-427.

Goemann, K. (2011) Challenges in electron probe micronalysis 60 years after Castaing: Examples from complex uranium and rare earth element minerals from northern Australian ore deposits. Microscopy and Microanalysis, 17, 578-579.

Goemann, K. (2012) Mineral analysis by EPMA. AMAS12 EPMA workshop presentation notes, p. 6-14. Australian Microbeam Analysis Society, Sydney, Australia.

Goldhaber, M.B., Hemingway, B.S., Mohagheghi, A., Reynolds, R.L. and Northrop, H.R. (1987) Origin of coffinite in sedimentary rocks by a sequential adsorption-reduction mechanism. Bulletin de Mineralogie, 110, 131-144.

Grandstaff, D.E. (1976) A kinetic study of the dissolution of uraninite. Economic Geology, 71, 1493-1506.

Gregory, M.J., Wilde, A.R. and Jones, P.A. (2005) Uranium deposits of the Mount Isa region and their relationship to deformation, metamorphism, and copper deposition. Economic Geology, 100, 537-546.

Groves, D.I.P., Bierlein, F.P., Meinert, L.D. and Hitzman, M.W. (2010) Iron oxide copper–gold (IOCG) deposits through Earth history; implications for origin, lithospheric setting, and distinction from other epigenetic iron oxide deposits. Economic Geology, 105, 641-654.

Gruner, J.W. (1959) The decomposition of ilmenite. Economic Geology, 54, 1315-1316.

Gu, Y. (2003) Automated scanning electron microscope based mineral liberation analysis: An introduction to JKMRC/FEI Mineral Liberation Analyser. Journal of Minerals & Materials Characterization & Engineering, 2, 33-41.

Hand, M., Reid, A. and Jagodzinski, E. (2007) Tectonic framework and evolution of the Gawler Craton, Southern Australia. Economic Geology and the Bulletin of the Society of Economic Geologists, 102, 1377-1395.

Hansley, P.L. and Fitzpatrick, J.J. (1989) Composition and crystallographic data on REE-bearing coffinite from the Grants uranium region, northwestern New Mexico. American Mineralogist, 74, 263-270.

Harlov, D.E., Förster, H.J. and Nijland, T.G. (2002) Fluid-induced nucleation of (Y+REE)-phosphate minerals within apatite: Nature and experiment. Part I. Chlorapatite. American Mineralogist, 87, 245-261.

Harlov, D.E. and Förster, H.J. (2004) Fluid-induced nucleation of (Y+REE)-phosphate minerals within apatite: Nature and experiment. Part II. Fluorapatite. American Mineralogist, 88, 1209-1229.

Harlov, D.E., Wirth, R. and Förster, H.-J. (2005) An experimental study of dissolution–reprecipitation in fluorapatite: fluid infiltration and the formation of monazite. Contributions to Mineralogy and Petrology, 150, 268-286.

Haynes, D.W., Cross, K.C., Bills, R.T. and Reed, M.H. (1995) Olympic Dam ore genesis: A fluid-mixing model. Economic Geology, 90, 281-307.

Hazen, R.M., Ewing, R.C. and Sverjensky, D.A. (2009) Evolution of uranium and thorium minerals. American Mineralogist, 94, 1293-1311.

Hidaka, H., Holliger, P., Shimizu, H. and Masuda, A. (1992) Lanthanide tetrad effect observed in the Oklo and ordinary uraninites and its implication for their forming processes. Geochemical Journal, 26, 337-346.

Hitzman, M.W., Oreskes, N. and Einaudi, M.T. (1992) Geological characteristics and tectonic setting of proterozoic iron oxide (Cu-U-Au-REE) deposits. Precambrian Research, 58, 241-287.

Hitzman, M.W. and Valenta, R.K. (2005) Uranium in iron oxide-copper-gold (IOCG) systems. Economic Geology, 100, 1657-1661.

Hoffmann, R. (1987) The metamist state. Contemporary Poetry Series - University Press of Florida, Gainesville.

Huang, Q., Kamenetsky, V., McPhie, J., Ehrig, K., Meffre, S., Maas, R., Thompson, J., Kamenetsky, M., Chambefort, I., Apukhtina, O. and Hu, Y. (2015) Neoproterozoic (ca. 820-830 Ma) mafic dykes at Olympic Dam, South Australia: Links with the Gairdner Large Igneous Province. Precambrian Research, 271, 160-172.

IAEA (2009) World distribution of uranium deposits (UDEPO) with uranium deposit classification. International Atomic Energy Agency, IAEA-TECDOC-1629, Vienna, 1-117.

Isobe, H., Murakami, T. and Ewing, R.C. (1992) Alteration of uranium minerals in the Koongarra deposit, Australia: Unweathered zone. Journal of Nuclear Materials, 190, 174-187.

Jagodzinski, E. (2014) The age of magmatic and hydrothermal zircon at Olympic Dam. Australian Earth Sciences Convention, Abstracts No. 110, p. 260. Newcastle, Australia.

Jamtveit, B., Putnis, C. and Malthe-Sørenssen, A. (2009) Reaction induced fracturing during replacement processes. Contributions to Mineralogy and Petrology, 157, 127-133.

Janeczek, J. and Ewing, R.C. (1991) X-ray powder diffraction study of annealed uraninite. Journal of Nuclear Materials, 185, 66-77.

—— (1992a) Coffinitization - a mechanism for the alteration of UO_2 under reducing conditions. Materials Research Society Symposia Proceedings, 257, 497-504.

—— (1992b) Dissolution and alteration of uraninite under reducing conditions. Journal of Nuclear Materials, 190, 157-173.

—— (1992c) Structural formula of uraninite. Journal of Nuclear Materials, 190, 128-132.

—— (1995) Mechanisms of lead release from uraninite in the natural fission reactors in Gabon. Geochimica et Cosmochimica Acta, 59, 1917-1931.

—— (1996) Phosphatian coffinite with rare earth elements and Ce-rich francoisite-(Nd) from sandstone beneath a natural fission reactor at Bangombe, Gabon. Mineralogical Magazine, 60, 665-669.

Janeczek, J., Ewing, R.C., Oversby, V.M. and Werme, L.O. (1996) Uraninite and UO_2 in spent nuclear fuel: a comparison. Journal of Nuclear Materials, 238, 121-130.

Janssen, A., Putnis, A., Geisler, T. and Putnis, C.V. (2010) The experimental replacement of ilmenite by rutile in HCl solutions. Mineralogical Magazine, 74, 633-644.

Jensen, K.A. and Ewing, R.C. (1998) Petrography and chemistry of uraninites and uraninite alteration phases from the uranium mineral deposits at Bangombé. In: D. Louvat and C. Davies Eds., Proceedings 1st Annual Progress Meeting of the OKLO-Natural Analogue Phase II Project, p. 139-159. Sitges, Spain.

Johnson, J.P. (1993) The geochronology and radiogenic isotope systematics of the Olympic Dam Copper-Uranium-Gold-Silver deposit, South Australia, Unpublished Ph.D. thesis, The Australian National University, Canberra, Australia.

Johnson, J.P. and Cross, K.C. (1995) U-Pb geochronological constraints on the genesis of the Olympic Dam Cu-U-Au-Ag deposit, South Australia. Economic Geology, 90, 1046-1063.

Johnson, J.P. and McCulloch, M.T. (1995) Sources of mineralising fluids for the Olympic Dam deposit (South Australia) : Sm+Nd isotopic constraints. Chemical Geology, 121, 177-199.

Kelly, A.A., Knowles, K.M. and Kelly, A. (2012) Crystallography and crystal defects. 2nd ed., John Wiley and Sons, Chichester, West Sussex, UK.

Keppler, H. and Wyllie, P.J. (1990) Role of fluids in transport and fractionation of uranium and thorium in magmatic provinces. Nature, 348, 531-533.

—— (1991) Partitioning of Cu, Sn, Mo, W, U and Th between melt and aqueous fluid in the systems haplogranite-H/O-HCl and haplogranite-H_2O-HF. Contributions to Mineralogy and Petrology, 109, 139-150.

Kirchenbaur, M., Maas, R., Ehrig, K., Kamenetsky, V.S., Strub, E., Ballhaus, C. and Münker, C. (2016) Uranium and Sm isotope studies of the supergiant Olympic Dam Cu-Au-U-Ag deposit, South Australia. Geochimica et Cosmochimica Acta, 180, 15-32.

Komninou, A. and Sverjensky, D.A. (1996) Geochemical modeling of the formation of an unconformity-type uranium deposit. Economic Geology, 91, 590-606.

Kontonikas-Charos, A., Ciobanu, C.L., Cook, N.J., Ehrig, K., Krneta, S. and Kamenetsky, V.S. (in review) Feldspar evolution in the Roxby Downs Granite, host to Fe-oxide Cu-Au-(U) mineralisation at Olympic Dam, South Australia. Ore Geology Reviews.

Kotzer, T.G. and Kyser, T.K. (1993) O, U, and Pb isotopic and chemical variations in uraninite: Implications for determining the temporal and fluid history of ancient terrains. American Mineralogist, 78, 1262-1274.

Kramers, J., Frei, R., Newville, M., Kober, B. and Villa, I. (2009) On the valency state of radiogenic lead in zircon and its consequences. Chemical Geology, 261, 4-11.

Krneta, S., Ciobanu, C.L., Cook, N.J., Ehrig, K. and Kamenetsky, V.S. (2015) Apatite in the Olympic Dam Fe-oxide Cu-U-Au-Ag deposit. Proceedings for Mineral Resources in a Sustainable World, 3, p. 1103-1106. 13th Biennial SGA Meeting, Nancy, France, August 2015.

Kyser, K. and Cuney, M. (2009) Chapter 1: Introduction. In: M. Cuney and K. Kyser, Eds., Recent and Not-so-Recent Developments in Uranium Deposits and Implications for Exploration, Mineralogical Association of Canada, Short Course Series, Volume 39, p. 1-14.

Lapidus, D.F. (1990) Collins dictionary of geology. HarperCollins, Great Britain.

Laskorin, B.N., Metalnikov, S.S. and Terentiev, A.S. (1958) Extraction of uranium from natural water. Proceedings of the Second United Nations International Conference on the Peaceful Uses of Atomic Energy, 3, 211-215.

Leroy, J.L. and Turpin, L. (1988) REE, Th and U behaviour during hydrothermal and supergene processes in a granitic environment. Chemical Geology, 68, 239-251.

Li, K., Pring, A., Etschmann, B., Macmillan, E., Ngothai, Y., O'Neill, B., Hooker, A., Mosselmans, F. and Brugger, J. (2015) Uranium scavenging during mineral replacement reactions. American Mineralogist, 100, 1736-1743.

Ludwig, K.R. and Grauch, R.I. (1980) Coexisting coffinite and uraninite in some sandstone-host uranium ores of Wyoming. Economic Geology, 75, 296-302.

Ludwig, K.R. and Cooper, J.A. (1984) Geochronology of Precambrian granites and associated U-Ti-Th mineralisation, northern Olary province, South Australia. Contributions to Mineralogy and Petrology, 86, 298-308.

Lumpkin, G.R., Leung, S.H.F. and Ferenczy, J. (2012) Chemistry, microstructure, and alpha decay damage of natural brannerite. Chemical Geology, 291, 55-68.

Lumpkin, G.R., Gao, Y., Gieré, R., Williams, C.T., Mariano, A.N. and Geisler, T. (2014) The role of Th-U minerals in assessing the performance of nuclear waste forms. Mineralogical Magazine, 78, 1071-1095.

Lynd, L.E. (1960) Alteration of ilmenite. Economic Geology, 55, 1064-1068.

Macmillan, E., Cook, N.J., Ehrig, K., Ciobanu, C.L. and Pring, A. (2016) Uraninite from the Olympic Dam IOCG-U-Ag deposit: linking textural and compositional variation to temporal evolution. American Mineralogist, 101, 1295-1320.

McPhie, J., Kamenetsky, V., Allen, S., Ehrig, K., Agangi, A. and Bath, A. (2011a) The fluorine link between a supergiant ore deposit and a silicic large igneous province. Geology, 39, 1003-1006.

McPhie, J., Kamenetsky, V.S., Chambefort, I., Ehrig, K. and Green, N. (2011b) Origin of the supergiant Olympic Dam Cu-U-Au-Ag deposit, South Australia: Was a sedimentary basin involved? , Geology, 39, 795-798.

McPhie, J., Orth, K., Kamenetsky, V., Kamenetsky, M. and Ehrig, K. (2016) Characteristics, origin and significance of Mesoproterozoic bedded clastic facies at the Olympic Dam Cu-U-Au-Ag deposit, South Australia. Precambrian Research, 276, 85-100.

Mercadier, J., Cuney, M., Lach, P., Boiron, M.-C., Bonhoure, J., Richard, A., Leisen, M. and Kister, P. (2011) Origin of uranium deposits revealed by their rare earth element signature. Terra Nova, 23, 264-269.

Mortimer, G.E., Cooper, J.A., Paterson, H.L., Cross, K.C., Hudson, G.R.T. and Uppill, R.K. (1988) Zircon U-Pb dating in the vicinity of the Olympic Dam Cu-U-Au deposit, Roxby Downs, South Australia. Economic Geology and the Bulletin of the Society of Economic Geologists, 83, 694-709.

Moser, D.E., Cupelli, C.L., Barker, I.R., Flowers, R.M., Bowman, J.R., Wooden, J. and Hart, J.R. (2011) New zircon shock phenomena and their use for dating and reconstruction of large impact structures revealed by electron nanobeam (EBSD, CL, EDS) and isotopic U–Pb and (U–Th)/He analysis of the Vredefort dome. Canadian Journal of Earth Sciences, 48, 117-139.

Nemchin, A., Timms, N., Pidgeon, R., Geisler, T., Reddy, S. and Meyer, C. (2009) Timing of crystallization of the lunar magma ocean constrained by the oldest zircon. Nature Geoscience, 2, 133-136.

Nicolis, G. and Prigogine, I. (1977) Self-organization in non-equilibrium systems. Wiley, New York.

Nowell, M.M. and Wright, S.I. (2004) Phase differentiation via combined EBSD and XEDS. Journal of Microscopy, 213, 296-305.

Oreskes, N. (1990) American geological practice: Participation and examination. Part 1: Origin of REE-enriched hematite breccias at Olympic Dam, South Australia, Unpublished Ph.D. thesis, Stanford University, Stanford, CA.

Oreskes, N. and Einaudi, M.T. (1990) Origin of rare earth element-enriched hematite breccias at the Olympic Dam Cu-U-Au-Ag deposit, Roxby Downs, South Australia. Economic Geology, 85, 1-28.

—— (1992) Origin of hydrothermal fluids at Olympic Dam: Preliminary results from fluid inclusions and stable isotopes. Economic Geology, 87, 64-90.

Oreskes, N. and Hitzman, M.W. (1993) A model for the origin of the Olympic Dam-type deposits. In: R.V. Kirkham, W.D. Sinclair, R.I. Thorpe and J.M. Duke, Eds., Mineral Deposit Modelling, 40, p. 615-633. Geological Association of Canada Special Paper.

Ortoleva, P., Merino, E., Moore, C. and Chadam, J. (1987) Geochemical self-organization I: reaction-transport feedbacks and modeling approach. American Journal of Science, 287, 979-1007.

Pabst, A. (1954) Brannerite from california. American Mineralogist, 39, 109-117.

Pal, D.C. and Rhede, D. (2013) Geochemistry and chemical dating of uraninite in the Jaduguda Uranium Deposit, Singhbhum Shear Zone, India - Implications for uranium mineralization and geochemical evolution of uraninite. Economic Geology, 108, 1499-1515.

Parks, G.A. and Pohl, D.C. (1988) Hydrothermal solubility of uraninite. Geochimica et Cosmochimica Acta, 52, 863-875.

Pearce, M.A., Timms, N.E., Hough, R.M. and Cleverley, J.S. (2013) Reaction mechanism for the replacement of calcite by dolomite and siderite: implications for geochemistry, microstructure and porosity evolution during hydrothermal mineralisation. Contributions to Mineralogy and Petrology, 166, 995-1009.

Plant, J.A., Simpson, P.R., Smith, B. and Windley, B.F. (1999) Uranium ore deposits - products of the radioactive earth. In: P.C. Burns and R.J. Finch, Eds., Uranium:

Mineralogy, Geochemistry and the Environment, 38, p. 255-319. Mineralogical Society of America - Reviews in Mineralogy and Geochemistry, Washington D.C.

Pointer, C.M., Ashworth, J.R. and Ixer, R.A. (1988) The zircon-thorite mineral group in metasomatized granite, Ririwai, Nigeria 1. Geochemistry and metastable solid solution of thorite and coffinite. Mineralogy and Petrology, 38, 245-262.

Polito, P.A., Kyser, T.K., Marlatt, J., Alexandre, P., Bajwah, Z. and Drever, G. (2004) Significance of alteration assemblages for the origin and evolution of the Proterozoic Nabarlek unconformity-related uranium deposit, Northern Territory, Australia. Economic Geology, 99, 113-139.

Polito, P.A., Kyser, T.K. and Stanley, C. (2009) The Proterozoic, albitite-hosted, Valhalla uranium deposit, Queensland, Australia: a description of the alteration assemblage associated with uranium mineralisation in diamond drill hole V39. Mineralium Deposita, 44, 11-40.

Preiss, W.V. (1993) Neoproterozoic. In: J.F. Drexel, W.V. Preiss and A.J. Parker, Eds., The Geology of South Australia: The Precambrian, 1, Bulletin 54, p. 171-203. Geological Survey of South Australia, Adelaide.

Prior, D.J., Boyle, A.P., Brenker, F., Cheadle, M.C., Day, A., Lopez, G., Peruzzo, L., Potts, G.J., Reddy, S., Spiess, R., Timms, N.E., Trimby, P., Wheeler, J. and Zetterstrom, L. (1999) The application of electron backscatter diffraction and orientation contrast imaging in the SEM to textural problems in rocks. American Mineralogist, 84, 1741-1759.

Prior, D.J., Wheeler, J., Peruzzo, L., Spiess, R. and Storey, C. (2002) Some garnet microstructures: an illustration of the potential of orientation maps and misorientation analysis in microstructural studies. Journal of Structural Geology, 24, 999-1011.

Putnis, A. (2002) Mineral replacement reactions: from macroscopic observations to microscopic mechanisms. Mineralogical Magazine, 66, 689-708.

Putnis, A. and Putnis, C.V. (2007) The mechanism of re-equilibration of solids in the presence of a fluid phase. Journal of Solid State Chemistry, 180, 1783-1786.

Putnis, A. (2009) Mineral replacement reactions. In: E.H. Oelkers and J. Schott, Eds., Thermodynamics and kinetics of water-rock interactions, 70, p. 87-124. Reviews in Mineralogy and Geochemistry, Mineralogical Society of America, Chantilly, Virginia.

Putnis, C.V., Tsukamoto, K. and Nishimura, Y. (2005) Direct observations of pseudomorphism: compositional and textural evolution at a fluid-solid interface. American Mineralogist, 90, 1909-1912.

Pyle, J.M., Spear, F.S. and Wark, D.A. (2002) Electron microprobe analysis of REE in apatite, monazite, and xenotime: Protocols and pitfalls. In: M.J. Kohn, J. Rakovan and J.M. Hughes, Eds., Phosphates: Geochemical, Geobiological, and Materials Importance, 48, p. 337-362. Reviews in Mineralogy and Geochemistry, Mineralogical Society of America, Washington, D. C.

Ram, R., Charalambous, F.A., McMaster, S., Pownceby, M.I., Tardio, J. and Bhargava, S.K. (2013) Chemical and micro-structural characterisation studies on natural uraninite and associated gangue minerals. Minerals Engineering, 45, 159-169.

Ramdohr, P. (1957) Die "Pronto-Reaktion". Neues Jahrbuch für Mineralogie, Monatshefte, 10–11, 217-222.

—— (1969) The ore minerals and their intergrowths. 3rd ed., Pergamon Press Ltd, Oxford, London.

Ratke, L. and Voorhees, P.W. (2002) Growth and coarsening: Ostwald ripening in material processing. Springer-Verlag, Berlin.

Reddy, S.M., Timms, N.E., Trimby, P., Kinny, P.D., Buchan, C. and Blake, K. (2006) Crystal-plastic deformation of zircon: A defect in the assumption of chemical robustness. Geology, 34, 257-260.

Reddy, S.M., Timms, N.E., Pantleon, W. and Trimby, P. (2007) Quantitative characterization of plastic deformation of zircon and geological implications. Contributions to Mineralogy and Petrology, 153, 625-645.

Reeve, J.S., Cross, K.C., Smith, R.N. and Oreskes, N. (1990) The Olympic Dam copper-uranium-gold-silver deposit, South Australia. In: F.E. Hughes, Ed., Geology of Mineral Deposits of Australia and Papua New Guniea, 14, p. 1009-1035. Australian Institute of Mining & Metallurgy Monograph, Melbourne.

Roberts, D.E. and Hudson, G.R.T. (1983) The Olympic Dam copper-uranium-gold deposit, Roxby Downs, South Australia. Economic Geology, 78, 799-822.

Robit-Pointeau, V., Poinssot, C., Vitorge, P., Grambow, B., Cui, D., Spahiu, K. and Catalette, H. (2006) Assessment of the relevance of coffinite formation within the near-field environment of spent nuclear fuel geological disposals. Materials Research Society Symposia Proceedings, 932, 489-496.

Roudil, D., Bonhoure, J., Pik, R., Cuney, M., Jégou, C. and Gauthier-Lafaye, F. (2008) Diffusion of radiogenic helium in natural uranium oxides. Journal of Nuclear Materials, 378, 70-78.

Rubatto, D., Müntener, O., Barnhoorn, A. and Gregory, C. (2008) Dissolution-reprecipitation of zircon at low-temperature, high-pressure conditions (Lanzo Massif, Italy). American Mineralogist, 93, 1519-1529.

Ruello, P., Petot-Ervas, G., Petot, C. and Desgranges, L. (2005) Electrical conductivity and thermoelectric power of uranium dioxide. Journal of the American Ceramic Society, 88, 604-611.

Ruh, R. and Wadsley, A.D. (1966) The crystal structure of $ThTi_2O_6$ (brannerite). Acta Crystallographica, 21, 974-978.

Ryan, A.J. (1998) Ernest-Henry Copper-Gold Deposit. In: D.A. Berkman and D.E. Mackenzie, Eds., Geology of Australian and Papua New Guinean Mineral Deposits, Monograph 22, p. 759-768. Australian Institute of Mining and Metallurgy.

Saager, R. and Stupp, H.D. (1983) U−Ti phases from Precambrian quartz-pebble conglomerates of the Elliot Lake area, Canada, and the Pongola basin, South Africa. Tschermaks Mineralogische und Petrographische Mitteilungen, 32, 83-102.

Schauble, E.A. (2007) Role of nuclear volume in driving equilibrium stable isotope fractionation of mercury, thallium, and other very heavy elements. Geochimica et Cosmochimica Acta, 71, 2170-2189.

Schidlowski, M. (1966) Beiträge zur Kenntnis der radioaktiven Bestandteile der Witwatersrand-Konglomerate. II. Brannerit und "Uranpecherzgeister". Neus Jahrbuch für Mineralogie, Abhandlungen, 105, 310-324.

Schwartz, J.J., John, B.E., Cheadle, M.J., Wooden, J.L., Mazdab, F., Swapp, S. and Grimes, C.B. (2010) Dissolution–reprecipitation of igneous zircon in mid-ocean ridge gabbro, Atlantis Bank, Southwest Indian Ridge. Chemical Geology, 274, 68-81.

Shore, M. and Fowler, A.D. (1996) Oscillatory zoning in minerals: a common phenomenon. The Canadian Mineralogist, 34, 1111-1126.

Singh, K.D.P., Bhargava, L.R., Ali, M.A. and Swarnkar, B.M. (1990) An unusual brannerite from Tai, Arunachal Pradesh, India. Exploration and Research for Atomic Minerals, 1, 117-122.

Skirrow, R.G., Bastrakov, E.N., Barovich, K., Fraser, G.L., Creaser, R.A., Fanning, C.M., Raymond, O.L. and Davidson, G.J. (2007) Timing of Iron Oxide Cu-Au-(U) hydrothermal activity and Nd isotope constraints on metal sources in the Gawler Craton, South Australia. Economic Geology, 102, 1441-1470.

Smith, D.K. (1984) Uranium mineralogy. In: B. De Vivo, F. Ippolito, G. Capaldi and P.R. Simpson, Eds., Uranium Geochemistry, Mineralogy, Geology, Exploration and Resources, p. 43-88. The Institution of Mining and Metallurgy, London, England.

Smits, G. (1989) (U,Th)-bearing silicates in reefs of the Witwatersrand, South Africa. The Canadian Mineralogist, 27, 643-656.

Speer, J.A. (1980) The actinide orthosilicates. Reviews in Mineralogy and Geochemistry, 5, 113-135.

Steffen, K.J. and Selverstone, J. (2006) Retrieval of P-T information from shear zones: thermobarometric consequences of changes in plagioclase deformation mechanisms. Contributions to Mineralogy and Petrology, 151, 600-614.

Stieff, L.R., Stern, T.W. and Sherwood, A.M. (1956) Coffinite, a uranous silicate with hydroxyl substitution: a new mineral. American Mineralogist, 41, 675-688.

Stout, P.J., Lumpkin, G.R., Ewing, R.C. and Eyal, Y. (1988) An annealing study of alpha-decay damage in natural UO_2 and ThO_2. Materials Research Society Symposia Proceedings, 112, 495-504.

Swain, G., Hand, H., Teasdale, J.P., Rutherford, L. and Clark, C. (2005) Age constraints on terrain-scale shear zones in the Gawler Craton, southern Australia. Precambrian Research, 139, 164-180.

Szymanski, J.T. and Scott, J.D. (1982) A crystal structure refinement of synthetic brannerite UTi_2O_6 and its bearing on rate of alkaline-carbonate leaching of brannerite in ore. The Canadian Mineralogist, 20, 271-280.

TexSEM (2007) OIM Analysis 5.3 User Manual. EDAX, AMETEK, Materials Analysis Division.

Timms, N.E., Kinny, P.D. and Reddy, S.M. (2006) Enhanced diffusion of uranium and thorium linked to crystal plasticity in zircon. Geochemical Transactions, 7, 1-16.

Timms, N.E., Reddy, S.M., Healy, D., Nemchin, A.A., Grange, M.L., Pidgeon, R.T. and Hart, R. (2012) Resolution of impact-related microstructures in lunar zircon: A shock-deformation mechanism map. Meteoritics & Planetary Science, 47, 120-141.

Trueman, N.A., Long, J.V.P., Reed, S.J.B. and Chinner, G.A. (1986) The lead-uranium systematics, and rare-earth-element distributions of some Olympic Dam and Stuart Shelf mineralization. Internal Report, Western Mining Corporation, Adelaide.

Urai, J.L., Means, W.D.M. and Lister, G.S. (1986) Dynamic recrystallisation of minerals. In: B.E. Hobbs and H.C. Heard, Eds., Mineral and Rock Deformation: Laboratory Studies - The Paterson Volume, Geophysical Monograph 36, p. 161-199. American Geophysical Union.

Utsunomiya, S., Palenik, C.S., Valley, J.W., Cavosie, A.J., Wilde, S.A. and Ewing, R.C. (2004) Nanoscale occurrence of Pb in an Archean zircon. Geochimica et Cosmochimica Acta, 68, 4679-4686.

Uvarova, Y.A., Kyser, T.K., Geagea, M.L. and Chipley, D. (2014) Variations in the uranium isotopic compositions of uranium ores from different types of uranium deposits. Geochimica et Cosmochimica Acta, 146, 1-17.

Vance, E.R., Watson, J.N., Carter, M.L., Day, R.A. and Begg, B.D. (2001) Crystal chemistry and stabilization in air of brannerite, UTi_2O_6. Journal of the American Ceramic Society, 84, 141-144.

Vance, E.R., Zhang, Y., Zhang, Z., Gregg, D.J., McLeod, T. and Jovanovic, M. (2015) Solid solutions of higher valence actinides in TiO_2 and ZrO_2–Y_2O_3. Journal of Nuclear Materials, 462, 268-272.

Vaughan, D.J. and Craig, J.R. (1978) Mineral chemistry of metal sulfides. Cambridge University Press, Cambridge.

Watt, G.R. (1995) High-thorium monazite-(Ce) formed during disequilibrium melting of metapelites under granulite-facies conditions. Mineralogical Magazine, 59, 735-743.

Whittle, A.W.G. (1954) The radioactive minerals of South Australia and their petrogenetic significance. Journal of the Geological Society of Australia, 2, 21-45.

Williams, P.J., Barton, M.D., Johnson, D.A., Fontboté, L., de Haller, A., Mark, G., Oliver, N.H.S. and Marschik, R. (2005) Iron oxide copper-gold deposits: Geology, space-time distribution, and possible modes of origin. Economic Geology and the Bulletin of the Society of Economic Geologists, 100th Anniversary Volume, 371-405.

Williams, P.J. (2010) Classifying IOCG deposits. Short Course Notes, Vol. 20, Geological Association of Canada, 23-38.

Wilson, W.B., Alexander, C.A. and Gerds, A.F. (1961) Stabilization of UO_2. Journal of Inorganic and Nuclear Chemistry, 20, 242-251.

Wingate, M.T.D., Campbell, I.H., Compston, W. and Gibson, G.M. (1998) Ion microprobe U-Pb ages for Neoproterozoic basaltic magmatism in south-central Australia and implications for the breakup of Rodinia. Precambrian Research, 87, 135-159.

Wright, S.I. and Nowell, M.M. (2006) EBSD image quality mapping. Microscopy and Microanalysis, 12, 72-84.

Wright, S.I., Nowell, M.M. and Field, D.P. (2011) A review of strain analysis using electron backscatter diffraction. Microscopy and Microanalysis, 17, 316-329.

Wyckoff, R.W.G. (1963) Crystal structures. 2nd ed., Wiley Publishers, New York.

Xia, F., Brugger, J., Chen, G., Ngothai, Y., O'Neill, B., Putnis, A. and Pring, A. (2009a) Mechanism and kinetics of pseudomorphic mineral replacement reactions: a case study of the replacement of pentlandite by violarite. Geochimica et Cosmochimica Acta, 73, 1945-1969.

Xia, F., Brugger, J., Ngothai, Y., O'Neill, B., Chen, G. and Pring, A. (2009b) Three-dimensional ordered arrays of zeolite nanocrystals with uniform size and orientation by a pseudomorphic coupled dissolution−reprecipitation replacement route. Crystal Growth & Design, 9, 4902-4906.

Xia, F., Zhao, J., Etschmann, B., Brugger, J., Garvey, C., Rehm, C., Lemmel, H., Jan Ilavsky, J., Han, S.-Y. and Pring, A. (2014) Characterization of porosity in sulfide ore minerals: A USANS/SANS study. American Mineralogist, 99, 2398-2404.

Xu, G., Wang, A., Gu, Q., Zhang, J., Zhang, Z. and Huang, Y. (1981) Some characteristics of uranium oxides in China. Bulletin de Mineralogie, 104, 565-574.

Yermolayev, N.P. (1971) Processes of redistribution and extraction of uranium in progressive metamorphism. Geochemistry International, 8, 599-609.

Zhao, J.-x. and McCulloch, M.T. (1993) Sm-Nd mineral isochron ages of Late Proterozoic dyke swarms in Australia: evidence for two distinctive events of mafic magmatism and crustal extension. Chemical Geology, 109, 341-354.

Zhao, J., Brugger, J., Chen, G., Ngothai, Y. and Pring, A. (2014a) Experimental study of the formation of chalcopyrite and bornite via the sulfidation of hematite: mineral replacements with a large volume increase. American Mineralogist, 99, 343-354.

Zhao, J., Brugger, J., Ngothai, Y. and Pring, A. (2014b) The replacement of chalcopyrite by bornite under hydrothermal conditions. American Mineralogist, 99, 2389-2397.

APPENDIX A

SUPPLEMENTARY DATA FOR CHAPTER 3:

URANINITE FROM THE OLYMPIC DAM IOCG-U-AG DEPOSIT: LINKING TEXTURAL AND COMPOSITIONAL VARIATION TO TEMPORAL EVOLUTION

Edeltraud Macmillan[1,2], Nigel J. Cook[3], Kathy Ehrig[2], Cristiana L. Ciobanu[3] and Allan Pring[4]

[1]*School of Physical Sciences, The University of Adelaide, Adelaide, SA, 5000, Australia*

[2]*BHP Billiton Olympic Dam, Adelaide, SA, 5000, Australia*

[3]*School of Chemical Engineering, The University of Adelaide, Adelaide, SA, 5000, Australia*

[4]*School of Chemical and Physical Sciences, Flinders University, Bedford Park, SA, 5042, Australia*

Paper published in American Mineralogist

APPENDIX 1 – ANALYTICAL METHODS

ASSAY

Assay data was acquired using the services of Intertek Minerals, Adelaide. A total of 67 elements were measured using a variety of methods as outlined by Ehrig et al. (2012). A summary of data attained can be found in Table A1.

MLA

Automated mineralogy was completed using a Mineral Liberation Analyzer (MLA) at ALS Mineralogy, Brisbane, to attain bulk modal mineralogy (Table A3) and detailed uranium mineralogy (Table A4) for all samples. Details about the MLA system and measurement modes are documented in Gu (2003). Basically it consists of an automated SEM which is controlled by special software to allow for continuous measurement of data. Measurement modes used for the current study were x-ray modal (XMOD) and sparse phase liberation mapping (SPL_Lite). The XMOD method was utilized to attain bulk modal mineralogy of each sample (Table A3), whilst the SPL_Lite method was used to target U- and Pb-bearing grains to attain mineral association and more detailed compositional information pertaining to these phases. These results were then compared to SEM observations to ensure the main U-minerals had been identified. The detailed mineral list used can be found in Table A2, whilst a summary of minerals associated with uraninites can be found in Table A4. Mineral association data is acquired using the SPL_Lite measurement technique. The SPL_Lite method targets selected minerals (uraninite in this case), and a measurement of the perimeter of each uraninite grain is measured. Then the length of the boundary between any other mineral which is touching the uraninite is also measured. A relative proportion (in wt%) of each mineral found in contact with the uraninite can thus be estimated, and this is recorded as

the mineral association. For each sample, an average value is taken for all uraninite grains measured, as displayed in Table A4.

EPMA

Quantitative analysis of uraninites was obtained using a Cameca SX-Five Electron Probe Micro-Analyzer (EPMA) at Adelaide Microscopy, University of Adelaide. A total of 28 elements were measured. The standards used are listed below:

- Astimex Albite for Na Kα
- Astimex Almandine Garnet for Si Kα, Al Kα, Mg Kα, Fe Kα
- Astimex Apatite for P Kα, Astimex Barite for Ba Lα
- Astimex Celestite for Sr Lα
- Astimex Marcasite for S Kα
- Astimex Rhodonite for Mn Kα
- Astimex Rutile for Ti Kα
- Astimex Sanidine for K Kα
- Astimex Gallium Arsenide for As Lα
- Chalcopyrite (P and H Developments, UK) for Cu Kα
- Wollastonite (P & H Developments, UK) for Ca Kα
- Silver Telluride (P & H Developments, UK) for Te Lα
- Astimex Niobium for Nb Lα
- Synthetic Pb Glass – K227 (NIST) for Pb Mβ
- Rare Earth Glass Standard – REE1 (Drake and Weill 1972) for Y Lα
- Huttonite (David Steele) for Th Mα
- UO_2 (David Steele) for U Mβ

- single element synthetic REE glasses for Ce Lα, La Lα, Pr Lβ, Nd Lβ, Sm Lβ, Gd Lβ (Edinburgh Materials and Microanalysis Centre, University of Edinburgh)
- Zircon (C.M. Taylor Company) for Zr Lα.

Key aspects for EPMA include: 1) identification of all elements present; 2) determination of possible spectral interferences; and 3) selection of background positions which accommodate all elements present. High resolution wavelength spectrometer scans were completed to identify all possible elements and to allow for accurate background point setting. The selection of background positions is even more arduous when REY are present due to many cross-interferences (Donovan et al. 1993; Goemann 2011); and these elements are present in varying quantities at OD. Details of crystal type, count times and off-peak interference corrections can be found in Table A5. The HREE-oxides were <mdl (minimum detection limit; identified from full wavelength spectrometer scans).

Acquisition order was adjusted to optimize all spectrometer usage (roughly equal measurement times for all spectrometers) and also measure any elements that may be affected by beam damage first, namely: P Kα, Pb Mβ, Na Kα, Mn Kα, K Kα. Furthermore for these elements, the intensity data was corrected for Time Dependent Intensity (TDI) loss (or gain) using a self-calibrated correction. Both unknown and standard intensities were corrected for dead-time, with standard intensities also being corrected for standard drift over time.

Reproducibility of EPMA results was monitored by measuring select standards (UO_2, K227, REE1 and almandine garnet) as unknowns throughout each EPMA run. This highlighted the stability of the probe over time and also allowed for the removal of any data in cases of significant drift. The standard deviations (SD) for repeated analysis of these standards over a 4 month period were: 0.35 for U (n=44), 0.41 for Pb (n=41), 0.11 for Y (n=52), 0.10 for Si

(n=46), and 0.18 for Fe (n=46). This however is dependent on the availability and quality standards available.

Mean MDL values for each element were calculated and can be found in the footer of Tables A6-A10. Based on 1 σ, mean precision (wt%) was also estimated: U≈ 0.073, Pb≈ 0.037, Th≈ 0.017, Na≈ 0.010, Mg≈ 0.0045, Al≈ 0.0034, Si≈ 0.0048, P≈ 0.0043, S≈ 0.0059, K≈ 0.0034, Ca≈ 0.0075, Ti≈ 0.0039, Mn≈ 0.018, Fe≈ 0.013, Cu≈ 0.018, As≈ 0.013, Zr≈ 0.014, Nb≈ 0.017, Y≈ 0.024, Ce≈ 0.016, La≈ 0.012, Pr≈ 0.037, Nd≈ 0.042, Sm≈ 0.035, Gd≈ 0.037, Sr≈ 0.010, Ba≈ 0.012.

Elemental mapping was completed on a zoned uraninite with a total of 13 elements being mapped using PET and LPET crystals. Wavelength-Dispersive-Spectroscopy (WDS) was used to measure: Ce Lα, P Kα, Ca Kα, Y Lα, and Pb Mα. In contrast, Energy-Dispersive-Spectroscopy (EDS) was used to measure: Si Kα, Fe Kα, U Lα, S Kα, Cu Kα, La Lα, Nd Lα, and Ti Kα. Dwell time per point was 180 ms.

FIB-SEM

The FEI Helios NanoLab 600 DualBeam™ FIB-SEM platform (Adelaide Microscopy, University of Adelaide) is equipped with Energy Dispersive X-ray Spectroscopy (EDXS) detector, Electron Back-Scattered Diffraction (EBSD) detector, and solid-state Scanning Transmission Electron Microscopy (STEM) detector. The platform allows secondary electron and back-scatter electron imaging and mapping; *in-situ* preparation and thinning of TEM foils, 3D 'slice and view' analysis; phase and grain orientation data from Electron Back Scatter Diffraction, and compositional point analysis and mapping via EDXS. Furthermore, the Scanning Transmission Electron facility can be used to image textures and aid in phase identification and mapping of elements of TEM foils with sub-micron resolution. The

integrated use of all of these analytical instruments and examples of the methodologies and applications in ore mineralogy is given by Ciobanu et al. (2011).

HR-TEM

A Philips 200CM transmission electron microscope, equipped with a double-tilt holder and Gatan digital camera (Adelaide Microscopy, University of Adelaide), was used for electron diffraction and high-resolution imaging. Measurements on the diffractions were performed using DigitalMicrograph™ 3.11.1. Indexing of minerals was checked by diffraction simulations using WinHREM™ 3.0 software and data from the American Mineralogist Crystal Structure Database (http://rruff.geo.arizona.edu/AMS/amcsd.php). Winwulff© 1.4.0 (JCrystalSoft) was also used to interpret electron diffraction patterns. The instrument is also equipped with an Energy Dispersive X-ray (EDX) spectrometer allowing compositional information to be obtained on inclusions. Although qualitative rather than quantitative, the resolution of the EDS extends down to the scale of tens or hundreds of nanometers.

Table A1: Assay data for all samples.

Element	Unit	S1	S2	S3	S4	S5	S6	S7	S8	S9	S10	S11	S12	S13	S14	S15	S16	S17	S18	S19	S20	S21	S22	S23
Au [a]	ppb	31	660	382	1847	1306	958	603	75	1339	1292	2435	140	875	1029	1101	1438	258	265	133	1255	210	83	170
Ag [b]	ppm	2.79	1.20	0.89	7.04	26.46	2.84	0.57	22.80	11.37	5.63	2.27	0.12	0.94	4.56	2.35	0.62	7.10	6.89	2.84	5.50	54.09	9.90	25.27
Al [c]	%	5.72	0.45	3.11	2.93	1.47	1.11	0.85	4.27	2.56	2.2	0.97	0.42	2.09	0.81	2.13	4.03	5	2.44	4.64	3.32	4.28	4.54	4.05
As [b]	ppm	218.9	42.9	42.4	564	107	207	137.2	40.4	91.6	354.4	1185.1	108.3	211	182.7	232.9	61	308.8	80.1	49.4	30.6	272	27.3	33.6
Ba [c]	ppm	24918	90	9094	20190	2618	21185	27381	262	1362	7506	239	85	7439	1324	9362	1923	711	1032	973	447	6591	15552	7743
Ca [c]	%	1.14	1.86	1.09	3.28	2.15	4.37	1.51	0.18	8.17	3.88	2.75	0.51	1.57	2.24	2.28	1.46	6.14	4.26	2.47	0.12	0.87	1.32	3.48
Ce [c]	ppm	628	3744	2453	3017	4611	3754	2294	1831	6665	3918	1032	288	4337	5280	6110	4848	9701	8506	4420	1684	1330	2006	2235
CO_2 [d]	%	0.27	8.06	7.52	0.09	0.09	0.17	0.06	0.22	0.48	0.19	3.13	0.44	3.5	17.33	0.25	1.52	0.38	0.64	0.22	0.73	0.38	0.2	0.37
Cu [e]	ppm	13283	17658	10278	13589	73000	29543	28423	16065	66548	20891	34229	20878	19401	26309	27739	23794	96290	50709	75515	114085	58359	13092	14081
Dy [f]	ppm	44.46	44.23	24.13	42.79	33.5	18.23	11.21	29.44	24.45	22.27	447.33	4.72	49.94	35.48	61.01	37.6	79.93	59.17	31.19	11.65	90.69	21.04	17.85
Er [f]	ppm	19.44	21.2	11.66	22.08	19.7	9.96	5.82	14.58	11.48	11.48	246.34	2.82	29.3	13.05	30.58	19.27	36.24	28.95	14.08	5.44	43.05	11.53	8.85
Eu [f]	ppm	22.36	27.14	18.51	32.15	32.9	25.1	14.92	19.3	30.09	32.51	154.43	2.45	24.49	35.25	39.56	27.53	67.73	49.96	32.73	12.06	30.16	13.13	12.1
F [g]	ppm	9888	10870	9908	29736	19918	40781	14333	2622	69807	37212	2708	590	15150	20535	21905	14741	56417	40889	25388	1925	8805	13007	31800
Fe [c]	%	5.78	47.49	29.33	24.77	44	42.56	52.2	21.38	24.65	38.31	44.71	57.52	36.85	42.87	44.65	22.76	20.26	38.62	12.95	7.49	9.39	9.76	10.85
Gd [f]	ppm	40.55	77.28	46.96	39.7	40.82	30.98	18.71	56.64	55	35.05	542.71	8.84	64.8	84.07	89.61	58.29	147.31	98.69	52.6	22.07	72	32.9	27.93
K [c]	%	5.25	0.2	2.09	1.48	0.77	0.6	0.44	2.04	1.3	1.13	0.05	0.08	0.9	0.19	0.82	2.43	2.08	1.02	2.37	1.49	2.63	2.87	2.56
La [c]	ppm	294	2123	1537	2149	3551	3062	1746	918	4913	2958	235	180	2875	3419	3898	3286	6324	6147	2928	1247	865	1347	1646
Mg [c]	%	0.26	0.15	0.28	0.11	0.06	0.06	0.06	0.49	0.1	0.06	0.6	0.08	0.08	0.33	0.05	0.11	0.09	0.07	0.08	0.16	0.12	0.1	0.09
Mn [c]	%	0.03	0.25	0.31	<0.01	<0.01	<0.01	<0.01	0.03	<0.01	<0.01	0.21	0.02	0.12	0.74	<0.01	0.05	<0.01	<0.01	<0.01	0.1	0.01	<0.01	<0.01
Na [c]	%	0.17	0.03	0.04	0.05	0.04	<0.01	<0.01	0.07	0.04	0.01	0.2	0.06	0.02	<0.01	0.02	0.06	0.05	0.02	0.05	0.08	0.09	0.13	0.08
Nb [f]	ppm	21.3	145.2	28.1	43.6	55.4	12.3	11	176.4	10	11.7	482.6	442.5	192.7	217.8	213.8	168.7	230.7	159.7	29.3	15.8	45.2	53.7	32.3
Nd [f]	ppm	231.8	1141.6	707.7	638.6	857.2	688.9	412.7	648.3	1388.6	752.7	1327.6	87.6	1052.4	1511	1589.8	1085.8	2381.2	1885.6	1010.3	373.3	420.2	520.4	499.1
P [c]	%	0.02	0.49	0.19	0.13	0.23	0.09	0.07	0.13	0.1	0.1	0.12	0.08	0.3	0.32	0.35	0.24	0.59	0.28	0.16	0.07	0.06	0.09	0.05
Pb [e]	ppm	2514	120	50	665	126	120	79	98	43	99	5107	104	140	171	205	84	216	128	156	56	6272	53611	36628
Pr [f]	ppm	68.73	352.65	220.83	236.58	344.34	279.58	161.12	188.48	530.61	297.14	212.43	27.17	367.64	482.95	536.42	395.9	848.12	685.08	371.4	132.1	129.15	173.98	181.22
S [d]	%	1.37	9.21	2.4	1.33	3.36	3.54	3.4	0.59	2.93	2.26	3.58	2.84	3.11	2.96	3	2.39	4.77	2.25	3.37	15.99	2.49	1.72	2.05
Si [c]	%	28.28	3.88	16.04	18.55	6.45	8.08	5.2	24.33	13.26	11.19	2.13	3.16	11.77	2.67	7.31	20.3	12.12	8.88	22.86	16.61	27.56	27.12	26.12
Sm [f]	ppm	47.26	128.67	78.62	64.71	74.56	56.59	35.12	101.01	108.69	64.51	496.4	11.32	106.2	158.09	157.63	106.3	253.87	175.64	98.16	39.3	85.41	56.11	48.08
Sr [c]	ppm	466	75	483	321	33	393	245	124	114	197	69	51	818	624	1172	600	2009	758	146	74	308	575	445
Th [f]	ppm	42.61	16.15	26.02	35.72	17.97	12.81	10.53	27.31	23.19	21.28	23.22	9.02	24.13	13.61	20.86	51.34	34.99	21.39	43.53	27.96	44.38	51.66	37.3
Ti [c]	%	0.172	0.03	0.11	0.181	0.052	0.047	0.044	0.122	0.084	0.077	0.011	0.012	0.095	0.019	0.041	0.11	0.155	0.086	0.123	0.091	0.096	0.085	0.084
U_3O_8 [f]	ppm	21325.8	780.9	363.8	6914.4	597	408	369.4	1686.3	387.4	381.7	145840.4	119.3	2243.6	731.4	1293.2	637.5	1604.6	1152.7	425.2	138.8	11258.7	494.2	407.7
Y [c]	ppm	202	210	123	153	180	92	43	164	127	108	2090	34	285	136	270	188	373	246	144	49	302	112	99
Zn [e]	ppm	191	225	98	106	12	15	9	54	65	108	14	15	38	92	17	61	30	39	2396	203447	971	744	7156
Zr [c]	ppm	262	<20	145	287	66	85	65	142	131	111	<20	<20	130	<20	52	184	185	96	231	160	161	148	175
^{204}Pb [b]	%	0.23	0.3	0.51	0.12	0.31	0.31	0.3	0.28	0.41	0.41	0.06	0.35	0.27	0.2	0.25	0.44	0.2	0.19	1.02	1.13	1.24	1.43	1.44
^{206}Pb [b]	%	73.54	73.58	64.55	86.7	73.6	72.56	74.99	75.77	68.83	67.24	90.26	75.34	78.13	81.16	78.62	67.52	81.11	82.05	41.66	39.11	30.71	23.99	24.04
^{207}Pb [b]	%	8.54	10.25	11.77	7.8	9.75	9.91	9.57	9.25	11.66	11.3	6.46	9.9	9.59	9.8	10.29	11.98	10.06	9.72	17.93	18.18	20.77	22.37	22.39
^{208}Pb [b]	%	17.69	15.87	23.17	5.38	16.34	17.21	15.14	14.7	19.1	21.05	3.22	14.42	12.01	8.84	10.84	20.06	8.62	8.05	39.39	41.57	47.28	52.21	52.13

Note: Analyses conducted at Intertek Minerals, Adelaide, South Australia using methods outlined below.

a) Fire assay with inductively coupled plasma mass-spectroscopy (ICP-MS) finish.

b) Four acid digestion with ICP-MS finish.

c) Lithium borate fusion with inductively coupled plasma-optical emission spectroscopy (ICP-OES) finish.

d) Combustion furnace-infrared spectrometry.

e) Four acid digestion with ICP-OES finish.

f) Lithium borate fusion with ICP-MS finish.

g) Fusion with selective-ion-electrode finish.

Table A2: Detailed mineral list as used by MLA (SPL_Lite measurement technique).

Mineral	Formula
Al_Hydroxide	$Al_2(SO_4)_3 \cdot 17(H_2O)$
Albite	$NaAlSi_3O_8$
Altaite	PbTe
Anhydrite	$CaSO_4$
Ankerite	$Ca(Fe,Mg,Mn)(CO_3)_2$
Apatite	$Ca_5(PO_4)_3F$
Barite	$BaSO_4$
Barite_Sr	$(Ba,Sr)SO_4$
Bastnasite	$(Ce,La,Nd,Pr,Ca)(CO_3)F$
Bismuthinite	Bi_2S_3
Bornite	Cu_5FeS_4
Brannerite	$(U,Ca)(Ti,Fe)_2O_6$
Calcite	$(Ca,Mn)CO_3$
Carrolite	$CuCo_2S_4$
Cerussite	$PbCO_3$
Chalcocite	Cu_2S
Chalcopyrite	$CuFeS_2$
Chlorite_1	$(Mg,Fe,Al)_3(Al,Si)_4O_{10}(OH)_2$
Chlorite_2	$(Fe,Al)_3(Al,Si)_4O_{10}(OH)_2$
Chlorite_3	$Mg_2(Al,Fe)_3Si_3AlO_{10}(OH)_8$
Clausthalite	PbSe
Cobaltite	(Co,Fe)AsS
Coffinite-Si_7	$(U,Y,Ca,Ce,Nd,Fe)[(Si,Al)O_4,PO_4,(OH)_4]$
Coffinite-Si_9Y_7	$(U,Y,Ca,Ce,Nd,Fe)[(Si,Al)O_4,PO_4,(OH)_4]$
Coffinite-Si_9Y_9	$(U,Y,Pb,Fe,Er,Dy,Nd,Ce,La,Ca,K)[SiO_4,PO_4,(OH)_4]$
Coffinite-Si_{10}	$(U,Y,Ca,Ce,Nd,Fe)[(Si,Al)O_4,PO_4,(OH)_4]$
Coffinite-$Si_{10}Y_1$	$(U,Y,Pb,Fe,Nd,La,Ce,Ca,K)[(Si,Al)O_4,PO_4,(OH)_4]$
Coffinite-$Si_{10}Y_{10}$	$(U,Y,Ca,Ce,Nd,Fe)[(Si,Al)O_4,PO_4,(OH)_4]$
Coffinite-$Si_{12}Y_6$	$(U,Y,Pb,Fe,Nd,La,Ce,Ca,K)[(Si,Al)O_4,PO_4,(OH)_4]$
Corundum	$(Al,Fe)_2O_3$
Covellite	CuS
Crandellite_Grp	$(Ce,La,Nd,Ca,Sr)(Al,Fe)_3(SO_4,PO_4)_2(OH)_6$
Dolomite	$Ca(Mg,Fe,Mn)(CO_3)_2$
Domeykite	$(Cu,Fe)_3As$
FeO	Fe_2O_3
Florencite	$(Ce,La,Nd,Ca,Sr)(Al,Fe)_3(PO_4)_2(OH)_6$
Fluorite	CaF_2
Galena	PbS
Ilmenite	$(Fe,Mn)TiO_3$
Ilmenorutile	$(Ti,Nb,Fe,Mn)O_6$
Kaolinite	$Al_2Si_2O_5(OH)_4$
Lollingite	$(Fe,Co,Ni)As_2$
Molybdenite	MoS_2
Monazite	$(Ce,La,Nd,Fe,Ca,Th)PO_4$
Native_Copper	Cu
Orthoclase	$KAlSi_3O_8$
Pyrite	FeS_2
Pyrrhotite	$Fe_{1-x}S$ (x=0.0-0.2)
Quartz	SiO_2
Rutile	TiO_2
Safflorite	$(Co,Fe)(As,S)_2$
Scheelite	$CaWO_4$
Schorl	$NaFe_3Al_6(BO_3)_3Si_6O_{18}(OH)_4$
Sellaite	MgF_2
Sericite	$K(Fe,Mg,Al)_2(AlSi_3O_{10})(OH,F)_2$
Siderite	$(Fe,Mn)CO_3$
Siderite_Mn	$(Fe,Mn,Ca)CO_3$
Sphalerite	(Zn,Fe)S
Synchysite	$Ca(Ce,Nd,La,Sm,Gd,Y,Fe)(CO_3)_2F$
Tellurobismuthite	Bi_2Te_3
Tennantite	$(Ag,Cu,Zn,Fe)_{12}(As,Sb)_4S_{13}$
Thorite	$(Th,U,Fe,Y,P,Ca,Pb)SiO_4$
Topaz	$Al_2SiO_4(F,OH)_2$
Unknown	Un
Uraninite-Pb_5	$(U,Pb,Ce,Nd,Fe,Ca)O_2$
Uraninite-Pb_{10}	$(U,Pb,Y,Ce,Nd,Fe,Cu,Ca)O_2$
Uraninite-Pb_{15}	$(U,Pb,Ce,La,Nd,Sm,Gd,Y,Fe,Cu,Ca,K)O_2$
Uraninite-Pb_{20}	$(U,Pb,Fe,Nd,Ce,La,K,Y)O_2$
Uraninite_Si	$(U,Fe,Nd,Ce,La,Ca,K)(SiO_4,O_2)$
Uranothorite	$(U,Th,Y,P,Fe,Ca,Nd)SiO_4$
Xenotime	$(Y,Yb)PO_4$
Xenotime-U	$(Y,U,Dy,Nd,Sm,Gd,Fe)[(PO_4),(SiO_4)]$
Zircon	$ZrSiO_4$
Zircon-U	$(Zr,Hf,U,Ca,Fe,Fe,Dy,Er,Yb,Y)[(Si,Al)O_4]$

Table A3: Bulk modal mineralogy measured by MLA using XMOD measurement technique.

	wt % mineral																						
	S1	S2	S3	S4	S5	S6	S7	S8	S9	S10	S11	S12	S13	S14	S15	S16	S17	S18	S19	S20	S21	S22	S23
Uraninite [a]	0.6	0.0	0.0	1.0	0.0	0.0	0.0	0.3	0.0	0.0	29.5	0.0	0.0	0.1	0.1	0.0	0.1	0.0	0.0	0.0	0.4	0.0	0.1
Coffinite [b]	3.7	0.0	0.0	0.0	0.0	0.0	0.0	0.1	0.0	0.0	0.0	0.0	0.0	0.1	0.0	0.0	0.1	0.0	0.0	0.0	0.0	0.0	0.0
Brannerite	0.1	0.0	0.0	0.1	0.0	0.0	0.0	0.0	0.1	0.0	0.0	0.0	0.0	0.0	0.0	0.0	0.0	0.0	0.0	0.0	0.1	0.0	0.0
REE minerals [c]	0.2	1.7	0.6	0.5	1.6	1.0	0.6	1.0	2.5	1.2	0.0	0.2	0.9	1.5	1.0	1.5	5.8	3.5	1.0	2.9	0.9	0.9	1.7
Bornite	1.8	0.0	0.0	1.0	11.0	0.1	0.0	2.2	5.1	0.5	0.7	0.0	0.0	0.0	0.3	0.2	18.6	8.8	24.9	36.8	4.2	0.7	5.6
Chalcocite [d]	0.3	0.0	0.0	0.9	0.0	0.0	0.0	0.0	2.7	0.0	0.0	0.0	0.0	0.0	0.0	0.0	0.0	0.0	0.2	0.1	2.7	0.3	0.0
Chalcopyrite	0.5	6.0	3.8	0.0	0.9	14.2	9.3	0.1	0.0	4.4	9.9	4.3	5.6	8.2	6.2	7.0	0.4	0.2	0.2	0.1	0.0	0.0	0.0
Pyrite [e]	0.0	25.7	1.9	0.0	0.0	0.0	0.6	0.0	0.0	0.0	0.8	1.0	1.4	0.1	0.0	0.0	0.0	0.0	0.0	0.0	0.0	0.0	0.0
Pb minerals [f]	0.1	0.0	0.0	0.4	0.0	0.0	0.0	0.0	0.0	0.0	0.7	0.0	0.0	0.0	0.0	0.0	0.0	0.0	0.0	0.0	0.5	7.1	9.8
Other sulfides [g]	0.1	0.0	0.0	0.0	0.0	0.0	0.0	0.0	0.0	0.2	0.1	0.0	0.0	0.0	0.0	0.0	0.1	0.0	0.1	13.6	0.1	0.0	6.1
Hematite [h]	5.1	46.0	38.1	48.5	68.2	67.9	72.7	51.4	38.2	67.3	50.9	90.2	62.3	22.3	75.9	35.3	36.8	57.2	22.9	33.7	21.5	16.5	31.7
Carbonates [i]	0.2	11.3	21.7	0.0	0.0	0.0	0.0	0.1	0.2	0.1	4.7	1.1	11.0	48.7	0.0	3.7	2.1	4.1	0.3	5.0	0.2	1.7	0.1
Barite	4.7	0.0	1.0	4.2	0.1	0.3	4.4	0.0	0.2	1.2	0.2	0.0	1.1	0.2	1.9	0.1	0.0	0.2	0.3	0.1	1.0	0.9	0.5
Fluorite [j]	1.7	1.1	1.9	4.6	3.9	8.7	2.4	0.0	14.5	7.1	0.3	0.1	2.5	7.7	2.6	2.1	13.9	6.5	5.2	0.2	2.0	1.2	6.1
Quartz	31.4	7.2	17.3	31.5	9.0	5.1	7.7	33.9	22.0	12.7	0.5	2.4	12.7	8.3	7.0	28.3	7.8	9.4	26.1	0.6	44.3	40.3	21.8
Feldspar [k]	28.4	0.2	5.1	0.1	0.0	0.0	0.0	0.0	0.0	0.2	0.0	0.0	0.2	0.0	0.0	3.5	0.1	0.0	0.2	0.0	3.9	2.4	1.6
Sericite	20.8	0.7	7.8	7.0	5.4	2.6	2.3	10.5	14.3	5.1	0.3	0.5	2.2	2.8	4.8	18.2	13.9	9.8	18.5	6.8	18.0	27.7	14.8
Chlorite	0.2	0.1	0.7	0.0	0.0	0.0	0.1	0.2	0.0	0.0	1.4	0.2	0.1	0.0	0.1	0.0	0.1	0.1	0.0	0.0	0.0	0.0	0.0
Other [l]	0.2	0.0	0.1	0.0	0.0	0.0	0.0	0.1	0.0	0.0	0.0	0.0	0.0	0.1	0.0	0.1	0.1	0.0	0.1	0.1	0.1	0.1	0.0

Note: Individual minerals as defined in Table A2 with some minerals grouped as specified below.

a) "Uraninite" refer to the sum of all listed uraninite types.
b) "Coffinite" refers to the sum of all listed coffinite types, uranothorite and thorite.
c) "REE minerals" refers to the sum of bastnasite, crandellite, florencite, monazite, synchysite, xenotime and zircon.
d) "Chalcocite" refers to the sum of chalcocite, covellite and native copper.
e) "Pyrite" refers to the sum of pyrite and pyrrhotite.
f) "Pb minerals" refers to the sum of altaite, cerussite, clausthalite and galena.
g) "Other sulfides" refers to the sum of bismuthinite, carrolite, cobaltite, molybdenite, safflorite, sphalerite and tennantite.
h) "Hematite" is listed as FeO in Table A2.
i) "Carbonates" refers to the sum of ankerite, calcite, dolomite and siderite.
j) "Fluorite" refers to the sum of sellaite and fluorite.
k) "Feldspar" refers to the sum of albite and orthoclase.
l) "Other" refers to the sum of all remaining minerals listed in Table A2 not mentioned above.

Table A4: Mineral association data for uraninite measured by MLA using SPL_Lite method.

	% mineral associated with uraninite [a]																
	Brannerite	Coffinite	REE minerals	Bornite	Chalcocite	Chalco-pyrite	Pyrite	Pb minerals	Other sufides	Hematite	Barite	Fluorite	Quartz	Sericite	Feldspar	Carbonate	Other
S1	0.1	34.1	0.4	15.5	1.9	2.3	0.0	0.4	0.2	4.7	9.3	14.4	0.7	5.0	10.7	0.1	0.1
S2	0.0	0.0	0.0	0.0	0.0	18.7	7.7	0.0	0.0	63.2	0.0	2.1	3.7	0.0	0.0	4.6	0.1
S3	0.0	37.9	2.0	0.0	0.0	9.9	0.8	0.0	0.0	17.2	0.0	5.4	7.7	1.7	0.4	16.8	0.0
S4	0.0	0.0	0.0	7.4	42.1	0.1	0.0	0.0	0.0	32.9	1.1	0.5	12.4	3.2	0.1	0.1	0.0
S5	0.0	0.1	1.4	4.2	0.0	0.1	0.0	0.0	0.1	73.3	0.1	2.3	10.9	7.5	0.0	0.0	0.0
S6	0.2	0.7	1.1	0.0	0.0	8.0	0.0	0.0	0.0	70.5	1.1	9.1	4.8	3.7	0.0	0.0	0.5
S7	0.0	0.2	1.4	0.0	0.0	2.6	0.1	0.0	0.0	78.9	1.9	1.8	6.0	6.7	0.0	0.0	0.3
S8	0.0	0.1	0.5	0.1	0.1	0.0	0.0	0.0	0.1	79.2	0.1	0.0	15.9	3.3	0.0	0.5	0.2
S9	1.2	5.4	5.4	3.5	1.2	0.0	0.0	0.0	0.0	56.9	0.0	15.9	8.0	2.1	0.0	0.0	0.4
S10	0.8	1.5	1.0	0.0	0.0	3.5	0.0	0.0	0.0	44.4	0.0	26.3	4.8	13.3	1.5	2.8	0.0
S11	0.0	0.0	0.0	0.0	0.0	37.4	0.3	0.7	0.0	59.7	0.0	0.1	0.1	0.0	0.0	0.6	1.1
S12	0.0	0.0	0.0	0.0	0.0	0.0	0.0	0.0	0.0	97.4	0.0	0.0	0.8	1.3	0.0	0.6	0.0
S13	0.0	1.0	0.9	0.3	0.0	25.9	2.6	0.3	4.0	29.3	1.3	9.5	14.3	2.2	0.0	6.5	1.9
S14	0.0	0.0	0.0	0.1	0.0	80.1	0.0	0.0	0.0	2.3	0.0	2.0	0.0	0.0	0.0	15.3	0.0
S15	0.0	1.1	1.0	1.1	0.0	10.8	0.0	0.1	0.1	68.6	0.4	5.5	5.7	5.1	0.0	0.3	0.1
S16	0.1	8.2	0.6	0.4	0.2	28.3	0.0	0.0	0.0	17.5	0.3	5.0	18.9	3.2	1.7	15.4	0.2
S17	0.0	0.8	5.0	25.0	0.0	0.8	0.0	0.0	0.2	34.3	0.0	20.0	3.5	9.9	0.0	0.4	0.1
S18	0.0	3.3	3.8	36.9	0.0	0.2	0.0	0.0	0.0	40.7	0.2	7.0	3.5	3.0	0.1	1.0	0.3
S19	0.2	9.2	7.4	21.1	0.1	0.9	0.0	0.2	0.4	7.5	2.9	5.8	30.1	9.1	0.0	4.9	0.3
S20	0.0	0.0	0.0	100.0	0.0	0.0	0.0	0.0	0.0	0.0	0.0	0.0	0.0	0.0	0.0	0.0	0.0
S21	0.3	0.0	0.0	44.0	4.7	0.1	0.0	1.3	0.0	29.2	0.3	0.3	4.7	12.3	0.5	2.2	0.0
S22	5.5	0.0	0.9	1.5	0.6	0.0	0.0	9.6	0.0	34.9	0.3	1.2	28.9	16.0	0.3	0.0	0.2
S23	0.6	0.0	1.1	2.8	0.0	0.2	0.0	9.7	4.7	48.5	0.3	1.5	9.3	18.4	2.7	0.0	0.1

a) Mineral association data for uraninite, measured by the MLA system using the SPL_Lite method. The SPL_Lite method targets selected minerals (uraninite in this case). The perimeter of each uraninite grain is measured, and the length of the boundary between any other mineral which is touching the uraninite is also measured. A relative proportion (in wt%) of each mineral found in contact with the uraninite can thus be estimated, and this is recorded as the mineral association. For each sample, an average value is taken for all uraninite grains measured.

Table A5: Summary of EPMA set-up used for analysis of OD uraninites.

Element X-ray Line	Spectrometer/ Crystal	Primary Standard	On-Peak Count t (s)	Off-Peak High Count t (s)	Off-Peak Low Count t (s)	Interference with...	Off-Peak Correction
U-Mβ	SP1 (LPET)	UO_2	50	25	12.5	K, Th	Multi-Point
Pb-Mβ	SP1 (LPET)	Pb glass - K227	60	30	30	U, Ce, S, Y	Multi-Point
Th-Mα	SP1 (LPET)	Huttonite	50	12.5	12.5	-	Multi-Point
Na-Kα	SP2 (TAP)	Albite	20	5	10	U	Multi-Point
Mg-Kα	SP2 (TAP)	Almandine garnet	30	15	7.5	-	Multi-Point
Al-Kα	SP2 (TAP)	Almandine garnet	30	15	15	Ti	Multi-Point
Si-Kα	SP2 (TAP)	Almandine garnet	30	15	7.5	Y	Multi-Point
P-Kα	SP5 (LPET)	Apatite	30	15	7.5	Ca, Cu	Multi-Point
S-Kα	SP5 (LPET)	Marcasite	20	10	5	Nd, La	Multi-Point
K-Kα	SP4 (LPET)	Sanidine	20	10	10	U	Multi-Point
Ca-Kα	SP4 (LPET)	Wollastonite	30	15	15	-	Multi-Point
Ti-Kα	SP4 (LPET)	Rutile	30	15	15	U	Multi-Point
Mn-Kα	SP3 (LLIF)	Rhodonite	10	5	5	As	Slope (Hi)
Fe-Kα	SP3 (LLIF)	Almandine garnet	20	10	10	-	Multi-Point
Cu-Kα	SP3 (LLIF)	Chalcopyrite	20	10	10	-	Multi-Point
As-Lα	SP2 (TAP)	Gallium arsenide	40	10	10	Sm, Nd	Multi-Point
Zr-Lα	SP5 (LPET)	Zircon	20	20	20	Nd	Slope (Lo)
Nb-Lα	SP5 (LPET)	Niobium	20	10	5	Mn	Linear
Y-Lα	SP5 (LPET)	REE1	50	25	25	-	Multi-Point
Ce-Lα	SP1 (LPET)	Ce glass	30	15	15	-	Linear
La-Lα	SP1 (LPET)	La glass	30	15	15	Nd	Slope (Lo)
Pr-Lβ	SP3 (LLIF)	Pr glass	30	15	7.5	U	Multi-Point
Nd-Lβ	SP3 (LLIF)	Nd glass	30	7.5	7.5	-	Multi-Point
Sm-Lβ	SP3 (LLIF)	Sm glass	30	15	15	-	Multi-Point
Gd-Lβ	SP3 (LLIF)	Gd glass	30	15	15	U	Multi-Point
Sr-Lα	SP2 (TAP)	Celestine	30	15	7.5	-	Linear
Ba-Lα	SP4 (LPET)	Barite	20	10	5	Ti, U, Pr	Multi-Point
Te-Lα	SP4 (LPET)	Silver telluride	20	10	10	Sm, U	Multi-Point

APPENDIX 2 – COMPOSITIONAL DATA

EPMA DATA PRESENTATION AND FILTERING

Initial data collation involved calculation of means for each textural class within a given sample. However, compositional differences between grains in individual samples contribute to a dilution of the characteristic signatures of each class. For this reason, data are reported as means of analyses from the same grain; separate means are calculated for parts of the grain showing chemical and/or textural similarity.

Further data filtering was undertaken to remove spot analyses which do not correspond to compositionally homogenous uraninite. Points which had higher than expected Al_2O_3 (>0.5 wt%), SiO_2 (>7 wt%), Fe_2O_3 (>3 wt%), Cu_2O (>1.5 wt%), or SO_3 (>0.5 wt%) were excluded. 'Anomalous' concentrations of these components are attributable to mineral impurities and fine-grained intergrowths with sericite, chlorite, hematite and sulfides. In some cases, concentrations of one or more elements were <mdl in individual spot analyses. A value of half the individual spot analysis mdl was utilized for calculation of the mean given in Tables 2-5, A6-A10, and for all subsequent statistical analysis and data plotting.

Attempts were made to combine elemental oxide concentrations which displayed similar relative trends (i.e. elevated vs. depleted). The most apparent of these was wt% (SiO_2+CaO+Fe_2O_3), referred to as "Alteration Factor" (AF). Elemental ratios were also calculated to see if these aid data segregation and/or if trends could be recognized on the plots. The most important of these is Pb/U, which is commonly used to predict chemical age.

EPMA DATA

Additional EPMA data to complement data in Tables 2-5 can be found in Tables A6-A10.

Table A6: Electron probe microanalytical data for primary and zoned uraninites (Part 1)

Sample no.	S17.11 & S15.68 [a]				S17.12 [b]				S17.12 [c]				S17.28 [b]				S17.36 [b]				S17.47 [b]			
Valid N (analyses)	3 (Fig. 4a,b)				41 (Fig. 4c)				20 (Fig. 4c)				10				4				14			
(wt%)	Mean	SD	Min	Max	Mean	SD	Min	Max	Mean	SD	Min	Max	Mean	SD	Min	Max	Mean	SD	Min	Max	Mean	SD	Min	Max
UO_2	63.32	2.89	60.93	66.53	69.75	1.51	66.85	74.44	75.46	1.11	73.15	77.45	66.46	1.19	65.09	68.52	65.18	1.80	63.57	67.31	68.23	1.11	66.76	70.80
PbO_2	17.87	0.46	17.42	18.35	14.85	2.72	10.05	19.61	6.72	0.62	5.41	7.86	17.24	1.58	14.06	19.43	16.96	1.63	15.25	18.71	17.18	1.43	15.02	20.87
ThO_2	4.95	4.27	<mdl	7.42	<mdl	-	<mdl	0.07	0.06	0.04	<mdl	0.14	0.13	0.12	<mdl	0.34	0.30	0.33	<mdl	0.77	0.37	0.13	0.09	0.57
Na_2O	<mdl	-	<mdl	<mdl	0.32	0.10	0.08	0.48	0.21	0.05	0.15	0.35	0.20	0.11	0.03	0.39	0.11	0.07	<mdl	0.16	0.35	0.07	0.24	0.47
SiO_2	0.25	0.27	0.06	0.56	0.21	0.06	0.12	0.36	0.30	0.06	0.21	0.42	0.14	0.03	0.10	0.19	0.09	0.02	0.07	0.12	0.16	0.06	0.08	0.31
P_2O_5	<mdl	-	<mdl	<mdl	<mdl	0.01	<mdl	0.04	0.02	0.02	<mdl	0.05	<mdl	-	<mdl	<mdl	<mdl	-	<mdl	<mdl	<mdl	-	<mdl	<mdl
SO_3	<mdl	-	<mdl	<mdl	0.03	0.09	<mdl	0.43	0.12	0.16	<mdl	0.46	<mdl	-	<mdl	<mdl	<mdl	-	<mdl	<mdl	<mdl	-	<mdl	<mdl
CaO	1.06	0.12	0.97	1.20	1.59	0.53	0.85	2.63	3.42	0.27	2.83	4.01	1.20	0.34	0.85	1.92	1.26	0.29	0.87	1.53	1.23	0.26	0.67	1.85
TiO_2	0.02	0.02	<mdl	0.04	<mdl	-	<mdl	0.04	0.04	0.03	<mdl	0.10	<mdl	-	<mdl	<mdl	<mdl	-	<mdl	<mdl	<mdl	-	<mdl	<mdl
MnO	<mdl	0.02	<mdl	0.04	0.06	0.05	<mdl	0.19	0.25	0.06	0.11	0.35	<mdl	-	<mdl	0.06	<mdl	-	<mdl	<mdl	<mdl	-	<mdl	0.05
Fe_2O_3	1.58	0.32	1.30	1.93	0.54	0.32	0.15	1.37	0.63	0.09	0.51	0.94	0.32	0.17	0.10	0.62	0.43	0.18	0.32	0.70	0.71	0.54	0.16	2.18
Cu_2O	0.10	0.01	0.09	0.11	0.14	0.13	<mdl	0.67	0.16	0.15	<mdl	0.51	0.22	0.21	0.04	0.63	0.73	0.22	0.46	1.00	0.25	0.19	0.09	0.72
As_2O_3	<mdl	-	<mdl	<mdl	0.30	0.30	<mdl	1.00	1.12	0.14	0.81	1.37	0.07	0.11	<mdl	0.37	<mdl	-	<mdl	<mdl	0.05	0.05	<mdl	0.19
ZrO_2	0.06	0.02	0.05	0.07	0.06	0.02	<mdl	0.11	0.06	0.01	0.05	0.09	0.05	0.02	<mdl	0.08	0.05	0.01	0.04	0.07	0.06	0.01	0.03	0.08
Nb_2O_5	0.19	0.18	0.06	0.39	0.16	0.08	<mdl	0.30	0.39	0.08	0.25	0.58	0.19	0.19	0.07	0.67	0.20	0.21	0.09	0.51	0.15	0.07	<mdl	0.33
Y_2O_3	2.94	0.14	2.83	3.11	2.66	0.29	1.94	3.11	2.27	0.25	1.81	2.83	3.19	0.33	2.71	3.66	3.35	0.42	2.80	3.72	2.88	0.29	2.08	3.29
Ce_2O_3	4.31	0.16	4.12	4.41	4.01	0.66	2.52	5.14	1.48	0.65	0.71	3.28	4.43	0.73	3.51	5.80	5.11	0.92	4.07	6.17	3.56	0.53	2.18	4.23
La_2O_3	0.53	0.02	0.51	0.55	0.47	0.08	0.33	0.62	0.25	0.07	0.17	0.41	0.55	0.11	0.42	0.74	0.61	0.12	0.45	0.73	0.46	0.07	0.34	0.56
Pr_2O_3	0.49	0.04	0.45	0.53	0.49	0.08	0.31	0.70	0.31	0.08	0.20	0.50	0.54	0.13	0.40	0.78	0.63	0.14	0.50	0.80	0.45	0.08	0.26	0.56
Nd_2O_3	2.44	0.27	2.27	2.75	2.39	0.31	1.56	3.26	1.66	0.33	1.12	2.42	2.67	0.54	2.07	3.66	2.82	0.34	2.36	3.17	2.15	0.29	1.42	2.50
Sm_2O_3	0.46	0.07	0.38	0.52	0.48	0.08	0.30	0.69	0.55	0.04	0.49	0.64	0.52	0.10	0.38	0.71	0.55	0.03	0.51	0.58	0.44	0.07	0.32	0.56
Gd_2O_3	0.56	0.04	0.54	0.61	0.48	0.07	0.29	0.61	0.60	0.04	0.53	0.68	0.57	0.07	0.43	0.67	0.63	0.03	0.59	0.67	0.49	0.06	0.38	0.58
Total Oxide	101.19	0.74	100.43	101.91	99.03	1.06	96.50	102.22	96.10	0.52	94.90	96.82	98.74	0.76	97.94	100.06	99.07	1.14	97.90	100.16	99.22	1.17	98.00	102.52
SiO_2+CaO+Fe_2O_3	2.89	0.46	2.38	3.27	2.34	0.67	1.22	3.63	4.35	0.30	3.89	4.90	1.66	0.36	1.24	2.37	1.77	0.32	1.32	2.01	2.10	0.47	1.60	2.93
Pb/U	0.28	0.01	0.27	0.28	0.21	0.04	0.13	0.27	0.09	0.01	0.07	0.10	0.26	0.02	0.21	0.28	0.26	0.02	0.24	0.27	0.25	0.02	0.21	0.29

Note(s):

Average minimum detection limit (mdl) per element for 99% confidence interval (wt%): U ≈ 0.04, Pb≈ 0.04, Th≈ 0.04, Na≈ 0.02, Si≈ 0.01, P≈ 0.01, S≈ 0.01, Ca≈ 0.01, Ti≈ 0.01, Mn≈ 0.03, Fe≈ 0.02, Cu≈ 0.04, As≈ 0.03, Zr≈ 0.02, Nb≈ 0.04, Y≈ 0.03, Ce≈ 0.03, La≈ 0.02, Pr≈ 0.08, Nd≈ 0.09, Sm≈ 0.07, Gd≈ 0.08

HREE oxides were <mdl (identified from full wavelength spectrometer scans).

Sample ID is of the form: "SXX.xx" where "SXX" = sample ID as represented in Table 1, "xx" = grain number analysed

a) Primary Uraninite Composition.

b) Zoned Uraninite (with high PbO_2) associated with bornite.

c) Zoned Uraninite (with low PbO_2) associated with bornite.

Table A7: Electron probe microanalytical data for zoned uraninites (Part 2).

Sample no.	S17.52 [a]				S17.61 [a]				S17.63 [a]				S18.29 [b]				S18.2 [b]				S18.29 [a]	
Valid N (analyses)	23				7				14				9				39				2	
(wt%)	Mean	SD	Min	Max	Mean	SD	Min	Max	Mean	SD	Min	Max	Mean	SD	Min	Max	Mean	SD	Min	Max		
UO_2	66.22	1.61	62.13	67.79	67.11	1.94	62.79	68.28	66.47	1.42	64.12	68.69	77.39	0.97	75.94	78.54	78.13	0.83	76.40	79.36	74.97	75.38
PbO_2	16.52	1.16	13.29	18.22	17.57	0.99	15.77	18.79	17.43	1.44	13.87	19.61	3.64	1.69	1.64	5.76	6.25	0.54	4.91	7.23	13.41	13.58
ThO_2	0.10	0.06	<mdl	0.25	0.79	0.47	0.39	1.50	0.87	0.28	0.44	1.22	<mdl	-	<mdl	<mdl	0.05	0.04	<mdl	0.19	<mdl	<mdl
Na_2O	0.22	0.17	<mdl	0.47	0.24	0.20	<mdl	0.51	0.18	0.09	0.05	0.34	0.32	0.07	0.21	0.42	0.28	0.05	0.23	0.53	0.17	0.15
SiO_2	0.14	0.04	0.10	0.28	0.23	0.20	0.11	0.67	0.11	0.02	0.07	0.13	1.30	0.50	0.56	2.04	0.50	0.16	0.26	0.92	0.83	0.71
P_2O_5	<mdl	-	<mdl	0.02	<mdl	-	<mdl	<mdl	<mdl	-	<mdl	<mdl	0.09	0.03	0.04	0.13	0.04	0.02	<mdl	0.09	0.10	0.07
SO_3	<mdl	-	<mdl	<mdl	0.02	0.04	<mdl	0.10	<mdl	-	<mdl	<mdl	<mdl	-	<mdl	0.03	<mdl	-	<mdl	0.08	<mdl	<mdl
CaO	1.36	0.39	1.07	3.00	1.10	0.25	0.74	1.47	1.25	0.31	0.78	1.77	2.44	0.60	1.56	3.38	2.24	0.34	1.68	3.16	1.86	1.88
TiO_2	<mdl	0.01	<mdl	0.03	<mdl	-	<mdl	<mdl	<mdl	-	<mdl	<mdl	0.08	0.03	0.05	0.12	0.08	0.03	0.04	0.16	0.03	0.05
MnO	<mdl	-	<mdl	0.07	<mdl	0.03	<mdl	0.07	<mdl	-	<mdl	0.07	0.25	0.08	0.14	0.34	0.19	0.04	0.10	0.28	0.19	0.17
Fe_2O_3	0.66	0.38	0.22	1.68	1.34	0.82	0.48	2.72	0.40	0.21	0.15	0.69	2.04	0.85	1.04	3.21	0.73	0.21	0.50	1.62	1.33	1.45
Cu_2O	0.25	0.18	<mdl	0.72	0.33	0.24	0.15	0.82	0.15	0.19	<mdl	0.72	0.45	0.17	0.21	0.69	0.11	0.09	<mdl	0.38	0.55	0.75
As_2O_3	0.05	0.07	<mdl	0.28	<mdl	-	<mdl	<mdl	0.07	0.07	<mdl	0.23	0.68	0.16	0.43	0.87	0.87	0.06	0.71	0.97	0.35	0.30
ZrO_2	0.06	0.01	0.04	0.08	0.06	0.02	0.04	0.08	0.05	0.02	<mdl	0.08	0.08	0.02	0.06	0.12	0.08	0.02	0.05	0.13	0.04	0.08
Nb_2O_5	0.24	0.14	<mdl	0.63	0.15	0.09	<mdl	0.31	0.17	0.09	<mdl	0.29	0.50	0.16	0.32	0.86	0.28	0.06	0.20	0.49	0.48	0.50
Y_2O_3	3.28	0.11	3.12	3.56	3.02	0.14	2.88	3.30	3.17	0.22	2.74	3.58	2.24	0.43	1.56	2.79	2.99	0.12	2.71	3.20	1.45	1.46
Ce_2O_3	4.51	0.63	3.77	5.79	3.87	0.73	3.21	5.40	4.12	0.81	3.10	5.38	2.03	0.62	1.33	3.02	0.59	0.10	0.39	0.81	1.48	1.76
La_2O_3	0.56	0.08	0.46	0.74	0.48	0.10	0.38	0.68	0.51	0.10	0.37	0.65	0.28	0.04	0.23	0.34	0.19	0.02	0.16	0.24	0.32	0.36
Pr_2O_3	0.59	0.14	0.43	0.83	0.47	0.07	0.37	0.59	0.51	0.16	0.31	0.79	0.33	0.13	0.19	0.55	0.10	0.05	<mdl	0.18	0.17	0.23
Nd_2O_3	2.77	0.56	2.35	3.88	2.22	0.58	1.74	3.46	2.52	0.66	1.77	3.74	1.60	0.48	0.99	2.35	0.62	0.08	0.48	0.80	1.12	1.34
Sm_2O_3	0.55	0.09	0.44	0.72	0.45	0.10	0.31	0.63	0.51	0.12	0.36	0.70	0.42	0.09	0.28	0.55	0.25	0.04	0.14	0.33	0.38	0.36
Gd_2O_3	0.58	0.06	0.50	0.73	0.57	0.05	0.52	0.66	0.56	0.09	0.46	0.75	0.49	0.09	0.38	0.64	0.61	0.05	0.49	0.69	0.30	0.26
Total Oxide	98.70	1.16	96.21	100.84	100.08	1.07	98.04	100.91	99.10	0.43	98.21	99.98	96.68	0.82	95.88	98.28	95.21	0.49	94.21	96.66	99.66	100.75
SiO_2+CaO+Fe_2O_3	2.16	0.51	1.53	3.71	2.66	1.08	1.44	4.53	1.76	0.46	1.01	2.42	5.78	1.84	3.16	8.21	3.48	0.48	2.52	4.46	3.92	4.13
Pb/U	0.25	0.01	0.21	0.27	0.26	0.01	0.25	0.27	0.26	0.02	0.21	0.28	0.05	0.02	0.02	0.07	0.08	0.01	0.06	0.09	0.18	0.18

Note(s):

Average minimum detection limit (mdl) per element for 99% confidence interval (wt%): U≈ 0.04, Pb≈ 0.04, Th≈ 0.04, Na≈ 0.02, Si≈ 0.01, P≈ 0.01, S≈ 0.01, Ca≈ 0.01, Ti≈ 0.01, Mn≈ 0.03, Fe≈ 0.02, Cu≈ 0.04, As≈ 0.03, Zr≈ 0.02, Nb≈ 0.04, Y≈ 0.03, Ce≈ 0.03, La≈ 0.02, Pr≈ 0.08, Nd≈ 0.09, Sm≈ 0.07, Gd≈ 0.08.

HREE oxides were <mdl (identified from full wavelength spectrometer scans).

Sample ID is of the form: "SXX.xx" where "SXX" = sample ID as represented in Table 1, "xx" = grain number analysed

a) Zoned Uraninite (with high PbO_2) associated with bornite.

b) Zoned Uraninite (with low PbO_2) associated with bornite.

Table A8: Electron probe microanalytical data for cob-web uraninites (high PbO_2 zones).

Sample no.	S15.3 [a]				S15.51 [a]				S17.26 [b]				S17.38 [b]				S18.12 [b]				S18.51 [b]				S18.63 [b]
Valid N (analyses)	3 (Fig. 6d)				8				6 (Fig. 4d)				3				11 (Fig. 6a)				8				1 (Fig. 6b)
(wt%)	Mean	SD	Min	Max	Mean	SD	Min	Max	Mean	SD	Min	Max	Mean	SD	Min	Max	Mean	SD	Min	Max	Mean	SD	Min	Max	
UO_2	69.77	0.77	69.25	70.65	71.72	1.66	69.24	74.41	66.19	0.85	65.43	67.48	62.99	0.81	62.09	63.67	68.03	2.44	64.96	74.18	70.65	3.06	67.43	75.49	68.88
PbO_2	12.31	1.10	11.09	13.23	13.40	2.69	10.63	18.26	18.17	0.42	17.68	18.95	16.09	0.44	15.58	16.36	16.03	2.41	9.73	17.66	15.45	2.10	11.75	17.58	16.28
ThO_2	0.46	0.12	0.33	0.57	<mdl	-	<mdl	<mdl	0.12	0.15	<mdl	0.35	0.33	0.18	0.14	0.50	0.07	0.05	<mdl	0.17	0.34	0.15	0.15	0.55	0.18
Na_2O	0.19	0.03	0.16	0.21	0.23	0.06	0.15	0.34	<mdl	-	<mdl	<mdl	0.02	0.02	<mdl	0.04	0.10	0.10	<mdl	0.29	0.06	0.06	<mdl	0.16	0.14
SiO_2	0.10	0.02	0.08	0.11	0.12	0.03	0.09	0.17	0.21	0.09	0.14	0.37	0.12	0.02	0.11	0.15	0.35	0.27	0.17	0.99	0.90	0.77	0.17	2.24	0.41
P_2O_5	<mdl	-	<mdl	<mdl	0.01	0.02	<mdl	0.04	0.01	0.01	<mdl	0.04	<mdl	-	<mdl	<mdl	0.02	0.03	<mdl	0.11	0.05	0.09	<mdl	0.27	<mdl
SO_3	0.06	0.09	<mdl	0.17	0.07	0.16	<mdl	0.47	<mdl	-	<mdl	<mdl	<mdl	-	<mdl	<mdl	0.02	0.04	<mdl	0.15	<mdl	-	<mdl	<mdl	<mdl
CaO	1.97	0.50	1.55	2.53	2.16	0.64	0.93	2.99	1.06	0.13	0.90	1.29	2.04	0.33	1.73	2.38	1.14	0.46	0.32	2.22	0.90	0.42	0.28	1.49	1.01
TiO_2	<mdl	-	<mdl	<mdl	0.01	0.02	<mdl	0.06	<mdl	-	<mdl	<mdl	<mdl	-	<mdl	<mdl	0.01	0.02	<mdl	0.07	0.07	0.05	<mdl	0.13	0.05
MnO	0.12	0.05	0.09	0.17	0.12	0.07	<mdl	0.22	<mdl	-	<mdl	<mdl	<mdl	-	<mdl	<mdl	0.04	0.04	<mdl	0.13	0.07	0.07	<mdl	0.22	0.10
Fe_2O_3	0.39	0.11	0.30	0.51	0.46	0.13	0.30	0.68	0.74	0.28	0.45	1.19	0.97	0.07	0.93	1.06	0.88	0.44	0.31	1.58	1.27	0.74	0.38	2.58	1.41
Cu_2O	0.20	0.08	0.13	0.29	0.14	0.15	0.05	0.51	0.95	0.23	0.70	1.27	1.15	0.15	0.99	1.27	0.85	0.24	0.54	1.29	0.58	0.17	0.31	0.85	0.53
As_2O_3	0.46	0.20	0.33	0.69	0.52	0.21	0.13	0.75	<mdl	-	<mdl	<mdl	<mdl	-	<mdl	<mdl	0.09	0.16	<mdl	0.53	0.11	0.10	<mdl	0.30	0.09
ZrO_2	0.14	0.03	0.11	0.16	0.18	0.16	0.07	0.57	0.06	0.01	0.05	0.06	0.05	0.02	0.03	0.07	0.07	0.06	0.04	0.25	0.11	0.08	0.05	0.24	0.10
Nb_2O_5	0.30	0.11	0.24	0.42	0.19	0.09	<mdl	0.34	0.12	0.05	0.05	0.17	0.32	0.28	0.10	0.63	0.14	0.09	<mdl	0.31	0.30	0.12	0.14	0.47	0.12
Y_2O_3	2.94	0.29	2.66	3.24	2.25	0.20	1.96	2.59	3.22	0.25	2.94	3.52	3.62	0.13	3.49	3.76	3.33	0.48	2.71	4.05	2.93	0.31	2.52	3.46	2.85
Ce_2O_3	3.79	0.38	3.37	4.08	2.71	0.80	1.19	3.61	4.53	0.21	4.25	4.73	6.11	0.47	5.71	6.63	3.95	1.24	0.45	5.04	2.68	1.71	0.26	4.22	3.37
La_2O_3	0.45	0.06	0.39	0.51	0.34	0.07	0.23	0.45	0.52	0.03	0.50	0.57	0.77	0.08	0.71	0.86	0.47	0.11	0.16	0.56	0.39	0.17	0.15	0.54	0.42
Pr_2O_3	0.44	0.03	0.41	0.47	0.34	0.09	0.16	0.43	0.52	0.09	0.39	0.66	0.73	0.09	0.68	0.83	0.45	0.11	0.16	0.54	0.30	0.19	<mdl	0.50	0.38
Nd_2O_3	2.27	0.11	2.15	2.36	1.84	0.36	1.12	2.26	2.64	0.16	2.46	2.91	3.16	0.11	3.07	3.29	2.15	0.59	0.47	2.67	1.54	0.76	0.50	2.27	1.79
Sm_2O_3	0.51	0.03	0.47	0.53	0.44	0.06	0.36	0.54	0.51	0.03	0.46	0.55	0.55	0.05	0.50	0.59	0.44	0.09	0.25	0.54	0.38	0.11	0.25	0.56	0.38
Gd_2O_3	0.53	0.05	0.49	0.58	0.45	0.07	0.32	0.54	0.56	0.03	0.53	0.62	0.64	0.02	0.61	0.65	0.54	0.10	0.39	0.66	0.54	0.08	0.41	0.67	0.48
Total Oxide	97.42	0.26	97.13	97.61	97.74	1.03	96.50	99.50	100.18	0.69	99.35	101.25	99.72	0.36	99.39	100.10	99.18	0.93	97.39	100.55	99.61	0.74	98.40	100.31	98.97
SiO_2+CaO+Fe_2O_3	2.46	0.60	2.02	3.14	2.74	0.66	1.58	3.50	2.01	0.26	1.70	2.41	3.14	0.27	2.89	3.43	2.37	0.99	1.21	4.60	3.08	1.79	0.84	5.99	2.83
Pb/U	0.17	0.02	0.15	0.19	0.18	0.04	0.15	0.26	0.27	0.01	0.26	0.28	0.25	0.00	0.25	0.25	0.23	0.04	0.14	0.26	0.22	0.03	0.16	0.26	0.23

Note(s):

Average minimum detection limit (mdl) per element for 99% confidence interval (wt%): U≈ 0.04, Pb≈ 0.04, Th≈ 0.04, Na≈ 0.02, Si≈ 0.01, P≈ 0.01, S≈ 0.01, Ca≈ 0.01, Ti≈ 0.01, Mn≈ 0.03, Fe≈ 0.02, Cu≈ 0.04, As≈ 0.03, Zr≈ 0.02, Nb≈ 0.04, Y≈ 0.03, Ce≈ 0.03, La≈ 0.02, Pr≈ 0.08, Nd≈ 0.09, Sm≈ 0.07, Gd≈ 0.08.

HREE oxides were <mdl (identified from full wavelength spectrometer scans)

Sample ID is of the form: "SXX.xx" where "SXX" = sample ID as represented in Table 1, "xx" = grain number analysed

a) Cob-web uraninite (with high PbO_2) associated with chalcopyrite.

b) Cob-web uraninite (with high PbO_2) associated with bornite.

Table A9: Electron probe microanalytical data for cob-web uraninites (low PbO_2 zones).

Sample no.	S15.3 [a]				S15.51 [a]				S18.24 [b]				S18.59 [b]				S18.12 [b]		S18.63 [b]				S18.51 [b]
Valid N (analyses)	5 (Fig. 6d)				8				11				6				1 [c]	1 [c]	3 (Fig. 6b)				1
(wt%)	Mean	SD	Min	Max	Mean	SD	Min	Max	Mean	SD	Min	Max	Mean	SD	Min	Max			Mean	SD	Min	Max	
UO_2	75.51	0.69	75.06	76.68	76.05	1.19	74.81	77.99	77.80	0.44	77.15	78.47	75.94	1.16	74.22	77.31	69.52	71.35	74.62	2.15	72.67	76.92	72.67
PbO_2	7.05	0.32	6.59	7.42	6.86	0.72	6.13	8.39	5.61	0.69	4.33	6.88	5.47	1.11	3.79	7.16	7.70	8.13	5.25	2.62	2.90	8.08	7.38
ThO_2	0.57	0.07	0.46	0.63	<mdl	-	<mdl	<mdl	<mdl	-	<mdl	<mdl	0.27	0.11	0.16	0.47	0.10	<mdl	0.30	0.04	0.26	0.34	0.64
Na_2O	0.14	0.02	0.12	0.18	0.21	0.03	0.15	0.25	0.21	0.04	0.16	0.29	0.28	0.09	0.12	0.38	0.34	0.37	0.27	0.05	0.24	0.33	0.20
SiO_2	0.15	0.00	0.15	0.16	0.18	0.06	0.13	0.31	1.09	0.48	0.57	2.35	1.09	0.32	0.72	1.49	1.33	1.24	2.13	0.53	1.77	2.75	2.70
P_2O_5	0.02	0.02	<mdl	0.05	0.06	0.03	0.02	0.11	0.05	0.02	0.02	0.09	0.05	0.04	<mdl	0.11	0.13	0.10	0.07	0.01	0.05	0.08	0.07
SO_3	0.22	0.19	<mdl	0.42	0.02	0.03	<mdl	0.11	0.05	0.11	<mdl	0.36	0.02	0.04	<mdl	0.09	<mdl	<mdl	<mdl	-	<mdl	<mdl	<mdl
CaO	3.62	0.27	3.34	3.98	3.90	0.65	2.84	4.81	2.22	0.23	1.85	2.60	1.94	0.36	1.51	2.47	2.56	2.49	2.15	0.40	1.82	2.60	1.69
TiO_2	0.06	0.01	0.05	0.07	0.02	0.01	<mdl	0.03	0.15	0.07	0.07	0.27	0.22	0.03	0.19	0.25	0.03	0.03	0.36	0.18	0.21	0.55	0.18
MnO	0.36	0.02	0.33	0.37	0.32	0.08	0.18	0.44	0.23	0.04	0.17	0.31	0.17	0.08	0.06	0.29	0.17	0.12	0.26	0.07	0.18	0.31	0.17
Fe_2O_3	0.65	0.10	0.52	0.79	0.59	0.13	0.48	0.81	1.24	0.25	0.92	1.70	1.32	0.24	0.97	1.57	1.45	1.48	1.95	0.26	1.66	2.13	1.85
Cu_2O	0.60	0.32	0.22	1.05	0.18	0.12	0.05	0.35	0.29	0.24	0.09	0.94	0.58	0.29	0.29	0.95	0.76	0.47	0.83	0.10	0.74	0.95	0.31
As_2O_3	1.07	0.14	0.89	1.24	1.00	0.23	0.75	1.34	0.80	0.12	0.56	0.90	0.50	0.15	0.32	0.66	0.69	0.55	0.61	0.07	0.54	0.69	0.53
ZrO_2	0.16	0.03	0.13	0.20	0.16	0.04	0.11	0.21	0.07	0.03	<mdl	0.12	0.10	0.03	0.06	0.15	0.07	0.06	0.12	0.02	0.10	0.14	0.07
Nb_2O_5	1.30	0.08	1.16	1.35	0.35	0.07	0.23	0.43	0.99	0.41	0.44	1.65	0.30	0.09	0.20	0.43	0.14	0.13	0.26	0.10	0.19	0.38	0.63
Y_2O_3	1.58	0.06	1.53	1.68	1.80	0.14	1.58	2.03	2.53	0.24	2.22	2.94	2.83	0.22	2.55	3.08	3.58	3.00	2.36	0.23	2.14	2.60	2.27
Ce_2O_3	1.01	0.06	0.97	1.09	1.13	0.30	0.85	1.80	1.11	0.46	0.62	1.98	2.49	0.53	1.56	3.08	3.45	3.02	2.55	0.42	2.24	3.02	2.68
La_2O_3	0.19	0.02	0.16	0.22	0.23	0.05	0.18	0.32	0.23	0.02	0.20	0.27	0.31	0.05	0.25	0.38	0.42	0.36	0.35	0.02	0.33	0.38	0.37
Pr_2O_3	0.20	0.03	0.17	0.25	0.26	0.06	0.18	0.36	0.19	0.07	0.10	0.30	0.30	0.06	0.20	0.37	0.38	0.34	0.28	0.04	0.24	0.32	0.25
Nd_2O_3	1.17	0.07	1.11	1.28	1.25	0.15	1.09	1.58	1.01	0.38	0.58	1.76	1.63	0.21	1.24	1.87	2.07	1.82	1.34	0.15	1.25	1.51	1.54
Sm_2O_3	0.41	0.05	0.33	0.47	0.47	0.04	0.43	0.54	0.31	0.08	0.18	0.45	0.37	0.07	0.22	0.42	0.58	0.49	0.29	0.03	0.27	0.33	0.31
Gd_2O_3	0.49	0.04	0.44	0.54	0.52	0.05	0.43	0.60	0.55	0.06	0.49	0.64	0.50	0.04	0.44	0.55	0.55	0.51	0.40	0.10	0.31	0.50	0.42
Total Oxide	96.54	0.84	95.39	97.37	95.57	0.81	94.27	96.82	96.78	0.71	95.96	98.10	96.65	0.72	95.83	97.71	96.01	96.07	96.75	0.42	96.37	97.20	96.94
SiO_2+CaO+Fe_2O_3	4.42	0.29	4.01	4.73	4.67	0.66	3.46	5.49	4.55	0.65	3.83	5.99	4.34	0.76	3.37	5.18	5.21	5.34	6.23	0.87	5.25	6.89	6.24
Pb/U	0.09	0.00	0.09	0.10	0.09	0.01	0.08	0.11	0.07	0.01	0.05	0.09	0.07	0.01	0.05	0.09	0.11	0.11	0.07	0.04	0.04	0.11	0.10

Note(s):

Average minimum detection limit (mdl) per element for 99% confidence interval (wt%): U≈ 0.04, Pb≈ 0.04, Th≈ 0.04, Na≈ 0.02, Si≈ 0.01, P≈ 0.01, S≈ 0.01, Ca≈ 0.01, Ti≈ 0.01, Mn≈ 0.03, Fe≈ 0.02, Cu≈ 0.04, As≈ 0.03, Zr≈ 0.02, Nb≈ 0.04, Y≈ 0.03, Ce≈ 0.03, La≈ 0.02, Pr≈ 0.08, Nd≈ 0.09, Sm≈ 0.07, Gd≈ 0.08.

HREE oxides were <mdl (identified from full wavelength spectrometer scans).

Sample ID is of the form: "SXX.xx" where "SXX" = sample ID as represented in Table 1, "xx" = grain number analysed

a) Cob-web uraninite (with low PbO_2) associated with chalcopyrite.

b) Cob-web uraninite (with low PbO_2) associated with bornite.

c) Refer to Fig. 6a for BSE image of grain.

Table A10: Electron probe microanalytical data for massive uraninites.

Sample no.	S11.37 & S11.39 [a]				S11.46-48 & S11.52 & S11.55 [a]				S11.37 & S11.39 [b]				S11.46-48 & S11.52 & S11.55 [b]				S21 [c]				S4 [d]				S1 [e]			
Valid N (analyses)	72 (Fig. 7d)				39 (Fig. 7d)				32 (Fig. 7d)				9 (Fig. 7d)				11 (Fig. 7c)				4 (Fig. 7d)				28 (Fig. 7a)			
(wt%)	Mean	SD	Min	Max	Mean	SD	Min	Max	Mean	SD	Min	Max	Mean	SD	Min	Max	Mean	SD	Min	Max	Mean	SD	Min	Max	Mean	SD	Min	Max
UO_2	78.86	1.93	74.36	81.77	79.20	1.61	74.57	81.44	81.68	1.67	76.17	85.14	80.39	2.44	75.33	82.73	78.94	0.58	77.58	80.04	79.76	2.23	77.07	82.52	82.02	2.73	75.58	88.16
PbO_2	2.18	0.98	<mdl	3.71	2.21	0.84	0.24	3.41	3.76	0.90	1.14	5.36	2.77	1.34	0.39	4.06	6.92	0.59	5.77	8.83	6.41	1.55	4.84	8.54	4.38	1.26	1.95	8.18
ThO_2	<mdl	-	<mdl	<mdl	<mdl	-	<mdl	<mdl	<mdl	-	<mdl	<mdl	<mdl	-	<mdl	<mdl	<mdl	-	<mdl	<mdl	<mdl	-	<mdl	<mdl	<mdl	-	<mdl	<mdl
Na_2O	0.57	0.15	0.42	1.28	0.58	0.08	0.44	0.75	0.46	0.09	0.35	0.77	0.53	0.07	0.40	0.64	0.25	0.10	0.15	0.56	0.23	0.07	0.16	0.31	0.53	0.35	0.17	1.44
SiO_2	2.34	0.92	0.95	4.86	2.36	0.76	1.27	4.11	1.40	0.84	0.41	4.17	2.42	1.75	0.99	5.85	0.37	0.08	0.28	0.63	0.91	0.60	0.23	1.68	3.03	1.67	0.67	6.82
P_2O_5	0.18	0.05	0.09	0.32	0.19	0.06	0.12	0.48	0.11	0.03	0.04	0.17	0.16	0.06	0.09	0.26	0.04	0.01	0.03	0.07	0.01	0.01	<mdl	0.02	0.45	0.27	0.04	1.26
SO_3	0.03	0.08	<mdl	0.44	0.02	0.04	<mdl	0.20	0.02	0.04	<mdl	0.22	0.02	0.03	<mdl	0.09	0.16	0.14	<mdl	0.46	0.04	0.06	<mdl	0.13	0.11	0.14	<mdl	0.44
CaO	4.62	0.47	4.00	5.84	4.64	0.37	4.09	5.54	3.66	0.26	2.85	3.96	3.67	0.26	3.07	3.99	4.86	0.12	4.58	5.03	2.58	0.31	2.29	3.00	2.36	0.57	0.60	3.41
TiO_2	<mdl	-	<mdl	0.01	<mdl	-	<mdl	0.02	<mdl	-	<mdl	0.02	<mdl	-	<mdl	0.01	0.46	0.02	0.42	0.51	0.19	0.03	0.16	0.23	0.34	0.17	0.11	0.89
MnO	0.63	0.18	0.26	1.07	0.59	0.13	0.31	1.01	0.46	0.15	0.24	0.77	0.51	0.15	0.38	0.75	0.33	0.02	0.28	0.37	0.27	0.05	0.22	0.34	0.33	0.07	0.20	0.49
Fe_2O_3	1.08	0.43	0.49	2.05	0.98	0.27	0.61	1.82	0.76	0.46	0.24	1.87	0.99	0.43	0.53	1.78	0.70	0.24	0.49	1.60	1.58	0.77	0.90	2.45	0.76	0.20	0.42	1.23
Cu_2O	0.08	0.09	<mdl	0.44	0.09	0.07	<mdl	0.25	0.07	0.08	<mdl	0.27	0.12	0.10	<mdl	0.30	0.70	0.30	0.25	1.29	1.03	0.24	0.78	1.34	0.41	0.30	0.10	1.15
As_2O_3	0.34	0.12	0.15	0.71	0.33	0.10	0.18	0.60	0.21	0.09	0.09	0.44	0.32	0.15	0.18	0.60	0.50	0.02	0.46	0.52	0.99	0.25	0.82	1.35	0.15	0.05	0.04	0.23
ZrO_2	0.10	0.03	0.05	0.19	0.14	0.03	0.07	0.21	0.11	0.04	0.06	0.20	0.12	0.04	0.09	0.19	0.08	0.01	0.06	0.11	0.14	0.02	0.13	0.17	0.22	0.04	0.16	0.29
Nb_2O_5	<mdl	0.02	<mdl	0.13	0.04	0.03	<mdl	0.11	0.04	0.03	<mdl	0.11	0.04	0.03	<mdl	0.09	0.09	0.02	0.06	0.12	0.06	0.03	<mdl	0.09	<mdl	-	<mdl	<mdl
Y_2O_3	1.87	0.15	1.64	2.23	1.88	0.09	1.68	2.06	1.74	0.11	1.59	2.00	1.81	0.16	1.65	2.15	1.47	0.08	1.33	1.67	1.38	0.12	1.24	1.50	0.58	0.27	0.14	1.35
Ce_2O_3	0.52	0.06	0.44	0.75	0.53	0.05	0.46	0.70	0.44	0.03	0.38	0.50	0.46	0.04	0.40	0.53	0.88	0.03	0.83	0.93	0.96	0.03	0.94	1.00	0.64	0.19	0.15	0.99
La_2O_3	0.21	0.02	0.17	0.26	0.21	0.01	0.17	0.25	0.19	0.02	0.15	0.23	0.20	0.02	0.18	0.24	0.23	0.01	0.19	0.25	0.31	0.01	0.30	0.32	0.30	0.09	0.16	0.52
Pr_2O_3	0.11	0.05	<mdl	0.20	0.11	0.05	<mdl	0.26	0.11	0.05	<mdl	0.19	0.13	0.05	<mdl	0.17	0.17	0.04	0.11	0.26	0.14	0.04	0.11	0.20	<mdl	0.05	<mdl	0.17
Nd_2O_3	0.83	0.06	0.70	0.94	0.84	0.06	0.71	1.00	0.79	0.08	0.62	0.97	0.79	0.05	0.74	0.85	0.86	0.05	0.76	0.96	0.67	0.05	0.60	0.71	0.39	0.17	0.16	0.83
Sm_2O_3	0.27	0.04	0.16	0.37	0.29	0.03	0.21	0.34	0.24	0.05	0.15	0.36	0.29	0.03	0.25	0.32	0.37	0.04	0.29	0.46	0.19	0.03	0.16	0.22	0.09	0.06	<mdl	0.24
Gd_2O_3	0.42	0.05	0.25	0.54	0.40	0.05	0.28	0.52	0.41	0.04	0.35	0.49	0.39	0.03	0.33	0.44	0.44	0.04	0.35	0.52	0.20	0.03	0.17	0.23	0.11	0.06	<mdl	0.22
Total Oxide	95.30	1.11	91.44	96.98	95.66	0.93	92.50	96.98	96.68	1.05	93.83	100.23	96.17	1.48	92.94	97.41	98.84	0.57	97.52	99.85	98.08	1.68	95.59	99.16	97.32	1.15	94.88	100.49
SiO_2+CaO+Fe_2O_3	8.04	1.42	5.73	10.75	7.98	1.23	6.08	10.24	5.82	1.37	3.50	10.01	7.09	1.84	5.12	10.15	5.93	0.30	5.52	6.86	5.07	1.51	3.41	6.38	6.14	1.99	1.68	10.53
Pb/U	0.03	0.01	0.00	0.05	0.03	0.01	0.00	0.04	0.05	0.01	0.01	0.06	0.03	0.02	0.01	0.05	0.09	0.01	0.07	0.11	0.08	0.02	0.06	0.11	0.05	0.01	0.02	0.09

Note(s):

Average minimum detection limit (mdl) per element for 99% confidence interval (wt%): U ≈ 0.04, Pb≈ 0.04, Th≈ 0.04, Na≈ 0.02, Si≈ 0.01, P≈ 0.01, S≈ 0.01, Ca≈ 0.01, Ti≈ 0.01, Mn≈ 0.03, Fe≈ 0.02, Cu≈ 0.04, As≈ 0.03, Zr≈ 0.02, Nb≈ 0.04, Y≈ 0.03, Ce≈ 0.03, La≈ 0.02, Pr≈ 0.08, Nd≈ 0.09, Sm≈ 0.07, Gd≈ 0.08.

HREE oxides were <mdl (identified from full wavelength spectrometer scans).

Sample ID is of the form: "SXX.xx" where "SXX" = sample ID as represented in Table 1, "xx" = grain number analysed

a) Massive uraninite (with high CaO) associated with chalcopyrite.

b) Massive uraninite (with low CaO) associated with chalcopyrite.

c) Massive uraninite (crustiform) associated with bornite and/or chalcocite.

d) Uraninite pisoliths associated with bornite and/or chalcocite.

e) Massive uraninite intergrown with coffinite.

APPENDIX B

SUPPLEMENTARY DATA FOR CHAPTER 4:

CHEMICAL ZONING AND LATTICE DISTORTION IN URANINITE FROM OLYMPIC DAM, SOUTH AUSTRALIA

Edeltraud Macmillan[1,2], Cristiana L. Ciobanu[3], Kathy Ehrig[2], Nigel J. Cook[3] and Allan Pring[4]

[1]*School of Physical Sciences, The University of Adelaide, Adelaide, SA, 5000, Australia*

[2]*BHP Billiton Olympic Dam, Adelaide, SA, 5000, Australia*

[3]*School of Chemical Engineering, The University of Adelaide, Adelaide, SA, 5000, Australia*

[4]*School of Chemical and Physical Sciences, Flinders University, Bedford Park, SA, 5042, Australia*

Paper accepted for publication in American Mineralogist

APPENDIX B.1 – ANALYTICAL METHODS

SEM/EPMA

Initial scanning electron microscopy (SEM) analysis was conducted using a Quanta 450 field emission gun (FEG) SEM with silicon-drift detector (Adelaide Microscopy, University of Adelaide). Operating conditions used were 60 Pa chamber pressure, 20 keV accelerating voltage, 0° tilt, 10-11 mm working distance, with a spot size of 4-5.

Subsequent quantitative analysis of the uraninite composition was measured using a Cameca SX-Five electron probe micro-analyzer (EPMA) equipped with 5 tunable wavelength-dispersive spectrometers. For spot analyses, operating conditions included a 15 keV accelerating voltage, 100 nA beam current, 40° takeoff angle, with 0.5 to 1 μm-sized beam. A total of 28 elements were measured: U, Pb, Th, Na, Mg, Al, Si, P, S, K, Ca, Ti, Mn, Fe, Cu, As, Zr, Nb, Y, Ce, La, Pr, Nd, Sm, Gd, Sr, Ba, Te. The total acquisition time per point was 9 minutes 42 seconds. Elemental mapping was performed at 20 keV accelerating voltage, 100 nA beam current and 1 μm beam-size. A total of 13 elements were also mapped, with wavelength dispersive spectroscopy (WDS) being used for Ce Lα, P Kα, Ca Kα, Y Lα, and Pb Mα. Energy dispersive spectroscopy (EDS) was used to measure Si Kα, Fe Kα, U Lα, S Kα, Cu Kα, La Lα, Nd Lα, and Ti Kα. Further details of the methodology used for both point analysis and elemental mapping is outlined in Macmillan et al. (2016), as are all details of the standards used, measured element X-ray lines, estimates of minimum detection limits, and mean precision.

SAMPLE PREPARATION

Surface sample preparation is important for any electron back-scatter diffraction (EBSD) work since it is a surface sensitive technique and analysis is conducted in the top 10-50 nm region of the specimen (Wright et al. 2011). Thus, scratches caused by mechanical polishing and any oxide layers need to be removed prior to EBSD analysis, otherwise poor quality EBSD patterns will be obtained. Standard petrographic thin sections were prepared by Adelaide Petrographic Laboratories with additional polishing/cleaning steps to ensure optimal sample preparation. Preparation steps included:

- Impregnate drill-core rock sample with araldite GY191 and Hardener HY951 and then remove cured araldite from surface using 1200 grit fixed media (wet and dry sand paper).
- Polish sample on ceramic lap with 6 μm diamond paste for 2 to 10 minutes as needed.
- Polish sample using textmet (Buehler textmet 1500 8" PSA) cloth lap with 3 μm diamond paste for 30 – 60 minutes; with 1 μm diamond paste for 40 – 60 minutes; and with 1 or ¼ Kemet WP diamond solution for 30 – 60 minutes.
- Final polish of sample using Struers MD Chem lap Kent polisher with Struers colloidal silica product (OP-S non Dry) for 2 hours.
- Ultrasonic cleaning was also used as required to avoid cross-contamination.

To minimize charging, samples were coated with a 1.5 to 2 nm-thick carbon film via thermal evaporation using a Quorum Q150TE vacuum evaporator. The carbon coat thickness needs to be adequate to prevent surface charging, but not too thick as otherwise only a weak electron diffraction pattern will be observed.

FIB-EBSD

Electron back-scatter diffraction (EBSD) data were collected using the EDAX-TSL™ EBSD system equipped with a Hikari camera on a FEI Helios NanoLab DualBeam™ FIB/SEM platform at Adelaide Microscopy, University of Adelaide.

Samples were mounted onto an analysis stub using Ag-Dag rather than carbon tape which can melt during the long analysis times, causing the sample to move whilst mounted. The mounted sample was then fitted on a 45º tilted sample holder, and was subsequently tilted another 30º, so that the total tilt for analysis was 70º. EBSD patterns were collected at 20 kV and 2.7 nA with a working distance ranging between 10 and 13 mm. The OIM Data Collection (version 5.2) software was used for data collection, and the OIM Analysis (version 4.5) software was used for data analysis and interpretation.

Crystallographic structure files for uraninite (UO_2) were available as part of the standard TSL structural database. Other settings used for EBSD data collection and processing are displayed in Table A1. For the current study, measurement of the UO_2 was of greatest importance, thus all settings and parameters (i.e. gain, exposure) were optimized to attain the best possible electron back-scatter pattern (EBSP) for UO_2 rather than any other phase present in the mapped area (i.e., bornite, fluorite).

Since both bornite and fluorite have similar structures to uraninite, and were found in association with the analyzed uraninite grains, another method other than structural differences alone was required for phase identification. Thus EDS chemical data were simultaneously collected and Chemical Indexing (ChI-scan) was conducted after the raw data had been collected, using the procedure outlined by Nowell and Wright (2004). This allowed for individual mineral phases to be identified based on structural and chemical differences.

Table A1: EBSD data collection and processing settings.

General Parameters	
Binned Pattern Size	96
Theta Step Size (degrees)	1
Rho Fraction	90%
Max Peak Count	7
Min Peak Count	3

Hough Parameters	
Hough Type	Classic
Resolution	Low
Convolution Mask	Medium (9x9)
Min Peak Magnitude	5
Min Peak Distance	25
Peak Symmetry	0.7

	S17.12
Grid Type	hexagonal
Working Distance (mm)	13
X Length (µm)	206.5
Y Length (µm)	194.6
Step Size (µm)	0.7
Total Points	95151
Number UO_2 Indexed Points	53875
Average UO_2 CI	0.91
UO_2 Average Fit (degrees)	1.68

Once raw data had been collected and imported into the OIM Analysis software, data cleanup was required to minimize the number of incorrectly or non-indexed points and remove noise. Two methods were of relevance for this study: 'Grain CI Standardization' and 'Grain Dilation' (both with grain tolerance angle of 5º and minimum grain size of 2 µm). Grain CI Standardization recovers a portion of the data with a low CI value but the correct orientation. Grain Dilation modifies the orientations of points which do not belong to any grains but have neighboring points which do belong to grains. This method is particularly important for mapping at grain boundaries, where the diffracting volume may be a combination of different crystal lattices and may initially be indexed incorrectly. Data cleanup is a vital part of the data

analysis process, but caution must be taken to avoid unnecessary data smoothing that may result in the loss of microstructural detail.

The EBSD data were processed in a number of ways, with Inverse Pole Figure (IPF), Image Quality (IQ) and Grain Reference Orientation Deviation (GROD) mapping being of relevance for the current study. For GROD mapping, each pixel within a grain is colored by the degree of their rotation relative to a reference orientation within the grain. The reference orientation is user-defined, and for the current analysis, the point in the grain with the lowest kernel average misorientation was chosen. Low-angle boundaries have been superimposed on the GROD map (Figure 4.2a). These have been defined as being <10º in garnet (Prior et al. 1999), and range between <4 and <10º in zircon (Timms et al. 2006, 2012; Reddy et al. 2007). Thus, low-angle boundaries were defined as <10º for uraninite.

The automated indexing as used by the EBSD system involves matching the measured and theoretical EBSP bands, and there are typically several possible orientations which may satisfy any given pattern. Two methods are typically used to assess the reliability of the automated indexing process, the Confidence Index (CI) or the 'fit' between the measured and theoretical bands. For the uraninite analyzed as part of this study, the average CI was 0.91 and the average band 'fit' for UO_2 was 1.68º. The 'fit' value (often reported as the Mean Angular Deviation) is generally used rather than CI when comparing the quality of EBSD data. Much of the published zircon EBSD data have a 'fit' value of < 1.7º (Timms et al. 2006; Reddy et al. 2007; Moser et al. 2011). Uraninite has not traditionally been analyzed using EBSD, so comparison of this 'fit' value to other published uraninite works was not possible. However, due to the closeness of the average 'fit' value obtained for uraninite measured as part of the current study and that for the published zircon data, the results here were deemed acceptable.

The definition of the legend/coloring used to delineate variation in IQ was critical as if inappropriately defined variability in IQ may not be observed. Thus it would be near impossible to link IQ variation to parameters like chemical variability, porosity or even grain orientation. Numerous iterations of using both color and grayscale to illustrate the variation in IQ were required to clearly display patterns and variability. Thus minor lattice distortion may not be reflected in IQ, and careful definition of the color palette is required to illustrate any possible patterns which reflect variation in microstructure.

APPENDIX B.2 – ADDITIONAL FIGURES

Two additional figures are included here, the first of which are pole figures that indicate that the studied zoned uraninite grain (Figures 4.1 to 4.3) is orientated in the $\langle 11\bar{2} \rangle$ direction (Figure A1). The second additional figures (Figure A2) is a supplemental example of another studied uraninite grain (S17.25), highlighting that the relationship between chemical zoning and GROD, as observed for the studied uraninite grain (S17.12), is not atypical.

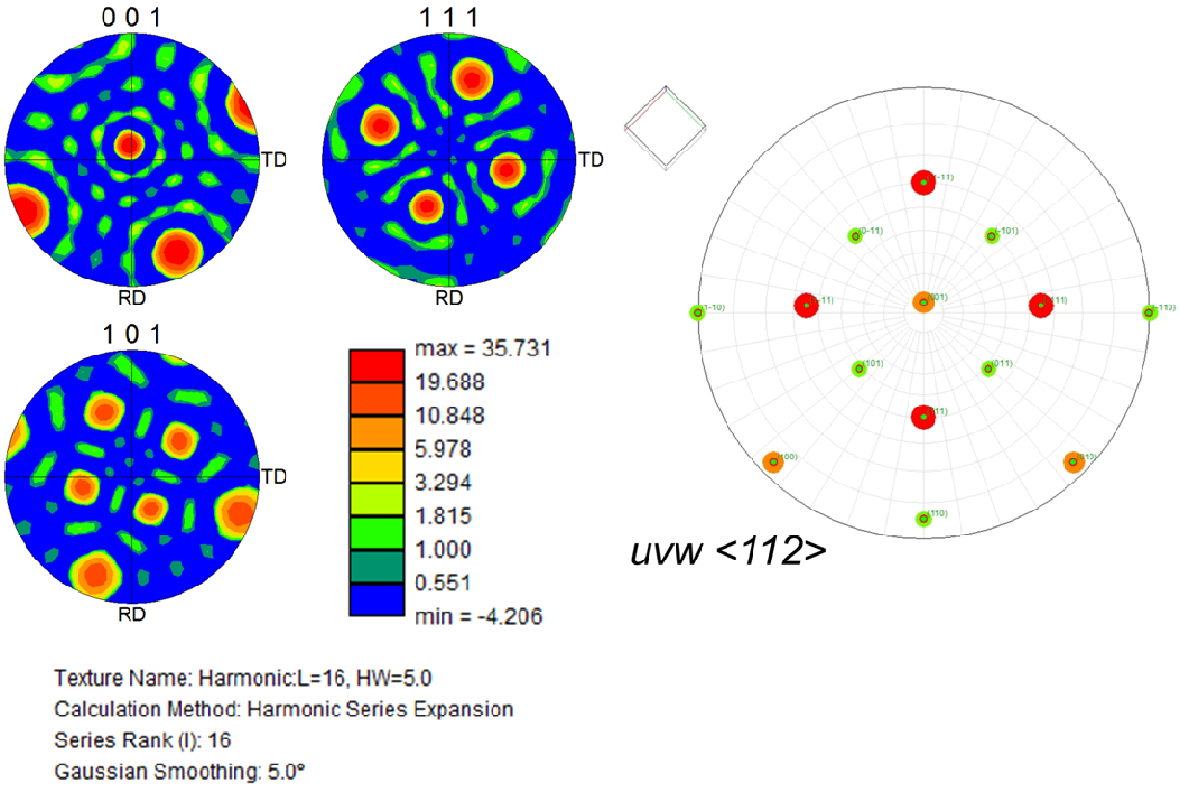

Figure A1: Stereographic projections (colored using a logarithmic scale) of crystallographic poles {001}, {110} and {111} of UO_2 for the EBSD data shown in Figure 4.1d (uraninite orientation is close to $\langle 11\bar{2} \rangle$).

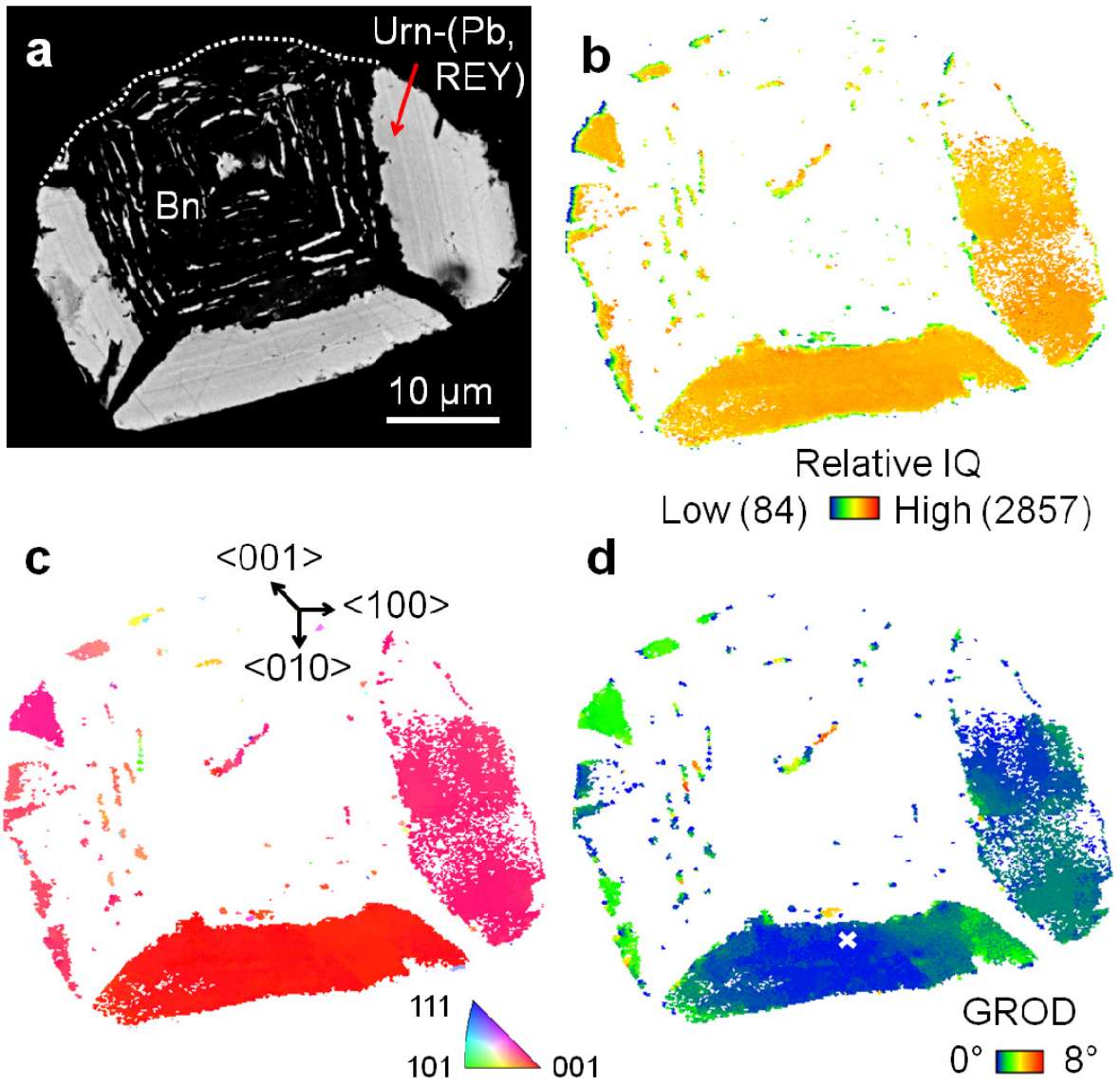

Figure A2: SEM- and EBSD-derived images of uraninite grain S17.25 **(a)** BSE image of uraninite with reduced brightness and contrast to highlight chemical zoning; **(b)** Image Quality (IQ) map – warmer colors (red-orange) represent areas of higher IQ (higher Pb concentration, low pore/inclusion content), and cooler colors (blue-green) represent areas of lower IQ (edge of grain, lower Pb concentration, higher pore/inclusion content); **(c)** ⟨001⟩ Inverse Pole Figure (IPF) map of UO_2. UO_2 is of one dominant orientation with some gradational color variation reflecting slight distortion of crystal lattice; **(d)** Grain Reference Orientation Deviation (GROD) map to show intragrain orientation variations. Each pixel is colored from reference orientation (blue, defined by white cross) with misorientation of up to 8°.

APPENDIX C

SUPPLEMENTARY DATA FOR CHAPTER 5:

REPLACEMENT OF URANINITE BY BORNITE VIA COUPLED DISSOLUTION-REPRECIPITATION: EVIDENCE FROM TEXTURE AND MICROSTRUCTURE

Edeltraud Macmillan[1,2], Cristiana L. Ciobanu[3], Kathy Ehrig[2], Nigel J. Cook[3] and Allan Pring[4]

[1]*School of Physical Sciences, The University of Adelaide, Adelaide, SA, 5000, Australia*

[2]*BHP Billiton Olympic Dam, Adelaide, SA, 5000, Australia*

[3]*School of Chemical Engineering, The University of Adelaide, Adelaide, SA, 5000, Australia*

[4]*School of Chemical and Physical Sciences, Flinders University, Bedford Park, SA, 5042, Australia*

Paper submitted to The Canadian Mineralogist

APPENDIX C – ANALYTICAL METHODS

SEM

Scanning electron microscopy (SEM) analysis was conducted using a Quanta 450 Field Emission Gun (FEG) SEM with silicon-drift detector (Adelaide Microscopy, University of Adelaide). Operating conditions were: 20 keV accelerating voltage, 60 Pa chamber pressure, 0° tilt, 10-11 mm working distance, a spot size of 4-5.

EPMA

All quantitative analysis of uraninite composition was obtained using a Cameca SX-Five electron probe micro-analyzer (EPMA) equipped with 5 tunable wavelength-dispersive spectrometers at Adelaide Microscopy, University of Adelaide. Operating conditions were 15 keV accelerating voltage, 100 nA beam current, 40° takeoff angle, with 0.5 to 1 μm-sized beam. Refer to Macmillan et al. (2016) for full details.

SAMPLE PREPARATION

Electron back-scatter diffraction (EBSD) analysis is a surface sensitive technique, with analysis being conducted within the top 10-50 nm region of a sample. It is therefore paramount that sample preparation is optimized to attain the best possible results. The presence of mechanical scratches and/or any dust or oxide layers on the surface will cause inelastic collisions of electrons and these will not be measured in the observed EBSD pattern, thus producing poor quality patterns. Any deformation that may be created during sample preparation may mask the true deformation and structural variability within a sample (Field et al., 2010). For this reason, sample polishing is a very important sample preparation step, as any mechanical scratches, dust, oxide layers *etc.* need to be removed from the surface the sample to ensure good quality EBSD patterns are produced.

Standard petrographic thin sections were prepared by Adelaide Petrographic. The first step involved impregnation of drill-core rock sample with araldite GY191 and Hardener HY951. Once cured, the surface araldite was removed by sanding using 1200 grit fixed media (wet and dry sand paper). Sample was then polished on a ceramic lap with 6 µm diamond paste for 2 to 10 minutes as needed. The next steps involved polishing the sample using textmet (Buehler textmet 1500 8" PSA) cloth lap with 3 µm diamond paste for 30 – 60 minutes; with 1 µm diamond paste for 40 – 60 minutes; and with 1 or ¼ Kemet WP diamond solution for 30 – 60 minutes. Then, additional polishing and cleaning steps were included to ensure optimal sample preparation for EBSD analysis. This included a final polish of the sample using Struers MD Chem lap Kent polisher with Struers colloidal silica product (OP-S Non-Dry) for 2 hours. Ultrasonic cleaning was also used as required to avoid cross contamination (especially important for the removal of colloidal silica).

Samples were then coated with a 1.5 to 2 nm thick carbon film via thermal evaporation using a Quorum Q150TE vacuum evaporator to minimize charging during the analysis. The carbon-coat thickness needs to be adequate to prevent surface charging, but needs to be thinner than standard SEM carbon-coating (5-20 nm) as otherwise only a weak electron diffraction pattern will be observed.

FIB-SEM AND FIB-EBSD

The FEI Helios NanoLab 600 DualBeam^{TM} FIB-SEM platform (Adelaide Microscopy, University of Adelaide) is equipped with energy dispersive X-ray spectroscopy (EDXS) detector, EBSD detector, and solid-state scanning transmission electron microscopy (STEM) detector. Due to the vast number of analytical detectors and dual electron and ion beams, the following can be attained: secondary electron and back-scatter electron imaging and mapping; the preparation of TEM foils and other 3D 'slice and view' microscopic analyses; phase and

grain orientation from EBSD; compositional point analysis and mapping from EDXS. Furthermore, the STEM detector can be used to image textures and aid in phase identification and mapping of elements of TEM foils at even higher nanometer resolution. The integrated use of these analytical instruments and their application to nano- to micron-scale characterization of ore minerals is discussed by Ciobanu et al. (2011).

The EBSD analysis (also referred to as Orientation Imaging Microscopy, OIM) was conducted on an EDAX-TSL^{TM} EBSD system which is equipped with a Hikari camera. Samples were mounted onto an analysis stub using Ag-Dag rather than carbon tape (since carbon tape can melt during the long analysis times, causing the sample to move whilst mounted). For EBSD analysis, the total sample tilt needs to be 70º. This was achieved by fitting the mounted sample on a 45º tilted sample holder, and then further tilting the specimen by 30º. EBSD patterns were collected at 20 kV and 2.7 nA with a working distance ranging between 10 and 13 mm. The OIM Data Collection (Version 5.2) was used for data collection, and the OIM Analysis (version 4.5) was used for data analysis and interpretation.

Successful EBSD analysis requires the availability of crystallographic structure files for all phases of interest. Structure files for both UO_2 and Cu_5FeS_4 can be found within the TSL database, and were used for EBSD indexing. Measurement of UO_2 was of most importance, so all settings and parameters (i.e., gain, exposure) were optimized to attain the best possible electron back-scatter pattern (EBSP) for UO_2 rather than other phases within the mapped areas (i.e., bornite, fluorite).

For cob-web crystals, the uraninite, bornite and fluorite are all found closely intergrown with one another and unfortunately these all have similar structures. Hence, structural variation alone is insufficient to distinguish between the phases. For this reason energy-dispersive spectroscopy (EDS) data were simultaneously collected. Chemical Indexing (ChI-scan) could

then be conducted where the measured element concentrations from EDS could be used as inputs for principal component analysis (PCA), and the components generated by this analysis assigned to individual mineral phases. This is a similar process to that outlined by Nowell and Wright (2004).

The raw data collected was then imported into the OIM Analysis software. EBSD data often requires cleanup when there are isolated points that are not indexed or have been indexed incorrectly due to the presence of dust particles on the sample surface, surface roughness, or from overlapping patterns at grain boundaries. The OIM Analysis program offers several cleanup routines, aimed at minimizing incorrect indexing. Two data cleanup methods were used: "Grain CI Standardization" and "Grain Dilation", both with grain tolerance angle of 5º and minimum grain size of 2 μm. The first of these methods is required to recover a portion of the data with a low Confidence Index (CI) value but the correct orientation, thus maximizing the fraction of points that are indexed correctly. The second method modifies the orientations of points which do not belong to any grains but have neighboring points which do belong to grains. This is particularly important for mapping grain boundaries, where the diffracting volume may be a combination of different crystal lattices and may initially be indexed incorrectly. Although cleanup procedures can rectify such issues, caution must be taken to avoid unnecessary data smoothing that may result in the loss of micro-structural detail.

There are a number of ways in which EBSD data can be processed, including: Confidence Index (CI), Image Quality (IQ), and Inverse Pole Figure (IPF) mapping. Additional details for these methods which are not covered within the manuscript can be found hereafter.

There are two main methods used to assess the reliability of the indexing process, the CI and the "fit" between the measured and theoretical bands. To attain EBSD data, automated indexing was used and involves matching the measured and theoretical EBSP bands. There

are usually several possible orientations which may satisfy any given pattern. CI is a measurement of the probability of an orientation solution based on using a voting scheme such that $CI = (V_1 - V_2)/V_{IDEAL}$, where V_1 and V_2 are the number of votes for the first and second solutions and V_{IDEAL} is the total possible number of votes from the detected EBSP bands (TexSEM, 2007). CI values range from 0 to 1, but can be misleading, and in many cases a low CI (~0.2) can be assigned to a pattern that is correctly indexed. The "fit" parameter defines the average angular deviation between the theoretical EBSP bands and the measured EBSP bands based on the orientation obtained from the voting procedure.

Indexing was completed based on the 'ideal' UO_2 and bornite structures (refer Analytical Methodology). To assess the quality of the obtained EBSD data, comparison of the "fit" value (often reported as the mean angular deviation) is generally used rather than CI. For the current study, "fit" values ranged between 1.3 and 2.0 for UO_2, and from 1.84 and 2.17 for bornite. Comparison of these fit" values to other published uraninite works is not possible since uraninite has not traditionally been analyzed using EBSD. However, much of the published EBSD analysis conducted on zircons requires MAD values of < 1.7º for the data to be considered of adequate quality (Timms et al., 2006; Reddy et al., 2007; Nemchin et al., 2009; Moser et al., 2011). The average "fit" values recorded for uraninite as part of this study are similar to those recorded for the published zircon work, hence the results achieved here were deemed acceptable.

Since optimization of the EBSP was conducted on the uraninite phase, comparison of bornite "fit" values to those in the literature was not conducted. Due to the extensive sample characterization already completed on these samples (Macmillan et al., 2016) and the simultaneous collection of EDS composition data for the main phases, phase assignment of UO_2 versus bornite was considered accurate. Other possible reasons for the poorer quality of

bornite indexing compared to UO_2 may be attributable to (Nowell and Wright, 2004): i) different polishing rates for UO_2 compared to bornite, thus causing surface relief differences; ii) large changes in the average atomic number of the phases may also lead to variation in the measured EBSP intensity. If these variations are large enough, it may be difficult to correctly identify the band positions within the patterns for all phases. Since measurement of the UO_2 was of greatest importance to this study, the settings and parameters were optimized to attain the best possible EBSP for UO_2 rather than bornite. Also, since uraninite has a higher atomic weight that bornite it is likely that stronger EBSP will be produced for uraninite.

HR-TEM

A Philips 200CM transmission electron microscope, equipped with a double-tilt holder and Gatan digital camera (Adelaide Microscopy, University of Adelaide), was used for electron diffraction and high-resolution imaging. Measurements on the diffractions were performed using DigitalMicrograph™ 3.11.1. Indexing of minerals was checked by diffraction simulations using WinHREM™ 3.0 software and data from the American Mineralogist Crystal Structure Database (http://rruff.geo.arizona.edu/AMS/amcsd.php). Winwulff© 1.4.0 (JCrystalSoft) was also used to interpret electron diffraction patterns. The instrument is also equipped with an energy dispersive X-ray (EDX) spectrometer allowing compositional information to be obtained on inclusions. Although qualitative rather than quantitative, the resolution of the EDS extends down to the scale of tens or hundreds of nanometers.

APPENDIX D

SUPPLEMENTARY DATA FOR CHAPTER 6:

CHEMICAL AND TEXTURAL INTERPRETATION OF LATE-STAGE COFFINITE AND BRANNERITE FROM THE OLYMPIC DAM IOCG-AG-U DEPOSIT

Edeltraud Macmillan[1,2], Nigel J. Cook[3], Kathy Ehrig[2] and Allan Pring[4]

[1]*School of Physical Sciences, The University of Adelaide, Adelaide, SA, 5000, Australia*

[2]*BHP Billiton Olympic Dam, Adelaide, SA, 5000, Australia*

[3]*School of Chemical Engineering, The University of Adelaide, Adelaide, SA, 5000, Australia*

[4]*School of Chemical and Physical Sciences, Flinders University, Bedford Park, SA, 5042, Australia*

Paper submitted to Mineralogical Magazine

APPENDIX D – ANALYTICAL METHODS

MLA

A Mineral Liberation Analyzer (MLA) was used to provide automated mineralogy results. Measurements were conducted by staff from ALS Mineralogy, Brisbane. The MLA system consists of an automated SEM and a special software program which allows for automated mineralogy measurement. Refer to Gu (2003) for details about the available measurement modes and setup of the MLA system. For the current study, measurement modes used were x-ray modal (XMOD) and sparse phase liberation mapping (SPL_Lite). Bulk modal mineralogy was measured via the XMOD method. Details of the mineral list used (Table A1) and bulk modal mineralogy measured via the XMOD method can be found in Macmillan et al. (2016). The SPL_Lite method was used to target only the U-bearing grains so that more detailed compositional and mineral association data pertaining to these grains could be attained. This method targets selected minerals (brannerite and coffinite in this case), and a measurement of the perimeter of each brannerite or coffinite grain is measured, as is the length of the boundary between any other mineral which is touching the mineral of interest. A relative proportion (in wt%) of each mineral found in contact with the brannerite or coffinite can thus be estimated, and this is recorded as the mineral association. For the current study, the mineral association value for each sample is the average value of all measured brannerite or coffinite grains in that sample. A summary of minerals associated with both brannerite and coffinite can be found in Table A2, as well as in Figures 6.7 and 6.8.

EPMA

All U-minerals that were to be compositionally analyzed were first identified using the SEM, on which back-scatter electron (BSE) images (Figures 6.1-6.6) of the region being studied and the key individual U-mineral grains were taken. Each image was given a unique ID (of the form Sxx.yy, where xx=sample number and yy=grain number). The locations of these regions were recorded on BSE image montages produced for each polished thin section from the MLA 650 Environmental SEM (Central Science Laboratory, University of Tasmania).

The Cameca SX-Five electron probe micro-analyzer (EPMA) at Adelaide Microscopy (University of Adelaide) was used to obtain quantitative compositional data. A total of 28 elements were measured. The standards used were originally published in the Appendix material of Macmillan et al. (2016), but are also listed below:

- Astimex Albite for Na Kα
- Astimex Almandine Garnet for Si Kα, Al Kα, Mg Kα, Fe Kα
- Astimex Apatite for P Kα, Astimex Barite for Ba Lα
- Astimex Celestite for Sr Lα
- Astimex Marcasite for S Kα
- Astimex Rhodonite for Mn Kα
- Astimex Rutile for Ti Kα
- Astimex Sanidine for K Kα
- Astimex Gallium Arsenide for As Lα
- Chalcopyrite (P and H Developments, UK) for Cu Kα
- Wollastonite (P & H Developments, UK) for Ca Kα
- Silver Telluride (P & H Developments, UK) for Te Lα
- Astimex Niobium for Nb Lα

- Synthetic Pb Glass – K227 (NIST) for Pb Mβ
- Rare Earth Glass Standard – REE1 (Drake and Weill 1972) for Y Lα
- Huttonite (David Steele) for Th Mα
- UO_2 (David Steele) for U Mβ
- single element synthetic REE glasses for Ce Lα, La Lα, Pr Lβ, Nd Lβ, Sm Lβ, Gd Lβ (Edinburgh Materials and Microanalysis Centre, University of Edinburgh)
- Zircon (C.M. Taylor Company) for Zr Lα

To identify all possible elements, minimize interferences, and to allow for accurate background point setting, high resolution wavelength spectrometer scans were completed. The HREE-oxides were <mdl (minimum detection limit; identified from full wavelength spectrometer scans). Details of crystal type, count times and off-peak interference corrections can be found in Table A3. Parameters are identical to those used for the uraninite study conducted by Macmillan et al. (2016).

Spectrometer usage was optimized by adjusting the acquisition order so that all spectrometers had approximately equal measurement times. Also, any elements that may be affected by beam damage were measured first namely: P Kα, Pb Mβ, Na Kα, Mn Kα, K Kα; and intensity data was corrected for Time Dependent Intensity (TDI) loss (or gain) using a self-calibrated correction for these elements. Both unknown and standard intensities were corrected for dead-time, with standard intensities also being corrected for standard drift over time.

To monitor the reproducibility of the EPMA data, a range of standards (UO_2, K227, REE1 and almandine garnet) were run as unknowns throughout each EPMA run. This showed that the probe was relatively stable, with the standard deviations (SD) for repeated analysis of these standards over a 4-month period being: 0.35 for U (n=44), 0.41 for Pb (n=41), 0.11 for Y (n=52), 0.10 for Si (n=46), and 0.18 for Fe (n=46).

Mean mdl values for each element in both brannerite and coffinite were calculated and can be found as a footnote in Tables 6.2, 6.3a and 6.3b. For brannerite, mean precision (wt%) based on 1 σ, was estimated as: U≈ 0.053, Pb≈ 0.015, Th≈ 0.015, Na≈ 0.012, Mg≈ 0.0036, Al≈ 0.0033, Si≈ 0.0068, P≈ 0.0035, S≈ 0.0039, K≈ 0.0034, Ca≈ 0.0057, Ti≈ 0.019, Mn≈ 0.014, Fe≈ 0.020, Cu≈ 0.018, As≈ 0.0090, Zr≈ 0.015, Nb≈ 0.017, Y≈ 0.017, Ce≈ 0.012, La≈ 0.0095, Pr≈ 0.032, Nd≈ 0.034, Sm≈ 0.031, Gd≈ 0.033, Sr≈ 0.0093, Ba≈ 0.011. For coffinite, mean precision (wt%) based on 1 σ, was estimated as: U≈ 0.062, Pb≈ 0.015, Th≈ 0.015, Na≈ 0.010, Mg≈ 0.0037, Al≈ 0.0038, Si≈ 0.012, P≈ 0.010, S≈ 0.0070, K≈ 0.0035, Ca≈ 0.0061, Ti≈ 0.0034, Mn≈ 0.016, Fe≈ 0.015, Cu≈ 0.017, As≈ 0.0092, Zr≈ 0.018, Nb≈ 0.024, Y≈ 0.035, Ce≈ 0.012, La≈ 0.010, Pr≈ 0.037, Nd≈ 0.041, Sm≈ 0.034, Gd≈ 0.038, Sr≈ 0.0089, Ba≈ 0.012.

Table A1: Details of mineral grouping used for MLA association data (SPL_Lite measurement technique).

Group Name	Mineral Name	Assumed Formula
Brannerite	Brannerite	$(U,Ca)(Ti,Fe)_2O_6$
Coffinite	Coffinite-Si_7	$(U,Y,Ca,Ce,Nd,Fe)[(Si,Al)O_4,PO_4,(OH)_4]$
	Coffinite-Si_9Y_7	$(U,Y,Ca,Ce,Nd,Fe)[(Si,Al)O_4,PO_4,(OH)_4]$
	Coffinite-Si_9Y_9	$(U,Y,Pb,Fe,Er,Dy,Nd,Ce,La,Ca,K)[SiO_4,PO_4,(OH)_4]$
	Coffinite-Si_{10}	$(U,Y,Ca,Ce,Nd,Fe)[(Si,Al)O_4,PO_4,(OH)_4]$
	Coffinite-$Si_{10}Y_1$	$(U,Y,Pb,Fe,Nd,La,Ce,Ca,K)[(Si,Al)O_4,PO_4,(OH)_4]$
	Coffinite-$Si_{10}Y_{10}$	$(U,Y,Ca,Ce,Nd,Fe)[(Si,Al)O_4,PO_4,(OH)_4]$
	Coffinite-$Si_{12}Y_6$	$(U,Y,Pb,Fe,Nd,La,Ce,Ca,K)[(Si,Al)O_4,PO_4,(OH)_4]$
	Thorite	$(Th,U,Fe,Y,P,Ca,Pb)SiO_4$
	Uranothorite	$(U,Th,Y,P,Fe,Ca,Nd)SiO_4$
Uraninite	Uraninite-Pb_5	$(U,Pb,Ce,Nd)O_2$
	Uraninite-Pb_{10}	$(U,Pb,Y,Ce,Nd,Fe,Cu)O_2$
	Uraninite-Pb_{15}	$(U,Pb,Ce,Nd,Sm,Gd,Y,Fe,Cu,Ca)O_2$
	Uraninite-Pb_{20}	$(U,Pb,Fe,Nd,Ce,La,K,Y)O_2$
	Uraninite_Si	$(U,Fe,Nd,Ce,La,Ca,K)(SiO_4,O_2)$
REY-minerals	Apatite	$Ca_5(PO_4)_3F$
	Bastnäsite	$(Ce,La,Nd,Pr,Ca)(CO_3)F$
	Crandallite_Grp	$(Ce,La,Nd,Ca,Sr)(Al,Fe)_3(SO_4,PO_4)_2(OH)_6$
	Florencite	$(Ce,La,Nd,Ca,Sr)(Al,Fe)_3(PO_4)_2(OH)_6$
	Monazite	$(Ce,La,Nd,Fe,Ca)PO_4$
	Synchysite	$Ca(Ce,Nd,La,Sm,Gd,Y,Fe)(CO_3)_2F$
	Xenotime	$(Y,Yb)PO_4$
	Xenotime-U	$(Y,U,Dy,Nd,Sm,Gd,Fe)[(PO_4),(SiO_4)]$
	Zircon	$ZrSiO_4$
	Zircon-U	$(Zr,Hf,U,Ca,Fe,Fe,Dy,Er,Yb,Y)[(Si,Al)O_4]$
Sulfides	Bismuthinite	Bi_2S_3
	Bornite	Cu_5FeS_4
	Carrolite	$CuCo_2S_4$
	Chalcocite	Cu_2S
	Chalcopyrite	$CuFeS_2$
	Cobaltite	$(Co,Fe)AsS$
	Covellite	CuS
	Domeykite	$(Cu,Fe)_3As$
	Löllingite	$(Fe,Co,Ni)As_2$
	Molybdenite	MoS_2
	Native_Copper	Cu
	Pyrite	FeS_2
	Pyrrhotite	$Fe_{1-x}S$ (x=0.0-0.2)
	Safflorite	$(Co,Fe)(As,S)_2$
	Sphalerite	$(Zn,Fe)S$
	Tellurobismuthite	Bi_2Te_3
	Tennantite	$(Ag,Cu,Zn,Fe)_{12}(As,Sb)_4S_{13}$
Pb-minerals	Altaite	$PbTe$
	Cerussite	$PbCO_3$
	Clausthalite	$PbSe$
	Galena	PbS
Hematite	FeO	Fe_2O_3
Barite	Barite	$BaSO_4$
	Barite_Sr	$(Ba,Sr)SO_4$
Fluorite	Fluorite	CaF_2
	Sellaite	MgF_2
Quartz	Quartz	SiO_2

Group Name	Mineral Name	Assumed Formula
Sericite/Chlorite	Sericite	$K(Fe,Mg,Al)_2(AlSi_3O_{10})(OH,F)_2$
	Chlorite_1	$(Mg,Fe,Al)3(Al,Si)_4O_{10}(OH)_2$
	Chlorite_2	$(Fe,Al)_5(Al,Si)_4O_{10}(OH)_2$
	Chlorite_3	$Mg_2(Al,Fe)_3Si_3AlO_{10}(OH)_8$
Feldspar	Albite	$NaAlSi_3O_8$
	Orthoclase	$KAlSi_3O_8$
Carbonate	Ankerite	$Ca(Fe,Mg,Mn)(CO_3)_2$
	Calcite	$(Ca,Mn)CO_3$
	Dolomite	$Ca(Mg,Fe,Mn)(CO_3)_2$
	Siderite	$(Fe,Mn)CO_3$
	Siderite_Mn	$(Fe,Mn,Ca)CO_3$
Ti-minerals	Ilmenite	$(Fe,Mn)TiO_3$
	Ilmenorutile	$(Ti,Nb,Fe,Mn)O_8$
	Rutile	TiO_2
Other	Al_Hydroxide	$Al_2(SO_4)_3{\cdot}17(H_2O)$
	Anhydrite	$CaSO_4$
	Corundum	$(Al,Fe)_2O_3$
	Kaolinite	$Al_2Si_2O_5(OH)_4$
	Scheelite	$CaWO_4$
	Schorl	$NaFe_3Al_6(BO_3)_3Si_6O_{18}(OH)_4$
	Topaz	$Al_2SiO_4(F,OH)_2$
	Unknown	Un

Table A2: Mineral association data for brannerite and coffinite measured by MLA using SPL_Lite method.

% mineral associated with brannerite

	Coffinite	Uraninite	REY minerals	Sulfides	Pb minerals	Hematite	Barite	Fluorite	Quartz	Sericite/ Chlorite	Feldspar	Carbonate	Ti minerals	Other
Group A	1.2	0.0	2.3	5.3	0.2	28.9	0.8	5.7	17.1	25.6	1.9	6.1	4.9	0.1
Group B	0.0	0.0	0.4	4.3	0.0	34.0	1.7	3.2	23.5	30.9	0.1	0.1	1.8	0.0
Group C	0.4	0.0	2.2	23.9	0.6	33.4	0.1	3.1	10.3	20.5	0.1	1.0	4.5	0.1
Group D	0.0	1.5	0.7	7.6	7.3	37.8	0.4	1.0	12.4	27.8	0.7	0.1	2.6	0.0

% mineral associated with coffinite

	Brannerite	Uraninite	REY minerals	Sulfides	Pb minerals	Hematite	Barite	Fluorite	Quartz	Sericite/ Chlorite	Feldspar	Carbonate	Ti minerals	Other
Group A	0.9	0.9	2.0	6.9	0.1	32.2	0.9	3.9	23.6	17.4	3.8	6.9	0.5	0.1
Group B	0.3	2.0	4.0	5.0	0.0	45.5	1.1	12.7	12.2	9.4	6.7	1.0	0.0	0.1
Group C	5.3	0.6	2.3	3.6	0.1	28.4	0.8	4.4	29.4	21.7	1.1	1.8	0.4	0.0

Note: Mineral association data for brannerite/coffinite, measured by the MLA system using the SPL_Lite method. The SPL_Lite method targets selected minerals (brannerite or coffinite in this case).

The perimeter of each brannerite/coffinite grain is measured, and the length of the boundary between any other mineral which is touching the brannerite/coffinite is also measured.

A relative proportion (in wt%) of each mineral found in contact with the brannerite/coffinite can thus be estimated, and this is recorded as the mineral association.

Table A3: Summary of EPMA set-up used for analysis of OD brannerite and coffinite.

Element X-ray Line	Spectrometer/ Crystal	Primary Standard	On-Peak Count t (s)	Off-Peak High Count t (s)	Off-Peak Low Count t (s)	Interference with…	Off-Peak Correction
U-Mβ	SP1 (LPET)	UO_2	50	25	12.5	K, Th	Multi-Point
Pb-Mβ	SP1 (LPET)	Pb glass - K227	60	30	30	U, Ce, S, Y	Multi-Point
Th-Mα	SP1 (LPET)	Huttonite	50	12.5	12.5	-	Multi-Point
Na-Kα	SP2 (TAP)	Albite	20	5	10	U	Multi-Point
Mg-Kα	SP2 (TAP)	Almandine garnet	30	15	7.5	-	Multi-Point
Al-Kα	SP2 (TAP)	Almandine garnet	30	15	15	Ti	Multi-Point
Si-Kα	SP2 (TAP)	Almandine garnet	30	15	7.5	Y	Multi-Point
P-Kα	SP5 (LPET)	Apatite	30	15	7.5	Ca, Cu	Multi-Point
S-Kα	SP5 (LPET)	Marcasite	20	10	5	Nd, La	Multi-Point
K-Kα	SP4 (LPET)	Sanidine	20	10	10	U	Multi-Point
Ca-Kα	SP4 (LPET)	Wollastonite	30	15	15	-	Multi-Point
Ti-Kα	SP4 (LPET)	Rutile	30	15	15	U	Multi-Point
Mn-Kα	SP3 (LLIF)	Rhodonite	10	5	5	As	Slope (Hi)
Fe-Kα	SP3 (LLIF)	Almandine garnet	20	10	10	-	Multi-Point
Cu-Kα	SP3 (LLIF)	Chalcopyrite	20	10	10	-	Multi-Point
As-Lα	SP2 (TAP)	Gallium arsenide	40	10	10	Sm, Nd	Multi-Point
Zr-Lα	SP5 (LPET)	Zircon	20	20	20	Nd	Slope (Lo)
Nb-Lα	SP5 (LPET)	Niobium	20	10	5	Mn	Linear
Y-Lα	SP5 (LPET)	REE1	50	25	25	-	Multi-Point
Ce-Lα	SP1 (LPET)	Ce glass	30	15	15	-	Linear
La-Lα	SP1 (LPET)	La glass	30	15	15	Nd	Slope (Lo)
Pr-Lβ	SP3 (LLIF)	Pr glass	30	15	7.5	U	Multi-Point
Nd-Lβ	SP3 (LLIF)	Nd glass	30	7.5	7.5	-	Multi-Point
Sm-Lβ	SP3 (LLIF)	Sm glass	30	15	15	-	Multi-Point
Gd-Lβ	SP3 (LLIF)	Gd glass	30	15	15	U	Multi-Point
Sr-Lα	SP2 (TAP)	Celestine	30	15	7.5	-	Linear
Ba-Lα	SP4 (LPET)	Barite	20	10	5	Ti, U, Pr	Multi-Point
Te-Lα	SP4 (LPET)	Silver telluride	20	10	10	Sm, U	Multi-Point

APPENDIX E

CONFERENCE ABSTRACT:

AN INTEGRATED ANALYTICAL APPROACH IN DECIPHERING COMPLEX URANIUM MINERAL TEXTURES

Edeltraud Macmillan[1,2] and Allan Pring[3]

[1]*School of Physical Sciences, The University of Adelaide, Adelaide, SA, 5000, Australia*

[2]*BHP Billiton Olympic Dam, Adelaide, SA, 5000, Australia*

[3]*School of Chemical and Physical Sciences, Flinders University, Bedford Park, SA, 5042, Australia*

Proceedings of the Joint International Conference on Nanoscience and Nanotechnology (ICONN) and Australian Conference on Microscopy and Microanalysis (ACMM) 2014, Adelaide, Australia

An integrated analytical approach in deciphering complex uranium mineral textures

E. Macmillan[1*] and A. Pring[2]
[1]School of Earth & Environmental Sciences, Geology and Geophysics, The University of Adelaide, Adelaide, SA 5000, Australia
[2]Department of Mineral Sciences, South Australian Museum, Adelaide, SA 5000, Australia
Email: edeltraud.macmillan@adelaide.edu.au

Abstract Summary: Understanding complex mineral textures is difficult, since the visible textures can usually be interpreted in a number of ways. Interpretation is often very subjective and a multi-facetted approach in understanding these textures is warranted.

Introduction: The complex uranium mineral textures found at Olympic Dam (OD) were studied. There are 3 dominant groups of uranium minerals at OD: the uranium oxides (uraninite or pitchblende), uranium silicates (coffinite and uranothorite), and the titaniferous uranium minerals (brannerite and uraniferous rutile) [1,2,3]. The average grain size of these minerals is ~20 um, but this ranges from <0.5 um to >1mm [1]. Both the uranium minerals and sulfides are often found in sericite and/or hematite altered zones. Furthermore, uraninite is thought to be more strongly associated with hematite than with non-hematite gangue or sulfides; whilst the brannerite and coffinite are more commonly associated with non-hematite gangue. The genesis of the U mineralisation at OD is still not well understood [2,4], hence the aim of this work is to characterise the complex uranium mineral intergrowths using a range of analytical techniques.

Analytical Methods: An integrated approach using many different analytical techniques has been adopted in deciphering these complex mineral textures. These include: optical microscopy and SEM for textural identification; MLA, EPMA and LA-ICPMS for quantification; and XAS and XFM for mechanism identification. Each of these techniques requires rigorous method development to ensure accurate data is attained. All data from these techniques need to be collated and interpreted in a systematic manner so that a thorough understanding of the mineral textures is established, as shown in Fig 1. Furthermore, this ensures that results attained from different methods validate one another, and any intrinsic shortcomings from one method are resolved by another.

Discussion: SEM BSE images can be used to qualitatively gain an understanding of the mineral textures, as shown in Fig 1 (a). To quantify some of the mineralogy (association, bulk modal mineralogy and grain size), the MLA system was then used [5]. Two measurement methods were used: 1) X-Ray Modal (XMOD), and 2) Sparse Phase Liberation (SPL) analysis. Hence the observations made on the SEM were validated using the MLA system, see Fig 1 (b) and it was ensured that all types of U phases had been identified in each sample. A provisional textural classification system was formulated from these results, and the next phase of work was to quantify the compositional similarities and differences between textural classes.

Accurate compositional data were then acquired by the integrated use of EPMA and LA-ICPMS. One of the key aspects for accurate EPMA, is in identifying spectral interferences particularly when rare-earth-elements (REE) are present [6]. Due to the small grain size of the U minerals, caution must be exercised when using any electron based technique to ensure the excitation volume and secondary fluorescence is representative of the phase of interest [6].

The final phase of work is mechanism identification. This encompasses the results from all previous phases, but also looks more closely at the molecular level interactions in these U minerals using synchrotron technology (Fig 1 (c),(d)). The use of both SXRF and XAS have become standard tools to measure element concentration, distribution at

micrometer- to nanometer-scale, and speciation in various geomaterials [7]. Both XANES and EXAFS data have been collected for selected U minerals contained in the various textural classes. The XANES data provides insight into valency of U, whilst the EXAFS data allows for interpretation of the local structure of elements (bond length, ligand type).

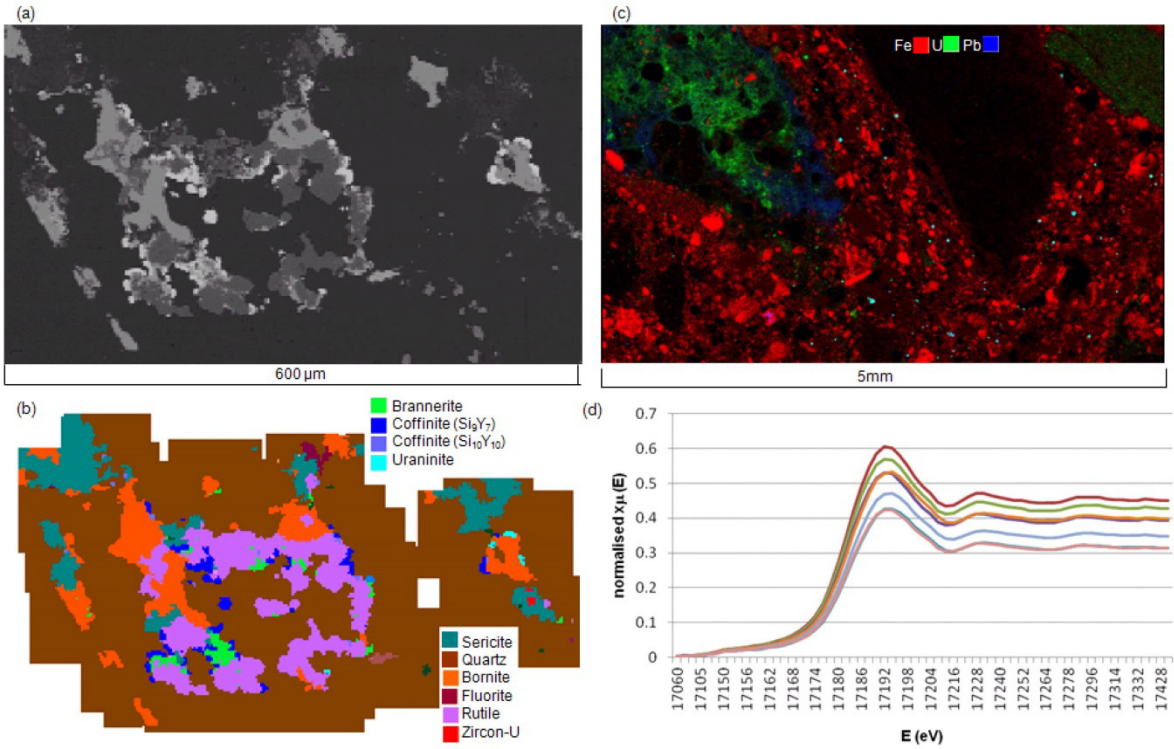

Fig. 1. (a) BSE image from an SEM; (b) false colour MLA image of area in (a) displaying various identified minerals; (c) XFM false colour map displaying concentration differences in Fe-U-Pb; (d) example of XANES spectra used to identify the valency of U.

Acknowledgements

This work forms part of the Ph.D. studies of E. Macmillan and has been gratefully supported by BHP Billiton. Kathy Ehrig (BHP Billiton) has offered much support and feedback on the work conducted. Staff at numerous research facilities have also provided training and support in the use of equipment. Joel Brugger and Barbara Etschmann are also acknowledged for their help with synchrotron experiments and data reduction.

References

[1] K. Ehrig, J. McPhie and V. Kamenetsky, “Geology and mineralogical zonation of the Olympic Dam iron oxide Cu-U-Au-Ag deposit, South Australia”, Geology and Genesis of Major Copper Deposits and Districts of the World, Society of Economic Geologists, Special vol. 16, pp. 237-267, 2012.

[2] M. Hitzman, N. Oreskes, and M. Einaudi, “Geological characteristics and tectonic setting of Proterozoic iron oxide (Cu-U-Au-REE) deposits”, Precambrain Research, vol. 58, pp. 241-287, 1992.

[3] M. Hitzman and R. Valenta, “Uranium in Iron-Oxide-Copper-Gold (IOCG) systems”, Economic Geology, vol. 100, pp. 1657-1661, 2005.

[4] M. Cuney, “The extreme diversity of uranium deposits”, Mineralium Deposita, vol. 44, pp. 3-9, 2009.

[5] Y. Gu, “Automated scanning electron microscope based mineral liberation analysis”, Journal of Minerals & Materials Characterisation Engineering, vol. 2, no. 1, pp. 33-41, 2003.

[6] K. Goemann, “Challenges in electron probe microanalysis 60 years after Casting: examples from complex uranium and rare earth element minerals from Northern Australian ore deposits”, Microscopy & Microanalysis, vol. 17 (suppl. 2), pp. 578-579, 2011.

[7] B. Etschmann, C. Ryan, J. Brugger, R. Kirkham, R. Hough, G. Moorhead, D. Siddons, G. De Geronimo, A. Kuczewski, P. Dunn, D. Paterson, M. de Jonge, D. Howard, P. Davey and M. Jensen “Reduced As components in highly oxidised environments: evidence from full spectral XANES imaging using the Maia massively parallel detector”, American Mineralogist, vol. 95, pp. 884-887, 2010.

APPENDIX F

CONFERENCE ABSTRACT:

EVOLUTION OF URANINITES AT OLYMPIC DAM: DECIPHERING COMPLEX TEXTURES, CHEMISTRY AND TEMPORAL HISTORY

Edeltraud Macmillan[1,2], Nigel J. Cook[3], Allan Pring[4], Kathy Ehrig[2] and John Foden[1]

[1]*School of Physical Sciences, The University of Adelaide, Adelaide, SA, 5000, Australia*

[2]*BHP Billiton Olympic Dam, Adelaide, SA, 5000, Australia*

[3]*School of Chemical Engineering, The University of Adelaide, Adelaide, SA, 5000, Australia*

[4]*School of Chemical and Physical Sciences, Flinders University, Bedford Park, SA, 5042, Australia*

Poster presented at the 11th South Australian Exploration and Mining Conference, Adelaide, Australia

Evolution of uraninites at Olympic Dam: Deciphering complex textures, chemistry and temporal history

Edeltraud Macmillan[1,3], Nigel Cook[1], Allan Pring[2], Kathy Ehrig[3] and John Foden[1]

[1]School of Earth & Environmental Sciences, The University of Adelaide, Adelaide, SA, 5000, Australia

[2]Department of Mineral Sciences, South Australian Museum, Adelaide, SA, 5000, Australia

[3]Resource Planning & Development, BHP Billiton – Olympic Dam, Adelaide, SA, 5000, Australia

Uraninites at Olympic Dam (OD) display a complex history, both chemically and texturally. The Olympic Dam iron-oxide-copper-gold (IOCG)-uranium-silver deposit is located 520 km NNW of Adelaide in South Australia, within the Gawler Craton. OD is the largest economic uranium resource in the world, but the genesis of uranium mineralization remains poorly constrained. The uranium minerals have a complex paragenesis with strong evidence for multiple stages of U dissolution and reprecipitation. This study aims to address a major gap in knowledge with respect to textural and compositional evolution of uraninite. A textural classification system is developed based on detailed mineralogical and micro-analytical investigation of selected samples, and a potential pathway for the oxidation of uraninite is postulated.

Unambiguous interpretation of complex mineral textures can be difficult, since observed relationships may commonly be understood in a number of ways. Interpretation is often very subjective and a multi-facetted approach is needed. For this reason an integrated analytical approach is required so that any shortcomings from one method are resolved by others.

The integrated analytical approach used for the current study, includes optical and scanning electron microscopy (SEM), mineral liberation analysis (MLA), electron probe micro-analysis (EPMA), and synchrotron-based X-ray fluorescence microscopy (XFM) and X-ray absorption spectroscopy (XAS).

A total of 24 samples from diamond drill-core were selected to target key mineralogical and chemical variability. All data obtained has been statistically analyzed to determine relationships between chemistry, texture and relative ages. Complex uraninite textures exist, as displayed by the example in Figure 1. The relationship between the uraninite and bornite in Figure 1, and the mechanism of formation of the uraninite morphology is explored.

There are four main classes of uraninites – primary, zoned, cob-web and massive. These are further subdivided based on chemistry and texture. Complementary Pb/U data is used as a proxy for chemical age on the same grains and indicate the uraninites are multi-generational.

Textures in uraninite from OD are comparable to the mineral textures found in the natural fission reactors of Oklo, Gabon, and to oxidized UO_2 in spent nuclear fuel, hence providing new insight to the genesis of uranium mineralisation at OD.

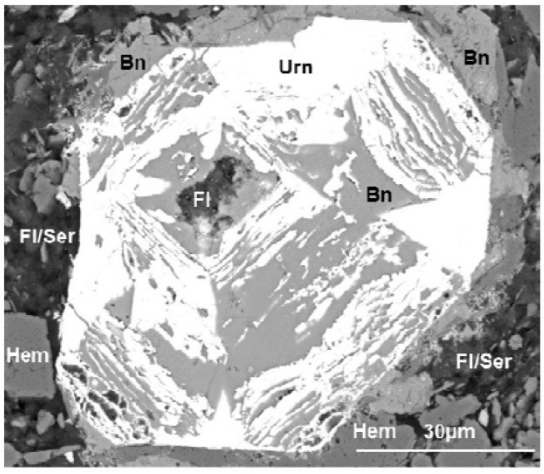

Fig.1: Back-Scatter Electron image of cob-web uraninite (Urn) with accessory bornite (Bn), fluorite (Fl), sericite (Ser) and hematite (Hem).

APPENDIX G

CONFERENCE ABSTRACT:

EVOLUTION OF URANIUM MINERALS AT OLYMPIC DAM, SOUTH AUSTRALIA

Edeltraud Macmillan[1,2], Nigel J. Cook[3], Cristiana L. Ciobanu[3], Kathy Ehrig[2], Vadim S. Kamenetsky[4], Jay Thompson[4] and Allan Pring[5]

[1]*School of Physical Sciences, The University of Adelaide, Adelaide, SA, 5000, Australia*

[2]*BHP Billiton Olympic Dam, Adelaide, SA, 5000, Australia*

[3]*School of Chemical Engineering, The University of Adelaide, Adelaide, SA, 5000, Australia*

[4]*School of Physical Sciences, University of Tasmania, Hobart, TAS, 7001, Australia*

[5]*School of Chemical and Physical Sciences, Flinders University, Bedford Park, SA, 5042, Australia*

Poster presented at the Conference of the Society of Economic Geologists (SEG2015): World-Class Ore Deposits: Discovery to Recovery, 2015, Hobart, Australia

Evolution of uranium minerals at Olympic Dam, South Australia

Edeltraud Macmillan,[1,2*] Nigel J. Cook,[3] Cristiana L. Ciobanu,[3] Kathy Ehrig,[2] Vadim S. Kamenetsky,[4] Jay Thompson[4] and Allan Pring[5]

[1]School of Physical Sciences, The University of Adelaide, Adelaide, SA, 5000, Australia
[2]BHP Billiton Olympic Dam, Adelaide, SA, 5000, Australia
[3]School of Chemical Engineering, The University of Adelaide, Adelaide, SA, 5000, Australia
[4]School of Physical Sciences, University of Tasmania, Hobart, TAS, 7001, Australia
[5]School of Chemical and Physical Sciences, Flinders University, Bedford Park, SA, 5042, Australia

The Olympic Dam (OD) iron-oxide-copper-gold (IOCG)-U-Ag deposit, South Australia, is the World's largest economic uranium resource, but the genesis of U-mineralization in the deposit remains poorly constrained. The three main U-minerals at OD are uraninite, coffinite and brannerite. Prior mineralogical-geochemical studies of U-minerals focused on limited sampling of higher-grade, massive or vein uraninite specimens. The current microbeam analytical study addresses a broader range of samples at the micron- to nanoscales.

Classification of uraninite here is based on detailed mineralogical and microanalytical investigation. The first category ('primary') occur as single, smaller grains (10-50 μm), with the simplest cubic euhedral morphology, are oscillatory-zoned and have the highest Pb-content. Electron diffraction (ED) and TEM-EDS carried out on a FIB-prepared TEM-foil cut through one of the smallest grains show uraninite is defect-free. The high Pb, REE+Y (REY) contents measured are locked within the oscillatory zonation pattern, inferring these elements are lattice-bound. A second category ('zoned') is defined by coarser, sub-euhedral grains, with internal zonation patterns defined by variation in Pb and REY, showing morphological changes (e.g., square-domains within a prismatic outline) from core to margin. EBSD mapping confirms zonation in a single grain with no differences in orientation from core to margin. This infers that the zonation is intrinsic to either a single growth process, or involves grain-scale element redistribution via mechanisms such as chemical-gradient diffusion or coupled-dissolution re-precipitation reaction (CDRR). A third category ('cob-web') includes a variety of grains that are still coarser (up to several hundred μm), have variable hexagonal to octagonal morphologies, varying degrees of rounding, and feature rhythmic intergrowths with sulfides+fluorite from core to margin. Greater complexity includes different orientation domains within single grains (EBSD and ED), as well as heterogeneity in terms of fields of inclusions (sulfides, fluorite, REE-minerals) with sizes down to nanoscale. Compositions for this category vary with respect to Pb-content (< than the primary) and other minor elements (Ca, ΣREY). ED and TEM-imaging on FIB-prepared foils on grains from this category confirm they are uraninite, and place constraints on REY-measurements, i.e., fields of nanoscale REY-mineral inclusions account, partially, for the REY-contents (EPMA data); EBSD mapping and ED show epitaxial relationships between uraninite and Cu-(Fe)-sulfides, backing-up CDRR-replacement. The fourth ('massive') category comprises uraninite occurring as μm-sized grains to massive varieties forming coarser aggregates/vein-filling. This category has the lowest Pb and variable REY contents albeit lower than previous categories.

Coffinite and brannerite, displaying intergrowths with uraninite, sulfides and gangue increase in abundance in samples containing 'massive' uraninite. Based on the above, there are at least two uraninite generations: early ('primary' through 'cob-web') and late ('massive'). EPMA Pb/U data are used as a proxy for chemical age and confirm that uraninite is multi-stage. Coffinite and brannerite are tied to the late generation. However, the complexity of mineral growth, replacement and recrystallization, as well as the formation of discrete REY-minerals, observed throughout the 'cob-web' uraninite indicates multiple cycles of U-remobilization and reprecipitation, which contributed to the observed distributions of U-minerals at OD.

APPENDIX H

CONFERENCE ABSTRACT:

THE EVOLUTION OF URANINITE, COFFINITE AND BRANNERITE AT THE OLYMPIC DAM IOCG-U-AG DEPOSIT – LINKING TEXTURAL OBSERVATIONS TO COMPOSITIONAL VARIABILITY

Edeltraud Macmillan[1,2], Nigel J. Cook[3], Kathy Ehrig[2], Cristiana L. Ciobanu[3] and Allan Pring[4]

[1]*School of Physical Sciences, The University of Adelaide, Adelaide, SA, 5000, Australia*

[2]*BHP Billiton Olympic Dam, Adelaide, SA, 5000, Australia*

[3]*School of Chemical Engineering, The University of Adelaide, Adelaide, SA, 5000, Australia*

[4]*School of Chemical and Physical Sciences, Flinders University, Bedford Park, SA, 5042, Australia*

Presentation to be given at The Australian Earth Sciences Convention 2016 (AESC16), Adelaide, Australia

The evolution of uraninite, coffinite and brannerite at the Olympic Dam IOCG-U-Ag deposit – linking textural observations to compositional variability

Macmillan, Edeltraud[1,2], Cook, Nigel J.[3], Ehrig, Kathy[2], Ciobanu, Cristiana L.[3] and Pring, Allan[4]

[1]*School of Physical Sciences, The University of Adelaide, Adelaide, SA, 5000, Australia*
[2]*BHP Billiton Olympic Dam, Adelaide, SA, 5000, Australia*
[3]*School of Chemical Engineering, The University of Adelaide, Adelaide, SA, 5000, Australia*
[4]*School of Chemical and Physical Sciences, Flinders University, Bedford Park, SA, 5042, Australia*

Uraninite, coffinite and brannerite are the dominant U-minerals in the Olympic Dam (OD) iron-oxide-copper-gold-(IOCG)-U-Ag deposit, South Australia. Two generations of uraninite have been identified and termed 'early' and 'late' [1]. 'Early' uraninites are typically small (10-100 μm) single uraninite grains containing higher concentrations of Pb and Σ(REE+Y) (REY). The 'late' generation of uraninite exists as μm-sized grains to aphanitic varieties which form larger (up to mm-sized) aggregates and vein-fillings, and typically have lower Pb, but higher Ca ± Si contents compared to the 'early' generation.

'Early' uraninites represent single uraninite crystals which have been progressively chemically and texturally altered. 'Primary' uraninites have the simplest cubic euhedral morphology and often exhibit oscillatory and sectorial zonation of lattice-bound Pb and REY. The next class are the 'zoned' uraninites which are typically coarser, sub-euhedral grains and are often prismatic, containing an internal zonation pattern defined by distinct zones of high- and low- Pb and REY. The final and most altered class are the 'cob-web' uraninites which display the greatest heterogeneity in terms of variable hexagonal to octagonal morphologies, varying degrees of rounding, and rhythmic intergrowths of uraninite with Cu-(Fe)-sulphides ± fluorite from core to margin.

Brannerite is classified into four texturally distinct types. Type 1 brannerite includes discrete bands of needle-like to bladed brannerite commonly intergrown with sericite, chlorite, fluorite and quartz. It also occurs within hematite and rutile and ranges in composition from what is effectively a uraniferous rutile to stoichiometric brannerite. Type 2 brannerite typically appears as irregularly-shaped blebs within bornite and chalcocite, whereas type 3 brannerite is intimately associated with barite and REY-minerals (i.e., zircon, monazite). Type 4 brannerite also occurs as irregular blebs, but is commonly contained within hematite laths. Patches of bornite and TiO_2 (possibly anatase) are found within this type of brannerite; galena inclusions are abundant. Compositionally, brannerite of types 1-3 are similar and all contain elevated Fe, As, Na and K compared to type 4 brannerite. Type 4 brannerite is distinguished by elevated Pb, REY, Si and Nb.

Coffinite is always found on the margins of quartz, and displays a range of compositions, which can be differentiated by Y and Si content. It can be found in association with massive uraninite where it appears as colloform growths surrounding quartz, enveloped by massive uraninite. In some cases, colloform coffinite growths completely encompass quartz grains, whilst in others they appear as more discrete globules nucleating on Cu-(Fe)-sulphide grains. Several 'early' uraninites also display incipient coffinitisation at their rims. When coffinite is found with brannerite, it is either very finely intergrown with brannerite, or occurs on the edges of brannerite masses.

Based on textural observations, supported by chemical composition, it is clear that there were at least two main uraninite mineralising events. Coffinite and brannerite may represent secondary U-minerals which formed via repeated dissolution and reprecipitation of uraninite originally precipitated at the time of ore formation, or may represent the products of a later U-mineralising event.

[1] Macmillan et al. American Mineralogist (in press), http://dx.doi.org/10.2138/am-2015-5411.

APPENDIX I

CONFERENCE ABSTRACT:

MINERALOGICAL AND MICROANALYTICAL CHARACTERIZATION OF URANIUM MINERALIZATION

Nigel J. Cook[1], Cristiana L. Ciobanu[1], Kathy Ehrig[2], **Edeltraud Macmillan**[2], and Angus Netting[3]

[1]*School of Chemical Engineering, The University of Adelaide, Adelaide, SA, 5000, Australia*

[2]*BHP Billiton Olympic Dam, Adelaide, SA, 5000, Australia*

[3]*Adelaide Microscopy, University of Adelaide, Adelaide S.A. 5005, Australia*

Presentation given at the Australian Institute of Mining and Metallurgy (AusIMM) Uranium Conference, Adelaide, June 2015

Mineralogical and Microanalytical Characterisation of Uranium Mineralisation

N J Cook[1], C L Ciobanu[1], K Ehrig[2], E Macmillan[3] and A Netting[4]

ABSTRACT

A sound mineralogical understanding of an orebody or prospect is critical for planning and optimisation of ore processing and waste management, can contribute to improved genetic models and can potentially be used in vector approaches to exploration targeting. This can apply to any ore system but is particularly applicable to uranium-bearing mineralisation. The high mobility of uranium, the often fine-grained nature of U-minerals and the high tendency for absorption onto clays and other minerals can often make for complex ore textures and paragenetic relationships.

Drawing on examples from different types of ore system (roll front uranium, iron oxide-copper-gold-(uranium), granite-hosted uranium), this presentation will show how we address these issues using a state-of-the-art range of microanalytical infrastructure at University of Adelaide.

The mineralogical deportment of elements of interest (U, other key components such as Th, and also potential unwanted elements), can be evaluated using a combination of scanning electron microscope (SEM), mineral liberation analyser (MLA) and quantitative techniques, including electron probe microanalysis and laser ablation inductively coupled plasma mass spectrometry (LA-ICP-MS). The latter offers micron-scale resolution combined with sub-ppm-level sensitivity. Grain-scale chemical mapping permits a visualisation of variation in the concentrations of major, minor and trace elements in the context of prevailing textures.

In many uranium ores, textural and compositional heterogeneity are present at a scale smaller than that of the microprobe beam or laser spot.

1. School of Chemical Engineering, University of Adelaide, Adelaide SA 5005.
2. MAusIMM, Principal Geometallurgist, BHP Billiton Olympic Dam, Level 2, 55 Grenfell Street, Adelaide SA 5001. Email: kathy.ehrig@bhpbilliton.com
3. MAusIMM, Senior Geometallurgist, BHP Billiton Olympic Dam, Level 2, 55 Grenfell Street, Adelaide SA 5001. Email: edeltraud.macmillan@bhpbilliton.com
4. Adelaide Microscopy, University of Adelaide, Adelaide SA 5005.

Advances in submicron-scale characterisation and, critically, the ability to microsample *in-situ* are offered by dual-beam focused ion beam (FIB)-SEM platforms. The FIB-SEM allows for cross-section imaging, 3D 'slice and view' microscopy and information on grain orientation via electron backscatter diffraction. The scanning transmission electron microscopy (STEM) detector on the FIB platform allows for imaging of textures, phase identification by energy-dispersive X-ray spectroscopy (EDXS) and element mapping at a resolution well below that of LA-ICP-MS. Importantly, FIB-SEM can be used to prepare and thin foils for nanoscale imaging and electron diffraction using transmission electron microscopy (TEM). In 2015, these nanoscale capabilities will be significantly expanded by the addition of a new FEI Titan Themis aberration-corrected TEM offering atomic-scale resolution, and the facility to obtain compositional data and chemical maps of 10 × 10 nm areas.

When used in combination, this portfolio of quantitative and qualitative techniques bridge nanometre to millimetre scales of observation. They also have application to assessment and interpretation of other mineralogically-complex deposits, including rare earth elements deposits.

APPENDIX J

CONFERENCE ABSTRACT:

URANIUM MINERALOGY VERSUS THE RECOVERY OF URANIUM AT OLYMPIC DAM

Kathy Ehrig[1], Vanessa Liebezeit[1], **Edeltraud Macmillan**[1], Chantelle Lower[1], Vadim S. Kamenetsky[2], Nigel J. Cook[3] and Cristiana L. Ciobanu[3]

[1]*BHP Billiton Olympic Dam, Adelaide, SA, 5000, Australia*

[2]*School of Physical Sciences, University of Tasmania, Hobart, TAS, 7001, Australia*

[3]*School of Chemical Engineering, The University of Adelaide, Adelaide, SA, 5000, Australia*

Presentation given at the Australian Institute of Mining and Metallurgy (AusIMM) Uranium Conference, Adelaide, June 2015

Uranium Mineralogy versus the Recovery of Uranium at Olympic Dam

K Ehrig[1], V Liebezeit[2], E Macmillan[3], C Lower[4], V S Kamenetsky[5], N J Cook[6] and C L Ciobanu[7]

ABSTRACT

The Olympic Dam iron-oxide Cu-U-Au-Ag deposit, located ~520 km NNW of Adelaide, is the world's largest reported uranium resource. Uranium is recovered from the ore via mildly aggressive oxidative, sulfuric acid leaching of Cu-sulfide depleted flotation tailings. Uranium is then extracted from the leach liquors via solvent extraction, ammonium diuranate precipitation and calcination to produce uranium ore concentrate (UOC). The mineralogical deportment of uranium is the fundamental driver of uranium recovery at Olympic Dam.

Uraninite, coffinite and brannerite are the three U-minerals (ie U is a major element). Chemical compositions of the U-minerals vary at the grain scale up to deposit scale. The average U-mineral grain size is ~20 microns. The U-minerals occur as isolated disseminated grains, massive aggregates and as microveinlets. They are associated with all major ore and gangue minerals, eg hematite, quartz, sericite, orthoclase, chlorite, fluorite, siderite, barite, chalcocite, bornite, chalcopyrite and pyrite. Absolute abundances and relative proportions of U-minerals also vary across the deposit. In general, uraninite is the dominant U-mineral when the whole rock concentration is >~500–600 ppm U; coffinite and brannerite are more abundant at U grades <~500 ppm.

1. MAusIMM, Principal Geometallurgist, BHP Billiton Olympic Dam, Level 2, 55 Grenfell Street, Adelaide SA 5001. Email: kathy.ehrig@bhpbilliton.com
2. Senior Process Engineer, BHP Billiton Olympic Dam, Level 2, 55 Grenfell Street, Adelaide SA 5001. Email: vanessa.liebezeit@bhpbilliton.com
3. MAusIMM, Senior Geometallurgist, BHP Billiton Olympic Dam, Level 2, 55 Grenfell Street, Adelaide SA 5001. Email: edeltraud.macmillan@bhpbilliton.com
4. Project Geometallurgist, BHP Billiton Olympic Dam, Level 2, 55 Grenfell Street, Adelaide SA 5001. Email: chantelle.lower@bhpbilliton.com
5. Professor, School of Physical Sciences, University of Tasmania, Hobart Tas 7005. Email: dima.kamenetsky@utas.edu.au
6. School of Chemical Engineering, University of Adelaide, Adelaide SA 5005. Email: nigel.cook@adelaide.edu.au
7. School of Chemical Engineering, University of Adelaide, Adelaide SA 5005. Email: cristina.ciobanu@adelaide.edu.au

Highly variable minor (0.1–1 wt per cent) or trace (<0.1 wt per cent) concentration levels of U are also present in hematite, florencite, apatite, zircon, xenotime, monazite, pyrite, chalcopyrite, bornite and chalcocite. Given that hematite is a dominant mineral in the ore, it is the fourth most abundant U-bearing mineral. Uranium occurs as lattice-bound U and as submicroscopic inclusions of uraninite in hematite. U contributions from the other minerals (excluding hematite) are relatively insignificant.

Uraninite, coffinite, brannerite and U-bearing hematite are all soluble during oxidative, sulfuric acid leaching, albeit at vastly different rates. However, targeted U-recovery is dependent on the selected leaching intensity (pH, Eh, temperature, residence time), which is a time-variable economic trade-off between the absolute and relative abundances of the U-bearing minerals in plant feed, uranium price, reagent costs and potential downstream effects.

APPENDIX K

URANIUM SCAVENGING DURING MINERAL REPLACEMENT REACTIONS

Kan Li[1], Allan Pring[2,4], Barbara Etschmann[1,2,7], **Edeltraud Macmillan**[3], Yung Ngothai[1], Brian O'Neil[1], Anthony Hooker[1,5], Fred Mosselmans[6] and Joël Brugger[2,7]

[1]*School of Chemical Engineering, The University of Adelaide, Adelaide, SA, 5000, Australia*

[2]*Division of Mineralogy, South Australian Museum, North Terrace, 5000, Adelaide, South Australia, Australia*

[3]*School of Earth and Environmental Sciences, The University of Adelaide, 5000, South Australia, Australia*

[4]*School of Chemical and Physical Sciences, Flinders University, 5001, South Australia, Australia*

[5]*Radiation Health, Radiation Protection Branch, Environment Protection Authority, Victoria SQ, 5000, Adelaide, South Australia, Australia*

[6]*Diamond Light Source Ltd., Diamond House, Harwell Science and Innovation Campus, Didcot, Oxfordshire OX11 0DE, U.K.*

[7]*School of Earth, Atmosphere, and Environment, Monash University, 3800, Clayton, Victoria, Australia*

Paper published in American Mineralogist

Li, K., Pring, A., Etschmann, B., Macmillan, E., Ngothai, Y., O'Neill, B., Hooker, A., Mosselmans, F. & Brugger, J. (2015) Uranium scavenging during mineral replacement reactions.
American Mineralogist, 100(8-9), 1736-1743.

APPENDIX L

CONFERENCE ABSTRACT:

URANIUM TRANSPORT AND DEPOSITION IN IRON-OXIDE-COPPER-GOLD DEPOSITS (IOCG'S): AN EXPERIMENTAL APPROACH

Kan Li[1], Joël Brugger[2,3], Allan Pring[3], Yung Ngothai[1], Barbara Etschmann[3], Jing Zhao[1] and **Edeltraud Macmillan**[2]

[1]*School of Chemical Engineering, The University of Adelaide, Adelaide, SA, 5000, Australia*

[2]*School of Earth and Environmental Sciences, The University of Adelaide, 5000, South Australia, Australia*

[3]*Division of Mineralogy, South Australian Museum, North Terrace, 5000, Adelaide, South Australia, Australia*

Poster presented (by Kan Li) at Goldschmidt 2013, Florence, Italy

Uranium transport and deposition in iron oxide copper gold deposits (IOCG's): An experimental approach

KAN LI[1], JOËL BRUGGER[2,3], ALLAN PRING[2], YUNG NOGTHAI[1], BARBARA ETSCHMANN[2], JING ZHAO[1] AND EDELTRAUD MACMILLAN[3]

[1] School of Chemical Engineering and [3]School of Earth and Environental Scinces, the University of Adelaide, 5005 Adelaide, Australia. Email: kan.li@adelaide.edu.au.
[2]Mineralogy Department, SA Museum, 5000 Adelaide, Australia.

Iron oxides Copper gold type deposits in southern Australia often contain quantities of uranium, both at economic and the subeconomic level. Olympic Dam (OD) is the largest U resources in the World, but uranium also at Prominent and Moonta where the uranium is subeconomic and a problem in ore concentrates. In South Australian IOCG deposits the ores are unusually oxidised, consisting of hematite, with bornite, chalcopyrite and pyrite as the main sulphide minerals. The uranium occurs in a variety of 'primary' minerals including uraninite and brannerite and these minerals exhibit a remarkably diverse range of textures suggesting extensive remoblization.

We initiated an experimental study of hydrothermal mineral reactions in the Fe-Cu-S-U system, focusing in particular on the fate of U during sulphidation reactions. Much of the U in these IOCG deposits is secondary (either remobilised, or added in hydrothermal events postdating Fe-Cu mineralization). Applying the principles of interface coupled dissolution-reprecipitation reactions, we were able to reproduce the IOCG mineral assemblages experimentally by reaction of a Cu-rich fluid with hematite. When U is added to the system as uranyl salt or UO_2(s), U precipitates during the sulphidation reaction. Synchrotron experiments were used to characterize the nature of the U in the ores as well as of U precipitated during sulphidation reactions, information critical for deciphering the mechanism of U scavenging. This information improves our understanding reactions at interfaces with conditions far-from-equilibrium in controlling metal endowment.

The characteristics of an old gas reservoir in Sinian strata, central Sichuan basin, south China

L. LI*, Z. C. WANG, T. S. WANG AND H. JIANG

PetroChina Research Institute of Petroleum Exploration & Development,Beijing,China (*correspondence:liling5551@126.com)

The study region is an important exploration area which has great prospect in Sichuan basin. By analyzing the formation conditions, accumulation periods and characteristics of Sinian gas reservoir in this area, we found that the natural gas is mainly oil cracking gas and the main source rocks were black sapropelic shales at the bottom of Qiongzhusi formation in Lower Cambrian, followed by dark algae dolomite and shale in the third member of Dengying formation. The formation of effective reservoir was controlled by supergene karstification and sedimentary facies. The reservoir was widely distributed with large thickness but strong heterogeneity. The area located at the east high point of an ancient uplift in a long period, whose structual evolution was inherited. It developed large-scale low-amplitude anticline in this region, and the trap formed by top of Sinian System could be 1128km^2, whose closure was over 200 meters [1]. The trap had strong oil and gas capability.

Analysis of the structural evolution history of the region and thermal history of the source rocks showed that: the source rocks in the 3rd member of Dengying Formation started to generate a large sum of hydrocarbon from the Ordovician to Silurian, the liquid hydrocarbon generated accumulated in top of ancient uplift to form paleo-reservoir; the structural uplift at end of the Silurian terminated the first stage of hydrocarbon generation. They entered the second stage of hydrocarbon generation from the Late Permian. While source rocks in Qiongzhusi formation entered the main phase of hydrocarbon generation from the Triassic to the Middle Jurassic, the hydrocarbon accumulated in the weathered crust of Dengying formation at top of ancient uplift to form paleo-reservoir. They entered the main stage of gas generation from the Late Jurassic to the Early Cretaceous, the liquid hydrocarbon of paleo-reservoir cracked to gas, which accumulated as present gas reservoir [2]. The homogenization temperature of fluid inclusion in Sinian carbonate of this area also supported this view.

[1] Zhang Lin, *et al*..(2004),Natural Gas Geoscience15,584-589. [2]Yao Jianjun,et al.(2003),Petroleum Exploration and Development30,7-9.

www.minersoc.org
DOI:10.1180/minmag.2013.077.5.12